

Reactor Design, Modeling and Optimization

for the High-Temperature Methane Pyrolysis and the Reverse Water-Gas Shift Reaction

Zur Erlangung des akademischen Grades eines

Dr.-Ing.

von der Fakultät Bio- und Chemieingenieurwesen
der Technischen Universität Dortmund

genehmigte Dissertation

vorgelegt von

M. Sc. Alejandro Augusto Munera Parra

aus

Bogotá, D.C., Kolumbien

Tag der mündlichen Prüfung: 3. Mai 2018

1. Gutachter: Prof. Dr. David W. Agar
2. Gutachter: Prof. Dr.-Ing. Jörg Sauer

Dortmund 2018

"To my parents:

They made my life so easy that the only thing I had to do was to study."

Acknowledgements

First and foremost, I would like to express my sincere gratitude to Prof. Agar, for giving me the opportunity to conduct my research under his supervision, for the flexibility he allowed me to conduct my research, for his profound insights and knowledge I could draw from every time I needed it and for taken an interest not only in my academic but also in my personal life. It was my pleasure working in his chair during my PhD and I will always look back to those times with great happiness, I can not imagine a better person to have had as an advisor and mentor.

I would also like to thank my thesis committee, Prof. Sauer, for his revision and commentary of my work, and to Prof. Engell and Prof. Gorak, not only for the evaluation of this work but also for being role models I could look up to both during my master studies as well as my research. From both of them I have learned greatly both scientifically and personally, and for that, they have my utmost respect and gratefulness.

A doctoral research cannot be carried out by a single person, I would like to thank all the students, who contributed in greater or lower degree to this work, it was an honor for me having had the responsibility to guide and supervise them and I most definitely grew a lot from those experiences.

To all my colleagues in the CVT chair, thank you for all those years and for providing an environment where it was a pleasure to work in. Special thanks go to Jesus and Mamoon for the long discussions about both scientific and non-scientific topics.

To Julian, Michael and Klaus, thank you for your support on my experimental endeavors, and to Prof. Frank Platte for his support on the applied mathematic topics.

To all the colleagues from the FfPaG project, for all the learnings I could take from such and experienced group of people. Particularly, I would like to thank Dr. Bode for the flawless coordination of the project and for being always ready to help and for the interest he took in me.

To Johnatan, Liliana, Javier, Reinaldo, Kutup, Felipe, Diego, Sergio thank you for your friendship and support during different periods of my stay in Dortmund, from all of you I have learned a lot and you have a special place in my heart.

To Kara, for her support over the years, for proofreading most of the work, and for being such a wonderful person.

Last but no least, to my parents, for everything.

Abstract

In this work, two reactions are studied as a mean to deal with the current CO₂ conundrum.

The first reaction is the high-temperature pyrolysis of methane. This reaction serves as a way to avoid the stoichiometric production of CO₂ when producing hydrogen, which could either be used for energy production or as a base chemical. The second reaction is the reverse Water-Gas Shift (rWGS) reaction. By means of this reaction, CO₂ that is unavoidably produced and has been captured, can be activated to the more reactive CO and subsequently mixed with hydrogen to produce syngas.

For the methane pyrolysis, liquid- and solid-based reactors are studied. The former are reactor concepts based on the use of molten media. Capillary, falling-film and rotating reactors are introduced as alternatives to carry out the pyrolysis with efficient heat transfer and to avoid carbon deposition. Solid-based reactors, in the form of moving-bed, are studied from a theoretical perspective. First the operation stability of the reactor is investigated by means of bifurcation analysis, and then several heat input strategies are modeled and optimized to determine solutions in the short, mid and long-term.

For the rWGS, multifunctional adsorptive reactors are studied as a workaround to the problem of low equilibrium conversion, as well as heat input for more attractive low-temperature rWGS, as compared to the industrially common high-temperature counterpart. Two concepts are investigated; a fixed-bed and a moving-bed reactor. Their potential for optimization is determined, and a comparison between the concepts is achieved.

Contents

Nomenclature	iv
Introduction	1
I. Methane Pyrolysis: Fluid Reactors	11
1. Molten Metal Capillary Reactor	13
1.1. Introduction	13
1.2. Experimental Set-Up	14
1.2.1. Existing Set-Up	14
1.2.2. Modified Set-Up	15
1.2.3. Current Set-Up	16
1.3. Materials and Methods	17
1.4. Experimental Results and Discussion	17
1.4.1. Methane Pyrolysis in Existing Set-Up	17
1.4.2. Wettability of Alloys	20
1.4.3. Operation of the Modified Set-Up	21
1.4.4. Operation of Current Set-Up	23
1.5. Conclusions	24
2. Falling-Film Reactor	27
2.1. Introduction	27
2.2. Experimental Set-up and Materials	29
2.2.1. Falling-Film Reactor	29
2.2.2. Rotating Reactor	30
2.2.3. Materials	31
2.3. Mathematical Modeling	31
2.3.1. Liquid Phase	31
2.3.2. Gas Phase	34
2.3.3. Carbon Formation	36
2.3.4. Numerical Methods	37
2.4. Results and Discussion	38
2.4.1. Falling-Film Reactor	38

2.4.2. Rotating Reactor	46
2.5. Conclusions	48
II. Methane Pyrolysis: Moving-Bed Reactor	51
3. Multiplicities in Moving-Bed Reactors	53
3.1. Introduction	53
3.2. Mathematical Modeling	54
3.2.1. General Model	54
3.2.2. Model for the Pyrolysis of Methane	54
3.3. Numerical Methods	56
3.4. Results	57
3.4.1. Previous Work	57
3.4.2. Model Extension	58
3.4.3. Methane Pyrolysis	65
3.5. Conclusions	69
4. Heat Input Strategies	72
4.1. Introduction	72
4.2. Mathematical Modeling	74
4.2.1. Side-Stream	75
4.2.2. Plasma	76
4.2.3. Resistive Heating	78
4.3. Numerical Methods	78
4.4. Results	80
4.4.1. Simulation Results	80
4.4.2. Optimization Results	82
4.4.3. CO ₂ -Emissions and Technical Feasibility	94
4.5. Conclusions	96
III. Reverse Water-Gas Shift Reaction	99
5. Fixed-Bed Adsorptive Reactor	101
5.1. Introduction	101
5.2. Problem Definition	102
5.3. Mathematical Modeling	103
5.3.1. Molar Balances	103
5.3.2. Energy Balances	104
5.3.3. Velocity Profile	105
5.4. Numerical Methods	105
5.4.1. Cyclic Steady-State	105
5.4.2. Optimization	106

5.5. Results	107
5.5.1. Calculation of the CSS	107
5.5.2. Analysis of System	108
5.5.3. Optimization	112
5.6. Conclusions	116
6. Moving-Bed Adsorptive Reactor	118
6.1. Introduction	118
6.2. Mathematical Modeling	121
6.3. Numerical Methods	124
6.4. Results	125
6.4.1. Modeling and Simulation	125
6.4.2. Optimization	130
6.5. Summary and Conclusions	137
Conclusions	139
Bibliography	145
A. Supplementary Data to Chapter 2	157
A.1. Material Properties	157
A.2. Heat and Mass Transfer Correlations	158
B. Supplementary Data to Chapter 4	159
C. Supplementary Data to Chapter 5	165
D. Supplementary Data to Chapter 6	168
Curriculum Vitae	173

Nomenclature

Due to the breadth and distribution of the topics covered in this work, the nomenclature is given for each chapter separately.

Chapter 1

Abbreviations

GaInSn Gallium Indium Tin eutectic
IASS Institute For Advanced Sustainability Studies e.V.

Symbols

Ca	/ –	Capillary number ($\frac{\mu \cdot u_{TP}}{\sigma}$)
ΔH_R	/ J mol ⁻¹	Enthalpy of reaction
ΔG_R	/ J mol ⁻¹	Gibbs free energy of reaction
k	/ s ⁻¹	Reaction rate constant
L	/ m	Length
P	/ Pa	Pressure
R	/ J mol ⁻¹ K ⁻¹	Ideal gas constant
T	/ K	Temperature
u	/ m s ⁻¹	Velocity
X	/ –	Conversion
z	/ m	Axial coordinate

Greek Symbols

β_G	/ –	Gas fraction in the slug-flow
μ	/ Pa s	Dynamic viscosity
σ	/ N m ⁻¹	Interfacial tension
τ	/ s	Mean residence time

Sub- and Superscripts

- 0 Initial/at standard conditions
- G Relative to the gas phase
- L Relative to the liquid phase
- N Normal conditions
- R Reaction/reactor
- TP Two-phase

Chapter 2

Abbreviations

FLiNaK	Lithium, Sodium and Potassium Fluoride eutectic
GaInSn	Gallium Indium Tin eutectic
ODE	Ordinary differential equation
PDE	Partial differential equation

Symbols

A	/ m ²	Area
A_{rad}	/ –	Geometry dependent absorption coefficient
C	/ mol m ⁻³	Concentration
c_p	/ J mol ⁻¹ K ⁻¹	Heat capacity
d	/ m	Diameter
dW	/ m	Wall thickness
E_A	/ J mol ⁻¹	Activation energy
f	/ –	Friction factor
\vec{f}	/ –	Vector of residuals
g	/ m s ⁻²	Gravitational constant
ΔG_R	/ J mol ⁻¹	Gibbs free energy of reaction
h	/ W m ⁻² K ⁻¹	Heat transfer coefficient
h_m	/ m s ⁻¹	Mass transfer coefficient
H	/ J mol ⁻¹	Enthalpy
ΔH_R	/ J mol ⁻¹	Enthalpy of reaction
k_{hom}	/ s ⁻¹	Reaction rate constant for the homogeneous reaction
k_{het}	/ m s ⁻¹	Reaction rate constant for the homogeneous reaction
K	/ –	Equilibrium constant
L	/ m	Length
\dot{m}	/ kg s ⁻¹	Mass flow
N	/ –	Number of discretization points
\dot{n}	/ mol s ⁻¹	Molar flow
P	/ Pa	Pressure
\dot{Q}	/ W m ⁻²	Heat flux
r	/ mol m ⁻³ s ⁻¹	Reaction rate
R	/ J mol ⁻¹ K ⁻¹	Ideal gas constant
s_{gl}	/ m	Equivalent layer thickness
T	/ K	Temperature
U	/ W m ⁻² K ⁻¹	Overall heat transfer coefficient
\dot{V}	/ m ³ s ⁻¹	Volumetric flow rate
w	/ m s ⁻¹	Velocity
x	/ m	Radial coordinate

\vec{x}	/ –	Vector of independent variables
X	/ –	Conversion
z	/ m	Axial coordinate

Greek Symbols

Γ	/ $\text{m}^2 \text{s}^{-1}$	Volume flow rate per unit of wetted perimeter
δ	/ m	Thickness
ϵ	/ –	Emission coefficient
λ	/ $\text{W m}^{-1} \text{K}^{-1}$	Thermal conductivity
η	/ Pa s	Dynamic viscosity
θ	/ °	Contact angle
ρ	/ kg m^{-3}	Density
σ	/ N m^{-1}	Interfacial tension
σ_B	/ $\text{W m}^{-2} \text{K}^{-4}$	Boltzmann constant
τ	/ N m^{-2}	Shear stress

Sub- and Superscripts

0	Initial/at standard conditions
C	Based on concentration/Relative to carbon
G	Relative to the gas phase
GL/LG	Relative to the gas-liquid interphase
het	Relative to the heterogeneous reaction
hom	Relative to the homogeneous reaction
inter	At the interphase
mol	Molar property
L	Relative to the liquid phase
N	Normal conditions
P	Based on pressure
R	Reaction/reactor
rxn	Relative to reaction
rad	Relative to heat transfer by radiation
W	Wall
WL	Wall-Liquid

Chapter 3

Abbreviations

CCS	Carbon Capture and Storage (or Sequestration)
MSS	Multiple Steady-States
OCFE	Orthogonal Collocation on Finite Elements
SS	Steady-State
SSS	Single Steady-State

Symbols

a	/ $\text{m}^2 \text{m}^{-3}$	Specific surface area
A	/ –	Derivative matrix
a_1	/ –	Parameter for the Gnielinski correlation
b	/ –	Vector including non-linearities
b_1	/ –	Parameter for Nusselt correlation
B	/ –	Benchmark
C	/ mol m^{-3}	Concentration
c_p	/ $\text{J mol}^{-1} \text{K}^{-1}$	Heat capacity
Da	/ –	Damköhler number
E_A	/ J mol^{-1}	Activation energy
F_1	/ –	Ratio of gas to solid molar flow-rates
F_2	/ –	Ratio of gas to solid thermal energy
g	/ –	Value representing the equation relating the arc-length and the variables
G	/ –	System of equations describing the system
ΔG_R	/ J mol^{-1}	Reaction free energy
h	/ $\text{W m}^{-2} \text{K}^{-1}$	Heat transfer coefficient
ΔH_R	/ J mol^{-1}	Reaction enthalpy
I	/ A	Electric current
J	/ –	Jacobian matrix
k	/ s^{-1}	Reaction rate constant
K_c	/ –	Concentration based equilibrium constant
K_p	/ –	Pressure based equilibrium constant
K	/ –	Arbitrary equilibrium constant
K_2	/ –	Arbitrary adsorption constant
L	/ m	Reactor length
N	/ mol s^{-1}	Molar flowrate
δn	/ mol	Change in the number of mols
P	/ Pa	Pressure
Pr	/ –	Prandtl number
Q	/ W	Heat flow

r	/ mol m ⁻³ s ⁻¹	Reaction rate
R	/ J mol ⁻¹ K ⁻¹	Ideal gas constant
Re	/ –	Reynold's number
s	/ –	Arc-length parameter
St	/ –	Stanton number
T	/ K	Temperature
ΔT_{ad}	/ K	Adiabatic temperature rise/decrease
U	/ V	Electric potential
U	/ –	Vector containing lumped variables
V	/ m ³	Volume
x	/ –	Conversion
z	/ m	Length coordinate

Greek Symbols

γ	/ –	Arrhenius number
λ	/ –	Parameter for constructing bifurcation curves
ν	/ –	Current step in the correction procedure
ξ	/ –	Dimensionless reactor length
ρ	/ Ω m	Electrical resistivity
ϕ	/ –	Temperature and conversion dependence on the Damköhler number

Sub- and Superscripts

0	At feed/initial conditions
*	Dimensionless
A	Related to component A
ad	Adiabatic
B	Related to component B
C	Carbon
con	Converged
eq	Equilibrium
g	Gas phase related
g,s	Related to both solid and gas phases
in	Initial
M	Medium
n	Step n of a continuation procedure
R	Reaction
ref	Reference
s	Solid phase related
sol	Solution
x	Related to either gas or solid phase

Chapter 4

Abbreviations

rhs Right-hand-side
 SMR Steam Methane Reforming

Symbols

A	/ m ²	Area
C	/ mol m ⁻³	Concentration
c_p	/ J mol ⁻¹ K ⁻¹	Heat capacity
d/D	/ m	Diameter
f	/ varied	Objective function
F	/ mol s ⁻¹	Molar flow
ΔG_R	/ J mol ⁻¹	Gibbs free energy of reaction
h	/ W m ⁻² K ⁻¹	Heat transfer coefficient
ΔH_R	/ J mol ⁻¹	Enthalpy of reaction
I	/ A	Electrical current
k	/ s ⁻¹	Reaction rate constant
K_C	/ -	Concentration-based equilibrium constant
K_P	/ -	Pressure-based equilibrium constant
L	/ m	Length
N_{pts}	/ -	Number of discretization points
Nu	/ -	Nusselt number
P	/ bar	Pressure
Pr	/ -	Prandtl number
Q	/ W	Heat flow
R	/ Ω	Electrical resistance
r	/ mol m ⁻³ s ⁻¹	Reaction rate
Re	/ -	Reynold's number
T	/ K	Temperature
U	/ V	Voltage
V	/ m ³	Volume
X	/ -	Conversion
y	/ -	Molar fraction

Greek Symbols

ϵ	/ -	Porosity
κ	/ W m ⁻¹ K ⁻¹	Thermal conductivity
θ	/ -	Dimensionless temperature

ρ	/ Ω m	Electrical resistivity
ϑ	/ mixed	Vector of decision variables
ψ	/ mixed	Vector of additional decision variables
ξ	/ –	Dimensionless axial coordinate

Sub- and Superscripts

bottom	Bottom region of the reactor for the resistive heating strategy
C	Related to carbon
feed	At the feed of the side-stream and plasma strategies
G	Related to the gas phase
inlet	At the inlet. For gas bottom of the reactor, for solids top of the reactor
input	Self-explanatory
middle	Middle region of the reactor for the resistive heating strategy
mix	At mixing point in the side-stream strategy
out	At the point of stream removal in the side-stream strategy
p	Particle
plasma	Related to the plasma strategy
pre-mix	Related to the stream coming into the mixing point
R	Pertaining to the reactor
recom	Related to the recombination of the hydrogen atoms
rxn	Related to the pyrolysis reaction
S	Related to the solid phase
side	Related to the side-stream in the side-stream strategy
start	Initially available temperature for the side-stream strategy
T	Total
top	Top region of the reactor for the resistive heating strategy

Chapter 5

Abbreviations

CCS	Carbon Capture and Storage (or Sequestration)
CSS	Cyclic Steady-State
DS	Direct substitution
FD	Full discretization
LDF	Linear Driving Force
MADS	Mesh Adaptive Direct Search
NOMAD	Nonlinear Optimization by Mesh Adaptive Direct Search
NLOpt	Non-linear Optimization
ODE	Ordinary differential equation
PDE	Partial differential equation
PSWARM	Particle Swarm
rWGS	Reverse Water-Gas Shift
STY	Space-Time Yield

Symbols

b	/ Pa ⁻¹	Parameter for Langmuir isotherm
C	/ mol m ⁻³	Concentration
c_p	/ J mol ⁻¹ K ⁻¹	Heat capacity
D	/ m	Diameter
K_{eq}	/ –	Equilibrium constant
k_G	/ m s ⁻¹	Overall mass transfer coefficient
k_{LDF}	/ s ⁻¹	Mass transfer coefficient for adsorption
f_1	/ mol m ⁻³ s ⁻¹	Objective function for the STY
f_2	/ mol m ⁻² s ⁻¹	Objective function for fixed reactor length
F_p	/ –	Correction term for the rWGS kinetics
h	/ W m ⁻² K ⁻¹	Heat transfer coefficient
ΔH_R	/ J mol ⁻¹	Change of enthalpy
L	/ m	Length
N	/ –	Number of discretization points/ reactor sections
Nu	/ –	Nusselt number
p	/ Pa	Partial pressure
P	/ Pa	Total pressure
Pr	/ –	Prandtl number
q	/ mol kg ⁻¹	Adsorbent loading
r	/ mol m ⁻³ s ⁻¹	Reaction rate
R	/ J mol ⁻¹ K ⁻¹	Ideal gas constant
R	/ m	Radius
Re	/ –	Reynold's Number

t	/ s	Time
T	/ K	Temperature
u	/ m s ⁻¹	Velocity
x	/ m	Axial coordinate
y	/ –	Molar fraction

Greek Symbols

γ	/ –	Parameter for Langmuir isotherm
δ	/ –	Parameter for Langmuir isotherm
ϵ	/ –	Porosity
ϑ	/ mixed	Vector of decision variables
ν	/ –	Stoichiometric coefficient
ρ	/ kg m ⁻³	Density
τ	/ –	Tortuosity
ϕ	/ –	Fraction of either catalyst or adsorbent in the bed
Ψ	/ mixed	Vector containing the variables (temperature, molar fractions, velocity)

Sub- and Superscripts

0	Initial/standard conditions
ads	Adsorbent
bed	Referring to the fixed-bed
cat	Catalyst
cycle	Operating cycle
eff	Effective
eq	Equilibrium
G	Gas phase
GS	Pseudo-homogeneous
GW	Between gas and wall
initial	At the start of operation
inlet/in	At reactor inlet
max	Maximum
outlet	At the reactor outlet
p	Particle
prod	Product
R	Reactor
reg	Regeneration
rxn	Reaction
s	Saturation
start	Start of the product production
step	Step of a cycle
T	Total
W	Wall

Chapter 6

Abbreviations

CCS	Carbon Capture and Storage (or Sequestration)
CCU	Carbon Capture and utilization
CCUS	Carbon Capture, Utilization and Sequestration
COP	Conference of the Parties
LDF	Linear Driving Force
MADS	Mesh Adaptive Direct Search
NOMAD	Nonlinear Optimization by Mesh Adaptive Direct Search
ODE	Ordinary differential equation
rWGS	Reverse Water-Gas Shift
SMB	Simulated Moving Bed
STY	Space-Time-Yield
VNS	Variable Neighborhood Search

Symbols

A	/ m^2	Area
b	/ Pa^{-1}	Parameter for Langmuir isotherm
c	/ mol m^{-3}	Concentration
C	/ mol m^{-3}	Dimensionless concentration
cp	/ $\text{J mol}^{-1} \text{K}^{-1}$	Heat capacity
D	/ m	Diameter
Da	/ –	Damköhler number
Keq	/ –	Equilibrium constant
kG	/ m s^{-1}	Overall mass transfer coefficient
$kLDF$	/ s^{-1}	Mass transfer coefficient for adsorption
$f1$	/ $\text{mol m}^{-2} \text{s}^{-1}$	First objective function (molar flux)
$f2$	/ mol kg^{-1}	Second objective function (outlet adsorbent loading)
Fp	/ –	Correction term for the rWGS kinetics
h	/ $\text{W m}^{-2} \text{K}^{-1}$	Heat transfer coefficient
	/ J mol^{-1}	Change of enthalpy
L	/ m	Length
N	/ –	Number of discretization points/Number of reactor sections
	/ $\text{mol m}^{-2} \text{s}^{-1}$	Mole flux
Nu	/ –	Nusselt number
p	/ Pa	Partial pressure
P	/ Pa	Total pressure
Pe	/ –	Péclet number
Pr	/ –	Prandtl number
q	/ mol kg^{-1}	Adsorbent loading

Q	/ –	Dimensionless adsorbent loading
r	/ mol m ⁻³ s ⁻¹	Reaction rate
R	/ J mol ⁻¹ K ⁻¹	Ideal gas constant
R	/ m	Radius
Re	/ –	Reynold's Number
St	/ –	Stanton Number
t	/ s	Time
T	/ K	Temperature
u	/ m s ⁻¹	Velocity
U	/ –	Dimensionless velocity
V	/ m ³	Volume
x	/ m	Axial coordinate
X	/ –	Dimensionless axial coordinate
y	/ –	Molar fraction

Greek Symbols

γ	/ –	Parameter for Langmuir isotherm
δ	/ –	Parameter for Langmuir isotherm
ϵ	/ –	Porosity
ϑ	/ mixed	Vector of decision variables
κ	/ –	Parameter describing the change in thermal conductivity
λ	/ J K ⁻¹ m ⁻¹ s ⁻¹	Thermal conductivity
ν	/ –	Stoichiometric coefficient
ρ	/ kg m ⁻³	Density
τ	/ –	Tortuosity
τ	/ s	Mean residence time
ϕ	/ –	Fraction of either catalyst or adsorbent in the bed
θ	/ –	Dimensionless temperature
Ψ	/ mixed	Vector containing the variables (temperature, molar fractions, velocity)

Sub- and Superscripts

0	Initial/standard conditions
ad	Adiabatic
ads	Adsorbent
bed	Referring to the moving-bed
cat	Catalyst
eff	Effective
eq	Equilibrium
G	Gas phase
GS	Between gas to solid
GW	Between gas and wall
inlet/in	At reactor inlet
max	Maximum

Nomenclature

mf	Minimum fluidization
outlet	At the reactor outlet
p	Particle
prod	Product
R	Reactor
rxn	Reaction
s	Saturation
S	Solid phase
SG	Between solid and gas
SW	Between solid and wall
T	Total
W	Wall

Introduction

Motivation

In the past few decades, the human population has rapidly increased. The question of how energy and commodities will be provided for the expected increase in the standard of living is now pressing. Furthermore, this population growth and its concomitant industrialization has led to an increase in carbon dioxide concentration in the atmosphere.

Concerns about the resulting climate change led to the adoption of the Paris Agreement after the COP21 meeting (UNFCCC. Conference of the Parties (COP) 2015). The proposed goal is to minimize CO₂ emissions in order to keep the mean global temperature increase below 2 °C. To accomplish this goal, it is clear that drastic reductions must be achieved in all CO₂ emitting industries.

In some industries, CO₂ is avoidable and so-called CO₂-free technologies have started to emerge. Nonetheless, when CO₂ emissions are unavoidable, it is crucial to address what needs to be done with the CO₂ produced.

In this work, a solution for each of the two cases is proposed based on the application of reaction engineering methodology to conceive, design, model, and optimize reactor concepts that either circumvent the CO₂ emissions or allow the utilization of CO₂. The proposed solutions are the high-temperature pyrolysis of methane for the former, and the reverse Water-Gas Shift (rWGS) reaction for the latter. These reactions are introduced in the following sections.

Methane Pyrolysis

Nowadays, energy production is mainly based on fossil fuels and to some extent in nuclear energy. However, each one of them has received major criticism and alternatives have been gaining increasing interest in the last couple of years.

Nuclear energy, once thought to be the energy of the future due to its high power generation and minor emissions, has had major setbacks due to large-scale accidents, Fukushima being the latest (2011). In addition, no satisfactory solution has been found regarding the difficulty of dealing with the nuclear waste in an effective and hazardless way. A new generation of reactors is actively being researched and plans for commercial deployment by 2020-2030 are being set (Abram and Ion 2008). How-

ever, some countries, Germany included, have started to plan a nuclear-free energy production economy. Following Fukushima, eight of seventeen nuclear power plants in Germany were shut down and by 2022 there will be no more in operation.

Fossil fuels, on the other hand, have been the primary source of energy since the discovery of fire, starting with wood, followed by with coal, oil, and natural gas in the last decades. It was once thought that humanity was on the verge of exhausting its reserves. However, over the past couple decades, the world's proven natural gas reserves have been increasing steadily, from 2592 trillion cubic feet in 1980 to 6972 trillion cubic feet in 2014 (*International Energy Statistics*), and if non-conventional sources like methane hydrates or shale gas are included, the availability could be greater.

Besides nuclear and fossil fuels, a surge in renewable energy sources has occurred. Lots of effort has been given to renewable and sustainable energies like solar and wind power production. Solar energy presents itself as unlimited, free and, in principle, free of negative environmental connotations. On the other side, solar energy is not very concentrated, is intermittent and not evenly distributed across the globe.

Wind power production has also been increasing steadily over the last years, but the environmental impacts are still unknown and as in the solar energy, it is not equally distributed across the globe. Improvements in power grid optimization and alternatives for storing excess energy are currently being developed, which in the long-term will eliminate most of those disadvantages.

As renewable energies seem to be the long-term solution, with recently proposed road-maps for most countries, for a full transition in 2050 (Jacobson et al. 2017) there is still a gap to be filled regarding the short- and mid-term solutions, and, in addition, the agreement upon the policies must be first agreed upon. Thus, continuing the path of the decarbonization seems to be the logical way. Hydrogen has been seen as the most viable option for a secondary energy carrier since at least the late 80's (Steinberg 1989; Veziroglu 1987) and a consensus supporting this view seems to have been reached by the beginning of the 21st century (Ausubel 2000; Barreto et al. 2003; Dicks 1996; Dunn 2002; Gaudernack and Lynum 1998; Kreysa 2009; Marbán and Valdés-Solís 2007; Moriarty and Honnery 2007; Muradov 2000, 2001; Muradov et al. 2005; Steinberg 1999; Turner 1999). More recent studies also point in the same direction (Machhammer et al. 2016; Muradov 2017; Weger et al. 2017).

Hydrogen is the ultimate energy carrier in the increasing chain of hydrogen to carbon ratio throughout history (wood: ~ 0.1 , coal: 1, oil: 2, methane: 4, hydrogen: ∞) and can be used to produce energy without any harmful emissions. In addition, a transition from natural gas and fossil fuels to hydrogen in the short-term will be possible due to the already existent infrastructure. As a secondary energy carrier, the process used to produce the hydrogen will determine whether additional emissions are produced or not.

As of today (2018) up to 98% of the hydrogen produced, relies either directly or indirectly, i.e. electricity source, on fossil fuel utilization (Muradov 2017). Worldwide, the most common processes for producing hydrogen are: steam reforming ($\sim 40\%$), partial oxidation ($\sim 25\%$), reforming of benzene ($\sim 20\%$ by-product), and gasification ($\sim 10\%$ by-product), with electrolysis, plasma pyrolysis and chlor-alkali with minor contributions. All these processes produce CO_2 and thus partly defeat the purpose

Table 0.1.: CO₂ emissions in kg CO₂ per kg H₂ for hydrogen producing technologies from (Muradov 2017)

Process	Feedstock	Reaction (net)	CO ₂ /H ₂ ratio (kg/kg)	
			Stoichiometric	Process (plant + electricity)
Steam reforming	Natural gas	CH ₄ + 2H ₂ O → CO ₂ + 4H ₂	5.5	8.7-10.4
Steam reforming	Naphta	C ₆ H ₁₄ + 12H ₂ O → 6CO ₂ + 19H ₂	6.9	10.5
Partial oxidation	Natural gas	CH ₄ + 1/2O ₂ + H ₂ O → CO ₂ + 3H ₂	7.3	9-10
Gasification	Heavy residual oil	CH _n + 1/2O ₂ + xH ₂ O → CO ₂ + yH ₂	13.7 (for n=1.2)	17-21
Gasification	Coal	CH _n + 1/2O ₂ + xH ₂ O → CO ₂ + yH ₂	15.7 (for n=0.8)	19-24
Plasma pyrolysis	Natural gas	CH ₄ + Electricity → C + 2H ₂	0	12
Electrolysis	Water	H ₂ O + Electricity → H ₂ + 1/2O ₂	0	24-28

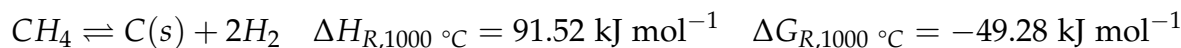
of a clean energy production via hydrogen. The emissions associated to each process have been compiled by Muradov (2017) and are presented in Table 0.1.

In order to reduce the emissions associated with the production of hydrogen, several alternatives have been proposed: the first alternative is the so-called carbon capture and storage/sequestration (CCS) of the CO₂ produced in the above mentioned processes. However, the technology lacks public acceptance and does not offer a short-term solution. The main challenges in CO₂ sequestration are still: (i) reduction of costs, (ii) understanding of long term risk factors and (iii) quantification and understanding of reservoir options (Muradov and Veziroglu 2008; Muradov 2017).

Another alternative to produce hydrogen without CO₂ emissions is the use of nuclear reactors coupled with water electrolysis or thermo-chemical water-splitting cycles. This alternative is, however, bound to nuclear energy and as already mentioned has its advantages and disadvantages.

The final alternative deals with the problem in a different way. Instead of trying to deal with an already produced CO₂, it could be more effective not to produce CO₂ in the first place. In the past two decades, the pyrolysis of methane has gained the attention of researchers as a CO₂-free/near-zero/ultra-low/low hydrogen production route. The definition for the last three terms is given by Muradov (2017) and depicted in Figure 0.1.

The pyrolysis of methane:



has as products solid carbon and hydrogen. For this process to be economically feasible, it is important to bear in mind that carbon has to be sold as by-product and depending on the carbon formed, it can be even more cost effective than the state of the art (Muradov and Veziroglu 2008). Possible carbon utilization areas include the steel industry, carbon as a structural and force resisting material in both tensile and compressive applications for example (Muradov and Veziroglu 2008).

The pyrolysis reaction is endothermic and becomes thermodynamically spontaneous at 820 K and kinetically feasible at temperatures around 1073 K. However, in order to break the strong C-H bond, very high temperatures are required, which in principle is not an attractive option. In theory, it could be possible to operate the reaction at lower temperatures. For this, several options have been investigated:

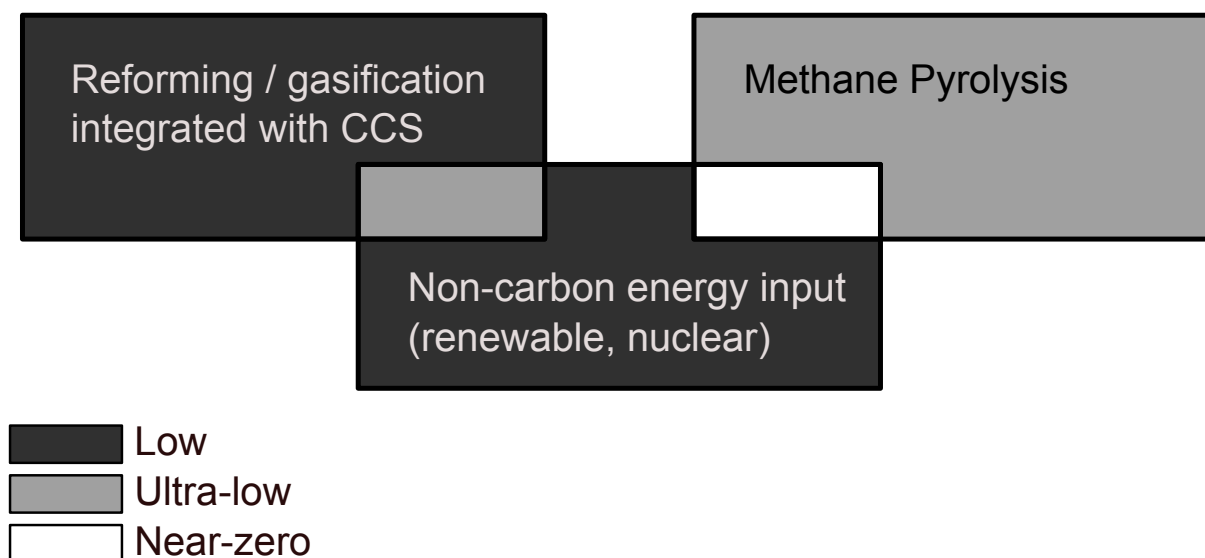


Figure 0.1.: Levels of CO₂ emissions associated to hydrogen production technologies, adapted from (Muradov 2017)

The first one was to use a metal catalyst at moderate temperatures (500-700 °C). This option is appealing first due to the decreased energy demands and the possibility to form valuable by-products like carbon nanotubes and filamentous carbon, which could compensate the price of the catalyst. Several transition metal catalysts have been investigated (Abbas and Wan Daud 2010; Szymanska et al. 2015). Regeneration of the catalysts due to carbon deposition (in some cases burning of the carbon, producing CO₂) with its inherent activity loss, and sensibility to other compounds which can be present in natural gas (like sulfur), remain as challenges to be solved. In addition, the thermodynamics of the reaction does not allow for high conversions and the problems of downstream processing and stream recycles remain to be solved efficiently.

The use of carbon catalysts was proposed as an alternative to metal catalysts since they are cheaper, thermally more stable and, in principle, should not be deactivated by carbon deposition. Additionally, the reaction product could be used as a catalyst itself. Several types of carbon including carbon black, activated carbon, among others, were investigated experimentally by several researchers (Bai et al. 2005; Bautista et al. 2008; Kim et al. 2004; Muradov 2000; Suelves et al. 2007). Temperatures up to 1000-1100 °C have been investigated.

However, experimental results have shown that activity from different types of carbon catalysts is lost with time and that sometimes, the formed carbon cannot be used as a catalyst itself, which eliminates some of the advantages previously mentioned. In addition, as with the metal catalyzed reactors, this process is thermodynamically limited and requires additional efforts in the downstream processing.

The final alternative is then the use of a non-catalytic high-temperature methane pyrolysis. The main challenges in the operation of this reaction are the carbon deposition and the need to introduce heat for the endothermic reaction at high temperatures.

To circumvent those issues, the pyrolysis of methane has been carried out in several reactor types: plasma reactors (Czernichowski and Czernichowski 2000; Fincke et

al. 2002; Fulcheri and Schwob 1995; Nozaki et al. 2002; Potapkin et al. 1999), solar reactors (Abanades and Flamant 2006; Dahl et al. 2001; Hirsch 2001; Kogan and Kogan 2003; Maag et al. 2009; Ozalp et al. 2009; Rodat et al. 2009; Steinfeld et al. 1997), microwave heated reactors (Domínguez et al. 2007), fluidized-, moving- and packed-beds (Dunker and Ortmann 2006; Jahnig et al. 1964; Muradov 2000; Pinilla et al. 2007), bubble columns (Abánades et al. 2016; Geissler et al. 2015, 2016; Gulevich et al. 2008; Martynov et al. 2005; Parkinson et al. 2017; Paxman et al. 2014; Steinberg 1999; Tyrer 1931), slag reactors (Kashiwaya and Watanabe 2012), micro-reactors (Schultz and Agar 2015; Serban et al. 2003), double walled reactors (Abanades et al. 2009) and porose-wall reactors (Schultz and Agar 2015). Reviews by Muradov and Veziroglu (2008) and by Abbas and Wan Daud (2010) sum up the works in the area of methane decomposition in the 2000s, and a more recent review by Muradov (2017) sums up the developments since.

As can be seen, solar reactors have attracted the most research attention during the 2000s. A pilot plants has already been built (Rodat et al. 2010), with 1 MW capacity, and a 55 MW plant has been proposed (Rodat et al. 2011). Reviews of the topic have been written by Steinfeld (2005), Pregger et al. (2009) and Ozalp et al. (2009). As promising as solar energy is, it is bound to work only in specific regions of the earth if high efficiency wants to be obtained. Therefore the search for other alternatives keeps being of high priority.

From the reactors used, two classifications can be observed. The first category is the use of different media as heat carrier. The options are: gas-based, as in the porose-wall reactor; liquid-based, like the bubble columns; solid-based, as in the fluidized bed; and plasma-based. The second classification is given depending on the method of heat input. The methods are given by Agar (2003) as recuperative, regenerative, reactive, convective and electromagnetic.

In this work, several concepts are studied in order to achieve technically feasible reactor configurations that overcome the main challenges faced. In the outline, it is described how those concepts are based on the above mentioned classifications.

Reverse Water-Gas Shift Reaction

In the previous section, an alternative to dealing with CO₂ emitting industries, when the emissions are avoidable was presented. However, in some cases, as in the cement industry, there exists no alternative technology which does not emit CO₂. For those cases it is necessary to find a use for the produced CO₂.

As mentioned already in the previous section, the storage of the produced CO₂ via CCS lacks public acceptance. Nonetheless, the technologies for capture are mostly well developed and thus, should the CO₂ be captured, it could be seen as a potential chemical feedstock. This approach is now referred to as carbon capture and utilization (CCU). It has been calculated (Aresta 2010) that a 10% of the total emissions could be recycled via this approach, and thus, the net amount of CO₂ emitted would be reduced accordingly. In addition, some authors have mentioned the possibility of joint sequestration and utilization (CCUS) as another viable alternative (Hasan et al.

2015).

The main problem with CO₂ is that being the end product of any combustion process, it is a relatively non-reactive molecule and processes to use it on an industrial scale are few and far between. A recent review by Klankermayer et al. (2016) elucidates the various transformations for CO₂ and classifies them according to the reduction level and the bond-forming processes. From an application point of view, it divides them into high-volume and high-value products.

For the sake of reducing emissions it is clear that high-volume products are of interest. These include methanol, formaldehyde and formic acid derivatives. These products can not only be used as base chemicals, but they also have potential as energy carriers or storage systems. The common denominator in these products is the need for hydrogen in the reactions involved. For these processes to be environmentally friendly it is thus necessary to have a source for low-CO₂ hydrogen, this can be either generated via renewable powered electrolysis, or by low-CO₂ methods such as the pyrolysis of methane introduced in the previous section.

At the core of these reaction networks, the reverse water-gas shift (rWGS) reaction is encountered:



this reaction is endothermic and can be used to activate CO₂ to more reactive CO, which in turn can be turned to formic acid via carbonylation, or it can be mixed with hydrogen to obtain syngas. Syngas can namely be employed, among other processes, in the Fischer-Tropsch, methane or methanol synthesis (Baliban et al. 2012).

Industrially, the rWGS reaction has not been used for this purpose and is mostly used to control the C/H ratio in gas mixtures. The main challenge in carrying out this reaction is the unfavorable equilibrium which requires high temperatures, around 600 °C in theory but commonly over 800 °C, for reasonable conversions. As with the methane pyrolysis, the introduction of heat for an endothermic reaction at high temperatures is unattractive.

To circumvent both those issues, a low-temperature adsorptive reactor, around 250 °C, has been proposed as a solution (Agar 2005). By removing the water vapor formed via selective adsorption, the equilibrium can be shifted to the products side. In addition, the exothermicity of the adsorption provides with the heat necessary for the reaction to take place, minimizing the need for external heat input.

As with the methane pyrolysis, in this work different reactor configurations were studied to prove their technical feasibility.

Preliminary Work and Outline

As already suggested, this work is divided into two main parts; the first concerning the methane pyrolysis as a mean to produce low-CO₂ hydrogen, and the second regarding the rWGS as a method to activate CO₂.

The first part on its own could be divided into four main parts. Gas-based, liquid-based, solid-based and plasma-based reactors. As for plasma reactors, when plasma

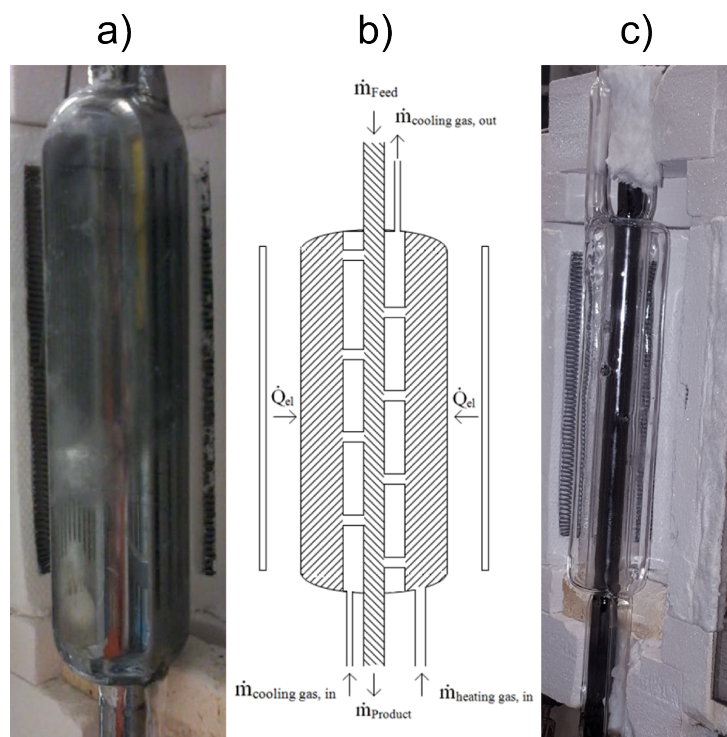


Figure 0.2.: Gas-based concepts: a) Porose-wall reactor with outer chamber carbon deposition (Hellmann 2013) b) Improved side-jet reactor concept. c) Experimental result with carbon deposition in the inner chamber of the side-jet reactor

is the only medium present, technical solutions have been already tested as in the Kvaerner process, and thus it was decided not to study this alternative.

For gas-based reactors, the only purely gas-based reactor was that of the porose-wall reactor (Schultz and Agar 2015). From that concept, it was clear that, using the current set-up, it was not possible to suppress methane diffusion into the outer chamber, as shown in Figure 0.2a, where the carrier gas was preheated, and thus, the advantage that was aimed for was not attained.

As an alternative, it was thought that a side-jet reactor as depicted in Figure 0.2b, could be a potential improvement, since the increased velocity at the jets would impede the methane diffusion. Nonetheless, preliminary studies showed that, although the methane diffusion was suppressed, it was not possible to suppress carbon formation in the inner wall for high-conversion operation, as seen in Figure 0.2c, even after testing some cooling concepts for the wall. Thus it was decided to not pursue gas-based concepts since their feasibility was limited.

Therefore, only two options remained; the liquid-based reactors and the solid-based reactors.

Part one of this work deals with the liquid-based reactor concepts. Liquid media present themselves as attractive solutions for the challenges in carrying out the pyrolysis of methane. On one hand, the molten medium offers excellent heat transfer properties, and also shields the wall from the carbon deposition, thus allowing for the simplest of the heat input methods, i.e. a mixture of convective and recuperative heat.

- Chapter 1 introduces the use of molten media for a capillary reactor based on

the work of Schultz and Agar (2015). The improvements of the shortcomings encountered in that work and the modifications of the set-up to improve its operability are presented there.

- Chapter 2 introduces a falling-film reactor as an improvement for the shortcomings found in the capillary reactor, as well as discusses the possibility of using molten salts instead of metals. In addition, a rotating reactor is presented as a fall-back concept should the falling-film reactor not be adequate.

Part two deals with the solid-based reactors. In this case only the moving-bed reactor is studied as a feasible solution. Fixed-bed concepts are not possible to operate due to carbon deposition leading to the blockage of the reactor. Other options as fluidized-bed reactors, although providing excellent heat transfer, are limited in particle size. Additionally, the inherent back-mixing of its operation as well as the attrition caused by the particles make its use unappealing.

- Chapter 3 deals with an interesting behavior present in moving-bed reactors which is the possibility of multiple steady-states in its operation. First, a generalized model is developed and the influence of several model adaptations is presented, finishing with the application of the results for the pyrolysis of methane.
- Chapter 4 presents the strategies that are available to provide heat for the reaction. Since the simpler recuperative heat is not available, the convective, and electromagnetic options are studied and optimized

Finally, the third part of this work deals with the rWGS. For this reaction, preliminary work was carried by Jung et al. (2013). The multifunctional adsorptive reactor is an elegant way to make the rWGS attractive.

- Chapter 5 introduces the standard fixed-bed adsorptive reactor. The concept is modeled and optimized to prove the potential that the concept has for its application.
- Chapter 6 builds upon the results from Chapter 5 and presents a moving-bed adsorptive reactor as a possible improvement on the fixed-bed case. As for the fixed-bed, the reactor is modeled and optimized

Funding

Two sources of funding contributed to the development of this work:

- DFG - German Research Foundation (Deutsche Forschungsgemeinschaft). Grant No. AG 26/15-1
- BMBF - Federal Ministry of Education and Research (Bundesministerium für Bildung und Forschung). Grant No. 033RC1301-B

Chapter 1 and the experimental results of Chapter 2 were funded by the DFG. The remaining chapters and the theoretical part of Chapter 2 were funded by the BMBF.

The BMBF-project was carried out in cooperation with BASF AG, ThyssenKrupp AG (Industrial Solutions and Steel Europe), Linde AG, hte GmbH and the VDEh-Betriebsforschungsinstitut. The TU Dortmund was responsible for the kinetic simulations and analysis of the experimental data and the modeling, simulation and optimization of various reactors in the process.

Part I.

Methane Pyrolysis: Fluid Reactors

Preamble

The following chapter has been published as:

Munera Parra, A.A and D.W. Agar (2017): "Molten metal capillary reactor for the high-temperature pyrolysis of methane". In: *International Journal of Hydrogen Energy* 42.9, pp. 13641-13648

Some experimental results are part of Krieger's Master Thesis: "Untersuchungen zur Methanpyrolyse in einem Kapillarreaktor". Conceived and directed by myself and evaluated by Prof. Agar.

Additionally, the high-temperature experimental results obtained by Göbel in his Bachelor's thesis: "Experimentelle Untersuchungen zur Hochtemperatur-Methanpyrolyse im Schmelzmetall-Kapillarreaktor und analytische Betrachtung von Nebenprodukten". Directed by Ina Schulz and evaluated by Prof. Agar were expanded in this work.

Abstract

In this work, the further development of the molten metal capillary reactor in slug-flow regime is presented. The preliminary results from the high-temperature pyrolysis of methane at 1300 °C and 9 Nml min⁻¹ are presented with a calculated conversion of 80%, and, a mean residence time of 1.36 s. Due to carbon deposition, difficult gas separation and unstable slug-flow, it was deemed necessary to redesign the system. For that, several alloys were tested looking for improved wettability and more favorable hydrodynamics. The modified experimental set-up is described, which led to improvements in gas separation, but not enough stability in the slug-flow. Finally, the current experimental set-up is introduced. There, a characterization of the hydrodynamics is performed using a low temperature alloy of gallium, indium and tin, GaInSn, and, a stable regular slug-flow is established for various gas and liquid flows. The presence of a film in the slug-flow remains subject to question and the conclusions on the direction of the project are drawn towards an alternative reactor system or further hydrodynamic studies.

1

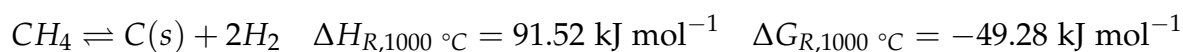
Molten Metal Capillary Reactor

1.1. Introduction

Contrary to popular belief, fossil energy consumption is not limited by its availability but rather is constrained by environmental considerations. Over the past decades, the world's proven natural gas reserves have been increasing steadily, from 2592 trillion cubic feet in 1980 to 6972 trillion cubic feet in 2014 (*International Energy Statistics*), and if non-conventional sources like methane hydrates or shale gas are included, the availability could be greater.

Many scenarios for the future production of energy or hydrogen without CO₂-emissions have been investigated (Machhammer et al. 2016; Muradov and Veziroglu 2008). The consensus seems to be directed towards renewable energy; however, a full transition to renewable energy is not foreseeable in the near future (Kreysa et al. 2010). It is thus necessary to search for bridging technologies. Among these, hydrogen presents itself as a very attractive alternative due to the possibility of using existing natural gas infrastructure as well as for its integration with fuel cells and other clean energy technologies.

Hydrogen can be generated with low to zero CO₂-emissions by pyrolysing hydrocarbons at high temperatures. The pyrolysis of methane can be described by the reaction:



This reaction is endothermic and becomes thermodynamically spontaneous at 820 K and kinetically feasible at temperatures around 1073 K. The reaction can be catalyzed for lower temperature operation, but the carbon deposition on the catalyst and the limited equilibrium conversions leading to a separation problem and stream recycles are still issues that have to be addressed. High-temperature pyrolysis remains an alternative, but does not come without challenges: carbon deposition is still a major hurdle (Abánades et al. 2012), which can lead to the blockage of the reactor. In addition, the endothermicity of the reaction necessitates the introduction of heat at higher temperatures, which is usually challenging due to the sources of energy at such temperatures being few and far between.

The use of liquid media, such as molten metals, has been used to circumvent both these problems. Not only does the liquid medium act as a barrier preventing the car-

bon deposition at the heat transfer surface, but it also serves as a heat transfer medium due to its excellent transport properties. Tyrer (1931) initially patented a molten iron based concept for decomposing methane into its elements. Furthermore, the use of molten metal, tin for his case, bubble columns was first performed by Steinberg (1999). A modified version was explored by Serban et al. (2003) exhibiting a relatively high conversion (57%) for a low temperature operation (750 °C). Nonetheless, in this publication, carbon deposition occurred at both the reactor surface and in the sparger used to feed the methane.

Other molten metal concepts include the works of Martynov et al. (2005) and Gulevich et al. (2008) using Pb-Bi as the molten medium. Paxman et al. (2014) presented some initial theoretical and experimental investigations on a solar-molten tin reactor, although the experiments with the molten media itself have not been published. Currently, a molten tin bubble column reactor is also being investigated by the group of Prof. Abanades in the IASS in Postdam in cooperation with the Karlsruhe Institute of Technology amongst others (Abánades et al. 2016; Geissler et al. 2015, 2016). Their first experimental results (Geissler et al. 2015) showed a hydrogen yield of 30% at 1000 °C with little carbon deposition on the reactor surface. Following experiments (Geissler et al. 2016) with the inclusion of a fixed-bed inside the bubble column, and operating with temperatures up to 1175 °C, resulted in hydrogen yields up to 78%. However, the lack of control over the residence times in bubble columns leads inherently to a decrease in conversion. To circumvent this issue, the use of a capillary reactor using molten metals in slug-flow regime was proposed as a solution at the TU Dortmund (Agar and Schultz 2014; Schultz and Agar 2015) since the slug-flow regime has a residence time closer to that of plug-flow (Trachsel et al. 2005).

The proposed system in (Schultz and Agar 2015) is presented in Figure 1.1. The operation mode was that of an alternating pressure reservoir which generates a quasi-continuous flow. Preliminary studies were carried out for a system of nitrogen water, and the initial experiment with methane reported an average conversion of 32% without carbon depositions at temperatures under 1100 °C.

1.2. Experimental Set-Up

During this work, three experimental set-ups were used to obtain the results. The next sections are devoted to the description of these set-ups.

1.2.1. Existing Set-Up

In the preliminary work (Schultz and Agar 2015), the results were obtained using an experimental set-up referred to in the text as the existing set-up and depicted in Figure 1.1. This set-up consisted of two glass reservoirs that could be filled with molten metals. These reservoirs were connected each to a T-piece in which the gas to form the slug-flow could be introduced. The T-pieces were connected by a 2.2 m long, 2 mm inner diameter, U-shaped quartz glass capillary. From this capillary, 1.8 m was located in a ceramic tube, which was placed inside a horizontal electric furnace

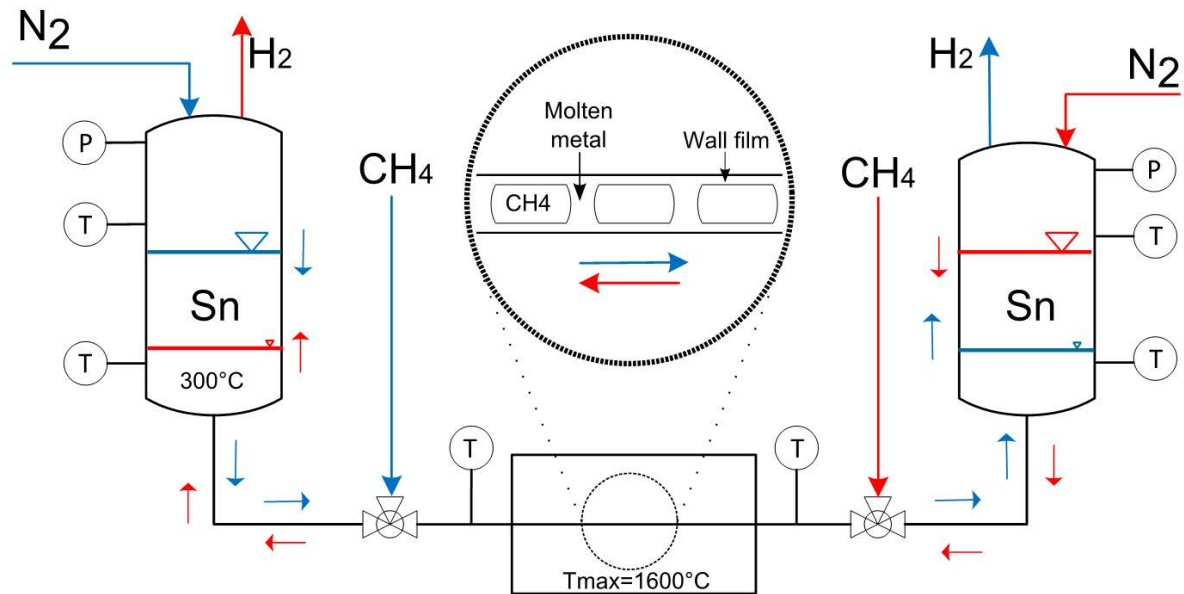


Figure 1.1.: Existing set-up for the molten Sn capillary reactor

(Carbolite).

The furnace can be heated up to 1600 °C, the capillary inside it comprises the pyrolysis zone. Experiments were only carried up to 1300 °C to avoid damaging the quartz glass capillary. The gas separation from the metals took place at the top of the reservoirs. The melt, molten tin, flowed from one reservoir to the other by applying pressure with nitrogen in one of the reservoirs, this procedure continued until the reservoir was empty and then the direction of the flow was reversed, on average each cycle lasted about 7 minutes. Methane flow was regulated using a flow controller and could be introduced in either of the T-pieces depending on the flow direction. As stated before, the operation of the system was a quasi-continuous reverse-flow operation.

However, after the first experiments at 1300 °C, due to carbon formation, in addition to complications with the gas analysis and separation, and the lack of stability of the flow, it was deemed necessary to make some changes to improve the performance of the system. These changes resulted in the modified set up presented in the next section.

1.2.2. Modified Set-Up

The first change was to separate the gas from the melt before entering the reservoirs in order to reduce any possible back mixing or non-homogeneities that could be introduced by the large volume of the reservoirs. In the first step, this was performed by using the same T-pieces to introduce the gas and form the slug-flow, to also separate the gas from the melt. Nonetheless, this was not completely successful because of the capillary forces, as well as the counteracting hydrostatic pressure, which forced the melt to rise in the pipe for the gas and destabilizing the system as well. To avoid the capillary forces, the solution was simply to build an additional T-piece with a larger

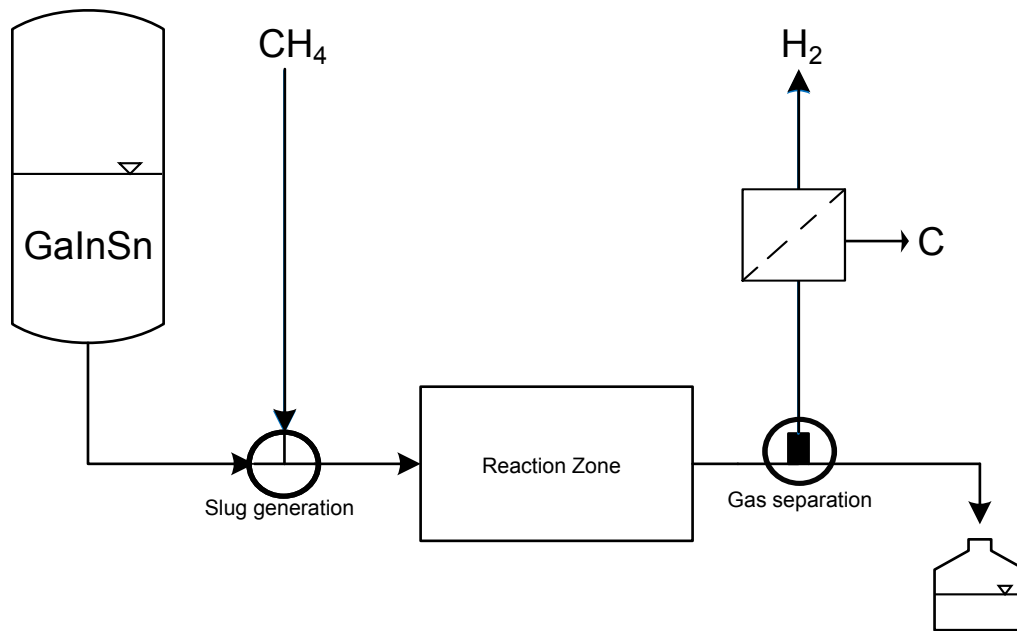


Figure 1.2.: Modified experimental set-up

diameter in the gas exit to break any capillary force.

However, the solution for the competing counteracting hydrostatic pressure was not that simple. Several attempts were made to counteract this problem, for example by using a vacuum pump to equate this pressure head, or by decoupling it from the reservoirs by carrying out the gas separation at the same level as the reservoirs. None of this proved adequate to keep a stable slug-flow, and, in the end, it was deemed better to abstain from using the second reservoir at all, leading to the experimental set-up presented in Figure 1.2. Using this set-up, the aim was first to prove whether the hydrodynamics of the system could be controlled and if that was the case then to carry out the pyrolysis experiments. The set up consisted of the same items as the existing set up, without one reservoir and one T-piece. The operation of the system is transient only.

1.2.3. Current Set-Up

The current experimental set-up is based on the use of low-temperature alloys, i.e. liquid at room temperature. This allows for the use of simple pumps and stable operation for hours. This set-up, consists of one reservoir, two peristaltic pumps (ISMATEC and Watson Marlow) used to circulate the melt, one T-Piece through which methane is fed and the slug-flow is generated, a T-Piece for the separation of the gas (equal to the one in the modified set-up), and a T-piece for the quench-cooling of the hot melt coming out of the oven to protect the pumping equipment. The system can be operated continuously in steady-state.

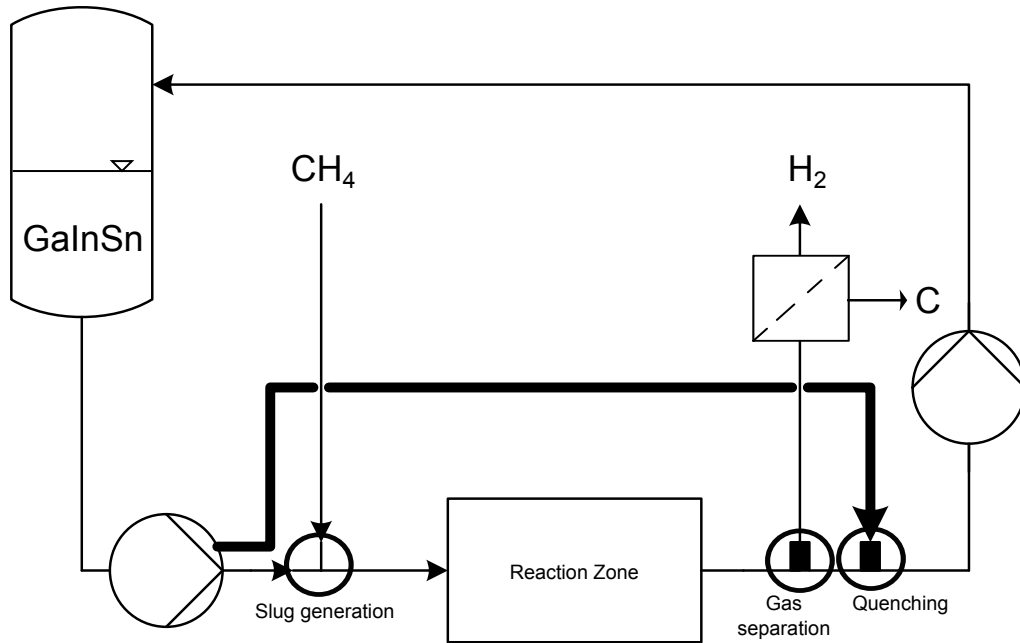


Figure 1.3.: New experimental set-up

1.3. Materials and Methods

In addition to the items described in the experimental set-up section, four thermocouples type K (CONATEX) are used to measure the temperature at diverse points in the experimental set-up, two pressure sensors (Afriso) are used to control the pressure of the system and a differential pressure device (MCC) is used to determine the pressure drop within the system. The materials used are presented in Table 1.1. All the glass pieces were manufactured internally in the glass blowing workshop of the faculty of biochemical and chemical engineering of the TU Dortmund. The analysis of the gas composition to determine the methane conversion was done using Fourier transform infrared spectroscopy (Shimadzu IRPrestige-21).

Indium and gallium were used to prepare the GaInSn and GaIn alloys, to study their wetting properties as well as for Field's metal. Glycerin was used in some preliminary tests to increase the viscosity of water, for the hydrodynamic test in the water/Nitrogen system, and the nitrogen and methane can be fed to the system using mass-flow controllers (Vögtlin instruments) with maximal throughput of 100 Nml min^{-1} and 50 Nml min^{-1} respectively. Argon was used in the existing set-up, to purge the system.

1.4. Experimental Results and Discussion

1.4.1. Methane Pyrolysis in Existing Set-Up

Using the existing set-up, some experiments were carried out (Goebel 2015) to test the pyrolysis at higher temperatures, since in the preliminary study (Schultz and Agar 2015), the previous furnace could only reach $1100 \text{ }^\circ\text{C}$ and no carbon formation

Table 1.1.: Materials and purities

Material	Producer	Purity
Glycerin	AppliChem	99%
Tin (Sn)	Gienger Lötmittel	99.90%
Indium (In)	Haines & Maassen	99.99%
Gallium (Ga)	MET-Chem Handel	99.90%
Field's Metal	Haines & Maassen	In: 51% Bi: 32.5% Sn: 16.5%
GaIn Eutectic	CVT TU Dortmund	Ga: 77% In: 23%
GaInSn Eutectic	CVT TU Dortmund	Ga: 68.6% In: 21.4% Sn: 9.9%
Methane	Air Liquide	100.00%
Nitrogen	Messer	100.00%
Argon	Messer	100.00%

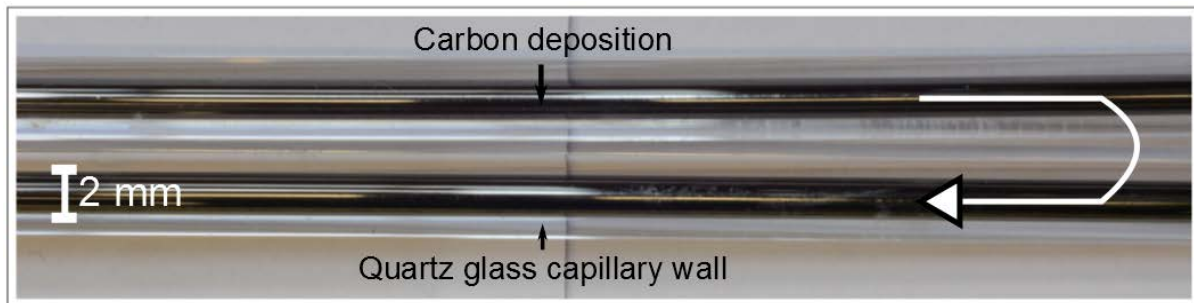


Figure 1.4.: Carbon deposition in the capillary. Adapted from (Goebel 2015)

was present up to that temperature. Nonetheless, running at higher temperatures to increase the low conversion obtained in the preliminary study resulted in carbon deposition as shown in Figure 1.4. The operating conditions for this preliminary experiment are presented in Table 1.2. Carbon could be also found in the filter from the gas phase as well as in the top of the molten metals as described in (Geissler et al. 2016). For the carbon depositions, they could only be removed by oxidizing the carbon to CO_2 .

Due to experimental difficulties in the measuring of the gas outlet concentration and the fact that the operating set up could be operated for only short periods, up to 7 minutes, in each direction. It was decided not to proceed with this set-up any further. However, it is possible to predict the conversion inside the reactor using the measured temperature and the kinetics available in the literature.

In Figure 1.5, the temperature profile measured in the region where the capillary

Table 1.2.: Operating conditions for preliminary experiments at high temperature

T / °C	u_L / m s^{-1}	$u_{G,N}$ / m s^{-1}	L_R / m
1300	0.11	0.048	1.1

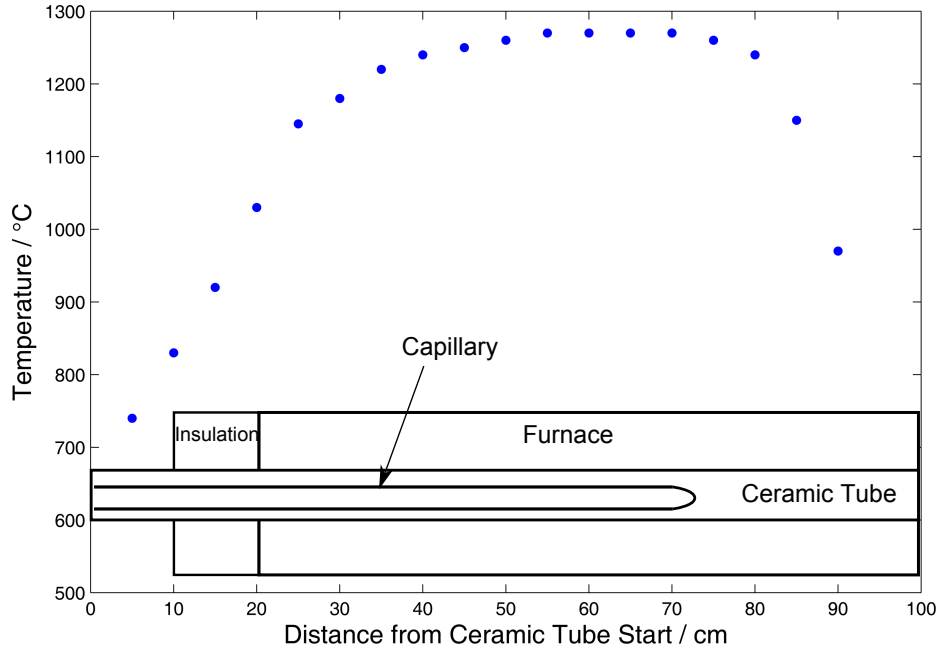


Figure 1.5.: Measured temperature profile

rests is presented. As it can be seen, for a set point of 1300 °C, the temperature was close to that value in the central region, but near the entrance and across the insulation layer, heat is lost resulting in lower temperatures. The profile is also non-symmetric because the furnace is completely closed on one end, whereas in the end where the capillary is introduced, the heat shield had to be drilled for the capillary and the thermocouples, hence leading to a greater heat loss.

Using this data, the conversion can be estimated when solving the following equation obtained from a differential mass balance:

$$\frac{dX}{dz} = \frac{k(T(z)) \cdot (1 - X) \cdot T_0}{u_{TP,0} \cdot T(z) \cdot (1 + X)} \quad (1.4.1)$$

For slug-flow, plug-flow can be assumed (Trachsel et al. 2005) for the gas phase. The velocity is the so-called two-phase velocity representing the addition of the velocities of the gas and liquid phases. The plug-flow is maintained even for the cases of increasing or decreasing volume due to either temperature or reaction (Munera Parra et al. 2014), hence the equation looking similar to that of a plug-flow reactor. In Eq. (1.4.1), the change in velocity due to thermal expansion and conversion is considered, as well as the temperature dependency on the reaction rate constant alongside the capillary, due to the temperature profile formed inside the furnace. Due to the excellent heat transfer properties of the slug-flow, the temperature of the reactor was assumed equal to that of the furnace at any given position. The reaction rate constant for the homogeneous pyrolysis (Patrianakos et al. 2011) can be estimated as:

$$k(T) = 10^{14} \text{ s}^{-1} \exp\left(-\frac{400000 \text{ J mol}^{-1}}{RT}\right) \quad (1.4.2)$$

Table 1.3.: Qualitative results of the contact angle measurement

Alloy	Literature	Measured
Field's metal	63 °C ¹	152°
Ga-In eutectic	15 °C ²	144°
GaInSn eutectic	From 10.5 °C ³ to -19 °C ⁴	143°

and the mean residence time can be calculated as:

$$\tau = \frac{L_R}{\frac{\int_0^{L_R} \frac{u_{TP,0} \cdot T(z) \cdot (1+X)}{T_0} dz}{L_R}} = \frac{L_R^2}{\int_0^{L_R} \frac{u_{TP,0} \cdot T(z) \cdot (1+X)}{T_0} dz} \quad (1.4.3)$$

By using the expressions above, the conversion for the experiment can be found to be 80.07% for a mean residence time of 1.36 s.

In the existing set-up, the carbon deposition found, pointed directly to the absence of liquid film. This, in addition to the difficulties in analyzing the system conversion and the unstable flow led to changing the system into the modified set up presented in Section 1.2.2. Furthermore, various molten metal were investigated further to look for an option with better wetting properties.

1.4.2. Wettability of Alloys

The first pyrolysis results showed that there was no film formation in the reaction zone leading to the carbon deposition. In the literature (Morley et al. 2008), it can be found that Ga, or Ga and Sn alloys easily wet glass. Qualitative experiments were then performed with different Sn alloys to try to improve the wettability of the melt. The melts studied were Field's metal, the Ga-In eutectic and the GaInSn eutectic. All these systems additionally offered, besides potentially better wetting properties, lower melting points than Sn, with most of them being close to room temperature, which facilitates the handling of the materials drastically. Other than Field's metal, which was obtained directly from the provider, all other alloys were prepared at our laboratory with the composition presented in Table 1.1.

To carry out the experiments to determine the contact angle, it is necessary to differentiate between the wetting of the glass and the that of the metal oxide layer that can form at the interface. This is necessary because the latter would imply measuring the contact angle between the melt and the melt-oxide instead of between the melt and the glass. To accomplish this, the glass surfaces were treated with a 1M hydrochloric acid solution in which the metal oxides are soluble (Xu et al. 2012) to emulate an oxygen-free system. The contact angle was then qualitatively determined using an image-editing program as shown in Figure 1.6. The results are presented in Table 1.3.

¹(Han et al. 2011)

²(Xu et al. 2012)

³(Morley et al. 2008)

⁴(Liu et al. 2012)

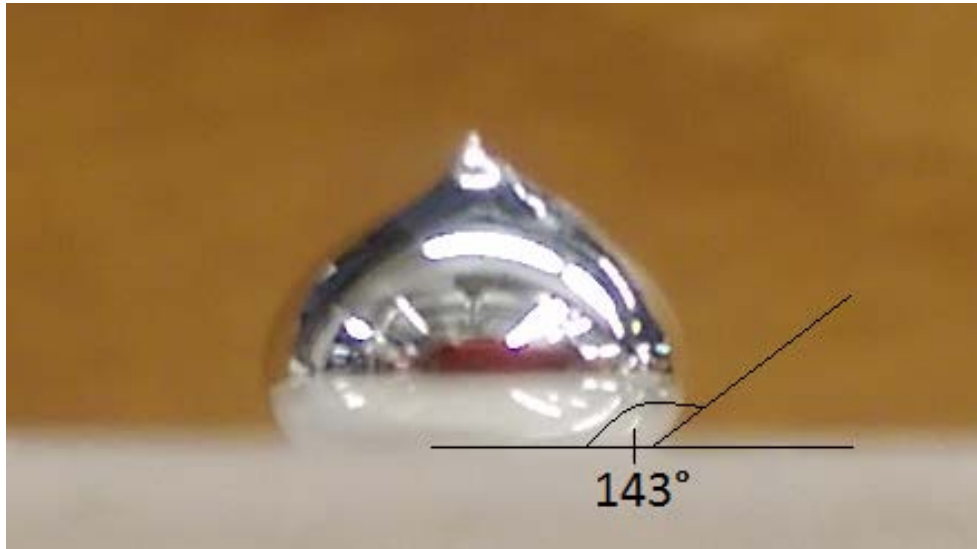


Figure 1.6.: Qualitative measurement of the contact angle for the Ga-In-Sn alloy

As can be seen, the wetting of the alloys is not as easy as described by Morley et al. (2008). Only in the cases where an oxide layer was present, the contact angles were slightly more favorable. However, since the pyrolysis of methane occurs in a completely oxygen-free environment, this favorable wetting behavior will not be encountered. Nevertheless, as an alternative, it is also possible to force the formation of the film hydrodynamically (Lee and Lee 2008; Rischen 2016). Since the GaInSn alloy had arguably the most favorable contact angle, but most importantly the lowest melting point, which allowed for the use of pumps and eliminated the need for any external heating, it was chosen as the melt for the rest of the experiments. However, for temperatures above 1300 °C, the stability of GaInSn has not been studied and in case the film can be forced for GaInSn it could be most likely also be formed for Sn which is a cheapest option and also more stable at higher temperatures.

1.4.3. Operation of the Modified Set-Up

With the selection of the melt, the modified set-up was put into operation. Since the results from the pyrolysis pointed to the fact that the film was not being formed, hydrodynamic experiments were carried out to observe if the film formation was possible. To find whether a film is present or not, when not optically possible, Lee and Lee (2008) observed that this could simply be done by carrying our experiments at a constant pressure drop and observing what would happen to the gas or liquid velocity when increasing the other. If both increase this means there is a film present, if one increases and the other decreases this means that there is not a film. This can be easily understood because the gas-wall contribution to the pressure drop is minimal. Additionally, in the work of Rischen (2016) a correlation to describe the region where the film exists was developed as:

$$Ca_{TP} > 2.86E - 3 \cdot (\beta_G + 0.185) \quad (1.4.4)$$

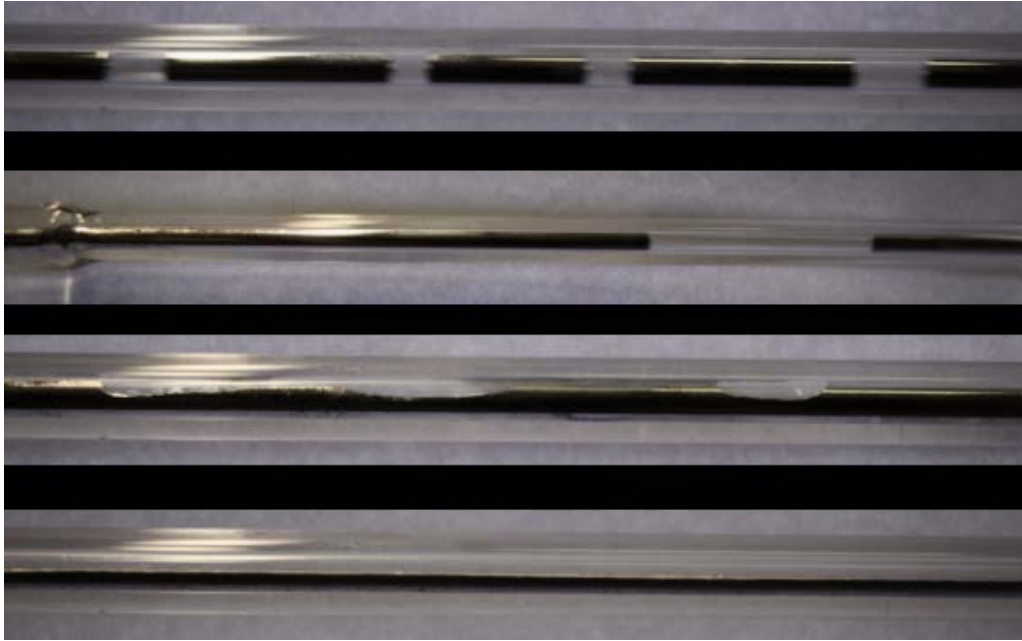


Figure 1.7.: Flow regimes in the modified set-up Gas velocity: 0.11 m s^{-1} . Liquid velocity: 0.03 m s^{-1}

where Ca is the capillary number from which the two-phase velocity can be obtained and β is the gas fraction in the slug-flow.

The correlation was tested in the system for the case of nitrogen and water, known to have a film for most of the cases, and for nitrogen and a mixture of water and glycerin to increase the viscosity of the water. The predicted values from Eq. (1.4.4) resulted, for the most part, in conservative values meaning the transition from no film to film could happen at higher velocities than predicted.

Using this correlation, the predicted value to reach the transition region for the GaInSn system was of 0.7 m s^{-1} (for room temperature conditions). However, this would necessitate high pressure in the reservoirs, and, thus could not be achieved with the modified experimental set-up. The maximum two-phase velocity achieved was 0.3 m s^{-1} .

Moreover, it was hard to obtain a stable operation as shown in Figure 1.7. In this case, for the same set of parameters, the flow regime could vary from slug-flow with different gas fractions and slug lengths as shown in the two upper figures, to wavy flow in the third or stratified flow as shown in the bottom picture. In this case, once a stable flow was achieved it would remain so until any disturbance, i.e. pressure build-ups among others, caused the system to shift from one state to the other. The velocities for this case were 0.11 m s^{-1} for the gas and 0.03 m s^{-1} for the liquid. Nonetheless, this behavior could be observed on most operating conditions.

Since the high velocities could not be achieved, and the stability was not satisfactory, the set up was changed to allow for the use of pumps as explained in the new set-up and shown in Figure 1.3.

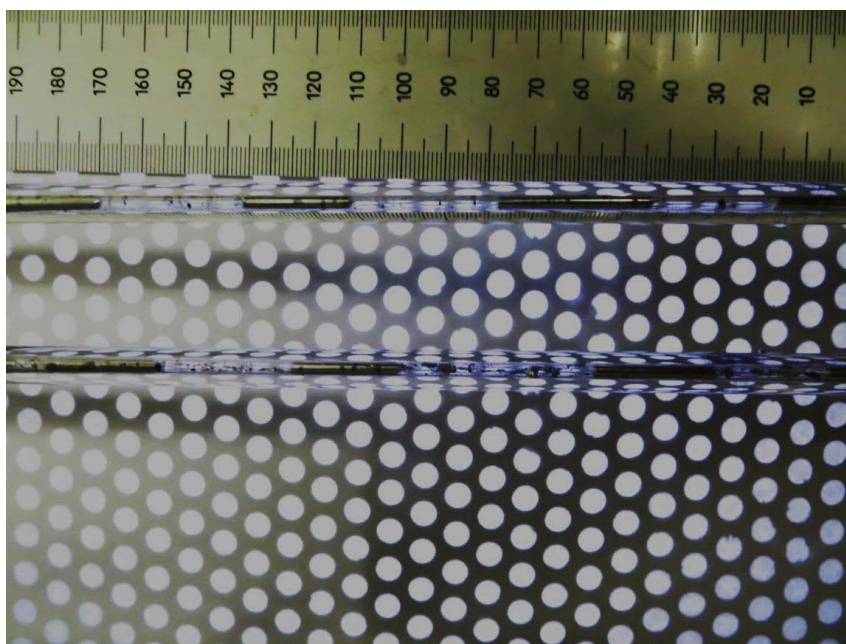


Figure 1.8.: Stable and uniform slug-flow operation. Gas velocity: 0.53 m s^{-1} . Liquid velocity: 0.05 m s^{-1}

1.4.4. Operation of Current Set-Up

As using pumps allows for operation with higher velocities and less disturbances, slug flow could easily be generated. Stable and uniform slug-flow was obtained from liquid flow rates varying from 1 ml min^{-1} to 40 ml min^{-1} and gas flow rates from 10 Nml min^{-1} to 100 Nml min^{-1} with Nitrogen, or to 50 Nml min^{-1} with Methane, which are also the limiting values of the current equipment. The main difference between the resulting slug-flow was the length of the slugs, ranging from 1 cm to 5 cm for the liquid phase and from 2 cm to 10 cm in the gas phase, and therefore the phases' ratio. An exemplary uniform and stable slug-flow is presented in Figure 1.8. Nonetheless, it can be seen that no film is present so the need for the pressure measurement, as proposed by Lee and Lee (2008), was not necessary.

For the maximum capacity of the system, the two-phase velocity was 0.74 m s^{-1} which is above the predicted value of 0.7 m s^{-1} using the correlation presented in the work of Rischen (2016) for which a film should occur. However as stated before, the correlation seems to underestimate these values. It was also observed that at higher velocities, the uniformity of the slug-flow was affected, as depicted in Figure 1.9, which would point more in the direction of the transition to a different flow regime, most likely churn flow. Based on the range of velocities in the system, this transition would be consistent with the flow maps established by Shao et al. (2009). From this, it can be concluded that it cannot be possible to obtain a slug flow with film using the current set-up, and as already observed in the preliminary pyrolysis experiments, any operation above $1100 \text{ }^\circ\text{C}$ will lead to carbon deposition.

Besides the experiments on hydrodynamics, the cooling concept was tested at high temperatures and temperature could be kept in a range tolerable to the peripherals by using a quenching flow to reaction flow ratio of at least 8 to 1. Experiments on

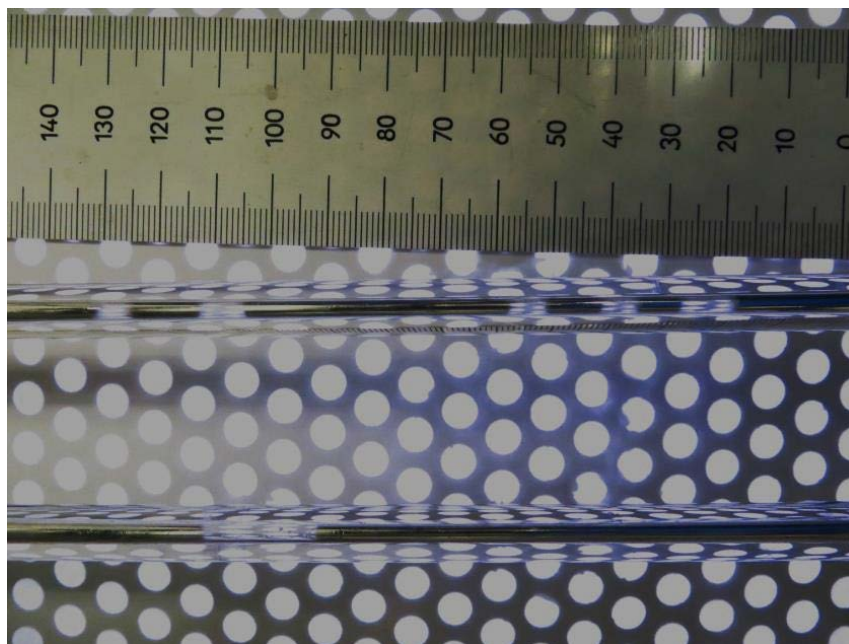


Figure 1.9.: Irregular slug-flow at higher velocities. Gas velocity: 0.53 m s^{-1} . Liquid velocity: 0.21 m s^{-1}

the residence time were not possible since the resolution of the current analytics (8 seconds) was not fast enough to capture the front of the response to a step experiment ($F(t)$), which ultimately means a very narrow residence time distribution.

1.5. Conclusions

Besides the formation of the film, all the challenges regarding the operation of the molten metal capillary reactor were solved. An efficient gas separation that did not interfere with the flow regime was implemented, and the analysis of the residence time showed that the flow was close to plug-flow. Studies using pressure to generate the liquid flow in the modified set-up yielded better results than those of the alternating pressure reservoir used in the existing set-up.

Finally, by using a quench cooling concept, and the introduction of low temperature alloys, the use of pumps was made possible in the current set-up, which allowed for an easy and robust way to establish the slug-flow for a very wide range of both gas and liquid velocities. The range of residence times was from 2 up to 15 seconds in cold operation, which at $1300 \text{ }^\circ\text{C}$ would range from 0.38 to 2.84 seconds or less depending upon the conversion achieved.

Using this flexibility, coupled with the narrow residence time, the control over the conversion of the pyrolysis at any given temperature could be achieved. Nonetheless, predictions about the presence of a film at higher velocities could not be confirmed, but the tendency showed that a change in regime was more likely than the appearance of the film. This, in addition with the longer capillaries that would be needed to maintain a reasonable residence time for high conversion, would then mean very high pressure drops and hence hurt the feasibility of this concept.

To circumvent this shortcoming, a study on different tube materials to improve the wetting properties, and therefore the film formation and pressure drop, in addition to the study of various geometries for the slug formation to better control the phase ratios will be carried out. Furthermore, an alternative concept using the low temperature alloys in a falling-film and rotating reactors will be presented in a following publication.

Preamble

The following chapter will be submitted for publication as:

Munera Parra, A.A, C. Asmanoglo, J. M. Voß, and D.W. Agar (2018): "Molten Metal Falling-Film and Rotating Reactors for the High-Temperature Pyrolysis of Methane".

The experimental results are part of Voß' Bachelor's Thesis: "Hydrodynamic Studies on Molten Metal Film Reactors for High Temperature Methane Pyrolysis". Conceived and directed by myself and evaluated by Prof. Agar.

The calculations are part of Asmanoglo's Bachelor's Thesis: "Modeling and Simulation of a Falling Film Reactor for the High Temperature Pyrolysis of Methane". Conceived and directed by myself and evaluated by Prof. Agar.

Abstract

In this work, a falling-film reactor is studied as an alternative concept to carry out the high temperature pyrolysis of methane. Experimental studies at room temperature are carried out for the water-nitrogen as well as the GaInSn-nitrogen systems. The minimum wetting rate for both systems is compared to correlations from the literature. Based on these results, high-temperature simulations are run to test the sensitivity of methane conversion to various parameters such as the wall material and chosen melt, which could be used to improve the wettability; and the liquid flow rate, to understand whether a precise correlation to determine the required flow rate is paramount to the concept. The simulations are carried out for molten tin and for a molten salt. Finally, as the worst-case scenario, a rotating reactor is presented as an alternative for when obtaining a stable film in the falling-film set-up is not possible. Experiments are performed to find out whether a film can be formed and the minimum amount of melt required to establish it.

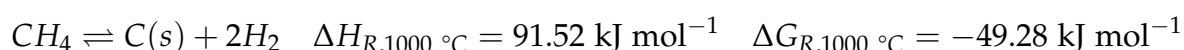
2

Falling-Film Reactor

2.1. Introduction

The question of how to meet the increasing energy demand in a sustainable way is pressing. After the adoption of the Paris Agreement (UNFCCC. Conference of the Parties (COP) 2015) after the COP21, it is clear that the need for low-carbon technologies is vital if the 2 °C scenario is to be met. The hydrogen economy has been proposed as a viable alternative to accomplish this goal (Barreto et al. 2003; Muradov et al. 2005; United Nations Environment Programme. Division of Technology 2006). Hydrogen presents an attractive alternative since its use for energy has only water as by-product. Many technologies and scenarios have been proposed to produce hydrogen with zero or low CO₂-emissions (Machhammer et al. 2016; Muradov and Veziroglu 2008; Muradov 2017). Although renewable energy offers the best solution long-term, a full transition is unlikely to happen in the near future (Kreysa 2009). Consequently, methane pyrolysis has been suggested as a viable bridge technology to the hydrogen economy (Weger et al. 2017).

Hydrogen can be generated with low to zero CO₂-emissions by decomposing methane into its basic molecules at high temperatures:



For this reaction to be kinetically feasible, temperatures above 1073 K are required. In theory, the reaction could be catalyzed for lower temperature operation, but the coking of the catalyst and the subsequent separation and large stream recycles resulting from the limited equilibrium conversion are still issues that need to be addressed. The high-temperature alternative presents, nonetheless, other challenges. Being an endothermic reaction, it is necessary to introduce heat at high temperatures, where there are rarely sources of energy. In addition, carbon deposition is still a major hurdle (Abánades et al. 2012) since it can, in the worst case, lead to the blockage of the reactor.

An elegant way to circumvent these problems is the use of liquid media. Molten metals, for example, can act as a shield protecting the wall from carbon deposition, and they possess excellent heat transport properties as well. A concept using molten iron as the liquid medium for methane pyrolysis was initially proposed by Tyrer

(1931). Other molten metals, such as tin, attracted attention in the late 90s. Steinberg (1999) proposed the use of bubble columns, and later Serban et al. (2003) expanded his work in a modified version. In their work, a relatively high conversion of 57% was achieved for operation at 750 °C. However, carbon deposits were found on both the reactor surface and the sparger used to feed the gas into the reactor. The use of Pb or Pb-Bi heavy liquid metal coolants in addition to steam and hydrocarbons to produce hydrogen was studied at Institute for Physics and Power Engineering in Russia (Gulevich et al. 2008; Martynov et al. 2005). More recently, Paxman et al. (2014) reported theoretical investigations on a solar-molten tin reactor as well as preliminary experiments, without tin, for methane conversion in the empty reactor. The experiments with the molten media itself have not been published yet.

Currently, a molten tin bubble column reactor is being investigated in a joint project with the Institute for Advanced Sustainability Studies in Postdam and the Karlsruhe Institute of Technology, amongst others (Abánades et al. 2016; Geissler et al. 2016). In the latest results (Geissler et al. 2016), at higher temperatures, 1175 °C, hydrogen yields up to 78% have been obtained after the inclusion of a fixed-bed in the bubble column. Furthermore, a different group recently studied the techno-economic feasibility of methane pyrolysis in molten metals (Parkinson et al. 2017) with emphasis in the required carbon-tax needed to make the process competitive with the methane steam reforming.

Nevertheless, a disadvantage of working with bubble columns in general is the lack of control over the residence time of the gas phase, which inherently decreases conversion. To circumvent this issue and deviating from the original bubble concept for molten metal reactors, a molten tin capillary reactor in slug-flow regime was proposed as an alternative at the TU Dortmund (Agar and Schultz 2014; Schultz and Agar 2015). However, recent developments (Munera Parra and Agar 2017) have shown that although a calculated conversion of 80% was found, the wetting properties of tin or other tin alloys are not good enough to prevent carbon deposition for the current system.

In this work, two concepts that can improve the performance of the capillary reactor are presented:

The first one is that of a falling-film reactor. Falling-film reactors can be widely found in the industry, especially in the field of absorption, e.g. heat pumps, sulphonation and chlorination. Analogously to the capillary reactor, the molten metal can act both as barrier to protect the wall from carbon deposition and as a heat transfer medium. In addition, the residence time distribution in the falling-film reactor although not as narrow as that of the capillary reactor, can still be assumed to be narrow enough to assure plug flow. The advantages of the capillary reactor are thus kept, with a minor sacrifice in heat transfer and residence time distribution. Nonetheless, in the falling-film reactor, the gas and liquid phase are decoupled which allow for a greater range in flows in comparison with the capillary reactor, and, when in counter-current operation, the occurrence of the back reaction is inherently prevented.

The second concept is an alternative to the falling-film reactor for the cases when the wettability is not enough to guarantee a stable film or improved heat transfer is required. Here, the film can be generated or stabilized by rotating the reactor along

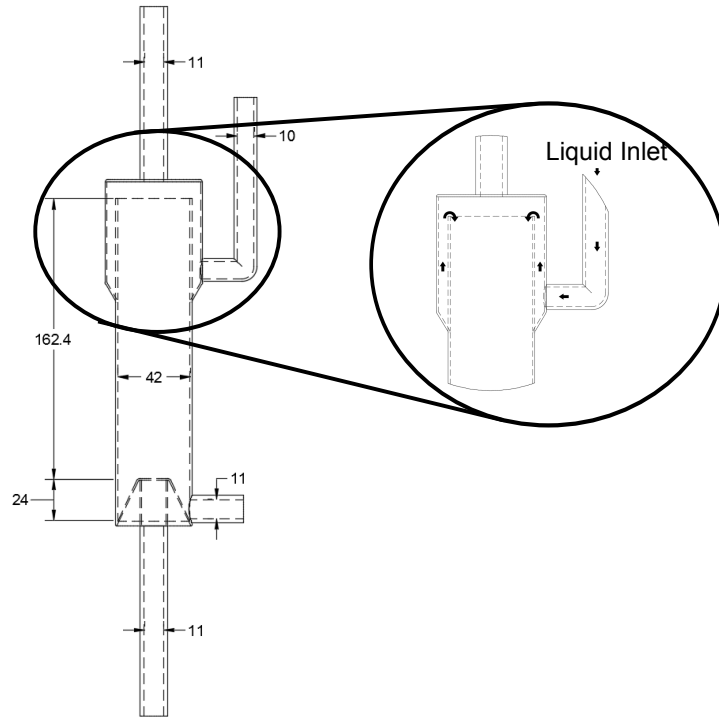


Figure 2.1.: Falling-film reactor with dimensions in mm

its axis in any given angle. Rotating reactors such as rotary kilns are common in the ore industry, or for waste treatment, but to the knowledge of the authors, a rotating film reactor as presented in this publication cannot be found in the literature.

2.2. Experimental Set-up and Materials

For the experiments, the focus was rather on the hydrodynamics of the system than on the actual high-temperature operation. Previous results (Munera Parra and Agar 2017) indicated that the wetting of the surfaces is paramount, and hence the focus of the experiments was first to study this behavior. The construction material was borosilicate glass, DURAN®, instead of high-temperature quartz glass for its intrinsic corrosion resistance towards molten metals as well as the facility that it represents in being able to observe the film formation with the naked eye.

All experiments were performed at room temperature with water and nitrogen as a base case and with the low temperature eutectic alloy composed of Gallium, Indium and Tin, GaInSn.

2.2.1. Falling-Film Reactor

The experimental set-up consists of a falling-film reactor as depicted in Figure 2.1. The dimensions are based upon the furnace that is available at our laboratory for future high-temperature experiments. The liquid distributor is a simple overflowing slit, which should ensure a uniform liquid distribution.

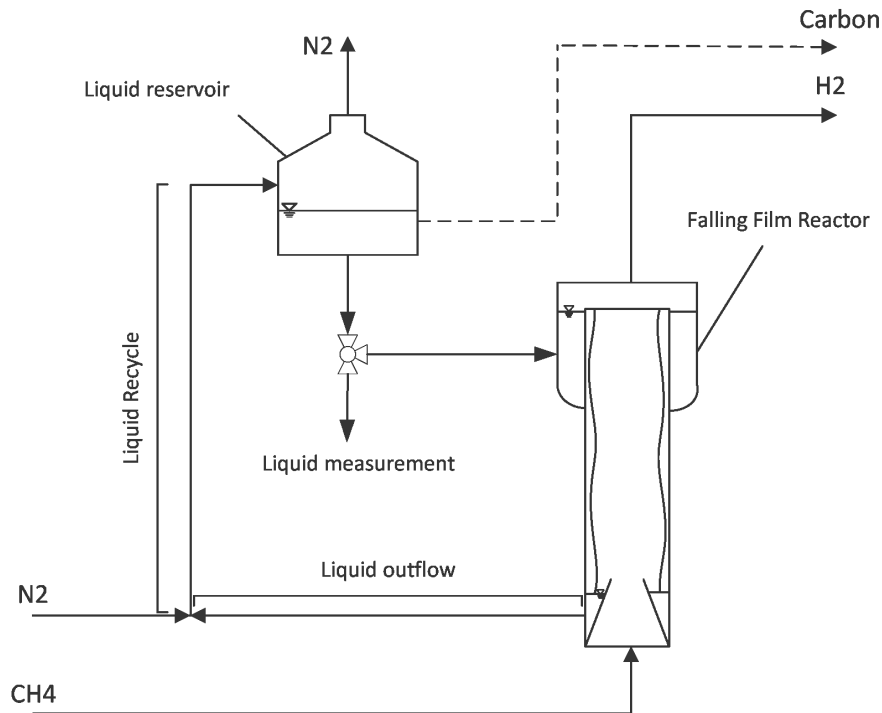


Figure 2.2.: Experimental set up with pumpless operation

In this set-up, the gas can be fed counter- or co-currently to the liquid. In addition to the reactor, it is desired to recirculate the molten metal. At lower temperatures and without solid formation, this can be performed by means of a pump. However, at high temperatures and with the solid carbon formed due to the reaction, pumping the metals could become challenging. For that purpose, a pumpless recycle was studied as presented in Figure 2.2. Here, a carrier gas can be used to recycle the metals to a temporary reservoir where the carbon separation could be carried out.

Experiments were conducted first in a system of water and nitrogen to determine the validity of the available correlations for the minimum wetting rates and to prove the stability of the film. The experiments were then carried out with the GaInSn alloy.

2.2.2. Rotating Reactor

The rotating reactor consists of a 14 cm long cylinder with a diameter of 4.4 cm, which are similar dimensions to those of the falling-film reactor. The cylinder is affixed to a rotating device with a maximum rotational speed of 3000 rpm. For simplicity, the reactor is mounted horizontally and stabilized with holders along the length to minimize vibrations.

The hydrodynamic measurements are based on the liquid phase only. Although it would be possible to perform the experiments with the gas phase, results from the falling-film showed that this phase has little to no influence, hence it was deemed unnecessary to go through the adaptations in order to operate continuously with a gas phase. As a result, the measurements were performed by introducing increasing quantities of the liquid phase until the surface was completely wetted.

Table 2.1.: Materials and purities

Material	Producer	Purity
Tin (Sn)	Gienger Lötmittel	99.90%
Indium (In)	Haines & Maassen	99.99%
Gallium (Ga)	MET-Chem Handel	99.90%
GaInSn Eutectic	CVT TU Dortmund	Ga: 68.6% In: 21.4% Sn: 9.9%

2.2.3. Materials

All glass parts and pieces were manufactured internally in the glass blowing workshop of the Department of Biochemical and Chemical Engineering of the TU Dortmund. Mass flow controllers (Bronkhorst) were used to regulate the gas flows. In addition, a peristaltic pump (Ismatec) was also used to circulate the molten metals. The materials used and their purities are listed in Table 2.1. The GaInSn alloy was prepared at the laboratory with the composition given.

2.3. Mathematical Modeling

The modeling of a falling-film reactor has been studied extensively for absorption processes (Akanksha et al. 2007; Gómez Mendoza et al. 2014; Gutierrez-Gonzalez et al. 1988; James Davis et al. 1979; Johnson and Crynes 1974; Talens-Alesson 1999; Torres-Ortega et al. 2009). These models normally include all transport phenomena, i.e. momentum, mass, and heat. In this case, an approach similar to that of Gómez Mendoza et al. (2014) was used to account for the possibility of change in the film thickness.

In this section, the model is described for both the gas and liquid phases as well as for their interactions. A summary of the model with its respective coordinates is presented graphically in Figure 2.3.

2.3.1. Liquid Phase

The liquid phase was modeled for both a laminar and a turbulent case. In the laminar case, the model is two-dimensional, whereas in the turbulent case the film is modeled one-dimensionally. Since the liquids used can be assumed non-volatile and the absorption of both methane and hydrogen can be neglected, the mass balance for the liquid phase needs not be taken into consideration.

2.3.1.1. Momentum Balance

For the momentum balance in the liquid phase for the laminar case, a balance over a finite element, assuming the liquid behaves as a Newtonian fluid, yields the following

2. Falling-Film Reactor

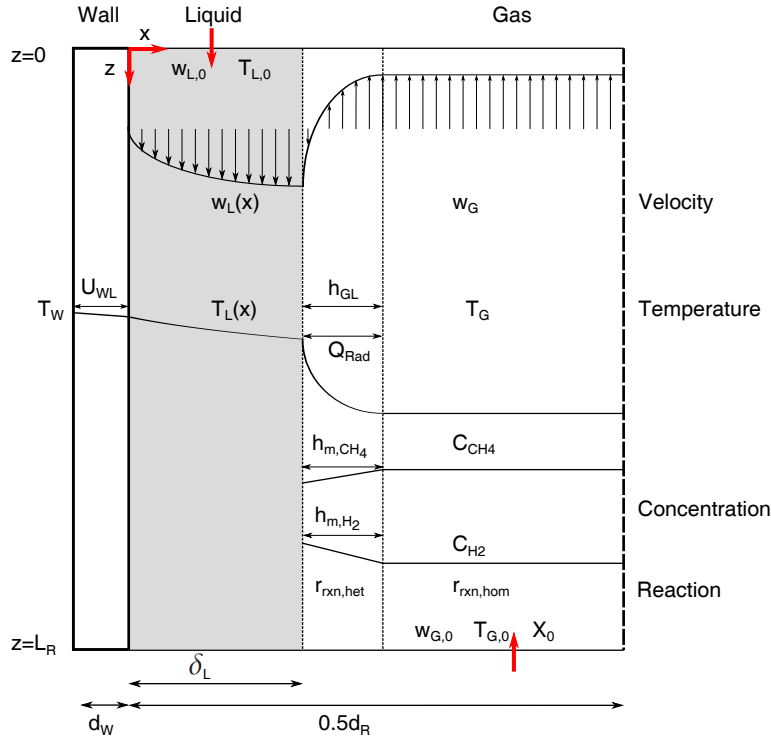


Figure 2.3.: Model of the falling-film reactor

equation with its respective boundary conditions:

$$\frac{\partial^2 w_L}{\partial x^2} = -\frac{\rho_L \cdot g}{\eta_L} \quad w_L|_{x=0} = 0 \quad \frac{\partial^2 w_L}{\partial x^2} \Big|_{x=\delta_L} = -\frac{\tau_{GL}}{\eta_L} \quad (2.3.1)$$

This equation can be solved to obtain:

$$w_L(x) = -\frac{\rho_L \cdot g}{\eta_L} \cdot \left(\frac{x^2}{2} - \delta_L \cdot x \right) - \frac{\tau_{GL}}{\eta_L} \cdot x \quad (2.3.2)$$

where τ_{GL} describes the shear stress at the gas-liquid interface. After integrating Eq. (2.3.2), an implicit function to obtain the film thickness, δ_L , from the volume flow per wetted area, Γ_L , can be defined as:

$$\Gamma_L = \int_0^{\delta_L} w(x) dx = \frac{\rho_L \cdot g}{3 \cdot \eta_L} \cdot \delta_L^3 - \frac{\tau_{GL}}{2 \cdot \eta_L} \cdot \delta_L^2 \quad (2.3.3)$$

for this equation, the determination of the interfacial shear stress is of importance, which can be calculated using the commonly used equation based on the modification of the equations developed for pipe flow:

$$\tau_{GL} = f_{GL} \cdot \frac{\rho_G}{2} \cdot w_{G,rel}^2 \quad (2.3.4)$$

Where the friction factor can be calculated for counter-current flow based in the work of Abe et al. (1991) as:

$$f_{GL} = 0.005 + \left(\frac{\delta_L}{\sqrt{\frac{\sigma_L}{g(\rho_L - \rho_G)}}} \right)^{1.27} \left(\frac{d_H}{\sqrt{\frac{\sigma_L}{g(\rho_L - \rho_G)}}} \right) \quad (2.3.5)$$

For the turbulent case, an average value of the velocity can be used as a simplification:

$$\bar{w}_L = \frac{\dot{m}_{L,0}}{\rho_L \cdot \delta_L \cdot \pi \cdot d_R} \quad (2.3.6)$$

And the formulation proposed by Trambouze and Euzen (2004) is used to yield an explicit formula for the film thickness:

$$\delta_L = 0.37 \left(\frac{3 \cdot \eta_L^2}{g \cdot \rho_L^2} \right)^{0.33} \cdot \left(\frac{\dot{m}_{L,0}}{\pi \cdot d_R \cdot \eta_L} \right)^{0.5} \quad (2.3.7)$$

2.3.1.2. Energy Balance

The energy balance for the liquid phase can be derived from a differential balance, neglecting heat conduction in the axial coordinate, as well as neglecting convection in the radial coordinate, yielding:

$$\frac{\partial T_L}{\partial z} = \frac{1}{\rho_L \cdot c_{p,L} \cdot w_L} \left(\lambda_L \frac{\partial^2 T_L}{\partial x^2} + \frac{\partial \lambda_L}{\partial x} \frac{\partial T_L}{\partial x} \right) \quad (2.3.8)$$

This is a partial differential equation (PDE) of first order in z and second order in x and thus three boundary conditions are required:

$$0 \leq x \leq \delta_L, \quad z = 0: \quad T_L = T_{L,0} \quad (2.3.9)$$

$$0 \leq z \leq L_R, \quad x = 0: \quad \lambda_L \frac{\partial T_L}{\partial x} \Big|_{x=0} = U_{WL} (T_L|_{x=0} - T_W) \quad (2.3.10)$$

$$0 \leq z \leq L_R, \quad x = \delta_L:$$

$$\lambda_L \frac{\partial T_L}{\partial x} \Big|_{x=\delta_L} = -h_{GL} (T_L|_{x=\delta_L} - T_G) - \dot{Q}_{LG,rad} - \dot{Q}_{rxn,het} \quad (2.3.11)$$

Eq. (2.3.9) represents the inlet conditions at the top of the film, Eq. (2.3.10) represents the heat exchange between the wall and the liquid, where is the global heat transfer coefficient that can be calculated for a cylindrical geometry (VDI-e.V. 2013) as:

$$U_{WL} = \frac{1}{\frac{d_R}{2 \cdot \lambda_W} \cdot \ln \left(\frac{d_R + 2 \cdot d_W}{d_R} \right)} \quad (2.3.12)$$

Eq. (2.3.11) represents the heat exchange at the gas-liquid interface, including the terms for convection, radiation, and the heat sinks for the carbon formation as well as the heterogeneous reaction that occurs at the interface.

The equations for the used thermal conductivities for the different wall materials and molten media used for the simulations are presented in the appendix.

For the turbulent case, the equations simplify greatly, reducing from a PDE to an ordinary differential equation (ODE) given by:

$$\frac{\partial T_L}{\partial z} = \frac{\pi \cdot d_R \cdot U_{WL}}{\dot{m}_{L,0} \cdot c_{p,L}} (T_W - T_L) - \frac{\pi \cdot (d_R - 2 \cdot \delta_L)}{\dot{m}_{L,0} \cdot c_{p,L}} (h_{GL} (T_L - T_G) + \dot{Q}_{LG,rad} + \dot{Q}_{rxn,het}) \quad (2.3.13)$$

With its respective boundary condition:

$$T_L|_{z=0} = T_{L,0} \quad (2.3.14)$$

Here, the heterogeneous heat of reaction includes the enthalpy of the surface reaction at the interface, as well as the energy used to get methane up to the reacting temperature. This can be expressed as:

$$\dot{Q}_{rxn,het} = r_{rxn,het} \left(\Delta H_R (T_L|_{\delta_L}) + H_{CH_4} (T_L|_{\delta_L}) - H_{CH_4} (T_G) \right) \quad (2.3.15)$$

In addition, the correlations used to calculate the heat transfer coefficient are given in the appendix, the radiative heat transfer is explained in Section 2.3.2.2.

2.3.1.3. Mass Balance

Although a mass balance is not required in the conventional way, when the change in film thickness is studied, it must be guaranteed that the total initial mass flow is conserved. This can be expressed as:

$$\Gamma_{L,0} \cdot \rho_{L,0} = \int_0^{\delta_L} \rho_L (T_L (x, z)) \cdot w_L (x, z) dx \approx \bar{\rho}_L (\bar{T}_L (z)) \int_0^{\delta_L} w_L (x, z) dx = \rho_L (\bar{T}_L (z)) \cdot \Gamma_L (z) \quad (2.3.16)$$

Here, by assuming the change of density along the radial coordinate is negligible, the density can be calculated by using the mean temperature value.

2.3.2. Gas Phase

For the gas phase, the usual assumptions for a falling-film are used: Ideal gas for pressures under 10 bar, that the carbon formation in the gas phase does not affect the flow, and that the pressure drop is negligible. Furthermore, the assumption of plug-flow is standard in the literature (Dabir et al. 1996; Gómez Mendoza et al. 2014) With this in mind, it is thus not necessary to solve the momentum balance for the gas phase and only the energy and mass balances will be considered.

2.3.2.1. Mass Balance

As done before, using a differential balance over a finite volume element and simplifying for the methane conversion, the following expression is obtained:

$$\frac{\partial X}{\partial z} = \frac{r_{rxn,hom} \cdot \pi \cdot \left(\frac{d_R}{2} - \delta_L\right)^2}{\dot{n}_{G,0}} + \frac{r_{rxn,heter} \cdot 2 \cdot \pi \cdot \left(\frac{d_R}{2} - \delta_L\right)}{\dot{n}_{G,0}} \quad (2.3.17)$$

The rates of reaction are based on the work of Patrianakos et al. (2011) as:

$$r_{rxn,hom} = k_{rxn,hom,0} \exp\left(-\frac{E_{A,hom}}{RT}\right) \left(C_{CH_4} - \frac{C_{H_2}^2}{K_C}\right) \quad (2.3.18)$$

with $k_{rxn,hom,0} = 10^{14} \text{ s}^{-1}$ and $E_{A,hom} = 400 \cdot 10^3 \text{ J mol}^{-1}$ and:

$$r_{rxn,heter} = k_{rxn,heter,0} \exp\left(-\frac{E_{A,heter}}{RT}\right) \left(C_{CH_4,inter} - \frac{C_{H_2,inter}^2}{K_C}\right) \quad (2.3.19)$$

with $k_{rxn,heter,0} = 2500 \text{ m s}^{-1}$ and $E_{A,heter} = 150 \cdot 10^3 \text{ J mol}^{-1}$. The concentration-based equilibrium constant can be obtained from thermodynamic databases (Linstrom and Mallard 2001) as:

$$K_C = \frac{K_P}{RT} = \frac{\exp\left(\frac{-\Delta G_R}{RT}\right)}{RT} \quad (2.3.20)$$

To calculate the heterogeneous reaction rate, the concentration of both methane and hydrogen at the interface has to be obtained. Since the reactor operates at steady state, no accumulation of either component occurs. Therefore, the amount coming in and leaving by convection must equal the reaction rate:

$$r_{rxn,heter} = h_{m,CH_4} (C_{CH_4} - C_{CH_4,inter}) = -\frac{h_{m,H_2}}{2} (C_{H_2} - C_{H_2,inter}) \quad (2.3.21)$$

From this, a relation between the interface concentrations can be obtained as:

$$C_{H_2,inter} = C_{H_2} + 2 \frac{h_{m,CH_4}}{h_{m,H_2}} (C_{CH_4} - C_{CH_4,inter}) \quad (2.3.22)$$

Finally, by combining Eqs. (2.3.19,2.3.21,2.3.22), the methane concentration can be found implicitly as:

$$\left(k_{rxn,heter} + h_{m,CH_4}\right) C_{CH_4,inter} - h_{m,CH_4} C_{CH_4} - \frac{k_{rxn,heter}}{K_C} \left(C_{H_2} + 2 \frac{h_{m,CH_4}}{h_{m,H_2}} (C_{CH_4} - C_{CH_4,inter})\right)^2 = 0 \quad (2.3.23)$$

In addition, since there is a change in the number of moles due to the reaction, the concentrations are calculated as a function of conversion as:

$$C_{CH_4} = C_{CH_4,0} \frac{(1-X) T_0}{(1+X) T_G} \quad (2.3.24)$$

$$C_{H_2} = C_{CH_4,0} \frac{2X}{(1+X)} \frac{T_0}{T_G} \quad (2.3.25)$$

The correlations used to calculate the mass transfer coefficients h_{m,CH_4} and h_{m,H_2} are given in the Appendix A.2.

2.3.2.2. Energy Balance

The energy balance for the gas phase can be obtained from a differential balance in an element by considering all terms as:

$$\frac{\partial T_G}{\partial z} = - \frac{2 \cdot \pi \left(\frac{d_R}{2} - \delta_L \right)}{\dot{n}_{G,0} (c_{p,CH_4} (1 - X) + 2 \cdot c_{p,H_2} \cdot X)} \left(\begin{array}{l} h_{GL} (T_L|_{x=\delta_L} - T_G) + \dot{Q}_{LG,rad} \\ - \frac{1}{2} r_{rxn,hom} \cdot \Delta H_R \cdot \left(\frac{d_R}{2} - \delta_L \right) \\ + \dot{Q}_{rxn,het} \end{array} \right) \quad (2.3.26)$$

With its respective boundary condition:

$$T_G|_{z=L_R} = T_{G,0} \quad (2.3.27)$$

Since the heterogeneous reaction is assumed to occur only in the liquid interface, the heat term due to this reaction is only due to the heat transferred from the reacted hydrogen leaving the interface as:

$$\dot{Q}_{rxn,het} = 2 \cdot r_{rxn,het} \left(H_{H_2} (T_L|_{x=\delta_L}) - H_{H_2} (T_G) \right) \quad (2.3.28)$$

The radiative heat transfer is only considered between the molten media and methane, since, according to Siegel and Howell (2013), symmetric two-atomic gases, like hydrogen, can be regarded as non-absorbing. The heat transfer can be described by:

$$\dot{Q}_{LG,rad} = \sigma_B \frac{\epsilon_{rad,L}}{1 - (1 - \epsilon_{rad,L})(1 - A_{rad,G})} \left(\epsilon_{rad,G} \cdot T_G^4 - A_{rad,G} \cdot T_G^4 \right) \quad (2.3.29)$$

Unfortunately, there exists no correlation to calculate the value of the geometry dependent absorption coefficient $A_{rad,G}$ for methane (VDI-e.V. 2013). Nonetheless, a good approximation can be found by using $A_{rad,G} = \epsilon_{rad,G}$.

The emission coefficient for methane $\epsilon_{rad,G}$ can be obtained as a function of the product $s_{gl} \cdot P_{CH_4}$ from (VDI-e.V. 2013), where s_{gl} , the equivalent layer thickness, is 90% of the reactor diameter, which is the norm for cylindrical geometries (VDI-e.V. 2013).

The only unknown is the emission coefficient for the liquid phase. However, since there is no available data for molten media in the literature, a best-case/worst-case approximation was used in the simulations.

2.3.3. Carbon Formation

The modeling of the carbon formed due to reaction requires the addition of some equations. First, the mass balance is required. For that, it is assumed that all carbon formed, either via heterogeneous reaction directly at the interface, or due to deposition from the carbon formed in the homogeneous gas reaction, will eventually deposit at the interface. A balance over an element yields:

$$\frac{\partial \dot{n}_C}{\partial z} = \pi \left(\frac{d_R}{2} - \delta_L \right)^2 r_{rxn,hom} + 2 \cdot \pi \left(\frac{d_R}{2} - \delta_L \right) r_{rxn,het} \quad (2.3.30)$$

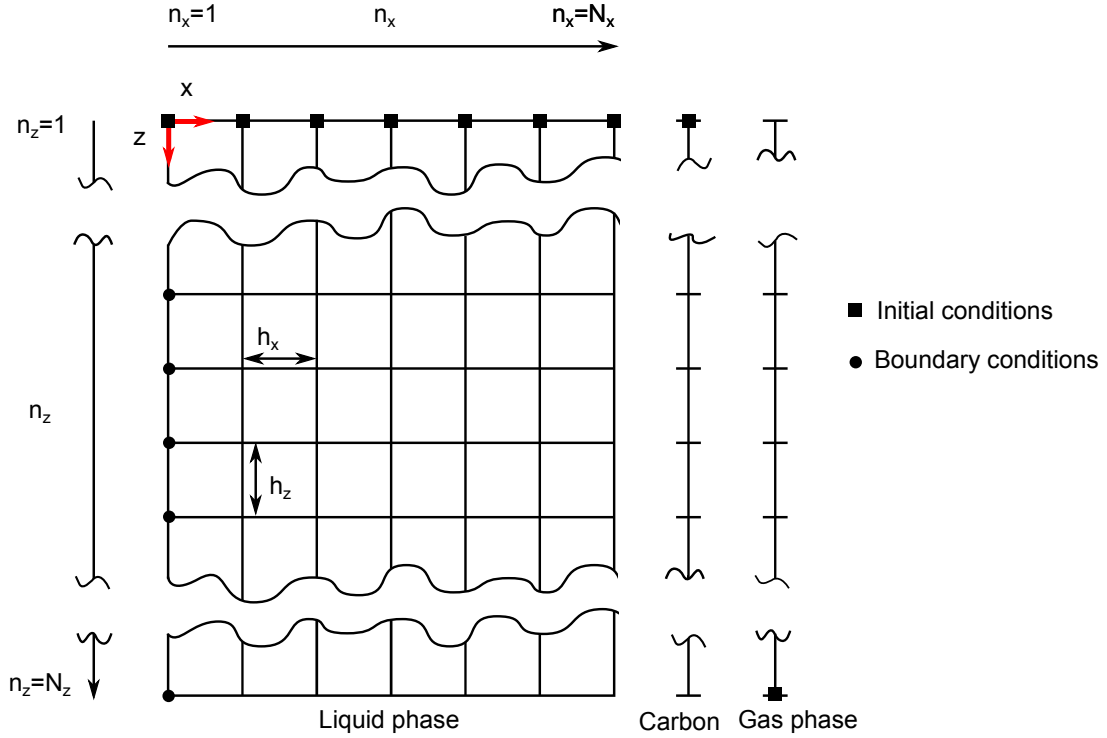


Figure 2.4.: Mesh structure for the discretization

With the boundary condition:

$$\dot{n}_C|_{z=0} = 0 \quad (2.3.31)$$

In addition, it is assumed that the temperature of the carbon will be equal to that of the liquid. If assumed that the deposited carbon will form a layer, its thickness can be calculated as:

$$\delta_C = \frac{\dot{n}_C}{\rho_{mol,C} \cdot 2 \cdot \pi \cdot \left(\frac{d_R}{2} - \delta_L\right) \cdot w_L|_{x=\delta_L}} \quad (2.3.32)$$

A layer need not necessarily be the way the carbon is formed, but it gives an order of magnitude for the amount of the carbon that is expected.

2.3.4. Numerical Methods

The model was implemented in MATLAB®, the mesh structure for the discretization is presented in Figure 2.4.

The discretization was that of an upwind scheme in the direction of the flow, and PDEs were transformed into ODEs using the method of lines approach. Since the problem is of counter-current nature, a normal consecutive or initial value solver was not adequate, and since an adaptive mesh was used, the built-in boundary value problem solver was not adequate.

Thus, a full discretization approach was used transforming all points into residuals in the form $f(\vec{x}) = 0$ where \vec{x} is the vector of independent variables. For a random distribution of this vector, the residuals can be built, and then can be solved using a Newton algorithm, where the Jacobian is calculated numerically. However, since the

mesh is adaptive, a two-step algorithm is used, first to solve for the residuals, then the liquid velocity profile and the film-thickness is recalculated, and these values are fed back into the original problem until convergence is achieved. This procedure is similar to that presented by Gómez Mendoza et al. (2014).

2.4. Results and Discussion

The results are divided into sections discussing the falling-film reactor, both experimental and simulated, and the experimental results for the rotating reactor.

2.4.1. Falling-Film Reactor

2.4.1.1. Experimental Results

Experimental studies were carried out at room temperature to test the validity of correlations for the minimum wetting rates, as well as to show the possible operation of a pumpless recycle.

2.4.1.1.1 Pumpless Recycle

The first experiments were performed to ensure that a pumpless recycle could be established with the proposed experimental set-up. The water-nitrogen system operated successfully although some nitrogen absorption was observed. For the GaInSn system, the amount of alloy available was not enough to obtain reliable measurements since the hold-up was too low in comparison with the previous system. Therefore, the exact values could not be measured, but the observed behavior was similar to that of the water-nitrogen system proving the concept would work for molten metals as well. In addition, and contrary to the other system, absorption of nitrogen in GaInSn was not observed. Figure 2.5 shows the results for the water-nitrogen system.

As it can be seen, and contrary to what intuitively could be expected, the liquid flow rate decreases with an increasing gas flow rate. This is mainly due to an oscillatory pattern consisting of gas build-up and liquid conveying when the pressure build-up is enough to transport the liquid. For higher gas flow rates, the gas build-up is faster, but the amount of liquid that is conveyed is reduced because the fraction of gas to liquid is higher than in the other cases and also the conveying time is lower. The opposite is then true for lower gas flow rates. It must be noted that the system is intrinsically constrained since a too-low gas flow rate will not allow the liquid to be conveyed, and a larger gas flow will push the liquid to leave through the gas inlet. For our case, the stable range is that depicted in Figure 2.5.

2.4.1.1.2 Minimum Wetting Rates

The main result obtained from the experiments with the falling-film in the water-nitrogen system was the sensitivity to contamination from the environment; one day

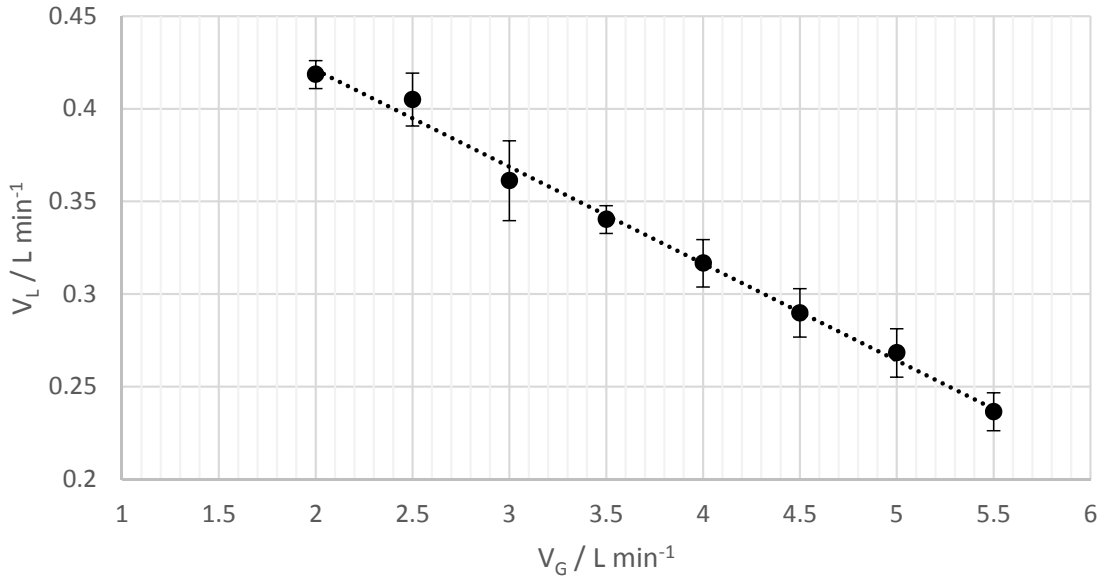


Figure 2.5.: Liquid flow as a function of gas flow for pumpless operation for the water-nitrogen system

Table 2.2.: Correlations for the minimum wetting rate in chronological order

Authors	Correlation
Hartley and Murgatroyd (1964)	$\Gamma_{min} = 1.69 \left(\frac{(1-\cos\theta) \cdot \sigma \cdot \rho^{1/3}}{\eta^{4/3} \cdot g^{1/3}} \right)$
Ponter et al. (1967)	$\Gamma_{min} = 1.116 \cdot (1 - \cos \theta)^{0.6} \left(\frac{\rho \eta \sigma^3}{g} \right)^{0.2}$
El-Genk and Saber (2001)	$\Gamma_{min} = \left(\frac{\rho \eta \sigma^3}{g} \right)^{0.2} \left(0.67(1 - \cos \theta)^{0.623} + 0.26(1 - \cos \theta)^{2.09} \right)$
Morison et al. (2006)	$\Gamma_{min} = 0.232 \left(\frac{(1-\cos\theta)\sigma \cdot \rho^{1/3}}{\eta^{4/3} \cdot g^{1/3}} \right)^{0.764}$

of operation was usually enough to substantially change the film behavior. For all experiments, the glass reactor was cleaned thoroughly and then inoculated at 600 °C.

The experiments were carried out first for the water-nitrogen system, where the liquid flow would be increased in small steps until the film wetted the surface completely. The experimental result compared to those predicted by the correlations given in Table 2.2 is shown in Figure 2.6.

As can be seen, the more recent correlations yield a better result than the previous ones. There are still some deviations, but given the empiric nature of the correlations, that is to be expected. In addition, measurements from the contact angles differ in the literature. For our system, the average contact angle of water on DURAN® was of 38°. Furthermore, it was noted that the operation with or without nitrogen yielded the same results, showing that there is very little influence of the shear forces at the interface.

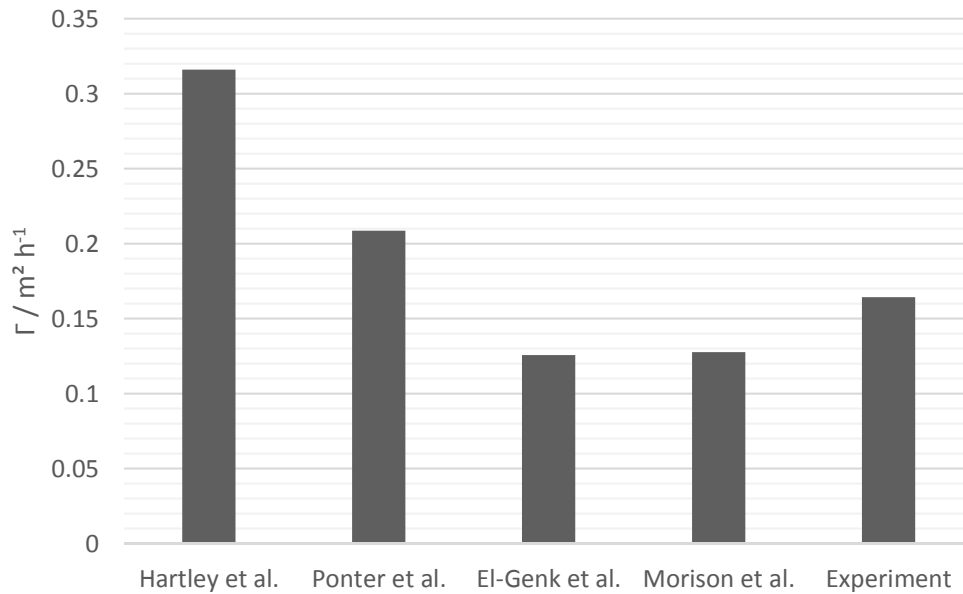


Figure 2.6.: Predicted minimum wetting rates from correlations and obtained experimental results for the water-nitrogen system

For the GaInSn-nitrogen system, a stable film could not be established for the current experimental set-up. As observed in another reactor system, a capillary reactor, by the authors (Munera Parra and Agar 2017), the wetting of the melt was not favorable. Qualitative values for the contact angles reported by the authors (Munera Parra and Agar 2017) were around 140° . Nonetheless, no precise measurements are available in the literature. The current flow, even though it could not be measured accurately, was too low compared from the predicted values by the correlations, even after correcting factors based on the results from the water-nitrogen system were introduced. These results are presented in Figure 2.7.

However, for the cases in which an oxide layer formed at the wall, a film could easily be established. This is because the contact angle from the melt and the melt oxide is well below 90° . Nonetheless, in the actual operation, the reducing atmosphere consisting of hydrogen and methane, and the lack of oxygen in the pyrolysis will not allow such an oxide layer to form. The concept is thus limited to finding an appropriate wall material, which the melt can wet, or switching from a molten metal to a more glass-compatible material like molten salts. In the next section, both alternatives are explored theoretically in the simulation of the high-temperature pyrolysis of methane.

2.4.1.2. Simulation Results

2.4.1.2.1 Molten Tin

From the experimental results, it is clear that the wall-melt interaction will be vital for the success of the concept. Although only DURAN® glass was studied experimentally, it is important to understand whether the wall material will have additional effects in the reactor besides film stability. Simulations were carried out for the

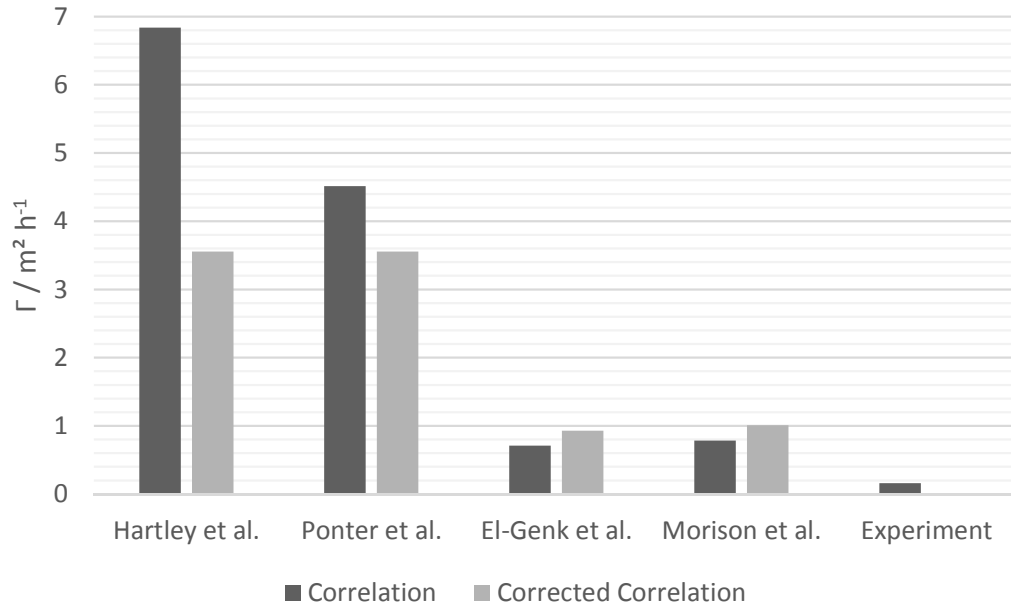


Figure 2.7.: Predicted minimum wetting rates from correlations and obtained experimental results for the GaInSn-nitrogen system

Table 2.3.: Parameters for simulating the wall material and thickness influence

\dot{V}_L / m ³ s ⁻¹	$T_{L,0}$ / K	$\dot{n}_{G,0}$ / mol s ⁻¹	$T_{G,0}$ / K	d_R / m	L_R / m	N_z /-	N_x /-	$\epsilon_{rad,L}$ /-
6.90E-06	1500	0.005	900	0.042	0.162	200	20	1

case of a low conductive material such as mullite or alumina, with their correlations given in the appendix, and for a metal-like conductor with a thermal conductivity of $40 \text{ W m}^{-1} \text{ K}^{-1}$. The dimensions of the reactor were first taken as those given in Figure 2.1. The complete set of parameters used is given in Table 2.3. The simulations were performed for a laminar film and assuming the melt as a black body. The chosen molten medium was tin, since for high temperatures operations the behavior of the GaInSn alloy has not been studied above $1300 \text{ }^\circ\text{C}$.

As shown in Figure 2.8, the wall material has only a minor influence in the resulting conversion of methane. For a thicker wall, the effect is slightly larger although still very minor. It can be thus assumed that if a material is found that allows for a stable film, apart from the hydrodynamic effects, it will have no major effect in the thermal behavior of the system. Since the above presented results span a region of one order of magnitude in both the thermal conductivity and the wall thickness, both can be chosen without bearing any major influence. The selected wall material for the rest of the simulations was mullite and the wall thickness was set to 2 mm.

Besides the wall material influence, it was of interest to study the effect of heat transfer through radiation, since there was no data available for the emission coefficients for molten tin. Simulations were carried out to test the best and worst case scenarios.

2. Falling-Film Reactor

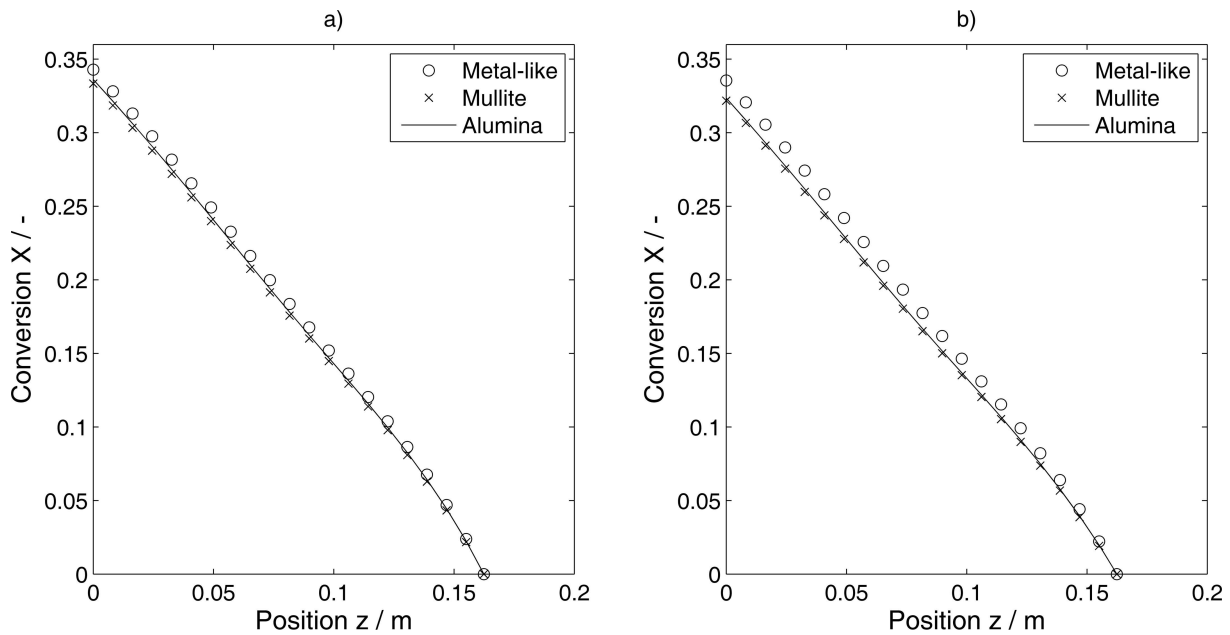


Figure 2.8.: Wall material and thickness influence: a) 2mm Wall thickness b) 20 mm wall thickness

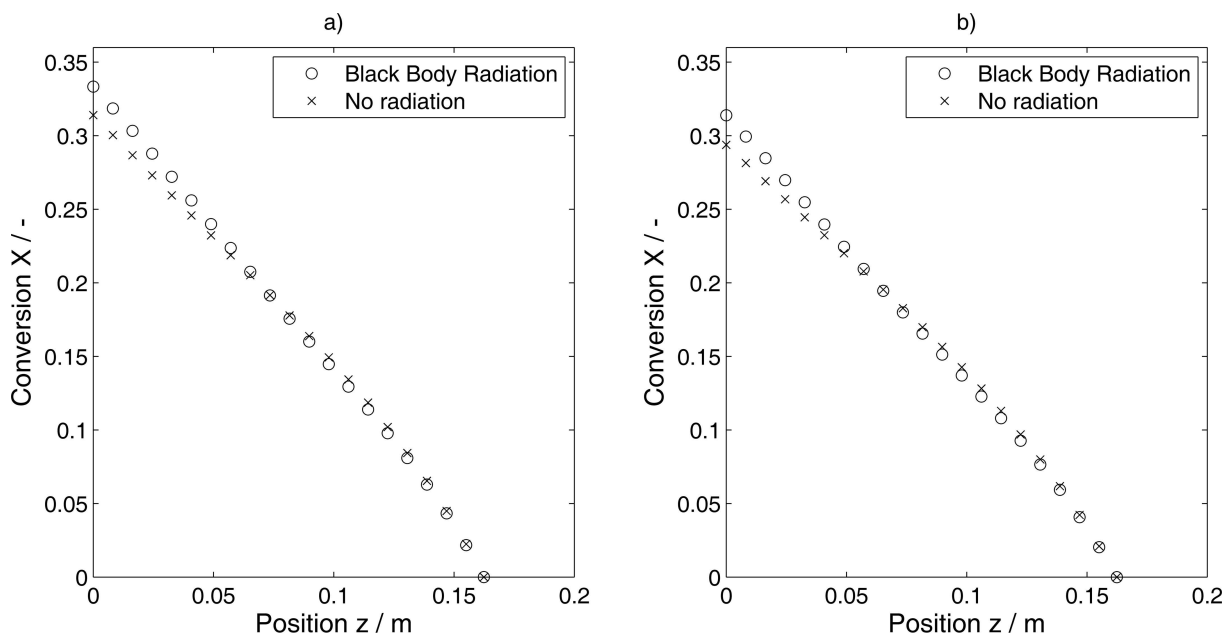


Figure 2.9.: Influence of the radiation for: a) laminar film b) turbulent film

In addition, the influence of the chosen model to represent the film, whether laminar or turbulent, was also studied. The results are presented in Figure 2.9.

As can be seen, the effect of radiation is minor compared to the other heat transfer mechanisms, and the actual is somewhere in between. The difference between laminar and turbulent is of more interest. Contrary to what would be expected, a turbulent film yields a lower conversion than the laminar case. This behavior can be reasoned based on the previous results as follows: As explained before, neither the heat transfer to through the wall, nor the heat transfer through radiation, have a major influence.

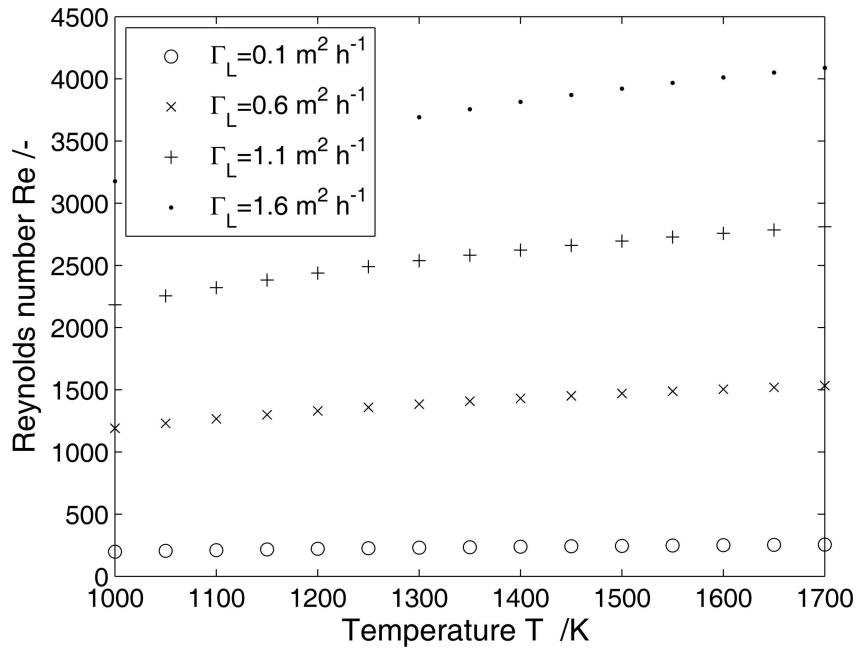


Figure 2.10.: Reynolds number as a function of temperature for different volume flows per wetted unit of perimeter

Table 2.4.: Parameters for simulating the reactor

\dot{V}_L / m ³ s ⁻¹	$T_{L,0}$ / K	$\dot{n}_{G,0}$ / mol s ⁻¹	$T_{G,0}$ / K	d_R / m	L_R / m	N_z / -	N_x / -	$\epsilon_{rad,L}$ / -
4.4E-05	1500	0.005	900	0.05	0.5	200	20	1

This points to the fact that the system is dominated by the heat transfer at the interface. For the laminar case, larger liquid velocities are found at the interface in comparison to the turbulent case, since in that case, an average velocity is assumed. Subsequently, the amount of heat transferred to the gas phase will be higher in the laminar film leading to higher conversions.

To choose the adequate model, the Reynolds number was calculated as a function of temperature for different values of Γ_L based in the results obtained in Figure 2.10.

From the results obtained in Figure 2.10, it is clear that a turbulent model is more appropriate for the proposed conditions. With that in mind, the detailed results for the largest reactor that could fit the existing furnace in the laboratory are now presented. The parameters used for the simulations are given in Table 2.4. The simulation results are presented in Figure 2.11.

From the simulations results, it can be observed that for the experimental set-up, a conversion of around 80% can be achieved at a furnace temperature of 1500 K. From the temperature profile, it can be observed that the gas heats up very quickly due to the large driving force, and then the increase is slowed down both due to the decreased driving force as well as the heat of reaction that is consumed. The gas velocity also increases first due to thermal expansion and then keeps increasing due to the increase in the number of moles with reaction. The calculated residence time for

2. Falling-Film Reactor

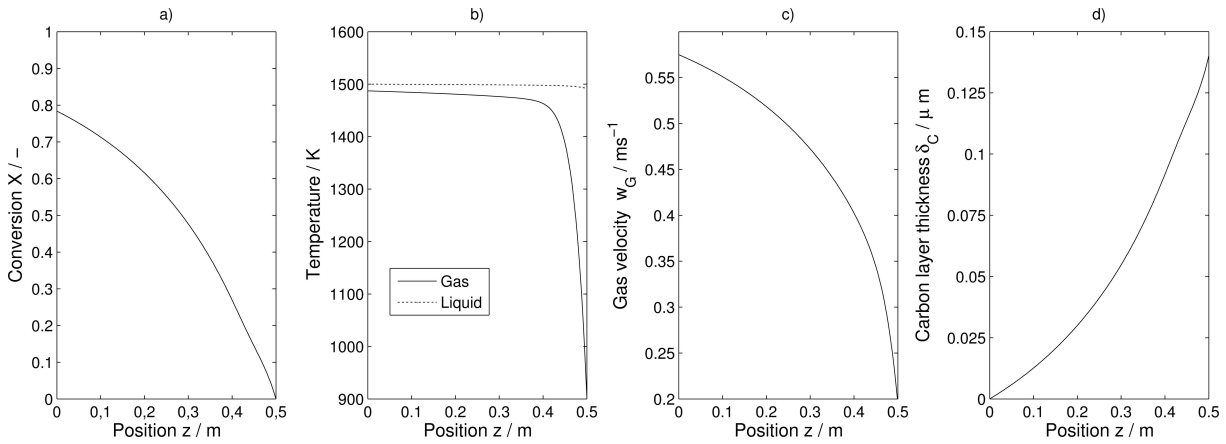


Figure 2.11.: Simulations results for: a) Methane conversion. b) Gas and liquid temperature. c) Gas velocity. d) Carbon layer thickness

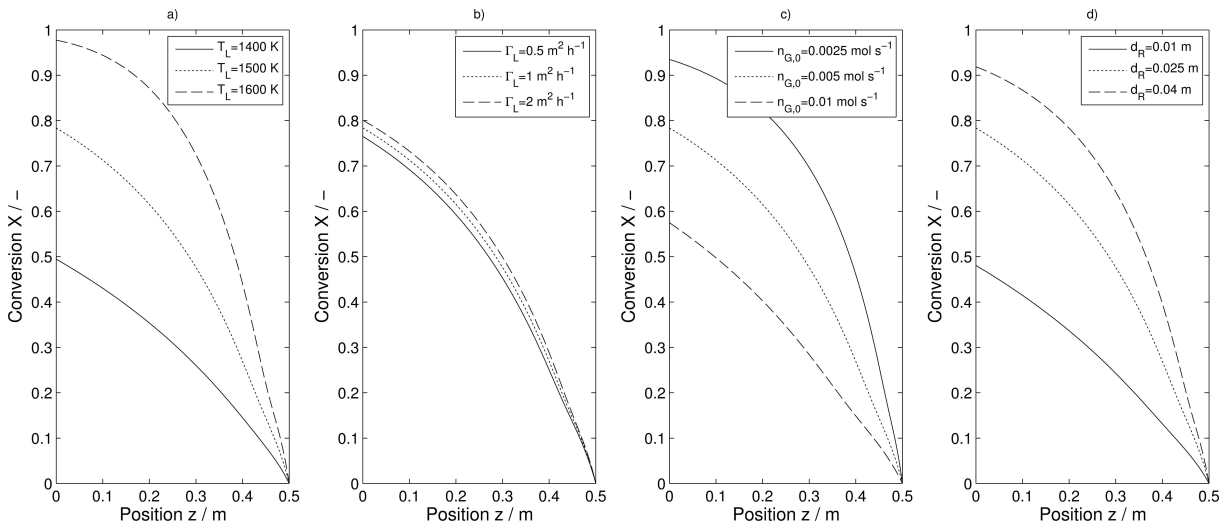


Figure 2.12.: Influence of different parameters on conversion: a) Furnace and inlet liquid temperature. b) Liquid volume flow rate per wetted unit of perimeter. c) Inlet gas molar flow. d) Reactor diameter

the given velocity profile is 1.056 s, which is in accordance with the results obtained from the capillary reactor for a similar temperature, i.e. residence time: 1.36 s, furnace temperature: 1573 K, conversion 80.07% (Munera Parra and Agar 2017). Finally, it is shown that if all the carbon was formed as a layer, its thickness at the bottom of the reactor would reach only about 0.15 micrometers which, taking into account that the calculated liquid film thickness is 290 micrometers, validates the assumptions that the solid particles bear little influence on either the momentum or heat transfer.

Finally, the influence of the most important parameters in the simulation was studied. The results are depicted in Figure 2.12.

From the system parameters, the gas inlet temperature has a negligible influence on conversion. This is because the gas heats up very quickly and hence pre-heating the gas offers no real advantage. The results shown are for a gas preheated to 900K, although even temperatures as low as 300 K could be used without any major changes

in conversion.

The liquid flow also showed little influence, as shown in Figure 2.12b. There, doubling or halving the flow led only to minor changes in conversion. This behavior actually favors this concept since it is still unclear what is the necessary amount of liquid needed to establish a stable film based in the correlations, but for a turbulent film, the effect of changing the volume flow rate and hence the film thickness would not be considerable.

The larger influences were given by the furnace temperature, the gas molar flow rate and the reactor diameter (Figure 2.12a, c, d). For the temperature, it is clear that an increase favors the reaction rate and hence higher conversions are achieved. A similar effect can be obtained by reducing the molar flow and thereby increasing the residence time, although at a loss of productivity. An analogous effect without the loss in productivity could be achieved by increasing the reactor length if a larger furnace was available. Finally, by increasing the reactor diameter, a comparable effect is achieved, although in this case the influence is limited. By increasing the diameter, the volume of the reactor is increased as well as the residence time. However, increasing the diameter is detrimental to the heat transfer at the interface and thus the effect is not as large as it is with an increase in temperature and length or a decrease in molar flow.

2.4.1.2.2 Molten Salts: FLiNaK

An alternative to studying wall materials is the study of substitute melts. Besides molten metals, molten salts can also be used as heat transfer media. They have found application in fields such as nuclear reactors among others, and in most cases, have more affinity towards glass or other solid materials (Morel 1970), although the range in contact angles can vary from 50 to 120° depending upon material, temperature and molten salt. A possible salt could be FLiNaK, which is the eutectic of lithium, sodium and potassium fluorides. This molten salt offers good heat transfer properties, low vapor pressures, and a temperature range from 727 K to 1843 K (Williams 2006). However, the wetting behavior for this salt is not available in the literature.

Due to the difference in the viscosity as well as density, the Reynolds numbers as well as the required liquid volume rates per wetted unit of perimeter are different from the results obtained for tin. In Figure 2.13, it can be seen that for the case of FLiNaK, the flow region is not completely turbulent and for some cases, it is very close to being laminar.

To compare the results obtained with tin, simulations were carried out for FLiNaK with the parameters given in Table 2.5. The model for the film was chosen to be laminar. Simulation results are given in Figure 2.14.

The results for molten FLiNaK are similar to those for molten tin; the conversion is slightly lower but that is mostly because the film is laminar. The gas temperature and velocity profiles are very close to those obtained before. In the liquid phase is where the difference of the results lays. As displayed in Figure 2.14c, the temperature at the interface is slightly lower than that of the wall, and hence lower than that of the turbulent case, where a mean temperature is assumed.

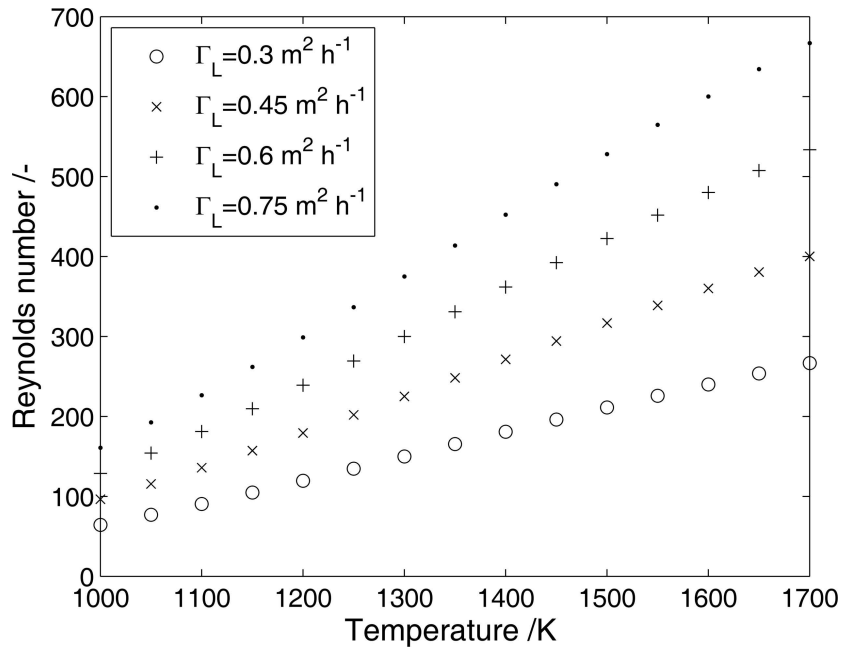


Figure 2.13.: Reynolds number as a function of temperature for different volume flows per wetted unit of perimeter

Table 2.5.: Parameters for simulating the reactor (FLiNaK)

\dot{V}_L / $\text{m}^3 \text{ s}^{-1}$	$T_{L,0}$ / K	$\dot{n}_{G,0}$ / mol s^{-1}	$T_{G,0}$ / K	d_R / m	L_R / m	N_z / -	N_x / -	$\epsilon_{rad,L}$ / -
1.5E-05	1500	0.005	900	0.05	0.5	200	20	1

An additional result is that a profile for the film thickness can be obtained instead of the mean value for the turbulent case. Nonetheless, the change in the thickness is negligible although the results prove that the adaptive mesh worked properly. The carbon layer presents a similar profile to that which was obtained before, although the thickness is slightly greater. This is because the liquid residence time was larger for this case and therefore allows for more growth.

The results for the shear stress validated the obtained results in the experimental section, since the values obtained were very low. In addition, the ratio of the gravitational to the friction contribution for the velocity was at least two orders of magnitude apart.

Finally, the radial liquid velocity profile is shown in Figure 2.14h. From there it can be seen that the profile varies, if anything, slightly along the reactor length. This is coupled with the fact that the film thickness remains almost constant, but for a case where the film thickness changed, this would be visible in the velocity profile.

2.4.2. Rotating Reactor

In the previous section, two alternatives were presented to accomplish a stable film. In the worst-case scenario, should neither an appropriate material be found nor the

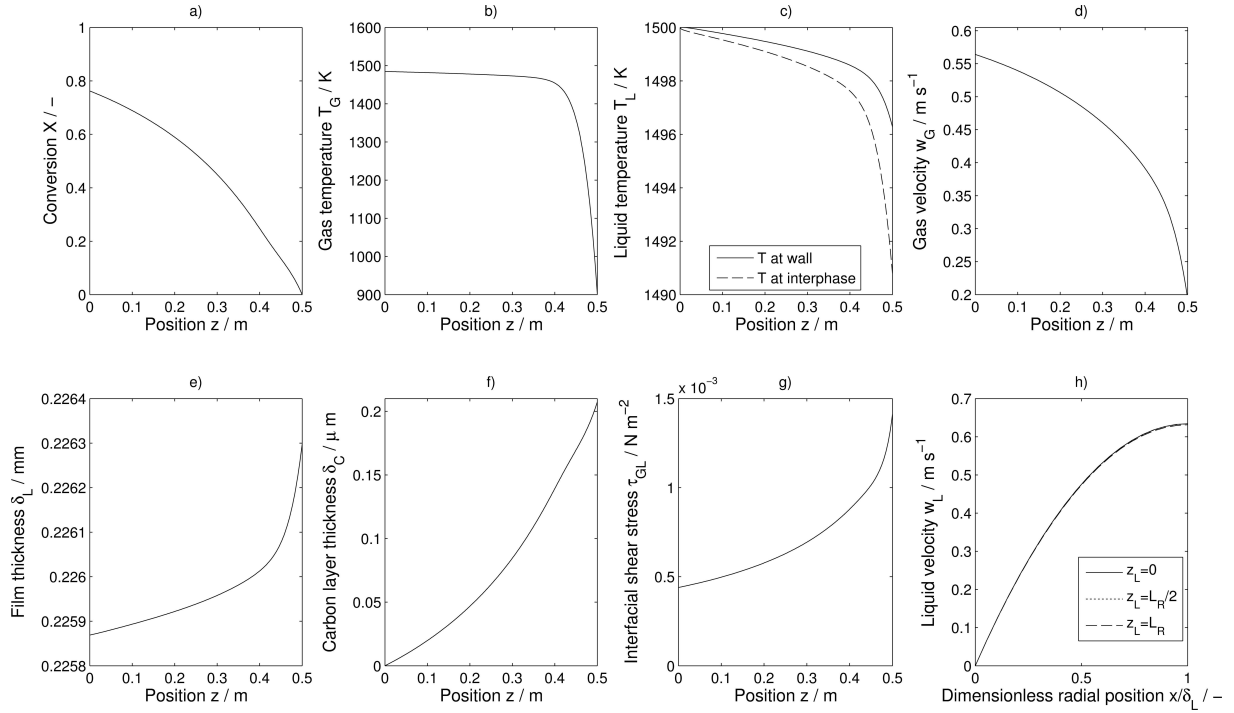


Figure 2.14.: Simulations results with FLiNaK as molten medium: a) Methane conversion. b) Gas temperature. c) Liquid temperature. d) Gas velocity. e) Film thickness. f) Carbon layer thickness. g) Interfacial shear stress. h) Liquid velocity radial profile

molten salt have better wetting properties, a rotating reactor concept could be an alternative.

For this reactor concept, experiments with water and GaInSn were carried out. For water, even 0.1 mL at the lowest rotational speed of 200 rpm was enough to wet the complete surface. The results for GaInSn are presented in Figure 2.15.

As can be observed, a full wetting of the reactor was achieved with 8 mL, which would be the minimum amount required to generate a film. Below 8 mL, the result would look like that presented in Figure 2.16, whereas the completely wetted reactor would be the same as the one presented in Figure 2.17.

For the partially wetted reactor, as shown, the melt would tend to go towards the extremes, due to the effect of the vibrations. For the completely wetted reactor, 500 rpm were needed to initially wet the wall. Analogously with the falling-film, once an oxide layer was built, this value could be reduced up to 350 rpm without breaking the film. Nonetheless, the initial value is the one of interest since, as mentioned before, the reducing atmosphere in the pyrolysis would not allow for the oxide layer formation. The amount of metal that formed the layer and remained in the reactor was of 1.1 mL. Assuming the 8 mL were distributed uniformly, a film thickness of around 400 micrometers can be calculated which is in the order of magnitude of the films found for the falling-film simulations.

With these results, it could be proven that given the right velocities, GaInSn would even wet DURAN® and thus, this concept could be used as a backup for the falling-film reactor.

2. Falling-Film Reactor

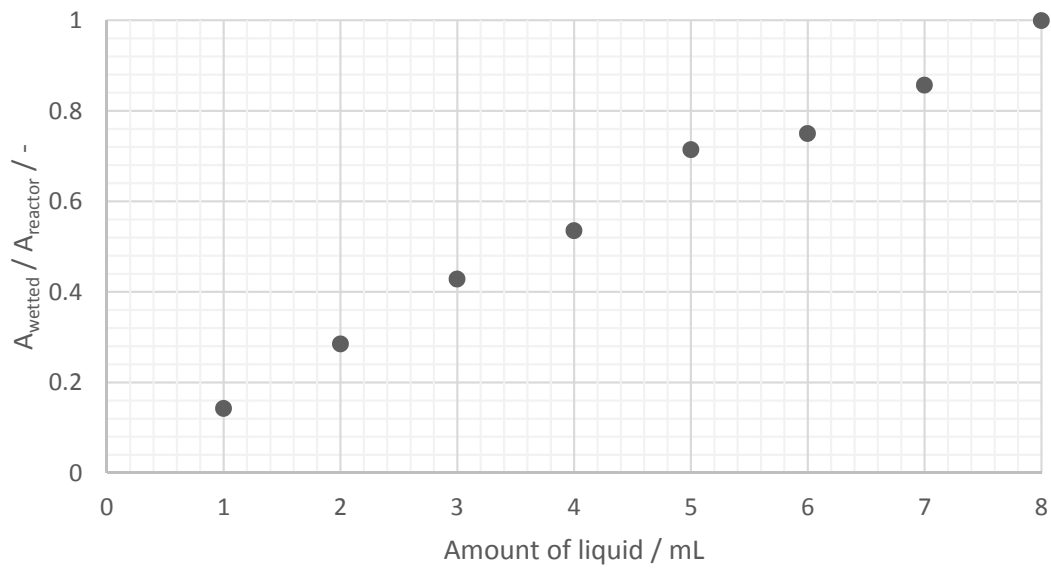


Figure 2.15.: Wetted area as a function of liquid inside the reactor



Figure 2.16.: Partially wetted reactor with 4mL of GaInSn

2.5. Conclusions

In this work, the experimental feasibility of a falling-film reactor was first studied experimentally. The results showed that the correlations for the water-nitrogen system were adequate. Based on this result, the required volume flow for the GaInSn was obtained. However, using the existing pumpless recycle, it was not possible to achieve the required flow for a stable film formation.

The normal course of action would be to test a higher flow rate or to try to find a



Figure 2.17.: Completely wetted reactor

wall material that has more affinity with the molten metals. To understand the effect that a different wall material would have, as well as the sensitivity of the conversion with respect to the liquid flow rate, the system was modeled and simulated. The chosen melt for the simulations was tin since it has a broader range of operation at higher temperatures than GaInSn.

Simulation results showed that both the wall material and the liquid flow rate have little influence on the obtained conversion for a given reactor. In addition, the influence of the influence of heat transfer through radiation was studied as well as the flow regime in the film. The simulation results are also in accordance with previous results in a different set up with conversion of around 80% for a residence time of about 1 second. In addition, a parametric study showed the influence of the remaining parameters.

An alternative for the concept, should the molten metals prove inadequate, was also studied. The first approach was to switch the molten metal for a molten salt, which could have better affinity with the wall material. Simulations for the molten salt FLiNaK were performed showing that for a change in flow regime, and with changing thermal and rheological properties from the salt, similar results to those obtain with tin could be expected.

The simulation results show that, due to the excellent heat transfer properties of both the molten metals and salts, the falling-film is a very robust concept since it is dominated by the heat transfer at the interface, allowing for changes in wall materials, melts, and liquid flows without having major changes in conversion.

A rotating reactor was studied experimentally as the worst-case scenario, for when it is not possible to wet the wall using a falling-film reactor. It was shown that the film can be forced hydrodynamically by rotating the reactor. The results indicated that a liquid hold up of at least 8 mL was required to form a stable film. Although

2. *Falling-Film Reactor*

the vibrations in the system could be worrisome, a more refined experimental set-up could be used in the future.

For future works, the wettability of the molten metals with various wall materials will be tested and if a promising candidate is found, the high temperature experiments will be performed to validate the results obtained with the model. If not, the rotating reactor will be carried out as the next step in the reactor design progression.

Part II.

Methane Pyrolysis: Moving-Bed Reactor

Preamble

The following chapter has been published as:

Munera Parra, A.A, F. Platte, and D.W. Agar (2016): "Multiplicity Regions in a Moving-Bed Reactor: Bifurcation Analysis, Model Extension, and Application for the High-Temperature Pyrolysis of Methane". In: *Chemie Ingenieur Technik* 88.11, pp. 1703-1714

The calculations and analysis were performed by myself, Prof. Platte served as consultant for numerical methods and introduced me to the continuation algorithms. Prof. Agar supervised the work.

Abstract

This paper reports studies on the bifurcation analysis and the generation of regions of multiplicity in the operation of moving-bed reactors. The studies were first carried out for a generalized model, which allows the investigation of the effect of various scenarios, such as changes in heat capacity or the number of moles with reaction, as well as the previously unstudied equilibrium and allothermic reactions. The insights gained from this extension were then applied to an actual reaction, namely the high temperature pyrolysis of methane.

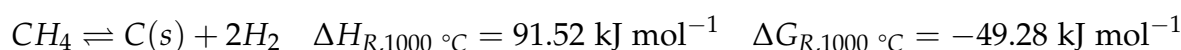
3

Multiplicities in Moving-Bed Reactors

3.1. Introduction

The question of how energy can be supplied to improve living standards of a growing population is becoming increasingly urgent. The limitations on fossil fuel consumption are imposed by environmental considerations rather than their availability. New extraction techniques mean that proven reserves are actually rising, even if vast novel sources, such as methane hydrates, are ignored. Using Carbon Capture and Storage (CCS) to curtail the environmental impact of fossil fuel consumption is controversial and cannot be implemented as rapidly as required. Several alternatives to produce hydrogen with low to zero carbon dioxide emissions have been studied (Machhammer et al. 2016; Muradov and Veziroglu 2008). Among them, the decarbonization of the fossil energy, especially the high temperature methane pyrolysis, constitutes a promising drop-in strategy (Kreysa 2009). To assess its potential, a research program has been set up to develop a novel two-step process for first generating hydrogen and carbon and then using the former to produce synthesis gas utilizing carbon dioxide (Bode et al. 2014).

To carry out the pyrolysis of methane,



the moving-bed reactor represents a promising approach, since it has been successfully operated at high temperatures in the metallurgical industry and elsewhere.

However, the modeling and operation of moving-bed reactors is non-trivial and can give rise to operational multiplicities, as originally identified by Vortmeyer's group (Marb and Vortmeyer 1988; Schaefer et al. 1974; Thoma 1978). In their studies, the presence of multiple steady-states in a moving-bed reactor was proven both experimentally and theoretically for an exothermic reaction, specifically for the oxidation of ethane. The study of the methane pyrolysis in a moving-bed reactor entails new challenges and extends the scope of previous work. The first and most obvious difference is the fact that the forward reaction is endothermic and hence leads to an allothermal operation, which until now has not been studied in the literature. In addition, at higher pressures, the effect of the exothermic back-reaction starts exerting a larger influence, leading to the second novel feature of this work: the study of multiplicities

for an equilibrium reaction. In addition, two factors that are not usually taken into account when modeling a chemical reactor, the change in number of moles and heat capacity, are considered. As can be seen in the following sections, these effects play a larger role than might have been anticipated.

3.2. Mathematical Modeling

3.2.1. General Model

The standard models for a moving-bed reactor with a heterogeneous reaction can be easily derived from differential balances under the usual assumptions of negligible axial and radial conduction and diffusion, plug flow in both the solid and gas phases and temperature independent properties.

The steady-state dimensionless model equations describing the mass and energy balances are:

$$\frac{dx}{d\xi} = -Da_{0,g} \cdot \phi(x, T_s^*, \gamma) \quad x(\xi = 1) = 0 \quad (3.2.1)$$

$$\frac{dT_g^*}{d\xi} = St_{g,s} \cdot (T_g^* - T_s^*) \quad T_g^*(\xi = 1) = T_{g,0}^* \quad (3.2.2)$$

$$\frac{dT_s^*}{d\xi} = St_{g,s} \cdot F_2 \cdot (T_g^* - T_s^*) + \Delta T_{ad} \cdot Da_{0,g} \cdot \phi(x, T_s^*, \gamma) \cdot F_1 \quad T_s^*(\xi = 0) = T_{s,0}^* \quad (3.2.3)$$

with the dimensionless quantities:

$$\xi = \frac{V}{V_R}, \quad x = 1 - \frac{n}{n_{initial}}, \quad T_x^* = \frac{T_x}{T_{ref}}, \quad \gamma = \frac{E_A}{R \cdot T_{ref}}, \quad F_1 = \frac{N_g}{N_s}, \quad Da_{0,g} = \frac{r(x=0, T_s=T_{ref}, \gamma) \cdot V_R}{N_g},$$

$$St_{g,s} = \frac{h \cdot a \cdot V_R}{N_g \cdot c_{p,g}}, \quad F_2 = \frac{N_g \cdot c_{p,g}}{N_s \cdot c_{p,s}} = F_1 \frac{c_{p,g}}{c_{p,s}}, \quad \Delta T_{ad} = \frac{-\Delta H_R}{c_{p,s} \cdot T_{ref}}$$

where $\phi(x, T^*, \gamma)$ describes the influence of conversion and temperature on the Damköhler number, which varies according to the reaction mechanism. The axial coordinate origin is set at the solid phase feed, as apparent from the boundary conditions.

3.2.2. Model for the Pyrolysis of Methane

For the pyrolysis of methane, being an endothermic high temperature reaction, the use of a heat integrated reactor offers several advantages. The reactor depicted in Figure 3.1, can be considered in 3 sections: The middle section is the reaction zone, where heat is only transferred into the reactor and the reaction occurs. In the top section, hot gas leaves the reaction and preheats the incoming carrier, in this case carbon, avoiding the need for a complicated, high temperature gas heat exchanger, and in the bottom section, hot solids leaving the reaction zone preheat the incoming gas.

The dimensionless equations resulting from differential balances are:

$$\frac{dx_{CH_4}}{d\xi} = -Da_{0,g} \cdot \phi(x, T_g^*, \gamma) \quad x_{CH_4}(\xi = 1) = 0 \quad (3.2.4)$$

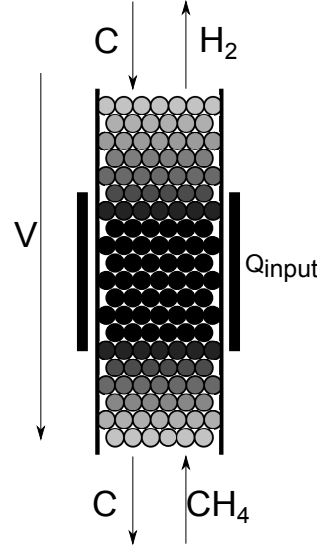


Figure 3.1.: Heat-Integrated moving-bed reactor

$$\frac{dT_g^*}{d\zeta} = \frac{St_{g,s} \cdot (T_g^* - T_s^*) + Da_0 \cdot \phi(x_{CH_4}, T_g^*, \gamma) \cdot \Delta T_{ad} - \frac{\dot{Q}_{input,g} \cdot V_R}{N_{CH_4,0} \cdot c_{p,CH_4} \cdot T_{ref}}}{1 - x_{CH_4} + 2 \cdot x_{CH_4} \frac{c_{p,H_2}}{c_{p,CH_4}}}$$

$$T_g^*(\zeta = 1) = T_{g,0}^* \quad (3.2.5)$$

$$\frac{dT_s^*}{d\zeta} = \frac{St_{g,s} \cdot (T_g^* - T_s^*) + \frac{\dot{Q}_{input,s} \cdot V_R}{N_{CH_4,0} \cdot c_{p,CH_4,0} \cdot T_{ref}}}{(N_{C,0}^* + x_{CH_4}(\zeta = 0) - x_{CH_4}) \left(\frac{c_{p,C}}{c_{p,CH_4,0}} \right)}$$

$$T_s^*(\zeta = 0) = T_{s,0}^* \quad (3.2.6)$$

For the solid phase, the molar balance can be given explicitly as:

$$N_C^*(x_{CH_4}) = N_{C,0}^* + (x_{CH_4}(\zeta = 0) - x_{CH_4}) \quad (3.2.7)$$

With:

$$N_C^* = \frac{N_C}{N_{CH_4,0}} \quad (3.2.8)$$

The reaction rate given by Patrianakos et al. (2011) is modified to allow for the reverse reaction yielding:

$$r_{CH_4}(T, C_{CH_4}, C_{H_2}) = k(T) \left[C_{CH_4} - \frac{C_{H_2}^2}{K_c(T)} \right] \quad (3.2.9)$$

where the reaction rate constant is given by:

$$k(T) = 10^{14} \text{ s}^{-1} \exp\left(-\frac{400000 \text{ J mol}^{-1}}{RT}\right) \quad (3.2.10)$$

and the concentration-based equilibrium constant can be obtained from thermodynamic databases (Linstrom and Mallard 2001) as:

$$K_c(T) = \frac{K_P}{RT} = \frac{\exp\left(\frac{-\Delta G_R}{RT}\right)}{RT} \quad (3.2.11)$$

When the Damköhler number is defined as in Section 3.2.1, the function ϕ can be expressed as:

$$\phi(x, T_g^*, \gamma) = \exp\left(-\gamma\left(\frac{1}{T_g^*} - 1\right)\right) \left[\left(\frac{1-x}{1+x}\right) - \frac{\left(\frac{2x}{1+x}\right)^2 R \cdot T_g^* \cdot T_{ref} \cdot C_{CH_4,0}}{K_P(T_g^* T_{ref})} \right] \quad (3.2.12)$$

All other dimensionless quantities as are defined as in Section 3.2.1. Note that, due to the temperature dependency of the heat capacity, some quantities like the Stanton number and the dimensionless adiabatic temperature rise are functions of temperature.

3.3. Numerical Methods

Several numerical methods have been developed to calculate bifurcation curves, an overview can be found in the book by Allgower and Georg (2003). For this particular case, it was decided to work with a predictor-corrector method, also known as the pseudo arc-length continuation described in the book of Keller (1987). This method proved effective in previous case studies (Günther et al. 2014; Nalpantidis et al. 2006; Salinger and Eigenberger 1996a,b). To calculate a bifurcation curve, the first step is to obtain a solution to the system. In this case, the three differential equations were discretized using the orthogonal collocation on finite elements (OCFE) scheme (Carey and Finlayson 1975), in which the collocation matrices can be calculated as presented in the work of Villadsen and Stewart (1967). The equations can thus be reduced to the form:

$$G(x, T_g^*, T_s^*, \lambda) = \begin{pmatrix} A & 0 & 0 \\ 0 & A & 0 \\ 0 & 0 & A \end{pmatrix} \begin{pmatrix} x \\ T_g^* \\ T_s^* \end{pmatrix} + b(x, T_g^*, T_s^*) = 0 \quad (3.3.1)$$

where A represents the derivative matrix obtained from the discretization, x , T_g^* , T_s^* represent the vectors with the values at the collocation points, b represents the non-linear vector that contains all the terms in the right hand sides of Eqs. (3.2.1-3.2.3), or Eqs. (3.2.4-3.2.6) for the pyrolysis, and λ represents the parameter for the bifurcation curve.

Eq. (3.3.1) can then be solved by any zero-value problem solver to obtain the initial point for the bifurcation curve at a parameter value λ_0 . For simplicity the variables x , T_g^* and T_s^* are lumped into a variable U .

To avoid singularities at the turning points, which are a feature of systems exhibiting multiplicities, the pseudo arc-length couples the variable U with the parameter λ in an arc length parameter s for which the following derivatives

$$\dot{U} = \frac{\partial U}{\partial s} \quad \dot{\lambda} = \frac{\partial \lambda}{\partial s} \quad (3.3.2)$$

are always defined, thus avoiding any singularity. The inclusion of the parameter s , implies the addition of a new equation, Keller defines s , so that a step taken in the s

direction is proportional to the above described derivatives, leading to the equation:

$$g(U_n, \lambda_n) = (U_n - U_{n-1}) \dot{U}_{n-1} + (\lambda_n - \lambda_{n-1}) \dot{\lambda}_{n-1} - \Delta s = 0 \quad (3.3.3)$$

Eq. (3.3.1) and Eq. (3.3.3) describe the full system of equations. From the starting point calculated, the first prediction step can now be taken. For the first operation, the derivatives with respect to s are taken as:

$$(\dot{U}_0, \dot{\lambda}_0) = \left(\frac{\partial U}{\partial \lambda}, 1 \right) \quad (3.3.4)$$

This vector is then normalized and the prediction is given by:

$$\begin{pmatrix} U_{n,initial} \\ \lambda_{n,initial} \end{pmatrix} = \begin{pmatrix} U_{n-1} \\ \lambda_{n-1} \end{pmatrix} + \Delta s \begin{pmatrix} \dot{U}_{n-1} \\ \dot{\lambda}_{n-1} \end{pmatrix} \quad (3.3.5)$$

This initial prediction is then corrected via:

$$\begin{pmatrix} U_{n,\nu+1} \\ \lambda_{n,\nu+1} \end{pmatrix} = \begin{pmatrix} U_{n,\nu} \\ \lambda_{n,\nu} \end{pmatrix} + \begin{pmatrix} \Delta U_{n,\nu} \\ \Delta \lambda_{n,\nu} \end{pmatrix} \quad (3.3.6)$$

where ν is the current step in the correction. The correction in the variables and λ can be calculated from the Jacobian as:

$$\begin{pmatrix} \Delta U_{n,\nu} \\ \Delta \lambda_{n,\nu} \end{pmatrix} = J_{n,\nu}^{-1} \begin{pmatrix} -G_{n,\nu} \\ -g_{n,\nu} \end{pmatrix} \quad (3.3.7)$$

These correction steps are repeated until convergence. The converged point then becomes the new initial point for the next prediction step, the derivatives with respect to s , are calculated as:

$$\begin{pmatrix} \dot{U}_n \\ \dot{\lambda}_n \end{pmatrix} = J_{n,converged}^{-1} \begin{pmatrix} 0 \\ 1 \end{pmatrix} \quad (3.3.8)$$

The vector is re-normalized and then the corrections steps applied again, and the same procedure is repeated until the bifurcation curve is complete. This procedure is presented schematically in Figure 3.2.

3.4. Results

3.4.1. Previous Work

The occurrence of multiplicities in a moving-bed reactor was first found by Schaefer et al. (1974). In their theoretical study, the heat generation was dealt with as an ignition-type curve instead of an actual reaction for simplicity. These results were successfully reproduced using the continuation method, but are not shown for the sake of conciseness.

A real system, the oxidation of ethane, was then investigated by Thoma (1978) in his PhD Thesis. In this work multiplicities were found both experimentally and theoretically. The oxidation of ethane is a strongly exothermic reaction and not exhibiting

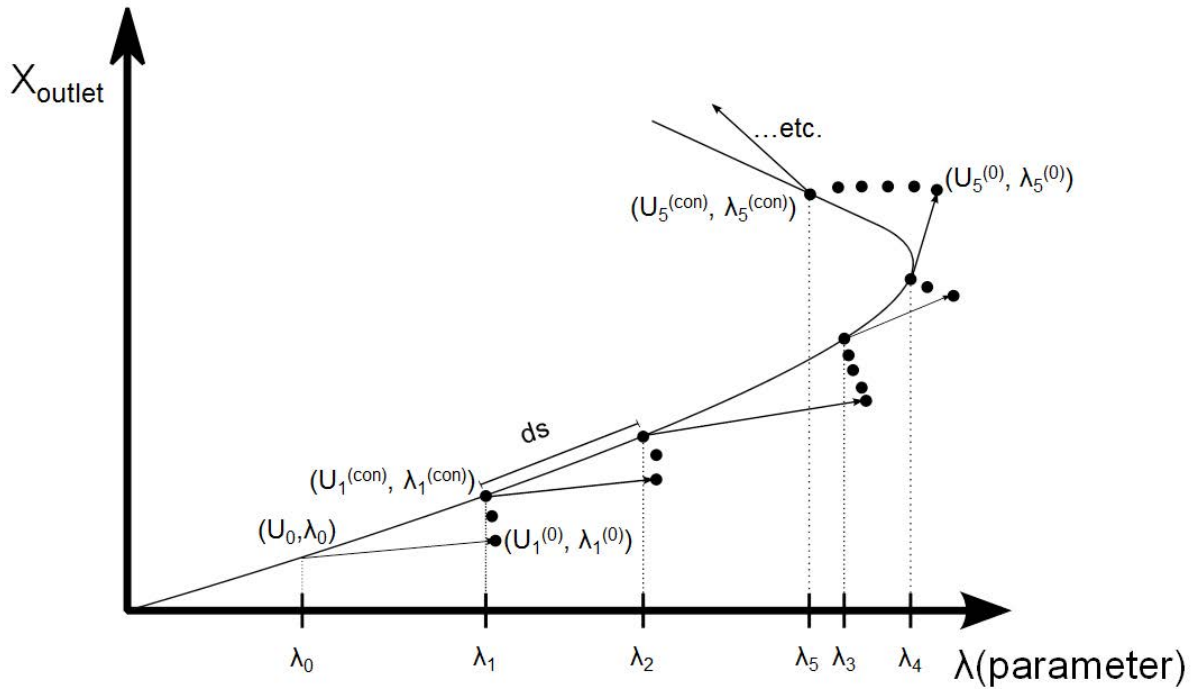


Figure 3.2.: Regions of multiplicity for the benchmark moving-bed reactor

a major change in the number of moles, and the heat capacity of the fluid and solid phase were lumped as constants. The introduction of a realistic heat input, due to chemical reaction, made the system of equations more challenging.

In Thoma's work, regions of multiplicity were defined as lower and upper steady-state curves, but no detailed information regarding the calculation of said curves was given. A reproduction of the results was not possible due to lack of parameters for the oxidation kinetics. However, the model of the reactor and the orders of magnitude for the heat exchange served as the base for the model extension used in Section 3.4.2 and described in Section 3.2.1.

The subsequent work of Marb and Vortmeyer (1988) dealt with the multiplicities in a cross-flow reactor. These results are not relevant to the reactor studied in this work and will not be discussed further.

3.4.2. Model Extension

As mentioned earlier, the system studied by Thoma, did not allow for change in the number of moles or heat capacity, and the reaction was exothermic and irreversible. In the following sections, a generic exothermic system is studied, represented by the dimensionless model presented in Section 3.2.1, for a general reaction rate representing a heterogeneously catalyzed reaction $A \rightarrow B$ given by:

$$r = \frac{kC_A}{1 + KC_A} \tag{3.4.1}$$

It is important to mention that a multiplicity will arise regardless of the choices of K (or almost any type of reaction kinetics), and the reaction rate, although arbitrarily

Table 3.1.: Parameters used to construct the bifurcation curve

Parameter	Da	γ	ΔT_{ad}	St	F_1	F_2	$T_{inlet,sol}$	$T_{inlet,gas}$	x_{inlet}
Value	2.6	5	1.5	3.7	0.8	1.25	0.6	λ	0

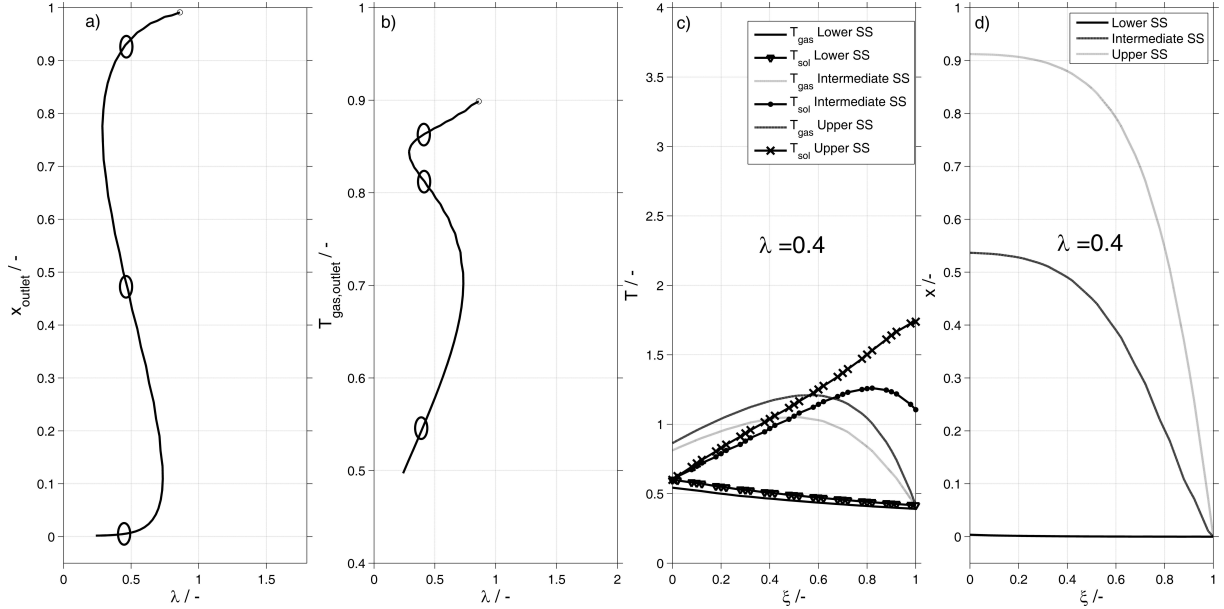


Figure 3.3.: a) Bifurcation curve for outlet conversion. b) Bifurcation curve for outlet gas temperature. c) Gas and solid temperature profiles for the multiple solutions. d) Conversion profile for the multiple solutions

chosen, is representative of a real system. The function ϕ can be then defined as:

$$\phi(x, T_s^*, \gamma) = \exp\left(-\gamma\left(\frac{1}{T_s^*} - 1\right)\right) \left(\frac{1-x}{1+KC_{A,0}(1-x)}\right) = \exp\left(-\gamma\left(\frac{1}{T_s^*} - 1\right)\right) \left(\frac{1-x}{1+K_2(1-x)}\right) \quad (3.4.2)$$

The value of K_2 was chosen to be twice the initial Damköhler number. With ϕ defined, Eqs. (3.2.1-3.2.3) can be solved at steady-state to obtain a starting point for the bifurcation curve. The result of the solution of numerical continuation for the set of parameters given in Table 3.1 is presented in Figure 3.3.

The parameter λ represents the inlet gas temperature, Figures 3.3a-b depict the bifurcation curve for the outlet conversion and temperature respectively. Figures 3.3c-d represent the temperature and conversion profiles along the reactor length for the three possible solutions for $\lambda = 0.4$ denoted by the markers in Figures 3.3a-b. Each of the solutions portrays the lower, upper and the intermediate (unstable) steady-states.

By calculating several of these bifurcation curves varying another parameter, e.g. F_1 , a region of multiplicity can be established. The regions of multiplicity are simply those in which more than one solution exists for a value of λ . An example of a multiplicity region is given in Figure 3.4 for the same parameters presented in Table 3.1, but varying F_1 (and therefore F_2) from 0.5 to 2. For the sake of conciseness, only the

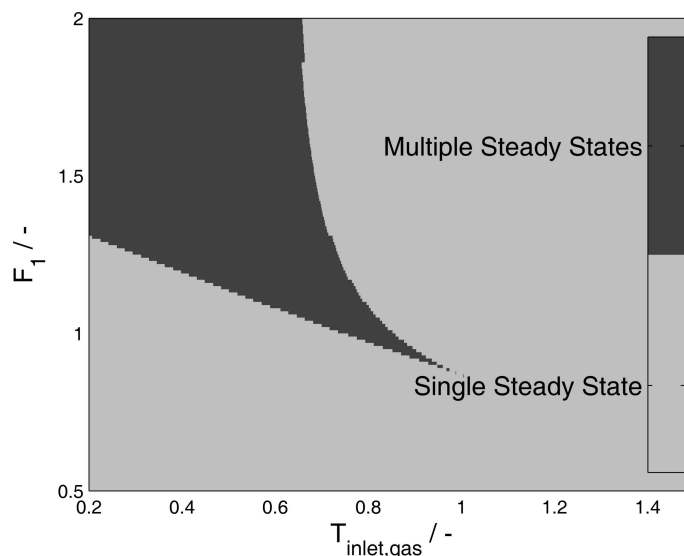


Figure 3.4.: Regions of multiplicity for the benchmark moving-bed reactor

regions of multiplicity will be shown from now on. Nonetheless, it should be noted that in the background of all multiplicity regions a figure like Figure 3.3 exists, illustrating the different conversion and temperature profiles and also the bifurcation curves.

In Figure 3.4 the lower left corner represents the complete extinction case: the low inlet gas temperature, coupled with the larger flow of solids does not allow any reaction to occur. Conversely, the upper right corner shows the complete ignition cases: where the high gas temperature, coupled with the longer solids residence time with respect to the gas only permit ignited states. The lower right corner always possesses some reaction activity. The high gas inlet temperature provides enough heat to start the reaction, but the ratio of solid to gas does not allow for the system to exhibit any multiple solutions. Finally, the upper left corner is where the multiplicities arise. As explained for the ignition-type curve, for a cold start, the system will remain in an extinct state, but for a hot start, the system will remain in an ignited state, as explained before, due to the higher heat feedback given by the larger gas molar flows. Naturally, there is the region in the middle where, depending upon the parameters, multiple solutions may or may not arise.

To determine which parameters have the greatest influence, a simple sensitivity analysis was performed, where the regions of multiplicity were mapped for different parameter combinations. A qualitative summary is given on Table 3.2 in which the benchmark (B) refers to Figure 3.4. A comparison to the size of the region is given by either '+' or '-' signs, this of course bearing in mind that the shape of the region and the position can vary slightly due to the strong non-linear coupling of the parameters, but the purpose is to give an idea of which parameters are most critical. In Table 3.2, a '0' represents a map without regions of multiplicity.

As it can be seen in Table 3.2, contrary to what might be thought intuitively, the Damköhler number is one of those exhibiting less influence in the multiplicity regions. As expected, for higher Damköhler numbers, e.g. fast reactions, the regions of

Table 3.2.: Sensitivity of the regions of multiplicity with respect to the model parameters

Sensitivity to Da	Da			Sensitivity to ΔT_{ad}	ΔT_{ad}			Sensitivity to St	St			Sensitivity to γ	γ						
	0.5	2.6	10		0.5	1	1.5		0.5	3.7	10		1	5	10				
γ	5			Da	2.6			Da	2.6			Da	2.6						
ΔT_{ad}	1.5	-	B	+	γ	5	---	-	B	γ	5	0	B	+++	ΔT_{ad}	1.5	0	B	--
St	3.6				St	3.6			ΔT_{ad}	1.5			St	3.7					

multiplicity become larger. However, this effect is limited by the reactant consumption and therefore the regions cannot change much. This effect is closely linked with the changes seen in the adiabatic temperature rise, but there, the effect is larger, since an increase in the reaction heat is directly proportional to the temperature rise, and it is not damped by the reactant consumption. The parameter with the largest effect is the Stanton number, since it captures the interaction between the gas and solid phase. As mentioned before, the heat feedback plays a major role in determining the occurrence of a multiplicity. For a very small Stanton number, the interaction between the gas and solid phase is minimal and therefore any feedback is negligible, leading to the disappearance of the multiplicity region. For a higher Stanton number, the interaction between the phases is greater, leading to larger heat feedbacks and thus more extensive regions of multiplicity. The final parameter is the Arrhenius number γ , for which the effect is not monotonic. A low Arrhenius number means that the reaction occurs evenly over a large range of temperatures, so that the heat is more evenly distributed along the reactor, which ultimately leads to no regions of multiplicity at all. On the other hand, a high Arrhenius number means that the reaction takes place only in a very narrow temperature interval leading to localized heat generation in the reactor and therefore to smaller multiplicity regions. For Arrhenius numbers that are not too high or low, there exists a maximum, where the region of multiplicity is the largest.

A detailed explanation of the regions of multiplicity has been given in this section since it provides the base from which the model extension is developed. In the next sections, individual phenomena like the changes in heat capacity, number of moles, reversible reactions and endothermic reactions will be elucidated.

3.4.2.1. Change in Number of Moles

The change in the number of moles in a reaction is usually taken to be negligible under the assumption of a dilute system. For a non-dilute system, the change in the number of moles can lead to longer/shorter residence times, increased/decreased heat and mass transfer properties affecting conversion among others. In this section, the effect of the change in the number of moles in the regions of multiplicity is shown for a reaction $aA \rightarrow bB$, where the change in the number of moles is defined as $\Delta n = b - a$. For simplicity and since it will be dealt with in the next section, the heat capacities of A and B are assumed to be the same.

The change in the number of moles affects the total molar flow rate and thus both the heat exchange and the concentrations. This is reflected in ϕ and in the Stanton

number as follows:

$$\phi(x, T_s^*, \gamma) = \exp\left(-\gamma\left(\frac{1}{T_s^*} - 1\right)\right) \left(\frac{\frac{1-x}{1+\Delta n \cdot x}}{1 + K_2 \frac{(1-x)}{1+\Delta n \cdot x}}\right) \quad (3.4.3)$$

$$St_{g,s} = \frac{h(x) \cdot a \cdot V_R}{N_g(x) \cdot c_{p,g}} = \frac{h(x) \cdot a \cdot V_R}{N_{g,0} \cdot c_{p,g}(1 + \Delta n \cdot x)} \quad (3.4.4)$$

The only thing missing is the relationship between heat exchange and conversion. Several correlations exist for determining heat transfer coefficients based on the Nusselt number, which usually they take the form of:

$$Nu = f\left(\text{Re}^{a_1}, \text{Pr}^{b_1}\right) \quad (3.4.5)$$

From Eq. (3.4.5), for a system with constant properties, the only effect on conversion is then that of the Reynolds number via the velocity. This can be represented as:

$$h(x) = \frac{Nu\kappa}{L} = f(\text{Re}(x)^{a_1}) = f(N_g(x)^{a_1}) = f(N_{g,0}(1 + \Delta n \cdot x)^{a_1}) \quad (3.4.6)$$

This result can be integrated in Eq. (3.4.4) to yield:

$$St_{g,s} = \frac{f(N_{g,0}(1 + \Delta n \cdot x)^{a_1}) \cdot a \cdot V_R}{N_{g,0} \cdot c_{p,g}(1 + \Delta n \cdot x)} = St_{g,s,0}(1 + \Delta n \cdot x)^{a_1-1} \quad (3.4.7)$$

where $St_{g,s,0}$ is the value of the Stanton number at the inlet conditions, in this case 3.7 as in the previous section, and the value of a is always smaller than unity. The results for multiplicity behavior showed little influence on the value of a so it was taken as 0.8, by simplifying the Gnielinski correlation, in which it ranges between 0.8 and 0.9 (Gnielinski 2010). In addition, the heat production term also changes because the heat is being distributed by a varying total molar flow. This can be represented as:

$$\dot{Q}_R = \frac{\Delta T_{ad} \cdot Da_{0,g} \cdot \phi(x, T_s^*, \gamma) \cdot F_1}{1 + \Delta n \cdot x} \quad (3.4.8)$$

The results for four different values of Δn are presented in Figure 3.5.

As can be seen, the change in the number of moles has a large influence in the multiplicity regions, for Δn greater than 0, the regions shrink considerably. This is mainly due to two factors: first, the increase in number of moles decreases the gas residence time and therefore the conversion and also the amount of heat that can be generated by the reaction, this combination leads to a shrinking of the regions as explained in the previous section. The second factor is in the Stanton number: an increase in the number of moles leads to decreased Stanton number and therefore to a shrinking of the region, this effect is not as large, since an increase in the number of moles leads to an increase in the heat transfer coefficient as well, and therefore slightly dampens the effect. The same reasoning can be used to explain the expansion of the regions for a decreasing number of moles.

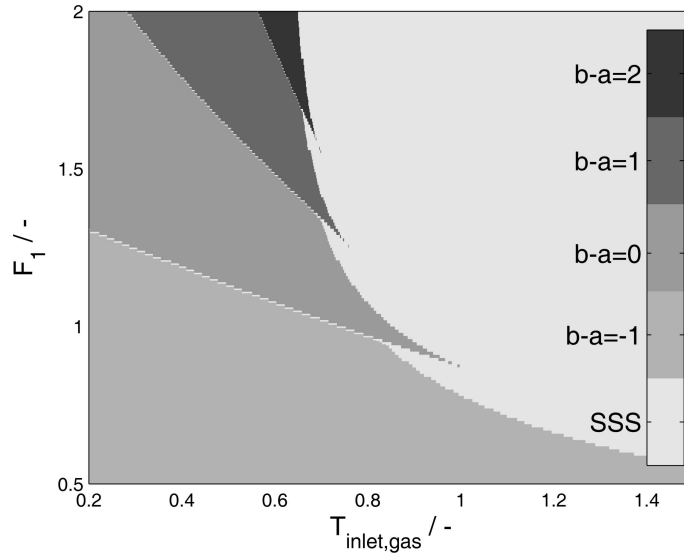


Figure 3.5.: Regions of multiplicity for different change in the number of moles

3.4.2.2. Change in Heat Capacity

The heat capacity of the phases are usually lumped in a single value and then assumed to be independent of the temperature, as in the previous section. The latter assumption is generally valid for a small temperature range, since the heat capacity changes only slightly. The former, however, is not always justifiable: products and reactants need not necessarily have the same heat capacity. In this section, the influence of this phenomenon on the regions of multiplicity is presented.

With respect to the model presented in Section 3.2.1, the only change is basically in the Stanton number. For the reaction $A \rightarrow B$, it can be represented as:

$$St_{g,s} = \frac{h \cdot a \cdot V_R}{N_A \cdot c_{p,A} \left(1 - x \left(1 - \frac{c_{p,B}}{c_{p,A}}\right)\right)} = \frac{h \cdot a \cdot V_R}{N_A \cdot c_{p,A} (1 - x (1 - ratio))} \quad (3.4.9)$$

For the case where $c_{p,A} = c_{p,B}$ or $ratio = 1$ the model reduces to the results presented in the previous section. Two cases, for higher and lower product heat capacity are presented in Figure 3.6 in which the multiple steady-state (MSS) regions are given for the different heat capacity ratios. The parameters are the same as given in Table 3.1, the Stanton number for $x = 0$ is kept at 3.7.

As can be seen, the change in heat capacity has a very large effect, which is difficult to anticipate a priori. This is of course because the change of heat capacity mostly impacts the Stanton number, and, as mentioned before, the Stanton number is the parameter with the largest sensitivity of all. By decreasing the heat capacity ratio, the Stanton number increases, i.e. the denominator becomes smaller. Physically this means that for the ignited state, the amount of heat that can be stored into the gas gets smaller with conversion and thus most of the heat will remain in the solids helping maintain the ignited state. On the other hand, for the extinction case, the amount of heat stored in the reactants is higher, leading to less heat being passed to the solids, helping maintain the extinct state. This is the reason why the multiplicity region

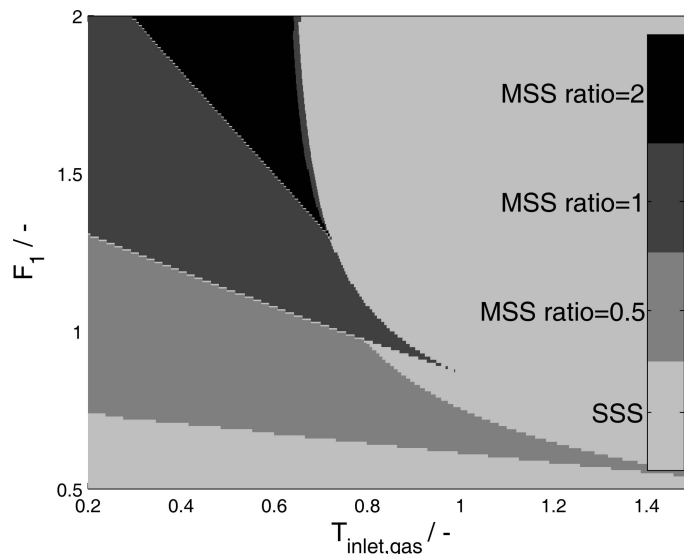


Figure 3.6.: Regions of multiplicity for different heat capacity ratios

becomes larger for heat capacity ratios smaller than one. The same reasoning can be applied to explain the shrinking of the regions for ratios larger than one.

3.4.2.3. Reversible Reactions

The effect of the equilibrium of the reaction is probably the simplest to explain and where the results can be predicted in advance. Until now, all the reactions considered were irreversible. For a reaction $A \rightleftharpoons B$, the effect can be seen only in the ϕ term as:

$$\phi(x, T_s^*, \gamma) = \exp\left(-\gamma\left(\frac{1}{T_s^*} - 1\right)\right) \left(\frac{1 - x - \frac{x}{K_{eq}}}{1 + K_2(1 - x)}\right) \quad (3.4.10)$$

The benchmark shown in Figure 3.4 is equivalent to the case $K_{eq}(T_g^* = 1) = \infty$. The cases for a reaction that favors the products, a case for a reaction favoring the reactants and a case where neither is favored, i.e. $K_{eq} > 1$, $K_{eq} < 1$, and $K_{eq} = 1$, are presented in Figure 3.7. The temperature dependency of the equilibrium constant was assumed negligible, and although this assumption does not hold in a real system, the purpose was to demonstrate the overall influence of including the equilibrium constant in the calculations. For the real test case, this temperature dependence is considered.

As might be expected, the larger regions are present for the higher K_{eq} values, and the regions shrink with decreasing K_{eq} until they finally disappear. A small K_{eq} value means that the forward exothermic reaction will reach the equilibrium conversion faster and without generating all the heat that would be generated for a higher equilibrium conversion as with the benchmark.

3.4.2.4. Allothermic Reactions

The study of multiplicities in endothermic/allothermic reactions has not been carried out previously, and not without reason, for in adiabatic operation, any endothermic

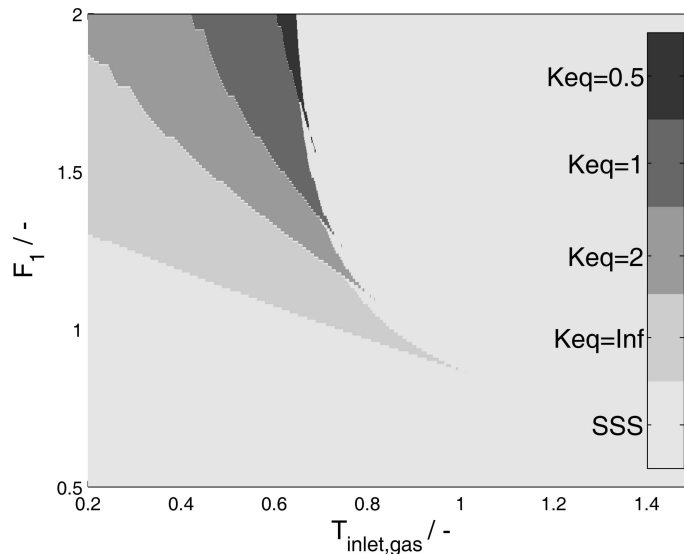


Figure 3.7.: Regions of multiplicity for different equilibrium constants

system will exhibit only a single steady state since the heat is being consumed instead of generated eliminating the main reason why multiplicity occurs in the first place. For allothermal operation, especially for recuperative systems, i.e. with heat transfer through the wall, the regions of multiplicity are also nonexistent, since the constant heat input does not allow for a fully extinct state and the heat sink through the reaction does not permit a fully ignited state.

However, for non-conventional heat inputs, regions of multiplicity can occur, and this will be dealt with in more detail in Section 3.4.3.2.

3.4.3. Methane Pyrolysis

To carry out the methane pyrolysis in a moving-bed reactor, the recuperative alternative is not viable due to carbon formation on the heat transfer surfaces, leading to clogging and reduced efficiency. An alternative is, for instance, to introduce the heat directly to the solids, e.g. inductive or ohmic heating. In this way, the carbon deposition will occur mostly in the solid phase, thus minimizing the carbon formation in the walls. These heating methods can be non-linear functions of temperature and this could, for instance, lead to cases where no heat is input to the system at lower temperatures and most heat being provided at higher temperatures, hence leading to a similar mechanism to an exothermic reaction opening the door for the possibility of regions of multiplicity to exist. In addition, the presence of an exothermic back reaction for high pressure operation could potentially be a source of multiplicities as well.

In the next sections, the regions of multiplicity are studied first for a reactor carrying the back reaction, then for a standard reactor and finally for a heat integrated reactor.

3. Multiplicities in Moving-Bed Reactors

Table 3.3.: Parameters for simulation of the reactor carrying out the back reaction at feed conditions

Parameter	Da_0	γ	$\Delta T_{ad,0}$	St_0	$T_{inlet,sol}$	x_{inlet}	F_1	F_2	$T_{inlet,gas}$
Value	0.036	37.78	2.296	4.378	0.6	0	Parameter	$f(F_1)$	Parameter

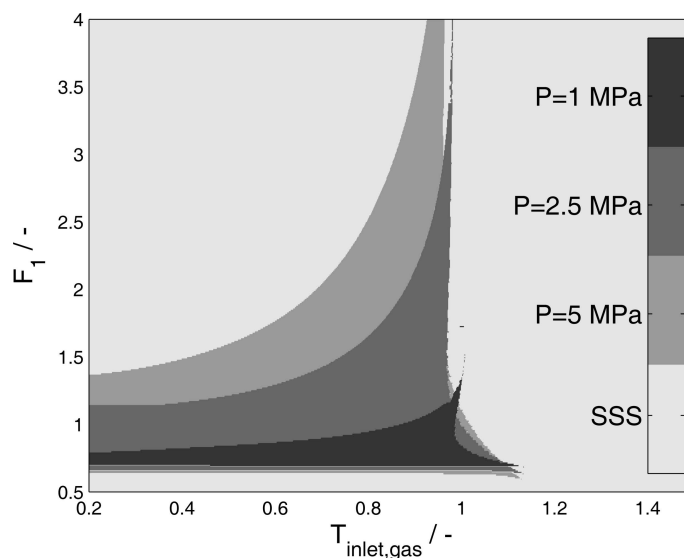


Figure 3.8.: Regions of multiplicity for different pressures

3.4.3.1. Reverse Reaction

The reverse reaction in methane pyrolysis, presents some features described in the previous section that can indicate where, if at all, multiplicity regions will occur. First and foremost, this reaction is strongly limited by equilibrium and hence the regions expected are small as seen in Section 3.4.2.3. The reaction reduces the number of moles with conversion which, as shown in Section 3.4.2.1, leads to an enlargement of the regions of multiplicity which is diminished by the increase in heat capacity from hydrogen to methane. The reactor is simulated with a cold feed of solids and varying gas inlet temperature. The parameters for the simulation at feed conditions can be found in Table 3.3. In order to obtain a fair comparison at different pressures, the volume of the reactor was adjusted to give the same residence time in all cases of 10 s. The results are presented in Figure 3.8

As can be seen, regions of multiplicities can only be found at high pressures, i.e. 1, 2.5 and 5 MPa. At lower pressures, no multiplicity regions were identified. In addition, the regions show different behavior to those presented earlier, since apparently the region of multiplicities is not complete in the upper left corner. However, this is due to the fact that the solver found solutions where the equilibrium was attained and therefore could not continue since other solutions would be not feasible, i.e. solutions beyond the thermodynamic equilibrium or with negative temperatures. The stability criteria always predict an odd number of solutions, and therefore an upper steady-state should be expected. However, it was not possible to find this solution, probably due to a very steep increase in the conversion, for which any small devia-

tion would cause it to fall back to the lower solution. As expected, the regions are larger for higher pressures, but since the main effect is the influence of the pressure on the Damköhler number was reduced by guaranteeing an equal residence time for all cases, the effect is not as large as one might have expected.

3.4.3.2. Standard Reactor

For allothermal operation, heat can be introduced into the reactor in several ways, e.g. chemically by using another reaction or by burning part of the methane/carbon in an auto-thermal operation, convectively, by feeding a heated inert gas, recuperatively, by transferring heat through the walls, or electrically, by passing a current through the solids to generate heat.

Of these alternatives, the convective and recuperative option cannot exhibit multiplicities since they imply a steady heat input that will not permit extinction. For auto-thermal operation, it might be possible to find multiplicities depending upon which reaction dominates and their respective rates of reaction. However, auto-thermal operation makes it difficult to control whether reactant or product will be combusted and also entails additional difficulties in downstream processing. For these reasons, only the studies on the ohmic heating will be presented, and also because there exists already a proof of concept for such reactors (Jahnig et al. 1964).

Based on Joule's first law, and for a system subject to a constant potential difference U , the amount of heat introduced to an element dV needed for Eq. (3.2.6) can be expressed as:

$$Q_{input,solids} = \left(\frac{I}{A}\right)^2 \rho_M = \frac{U^2}{\left(\int_0^L \rho_M dz\right)^2} \rho_M \quad (3.4.11)$$

Eidem et al. (2008) measured the electrical resistivity for three types of carbon. Their results were fitted to appropriate functions, as shown in Figure 3.9, in order to represent the temperature influence on the electrical resistivity for the heat generation. The resulting relations are as follows:

$$\rho_{zdzieszowice} = \begin{cases} \frac{5.24 \cdot 10^7}{T^3} - \frac{3.13 \cdot 10^5}{T^2} + \frac{6.24 \cdot 10^2}{T} - 0.404 & \text{for } 373K < T < 623K \\ 6.94 \cdot 10^{-9} T^2 - 1.27 \cdot 10^{-5} T - 0.0137 & \text{for } 623K \leq T < 1523K \\ -1 \cdot 09 \cdot 10^{-7} T^2 + 3.59 \cdot 10^{-4} T - 0.284 & \text{for } T \geq 1773 \\ 0.009 & \end{cases} \quad (3.4.12)$$

$$\rho_{Magnitogorsk} = \frac{0.039 \left(1 - \arctan\left(\frac{T-550}{80}\right) + \frac{\pi}{2}\right)}{\pi} - 0.009 \quad (3.4.13)$$

$$\rho_{coke} = \begin{cases} 4.857 \cdot 10^{-8} T^2 - 1.0523 \cdot 10^{-4} T + 8.2556 \cdot 10^{-8} & \text{for } 373K < T < 1173K \\ 2.2010 \cdot 10^{-8} T^2 - 8.4550 \cdot 10^{-5} T + 9.4092 \cdot 10^{-2} & \text{for } 1173K < T < 1873K \\ 0.013 & \text{for } T > 1873K \end{cases} \quad (3.4.14)$$

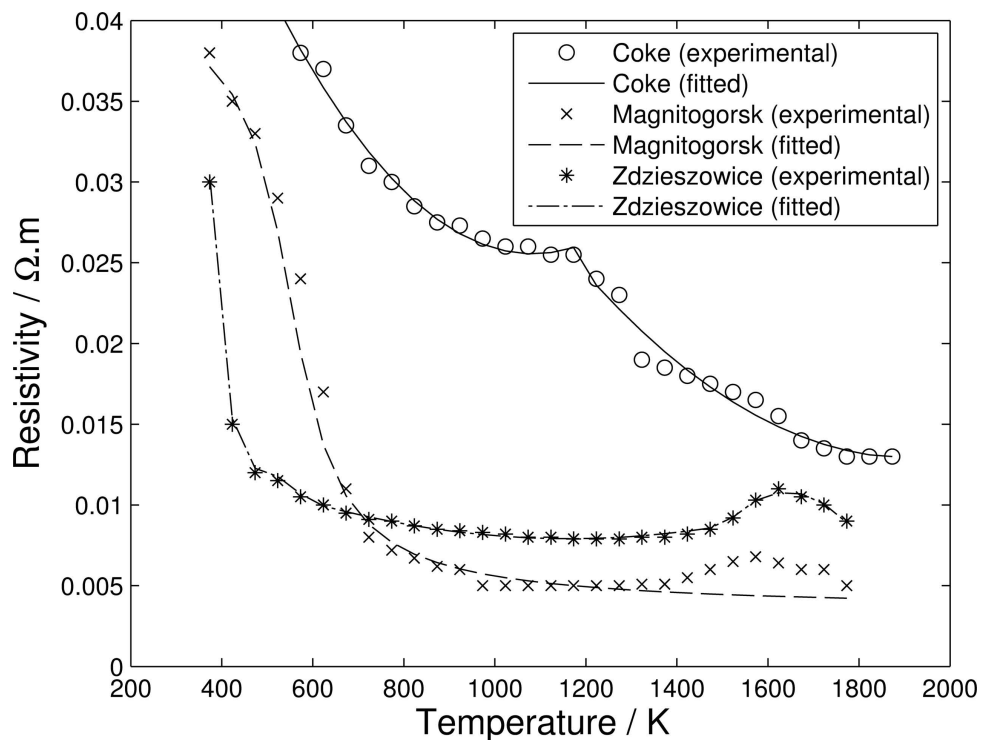


Figure 3.9.: Resistivity as a function of temperature for the carbon materials studied

Table 3.4.: Parameters for simulation of the standard reactor at feed conditions

Parameter	Da_0	γ	$\Delta T_{ad,0}$	St_0	$T_{inlet,sol}$	x_{inlet}	F_1	F_2	$T_{inlet,gas}$	U/V	P/MPa
Value	0.1385	37.78	0.8875	2.609	0.293	0	Parameter	$f(F_1)$	Parameter	120	2.5

It can be seen that the resistivity changes considerably and will thus play a major role in the heat generation. One can imagine that, depending on how the reactor is started, different steady-states could arise, e.g. for a cold start with a high resistivity and therefore low heat generation, or a hot start with low resistivity and high heat generation.

The reactor is then simulated without heat integration, meaning the gas and solids are fed directly into the reaction zone. It is evident that if the feed is preheated no multiplicity will be found. Therefore, both feeds were introduced without preheating. The parameters used for the simulation can be found in Table 3.4.

For all carbon types, no multiplicity behavior was found, although for the Magnitogorsk carbon, the progression of the bifurcation curve was close to that of systems exhibiting multiplicity behavior. In general, the change in the electrical resistivity occurred in a region of low temperature for the Zdzieszowice carbon, and therefore it was largely decoupled from the reaction. For the sponge pet coke, the change was not pronounced enough and therefore no multiplicity occurred. For the Magnitogorsk, the change occurred both at higher temperatures, around 600 K, and was also more pronounced. Simulations were run with displacement of this change to regions of higher temperature, 800, 1000 and 1200 K, resulting in the multiplicity behavior presented in Figure 3.10

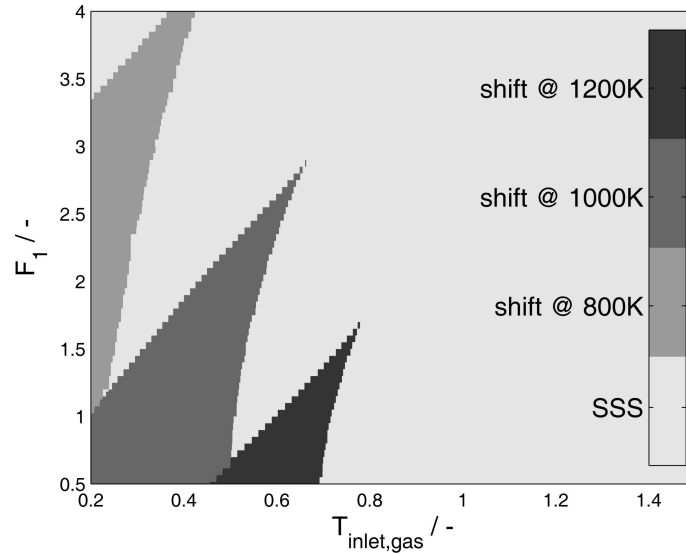


Figure 3.10.: Regions of multiplicity for shifted versions of the Magnitogorsk resistivity in a standard reactor

Table 3.5.: Parameters for simulation of the heat-integrated reactor at feed conditions

Parameter	Da_0	γ	$\Delta T_{ad,0}$	St_0	$T_{inlet,sol}$	x_{inlet}	F_1	F_2	$T_{inlet,gas}$	$U (V)$	$P (MPa)$
Value	0.014	37.78	0.8875	8.478	0.234	0	Parameter	$f(F_1)$	Parameter	120	2.5

It should be noted, that the way electrical resistivity varies with temperature can exhibit very different profiles, and as shown, under certain circumstances, this could lead to multiple steady-states. In the next section, the results for a heat-integrated reactor are presented for the Magnitogorsk carbon and the shifted behavior of the electrical resistivity.

3.4.3.3. Heat-Integrated Reactor

Finally, the heat-integrated reactor presented in Figure 3.1 is simulated using a direct electrical heat input. Both the gas and solid inlets are cold. The parameters used are presented in Table 3.5. The regions of multiplicity are presented in Figure 3.11.

In this case, as in the previous one, for the Zwieszowice and sponge pet carbon, no regions of multiplicity were found. However, for the Magnitogorsk, a multiplicity region appears for low temperature. The reason is a combination of the effects of the back reaction, which provides extra heat to keep the state ignited, or alternatively, does not provide heat if the reaction is extinct. In addition, there is an enhanced feedback that the heat exchange regions additionally provide, and, as shown before, this is one of the sources for multiplicities.

3.5. Conclusions

In this work, a generalized dimensionless model for a moving-bed reactor was developed and the influence of several parameters was investigated. The parameter found

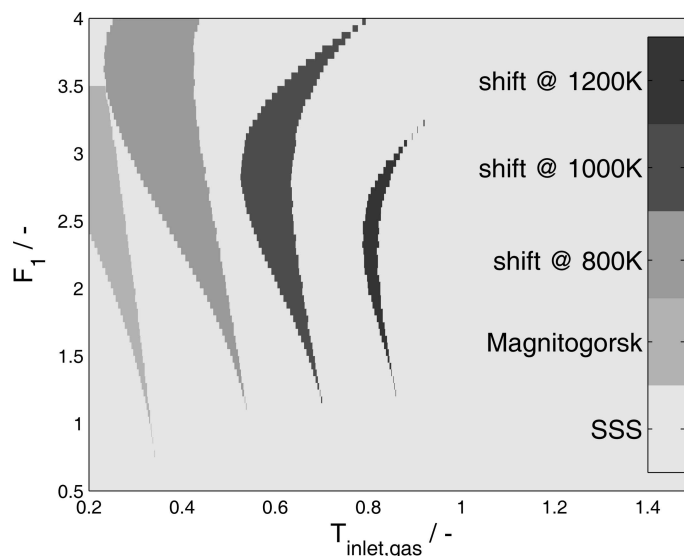


Figure 3.11.: Regions of multiplicity for Magnitogorsk and the shifted versions in a heat-integrated reactor

to have the greatest influence in the multiplicity behavior was the Stanton number. In addition, cases for system exhibiting changes in moles and heat capacities were studied, showing a larger influence than would have been predicted a priori, mainly because they influence the Stanton number most.

Furthermore, the insights gained from the generalized model were applied to a novel case, for the allothermal operation of the high temperature pyrolysis of methane. Here, the back reaction at higher pressures was identified as a possible source of multiplicity due to its exothermicity. In addition, for a non-linear heat input it could be shown that multiple steady-states can be found for particular cases. The interaction of these two effects was demonstrated in a heat-integrated reactor.

In general, although the case studied was perhaps not ideal, the results obtained could be used to show the existence of multiple steady-states in other allothermal systems, where the coupling of the reaction and the non-linear heat input occur in a narrower temperature range, as shown by the shifted curves in the previous sections.

Finally, the bifurcation methods proved a valuable tool when performing parameter studies, and although, depending on the complexity of the system, the simulation can demand considerable computational effort, a more refined coding, or the introduction of the Jacobian would improve the performance dramatically.

Preamble

The following chapter will be submitted for publication as:

Munera Parra, A.A, and D.W. Agar (2018): "Modeling and Optimization of Heat Input Strategies in a Moving-Bed Reactor for the High Temperature Pyrolysis of Methane".

The calculations and analysis were performed by myself. Prof. Agar supervised the work.

Abstract

In this work, three heat input strategies for the pyrolysis of methane, namely a side-stream, plasma and resistive heating, are studied. These strategies were modeled, simulated and optimized, and compared in terms of CO₂ emissions and technical feasibility. The results show that when including all emissions related to the process, all three strategies lay well below the state of the art for hydrogen production. In terms of feasibility the required equipment as well as their technological availability are evaluated and the strategies are proposed for the short-, mid- and long-term.

4

Heat Input Strategies

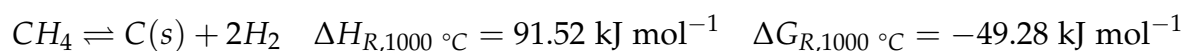
4.1. Introduction

Currently, hydrogen production is still mainly based on fossil fuels, with natural gas or coal being the major sources. Although some methods are not based directly on fossil fuels, the electricity to power them is still largely based on them. Globally, about half of all hydrogen is produced via steam methane reforming (SMR) (US Department of Energy, 2005), with the remainder being distributed among partial oxidation, gasification of coal, water electrolysis and some other minor contribution by chlor-alkali processes and biomass gasification, for instance.

For the CO₂ emissions related to each process, Muradov (2017) divides their contribution based upon the stoichiometric and the process, i.e. plant and electricity, emissions. For the stoichiometric contribution, the higher CO₂ emitting process are the gasification ones with 13.7 and 15.7 kg CO₂ per kg H₂ and the lowest being the water electrolysis with 0 kg CO₂ per kg H₂. SMR ranks in the middle with 5.5 kg CO₂ per kg H₂. Nonetheless, when considering the complete process, water electrolysis ranks last with around 24-28 kg CO₂ per kg H₂ and SMR being the highly optimized process it is, ranks first at 8.7-10 kg CO₂ per kg H₂.

In recent years, the pyrolysis of methane has gained interest as a potential competitor for the SMR. Stoichiometrically, the pyrolysis produces 0 kg CO₂ per kg H₂. The plasma pyrolysis, as one of the first types of pyrolysis industrially established, produces an estimated 12 kg CO₂ per kg H₂ (Fulcheri and Schwob 1995). As it can be seen, that value is larger than that of the SMR, but the pyrolysis is still far away from being an optimized technology. Given the shift towards renewable energies, in the near future, pyrolysis could be a viable way to produce hydrogen from fossil fuels with low/ultra-low/near-zero/no CO₂-emissions, depending on the available source of electricity.

The methane pyrolysis reaction:



is an endothermic reaction which, in order to be kinetically feasible, requires temperatures over 800 °C. In theory, the reaction could be catalyzed for lower temperature operation but the coking of the catalyst and the subsequent separation and large

stream recycles resulting from the limited equilibrium conversion are still issues that need to be addressed.

Nonetheless, the high-temperature alternative presents other challenges. Carbon deposition is still a major hurdle since it can, in the worst case, lead to the blockage of the reactor (Abánades et al. 2012). In addition, the pyrolysis is an endothermic reaction, and it is then necessary to introduce heat at high temperatures, where there are rarely sources of energy. Heat can be introduced into a reactor using several strategies: recuperative, regenerative, reactive, convective and electromagnetic (Agar 2003).

Most standard of all, recuperative heat transfer finds no use in the pyrolysis since any external heat provided through the reactor wall will lead to the coking of said surface and to the blockage of the reactor.

Regenerative heat, although in theory possible, would still need very high temperature differentials to be efficient, and materials would need to be found which could resist the inherent periodic temperature changes of the regenerative operation. Additionally, an efficient way to remove the carbon generated is required.

For the reactive option, initially it could be thought to use auto-thermal operation, for instance by combusting a part of the gas to provide for the reaction heat. Nonetheless, in the pyrolysis reactor, unless a selective combustion of hydrogen was possible, it would defeat its purpose since the combustion of any other element present, either carbon or methane, would lead to CO₂ production. Even with selective hydrogen combustion, the production of steam would lead to non-ideal conditions which could lead to reforming or gasification reactions.

A mixture of recuperative and convective heat has and is still being studied, using for instance molten media. Concepts like bubble columns (Abánades et al. 2016; Geissler et al. 2016; Gulevich et al. 2008; Martynov et al. 2005; Paxman et al. 2014; Serban et al. 2003; Steinberg 1999; Tyrer 1931), slag reactors (Kashiwaya and Watanabe 2012) and capillary reactors (Munera Parra and Agar 2017; Schultz and Agar 2015) have been proposed. Although promising, they are not still ready for their adoption in the industry.

The remaining strategies are thus, convective, by inserting a hot side-stream into the reactor to provide the heat, or electromagnetic, which can be either resistive heating or via plasma.

As for the reactor type, a moving-bed reactor seems the most promising alternative. The reactor provides excellent heat transfer between the phases, and although not as good as a fluidized-bed reactor, there is no back-mixing and the residence time can be closely controlled for both phases. In addition, the counter-current operation, allows for a heat-integrated reactor as presented in Figure 4.1. There, the hot gases leaving the reaction zone, heat the incoming solids, and the hot solids coming out of the reaction zone heat the incoming gases, guaranteeing a thermally efficient operation. A proof of concept for a similar reactor was patented in the 60s (Jahnig et al. 1964)

In this work, the moving-bed reactor will be modeled for three different heat strategies which in turn will be optimized.

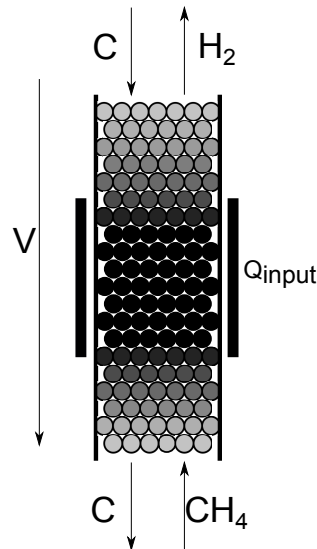


Figure 4.1.: Heat-integrated moving-Bed Reactor

4.2. Mathematical Modeling

For the moving-bed model, the axial coordinate is defined with its origin at the top of the reactor, i.e. the solids' inlet. The gas inlet is located at the bottom of the reactor as depicted in Figure 4.1. As explained before, the reactor is divided into 3 zones, top and bottom for heat recovery and middle for heat introduction.

The model for the reactor was derived from differential balances and the results are presented in Table 4.1.

As it can be seen, the derivatives are presented in dimensionless manner, with the variables defined in Table 4.2. However, the right-hand-side (rhs) is kept with its units. This was done for the sake of understanding and for an easier implementation of the code. The rhs could have been presented in dimensionless form with the inclusion of the usual dimensionless numbers, Damköhler, Stanton, adiabatic temperature rise, and so on. Nonetheless, since the system spans a large range of temperatures, most properties are a function of temperature and conversion, leading to the need of including additional dimensionless numbers and functions which make the formulation cumbersome.

Finally, to complete the model, some correlations were needed as well as the reaction rate and equilibrium constant, these are presented in Table 4.3.

From the model equations presented in Table 4.1, a couple of things are of importance: First, since the temperature range in this reactor configuration is broad, all properties, i.e. heat capacities, densities, thermal conductivities, viscosities, are calculated as a function of temperature and conversion.

Secondly, it can be seen that for the solid molar balance, an explicit solution can be found based on the rate of consumption for methane. This can also be extrapolated to the maximum particle growth which could be founded if all carbon was deposited as a new, uniform layer.

Finally, the heat input is only implemented for the middle region of the reactor, and

Table 4.1.: Model for the moving-bed reactor

Gas phase molar balance	$\frac{dX}{d\xi} = -\frac{V_R}{F_T y_{CH_4,0}} \cdot r_{CH_4} \cdot \varepsilon$ $X(\xi = 1) = 0$
Gas phase energy balance	$\frac{d\theta_G}{d\xi} = \frac{V_R}{T_{G,inlet} F_T} \frac{r_{CH_4} \cdot \varepsilon \cdot \Delta H_{rxn} - \frac{6(1-\varepsilon)}{d_p} \cdot h \cdot (T_S - T_G) - \frac{Q_{input}}{dV}}{[y_{CH_4,0} \cdot (1-X) \cdot c_{p,CH_4} + (y_{H_2,0} + 2 \cdot y_{CH_4,0} \cdot X) \cdot c_{p,H_2}]}$ $\theta_G(\xi = 1) = 1$
Solid phase molar balance	$F_C = F_{C,0} + F_T \cdot y_{CH_4,0} \cdot (X - X(\xi = 0))$
Solid phase energy balance	$\frac{d\theta_S}{d\xi} = \frac{V_R}{T_{G,inlet}} \frac{-\frac{6(1-\varepsilon)}{d_p} \cdot h \cdot (T_S - T_G) + \frac{Q_{input}}{dV}}{F_C(X) c_{p,C}}$ $\theta_S(\xi = 0) = \frac{T_{S,inlet}}{T_{G,inlet}}$
Particle size change	$d_p = d_{p,0} \left(\frac{F_C(X)}{F_{C,0}} \right)^{\frac{1}{3 \cdot (1-\varepsilon)}}$

Table 4.2.: Dimensionless variables

Variable	Reference value	Dimensionless form
ξ	V_R	$\xi = \frac{V}{V_R}$
X	$F_{CH_4,0} = F_T \cdot y_{CH_4,0}$	$X = 1 - \frac{F_{CH_4}}{F_T \cdot y_{CH_4,0}} = 1 - \frac{y_{CH_4}}{y_{CH_4,0}}$
θ_G	$T_{G,inlet}$	$\theta_G = \frac{T_G}{T_{G,inlet}}$
θ_S	$T_{G,inlet}$	$\theta_S = \frac{T_S}{T_{G,inlet}}$

the detailed equations will be given for each of the different heating strategies.

4.2.1. Side-Stream

Since the auto-thermal alternative is not viable, a work-around concept is the introduction of a hot side-stream. This side-stream could, for instance, be preheated in a furnace, but since the furnace would be powered by electricity, and the next two concepts are as well, it was decided to use a completely electricity-free strategy in this case. The advantage being that no CO₂-emissions are directly linked to this strategy.

To produce this side stream, a fraction of the produced hydrogen can be combusted

Table 4.3.: Additional model equations

Variable	Equation	Reference
Heat transfer correlation	$Nu = \frac{h \cdot d_p}{\kappa_G} = 2.0 + 0.39 \cdot Re_p^{1/2} \cdot Pr^{1/3}$	(Akiyama et al., 1993)
Reaction Rate	$r_{CH_4} = k(T_G) \left[C_{CH_4} - \frac{C_{H_2}}{K_C(T)} \right]$	(Patrianakos et al., 2011)
Reaction rate constant	$k(T_G) = 10^{14} s^{-1} \exp\left(\frac{-400000 J mol^{-1}}{R \cdot T_G}\right)$	(Patrianakos et al., 2011)
Equilibrium	$K_C(T_G) = \frac{K_P(T_G)}{R \cdot T_G} = \frac{\exp\left(\frac{-\Delta G_R}{R \cdot T_G}\right)}{R \cdot T_G}$	(Linstrom and Mallard, 2001)

in a regenerator, to produce steam. The heat produced by the reaction is stored in the regenerator and then used to heat another fraction of the hydrogen to be introduced as a side stream and supply the heat needed for the pyrolysis convectively. This concept is an elegant way to combine the reactive, regenerative and convective heat transfer strategies.

The model for this concept changes in the way that at the point where the side stream is introduced, the total gas flow is increased, therefore the denominator of the gas energy balance needs to be modified accordingly. Furthermore the increase in the volumetric flow-rate needs to be considered when calculating the concentrations for the reaction rate. At the mixing point where the stream is introduced, and assuming an efficient distribution, an enthalpy balance yields the temperature of the mixing point as:

$$T_{mix} = \frac{(1-X_{in}) \cdot c_{p,CH_4}(T_{G,in}) \cdot T_{G,in} + 2 \cdot X \cdot c_{p,H_2}(T_{G,in}) \cdot T_{G,in} + \frac{F_{side}}{F_T} \cdot c_{p,H_2}(T_{Side}) \cdot T_{Side}}{(1-X_{mix}) \cdot c_{p,CH_4}(T_{G,mix}) + \left(2 \cdot X + \frac{F_{side}}{F_T}\right) \cdot c_{p,H_2}(T_{G,mix})} \quad (4.2.1)$$

Using that temperature, the residual at the mixing point can be forced to that value. It is important to notice that for this case, there is no explicit value for Q_{input}/dV . This leads to a difficulty in numerical terms, since the solution will always change depending on the number of discretization points.

For this concept, it was then assumed that the mixing of the gases takes place in 5 cm regardless of the reactor length. Using this, the discretization scheme can be adapted so that by changing the reactor length, the results of the added heat remain consistent.

4.2.2. Plasma

For the plasma heat introduction, two options are available: thermal and non-thermal plasma. For the thermal plasma, methane pyrolysis has been carried out in the

Kvaerner process, which ran industrially to produce carbon black with hydrogen as a by-product. A review of thermal plasma technology including the Kvaerner process was performed recently by Lee (Lee 2015). The main drawback of this process is the amount of electricity required to reach such high temperatures, leading to very high costs, and depending on the location, additional CO₂-emissions.

The non-thermal plasma alternative, also known as warm plasma, although also electricity-intensive, operates through different mechanisms, and the energy is used to generate energy-active species rather than to increase the gas temperature as in the thermal case. In addition, warm plasma systems are easier to design since they do not require any special cooling and do not have such a strong erosion of the electrode material in comparison with the thermal plasma (Gutsol et al. 2011). Gliding-arc reactors (Czernichowski and Czernichowski 2000), barrier discharge plasma type reactors (Nozaki et al. 2002), and microwave plasma-assisted reactors (Potapkin et al. 1999) have been used for the decomposition of methane.

In this work, an alternative to these concepts is proposed in which, instead of using the plasma directly, the heat released by the recombination of atomic hydrogen is used to provide the reaction heat needed for the pyrolysis. To model this, a simplified approach was taken where the reaction heat is given by the recombination enthalpy of the hydrogen atoms. The reaction necessitates an additional molecule to take place as in:



The reaction rate constant varies depending upon molecules and temperature range but is always in the order of magnitude of $10E3-10E4 \text{ m}^6 \text{ mol}^{-2} \text{ s}^{-1}$ (Jones et al. 1973), which is very high. The heat of reaction is -437 kJ mol^{-1} . Thus, the heat input could be calculated as:

$$\frac{Q_{input}}{dV} = r_{recom} \cdot (-\Delta H_{recom}) \cdot \epsilon \quad (4.2.3)$$

Nonetheless, there is not enough information available in a way that can be interpreted to reproduce the kinetics, and thus, the heat input was simplified as a single burst of energy introduced into the system as:

$$\frac{Q_{input}}{dV} = \frac{F_H (-\Delta H_{recom})}{dV} \quad (4.2.4)$$

at the point where the atomic hydrogen enters the reaction zone. Although this approach is quite simplified, the obtained results should represent at least to a certain degree, the basic physics behind this heat strategy.

Analogously to the side-stream concept, a mixing volume of 2 cm was defined as the lower limit. Using smaller volumes could lead to slightly different solutions, but the number of nodes needed for discretization become prohibitive. The volume is smaller than the one of the side-stream concept, because the inflow is smaller and there is a very fast reaction taking place as well.

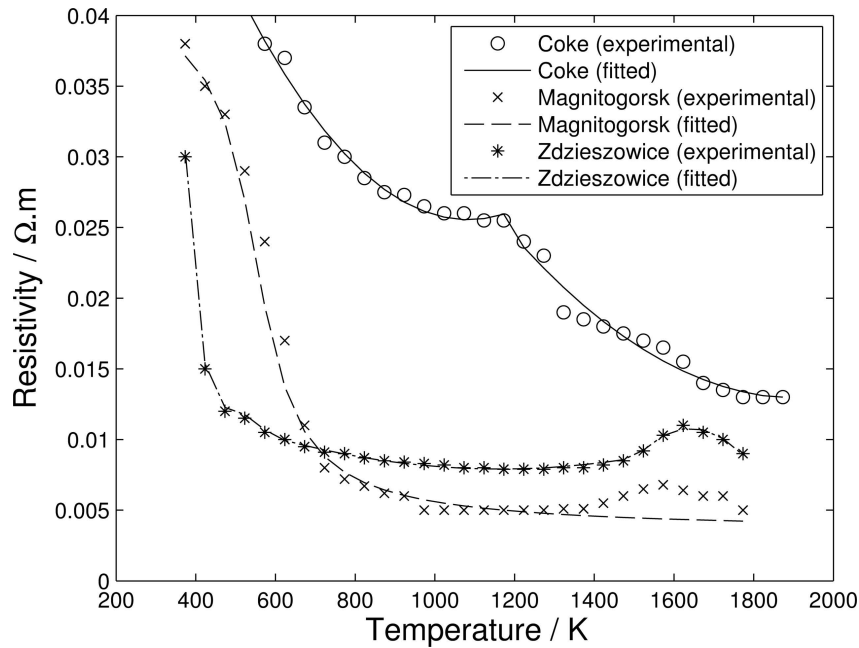


Figure 4.2.: Electrical resistivity as a function of temperature. Adapted from (Eidem et al. 2008)

4.2.3. Resistive Heating

The resistive heating, sometimes also known as joule or ohmic heating, is based upon passing an electric current through the bed and due to the resistivity, heat is released. A concept for a resistive heat-integrated moving-bed reactor was proposed in a patent in 1964 (Jahnig et al. 1964), although it was not further developed.

The most important parameter for representing ohmic heating is that of the electrical resistivity. For carbonaceous materials, Eidem et al. (2008) carried out the measurements as a function of temperature, these are presented in Figure 4.2. As it can be seen, the values between different types of carbon can vary greatly. The values were fitted using different functions (Munera Parra et al. 2016) and are summarized in Table 4.4 with the inclusion of limiting cases for higher and lower resistivity.

With the electrical resistivity being defined, the heat input for the solid phase in the model can be found as:

$$\frac{Q_{input}}{dV} = \frac{U^2 A^2}{\left(V_T \int_{Zone2} \rho_M d\zeta \right)^2 \rho_M} \quad (4.2.5)$$

4.3. Numerical Methods

The equations presented in the previous section were implemented in MATLAB®. For the discretization schemes, first the orthogonal collocation on finite elements was used, but for the heat integrated reactor, due to the presence of drastic changes in the solution, minor oscillations and numerical instability were observed. Therefore, a

Table 4.4.: Electrical resistivity as a function of temperature

Carbon type	Electrical resistivity (ρ_M) / Ω m	Temperature / K
1-Zdzieszowice	$\frac{5.24E7}{T^3} - \frac{3.13E5}{T^2} + \frac{6.24E2}{T} - 0.404$	373-623
	$6.94E - 9 \cdot T^2 - 1.27E - 5 \cdot T - 0.0137$	623-1523
	$-1.09E - 7 \cdot T^2 + 3.59E - 4 \cdot T - 0.284$	1523-1773
	0.009	1773-2000
2- Magnitogorsk	$\frac{0.039(1 - \arctan(\frac{T-550}{80}) + \frac{\pi}{2})}{\pi} - 0.009$	373-2000
3-Sponge-pet coke	$4.857E - 8 \cdot T^2 - 1.0523E - 4 \cdot T + 8.2556E - 8$	373-1173
	$2.201E - 8 \cdot T^2 - 8.455E - 5 \cdot T + 9.401E - 2$	1173-1873
	0.013	1873-2000
High-resistivity	0.04	373-2000
Low-resistivity	0.005	373-2000

simpler but denser upwind scheme in the direction of flow was used, i.e. backward for the solid phase and forward for the gas phase. For the first two concepts, the mesh was defined so that the minimum distance was that of the mixing region. For the resistive heating, a mesh sensitivity analysis was performed to choose the number of discretization points.

The solution was found directly, building the residuals, and then using a zero-value problem solver, e.g. MATLAB®'s `fsolve`, to find the solution. Nonetheless, since the aim of the work was to perform an optimization, the solution of the equations was obtained by building the optimization problem and setting the cost function to a constant so that the solver dedicates its efforts to fulfill the constraints, which in this case represent the model.

The optimization solver used was IPOPT, a primal-dual interior-point algorithm with a filter line-search method for non-linear programming (Wächter and Biegler 2006). The version used was the one implemented in the OPTI Toolbox (Currie and Wilson 2012).

Table 4.5.: Parameters for the simulation

\dot{V}	$T_{G,inlet}$	$T_{S,inlet}$	F_{solids}/F_{gas}	d_p	P	ϵ	D_R	L_R
/ $\text{Nm}^3 \text{h}^{-1}$	/ K	/ K	/ mol mol^{-1}	/ mm	/ bar	/ -	/ m	/ m
15000	298	298	3	4	1	0.35	3	6

Table 4.6.: Parameter to calculate the heat input for all three strategies

Side-stream		Plasma		Resistive heating								
F_{side}	/ mol s^{-1}	420	F_{plasma}	/ mol s^{-1}	30	Carbon type	1	2	3	4	5	
T_{side}	/ K	2073	N_{points}	/ -	120	Voltage	/ V	180	125	235	370	130
N_{points}	/ -	120	N_{points}	/ -	120	N_{points}	/ -	200				

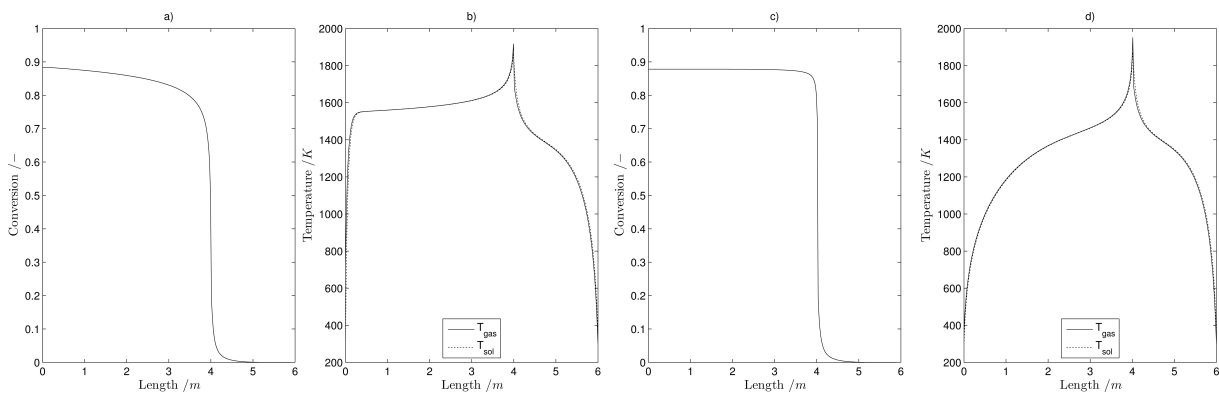


Figure 4.3.: Simulation results for: Side-stream strategy a) conversion b) temperature profile. Plasma strategy c) conversion d) temperature profile

4.4. Results

4.4.1. Simulation Results

To gain an insight into the simulation results, first all three concepts were run under similar conditions with the parameters presented in Table 4.5.

The parameters for the heat input for each strategy were set up to reach a similar conversion of around 90%. These parameters are given in Table 4.6. The capacity is based in the standard capacity for a large scale reformer, and the solid to gas ratio is based on the patent of Jahnig et al. (1964). For all concepts, the beginning of the reaction zone was set at two thirds of the reactor length. For the resistive strategy, the reaction zone has to be bounded on the top so the end was chosen as one third of the reactor volume. The results for the side stream and the plasma strategies are presented in Figure 4.3 and the results for the resistive heating are shown in Figure 4.4.

From the results for the side-stream, it can be seen that at the point where the hot stream is introduced ($L_R = 4 \text{ m}$), the temperature increases drastically in the direction of the gas flow, as seen in Figure 4.3b. After that, the endothermic reaction takes place

leading to a temperature decrease which finalizes with a very rapid quench with the cold solid stream introduced in the top of the reactor. From the conversion profile Figure 4.3a, it can be noted that where the temperature increases the fastest is where the conversion takes place. After that, the profile flattens due to the decrease in temperature, in addition to the dilution given by the large side-stream introduced.

For the plasma strategy, the resulting profiles show a slightly different behavior. As it was for the case of the side-stream, at the point of introducing the atomic hydrogen, the violent reaction that takes place leads to a rise in temperature as shown in Figure 4.3d. This surge in temperature leads to the drastic increase in conversion shown in Figure 4.3c. Nonetheless, in this case, since the stream added is an order of magnitude smaller than in the side-stream case, the temperature in the gas phase drops more rapidly only allowing the reaction to take place in a very narrow volume inside the reactor.

Comparing the results obtained from the resistive heating concept presented in Figure 4.4, it can be noted that the profiles look different to those obtained in the previous case. For the temperature, a steady increase is found from the gas perspective, compared to the drastic increase in the previous cases. This is of course due to the fact that the heat is distributed alongside the whole reaction zone and not localized at the beginning. This continuous heat input leads to a steady increase in conversion in comparison to the fast rise in the previous cases. In the temperature profiles, it can also be observed that once the reaction slows down near the end of the reaction zone, an increase in temperature occurs due to the liberation of resistive heat without the endothermic counterpart given by the heat of reaction.

From the results presented in Figure 4.4, it is clear that the profiles are almost identical for all 5 different types of carbon simulated. This can be explained because the range of temperature in which the reaction zone lays is between 1400 and 1600 K, in which the resistivity is almost constant for most carbon types. A priori it could be thought that the carbon type has thus little influence in the reactor performance. However, looking at Table 4.6, it can be seen that the voltage needed for each type of carbon varies considerably. For the ones with lower resistivity, i.e. Zdieszowice, Magnitogorsk, and the test case for a constant lower resistivity, a lower potential difference is required, whereas the opposite is true for the types with higher resistivity, i.e. sponge pet coke.

For the resistive heating simulations, for the cases where the resistivity is a function of temperature, it was necessary to initialize the solution in steps in order to reach convergence, should the initial solution not be adequate, the solver will not find the solution. The strategy used consisted of solving the equations for increasing fractions of the desired voltage, i.e. one tenth, one fifth, one third, half, etc. and updating the initial value until the full system could be solved.

As a general conclusion from the model, it can be seen that the difference in temperature between the two phases is negligible in the major part of the reactor, barring the inlet of both phases where the temperature vary slightly. The model was thus simplified to avoid the use of correlations and the heat transfer coefficient was set to a constant value of $105 \text{ W m}^{-2} \text{ K}^{-1}$.

4. Heat Input Strategies

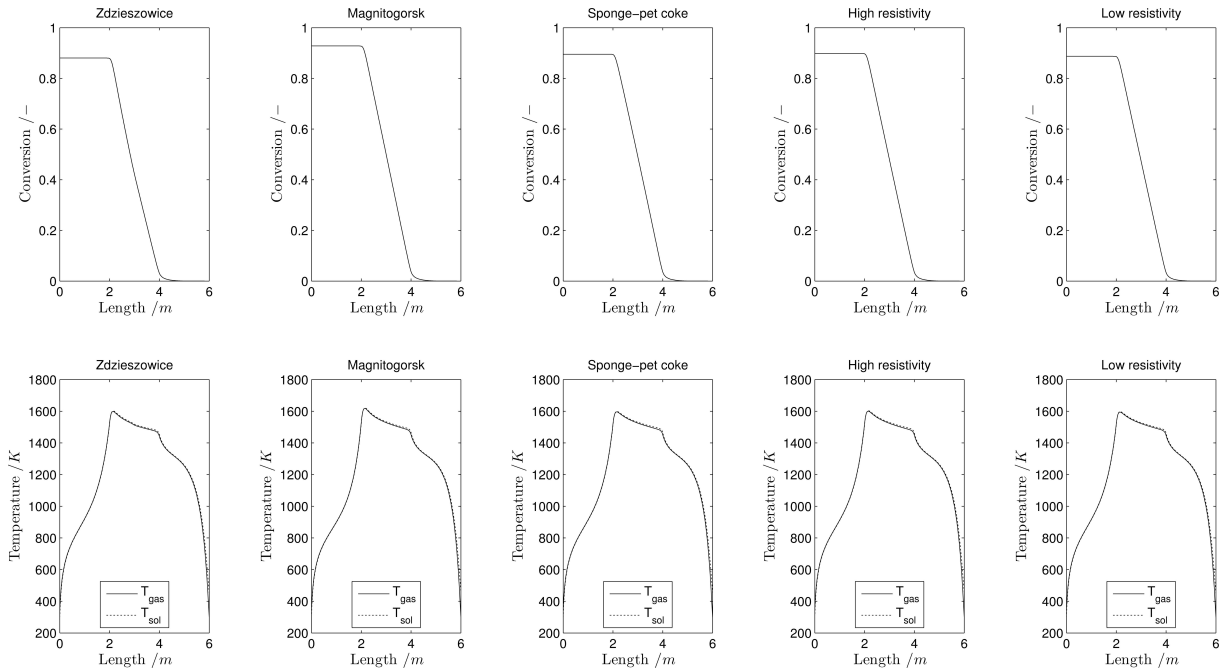


Figure 4.4.: Simulation results for the resistive heat strategy for all five types of carbon. Top row: conversion profiles. Bottom row: temperature profiles

4.4.2. Optimization Results

For the optimization, it is necessary to change the objective function for each strategy, but in general the constraints are the same. The optimization problem can be built as follows:

$$\min f(\vartheta) \quad (4.4.1)$$

s.t.

$$\text{Molar and energy balances} \quad (4.4.2)$$

$$1 \leq \theta_G, \theta_S \quad (4.4.3)$$

$$0 \leq X \leq 1 \quad (4.4.4)$$

$$X_{\xi=0} \geq 0.99 \quad (4.4.5)$$

$$\theta_{G,\xi=0}, \theta_{S,\xi=1} \leq \frac{800}{T_{inlet,G}} \quad (4.4.6)$$

$$\frac{L_R}{D_R} \geq 2 \quad (4.4.7)$$

Since the problem is set in its direct form, the molar and energy balances which represent the model are set as equality constraints. In addition, for all variables, at least a lower or upper bound is given.

The quality constraints, the purity of the product, i.e. the methane conversion at the outlet, and the gas and solid outlet temperatures were set to the given values. The first constraint is self-explanatory, and the second guarantees that heat will be recovered inside the reactor, which is the goal of a heat-integrated reactor. In addition, a constraint for the ratio of length to diameter is given.

The vector of decision variables consists of:

$$\vartheta^T = \left(\vec{X} \quad \vec{\theta}_G \quad \vec{\theta}_S \quad L_R \quad D_R \quad F_{C,inlet}/F_{T,inlet} \quad \psi \right) \quad (4.4.8)$$

where the first three positions consist of the discretized conversion and temperature vectors, the remaining decision variables are: the length and diameter of the reactor, the ratio of solid to gas molar flows and an additional vector of variables which will be different for each strategy and presented in the next sections.

For all optimizations, the parameters that were not used as decision variables remained with the values presented in Table 4.5.

The volumetric flow-rate is given for the production of hydrogen to be in the order of magnitude as that of a large scale reformer. Both solids and gas inlet temperature are set to ambient conditions. The particle diameter is also a fixed value, in this case, the value could change without having major influence in the system since the heat transfer between the phases is excellent. The pressure is set as atmospheric since it favors the methane equilibrium conversion, and to keep the CAPEX as low as possible since high temperature and high pressure operation usually lead to very expensive reactor constructions, especially with hydrogen present.

4.4.2.1. Side-Stream

For this strategy, the driving cost for optimization is the fraction of the product that needs to be combusted in order to provide enough convective heat for the reaction to take place. Although obviously in the reactor design, special care is needed to design an adequate gas distributor among others; those are beyond the scope of a technical optimization. Additionally, the regenerator system to preheat the gas is robust to changes in gas flows and temperatures. The regenerator consists basically of a vessel filled with material that can store the heat produced by the hydrogen combustion and then transfer this heat to the side stream. As this system is decoupled from the reactor itself, it is not a factor in the optimization. The cost function was then defined as:

$$\min f(\vartheta) = F_{H_2} = \frac{F_{side} \cdot c_{p,H_2} \cdot (T_{side} - T_{start})}{\Delta H_{combustion}} \quad (4.4.9)$$

which is basically the latent heat in the numerator divided by the combustion enthalpy in the denominator. The additional decision variables introduced are then:

$$\psi = \left(F_{side} \quad T_{side} \quad \zeta_{feed} \right) \quad (4.4.10)$$

The first two values represent the molar flow and the temperature of the side stream coming into the reactor. T_{start} represents the initial temperature at which the side stream is available, for instance the temperature of the gas leaving the reactor, and the last one represents the location of the side stream feed.

4.4.2.1.1 Preliminary Optimizations

Before carrying out the optimization with the full set of parameters, it was investigated how each of them would affect the solution of the problem.

The first result was that for all cases, the value of T_{side} always converged to the maximum value allowed. For the construction of this kind of reactor, it is typical to use refractory lining which usually is limited for maximal temperatures around 2073 K. This was then set to be the value for the side-stream. In addition the gas temperature leaving the reactor was usually inside the range from 345-355 K, so it was decided to assume it as constant. By doing this, the cost function simplifies to minimize the side-stream molar flow F_{side} .

To optimize the location, it was not possible to use it as a decision variable in the optimization because either it would lead to a MINLP problem, if the set was given as a finite set, or lead to problems with the consistency of the solutions by having the side-stream location be approximated to the nearest discretization point. Tests doing the latter resulted in solutions that were not optimal. It was then decided to carry out the optimization of the location manually. As a result from these studies it was noted that the optimal value was around the middle of the reactor (0.5-0.6), and that the influence of the location of the side-stream was reduced with increased outlet conversion.

For the volume, it was also not possible to use it as a parameter, as mentioned in Section 4.2.1, because the mixing volume for the gases is limited by a given length, assumed to be 5 cm for this case. This is independent of the reactor length, but it affects the discretization. For larger reactors, several more points are required to keep the resolution at 5 cm, meaning varying decision vector lengths. As in the case for the location, it was then decided to carry out the optimization manually. Nonetheless, the volume poses an additional challenge which is that looking at the preliminary optimizations, larger volumes yielded lower values for F_{side} . It could be thought that an indefinite volume increase would steadily minimize the need for the side stream. However, there is an intrinsic limit which is the amount of heat needed for the reaction to take place in order to reach the desired conversion, and therefore at some point the curve must flatten out.

Finally, for the ratio solid to gas, the optimization was completed successfully always finding the optimal solution.

4.4.2.1.2 Optimization

With the previous results in mind, it was decided to carry out the optimization for fixed volume and side-stream location. The vector of decision variables was then:

$$\vartheta^T = \left(\vec{X} \quad \vec{\theta}_G \quad \vec{\theta}_S \quad F_{C,inlet}/F_{T,inlet} \quad F_{side} \right) \quad (4.4.11)$$

For the reactor diameter, it was decided to limit the value to 4 meters, due to limitations in the transportation of equipment, for reactor constructions in-situ the diameter could be larger.

The optimizations were performed for 8 locations and 5 reactor lengths. The results are presented in Figure 4.5 and summarized in the appendix (Table B.1).

As it can be seen, the optimal location always lies between 0.5 and 0.6 and by increasing the reactor length, the location influence was minimized as anticipated.

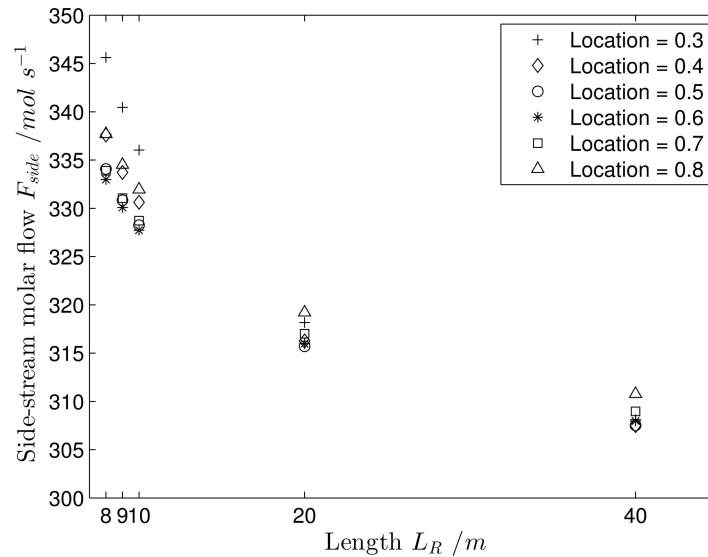


Figure 4.5.: Optimized results as a function of reactor length

For the solid to gas ratio, a decreasing tendency was observed as well with increasing length.

Furthermore, for the volume, the decreasing tendency is observed. However, even for lengths around 40 meters, the profile has not completely flattened, which means that the minimum heat needed to provide for the heat of reaction is still not achieved. Nonetheless, it was not possible to optimize larger reactors since the number of points for discretization became computationally prohibiting. In addition, for such large reactors, the CAPEX can no longer be assumed as low in comparison to the operation costs. Additional reinforcements for stability need to be guaranteed, as well as more complex solid transportation methods need to be devised in addition to the increased weight that the solid bed would have.

For common pneumatic transportation, the limit can be found around 20 meters of height (Mobley 2001) and thus this was set as the maximum allowed height for this reactor. The results for the optimized profiles for the location at the middle of the reactor and 20 meter length are shown in Figure 4.6.

The conversion profile in Figure 4.6a shows that most part of the reaction takes place above the inlet of the side stream as expected. Due to the heat transferred to the solids, some heat is carried down and some reaction occurs below the side stream inlet. The temperature profile depicted in Figure 4.6b indicates that the gas and solid temperatures are almost identical for the majority of the volume, only deviating slightly near their respective inlets. The gas outlet temperature was of 354.8 K, and the solid temperature was of 359.4 K, there is a slight asymmetry which is caused by the reaction taking place.

Should a higher purity in hydrogen be required, it was studied how that would affect the needed amount of hydrogen in the side stream. The results are presented in Table 4.7.

For pressures of 1 bar, it is usually assumed that the back reaction does not occur. Most of the times, this is supported due to the fact that the reaction products are

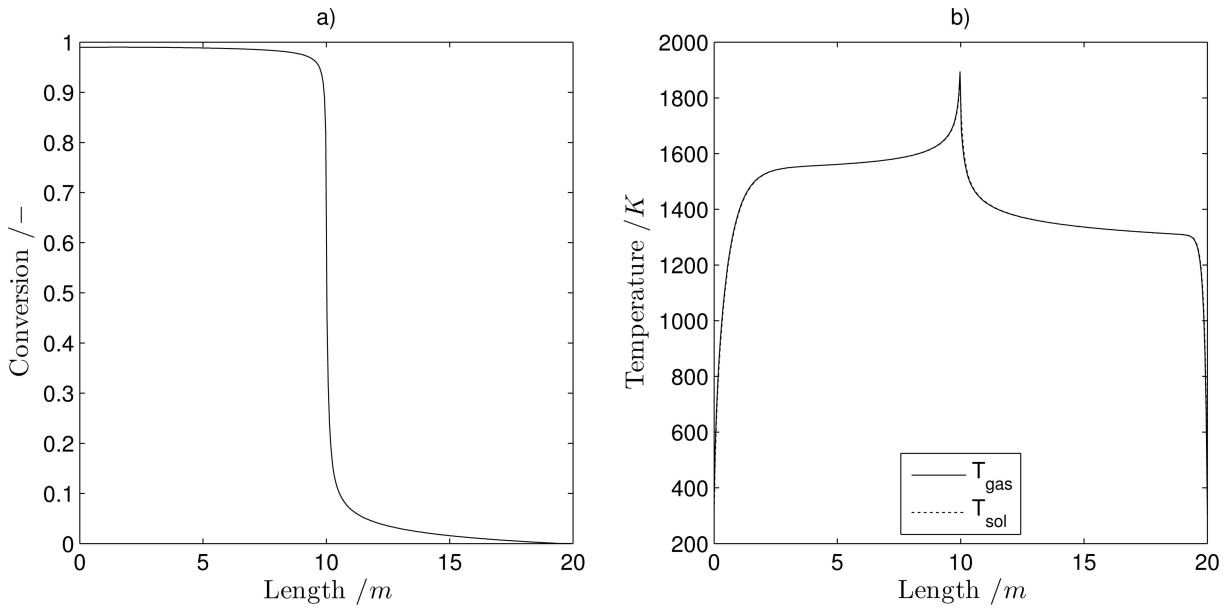


Figure 4.6.: Optimized profiles for the side-stream concept: a) conversion b) gas and solid temperature

Table 4.7.: Optimization results as a function of the desired conversion

X_{end} / -	With back reaction		Without back reaction	
	$F_{side}/F_{G,0}$ / -	$F_{C,0}/F_{G,0}$ / -	$F_{side}/F_{G,0}$ / -	$F_{C,0}/F_{G,0}$ / -
0.99	1.8368	4.7005	1.7977	4.5444
0.992	1.8642	4.778	1.8122	4.5661
0.994	1.923	4.9182	1.8285	4.595
0.996	3.1456	9.3232	1.8477	4.6364
0.998			1.8729	4.7053
0.999			1.8915	4.7691
0.9995	Not feasible		1.9058	4.8262
0.9999			1.92	4.932

present on different phases. Nevertheless, using the equilibrium constant, theoretically a maximal equilibrium conversion exists. The results presented were simulated for both cases. As it can be seen, for the case where the back reaction is included, the required side-stream increases steadily with the outlet conversion, until it nears the equilibrium, which in this case was around a conversion of 0.996. Then, as expected for an equilibrium reaction, the desired conversion becomes much harder to reach leading to much larger amounts of side stream required in addition to more solids to recover the heat of the gas stream. For the case without back reaction, the needed side stream increases steadily as does the amount of solid flow required.

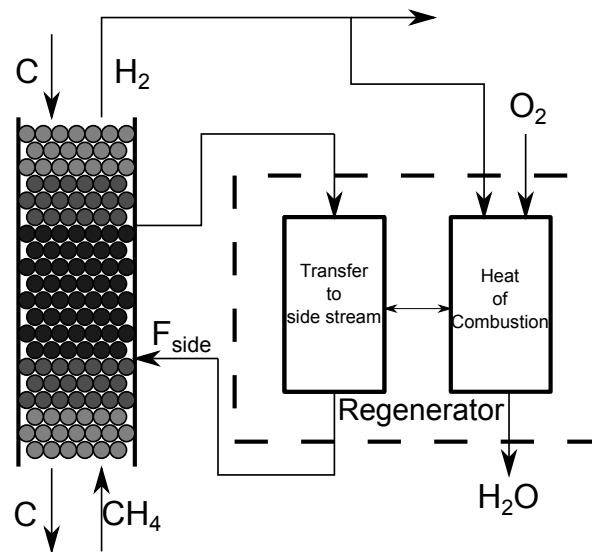


Figure 4.7.: Improved side-stream strategy

Finally, when operating this concept it is crucial to have the side stream available initially at high-temperatures to reduce the amount of hydrogen that needs to be combusted. For a starting temperature of 355 K, i.e. that from the gas leaving the reactor, the needed stream of hydrogen for combustion would be around 60 mol s^{-1} . This value is around 18% of the produced hydrogen.

By taking the stream from the side of the reactor, it can be obtained at higher temperatures than those that could potentially be reached by heat integration with most other processes. And thus the need for hydrogen to be combusted can be minimized. The proposed strategy is presented in Figure 4.7. In the figure, a secondary stream is showed as an alternative for hydrogen combustion, this is most likely not necessary since the adiabatic flame temperature for hydrogen combustion with oxygen lies around 3500 K and with air around 2500 K.

Using the results from the optimized reactor, it was then simulated how big the influence of taking a side stream would be by taking the stream out of the reactor at different locations. These results are presented in Table 4.8, and the temperature profiles are depicted in Figure 4.8. The conversion profiled looked all similar with only the final conversion shifting down, hence they are not presented.

From these results, it is important to notice that by increasing the location of the removal, the outlet conversion decreases but the temperature that would be available as starting temperature would be higher. Nonetheless, if the removal location is too close to the inlet location, conversion drops drastically, meaning there is a limit as to how high the temperature obtained from this side stream removal can be.

Based on the optimizations performed before, this means that using a side-stream removal, a higher side-stream would be needed to provide the heat and account for the minor loss in conversion, but the temperature delta in the cost function would be less, thus it is clear there must be an ideal combination.

Analogously to the case with the location of the inlet, for the removal it was not possible to include its location as a decision variable for optimization and thus, the

Table 4.8.: Influence of the location of the side stream removal in conversion

$\xi_{side,out}$	X_{end}	$T_{side,out}$
/ -	/ -	/ K
0.1504	0.9884	861.04
0.2005	0.9874	864.01
0.2506	0.9859	867.11
0.3008	0.9835	871.43
0.3509	0.9792	878.84
0.401	0.9696	895.46
0.4511	0.9395	953.84

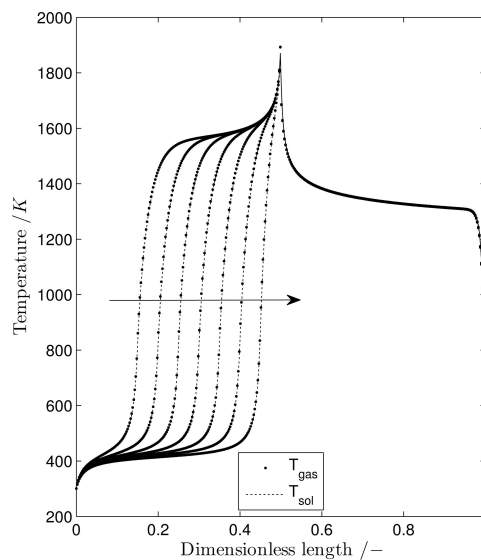


Figure 4.8.: Temperature profiles by changing the location of the side stream removal, the arrow points in the direction of increasing side stream removal location

optimization of this strategy was carried out manually from a finite set.

From the results, it is interesting to note, that at least two families of solutions exist. Starting from a non-converged solution, i.e. constant profiles, a profile similar to that presented in Figure 4.8 is found with the temperatures of the side-stream outlet ranging from 800-900 K. However, if a converged solution is given as the initial conditions, it is possible to obtain another solution, with outlet stream temperatures from 1100-1600 K. The compared profiles are given in the appendix (Figure B.1).

The second family of solutions would not represent a viable solution. Having outlet temperatures above the point where the pyrolysis is kinetically feasible would mean that the pyrolysis would carry on in the piping and also in the regenerator. The former could lead to blockage due to carbon formation and accumulation, and although the latter would not be technically problematic, it would lead to additional CO₂ pro-

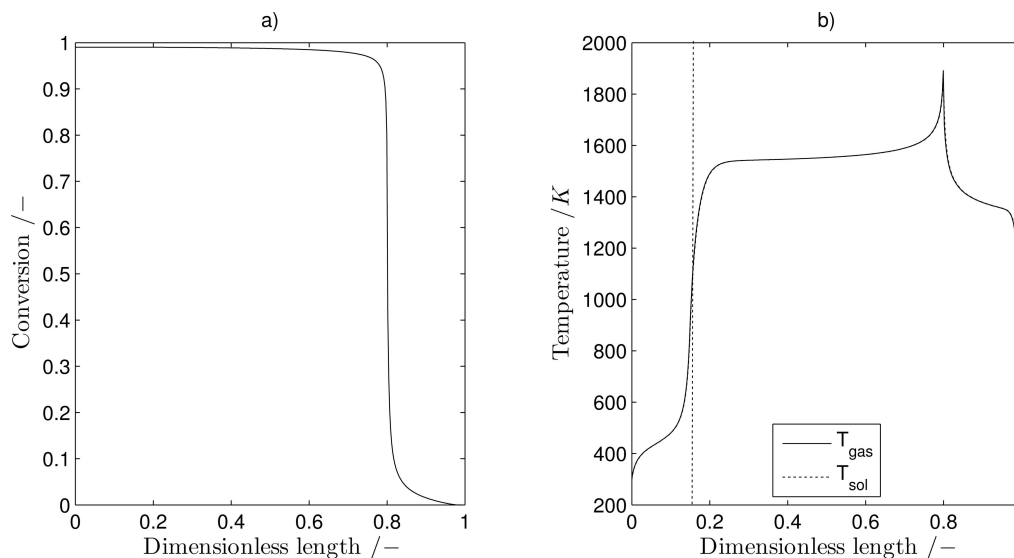


Figure 4.9.: Optimized profiles for the side-stream strategy: a) conversion b) gas and solid temperature

duction, since the carbon generated in the regenerator would be combusted in the combustion step.

Therefore, it was chosen to study the first family only. The results for the full optimization are presented in the appendix (Table B.2). From those results, it can be noticed that by increasing the location of the side stream-inlet, a lower consumption of hydrogen was favored which is the desired result. However, the effect of the outlet location was a bit erratic, and a real tendency could not be found. Nonetheless, unless there was some problem with the optimization, as in the three marked cases, the results are very close among each other and their influence is thus not that significant.

The location for the final inlet and outlet were chosen to be 0.8 and 0.15 and the resulting profiles are shown in Figure 4.9.

From the profiles it can be seen, that an additional feature is that the temperature near the solid outlet is not as high in comparison with the initial concept meaning that there is an extra layer of safety added for this process, since disturbances in the operation will not travel as fast towards the top which could lead to potential damage of peripherals near the top of the reactor.

Finally comparing the results with the previous strategy, the amount of hydrogen needed for this concept, 41.02 mol s^{-1} , was around 11% of the produced hydrogen which represented a 7% saving in the amount of hydrogen needed to provide the heat of reaction. Although the total amount will be higher taking into account heat losses and the efficiency of the regenerator, using the side-stream removal, considerable savings in this regard were obtained. In addition, a lower solid flow-rate is required in the second strategy since the gas flow that preheats the solids is less.

4.4.2.2. Plasma

For this strategy, the driving cost for optimization is the molar flow of plasma needed to provide the heat for the reaction to take place. This is due to the fact that the energy

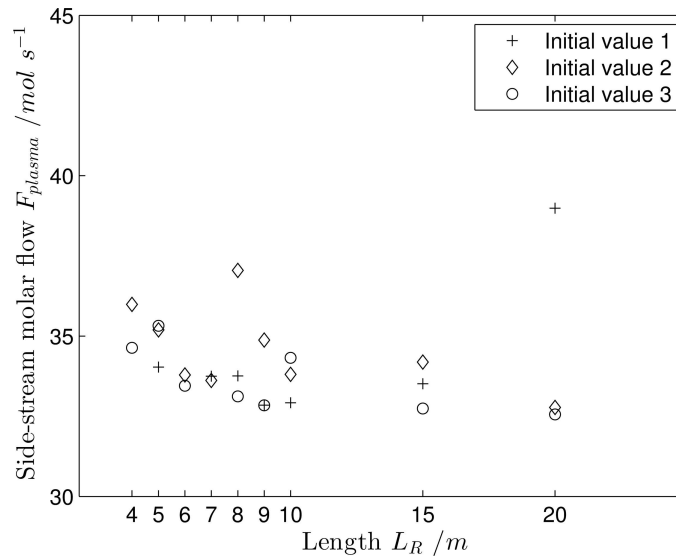


Figure 4.10.: Optimized results as a function of reactor length for different sets of initial values

required to generate plasmas can be very high. The cost function is then defined as:

$$\min f(\vartheta) = F_{plasma} \quad (4.4.12)$$

The additional decision variables introduced are:

$$\psi = (F_{plasma} \quad \xi_{feed}) \quad (4.4.13)$$

The first value represents the molar flow of the plasma coming into the reactor and the second one represents the location of the plasma feed. As for the side-stream strategy, the location and volume could not be optimized directly. Therefore, it was decided to investigate them individually. For the volume, the results are presented in Figure 4.10 and the full results are summarized in the appendix (Table B.3)

From the optimized results it can be seen that there is a steady decrease from 4 to 8 meters, which is the region where the reactor diameter is changing to keep the L/D ratio at 2. After that, there is not a clear tendency, except that the lowest value obtained seems to be pretty close for any given length. For the lengths that show only two results, it was due to the solver finding an infeasible solution, or not converging to a successful point.

Compared to the previous strategy, it thus makes sense to work with the larger diameter possible, but with the shortest length.

To determine location influence, the reactor length was set to be 8 m and the diameter 4 m. The results are presented in Figure 4.11a with the full results in the appendix (Table B.4).

From the results, the optimal location was found to be around 0.4. The conversion and temperature profiles corresponding to this feed are presented in Figures 4.11b-c.

From the profiles it can be observed that a higher temperature than that of the side-stream strategy is found inside the reactor, this high temperature leads to a faster reaction causing the conversion to take place in a very short span. In addition, the

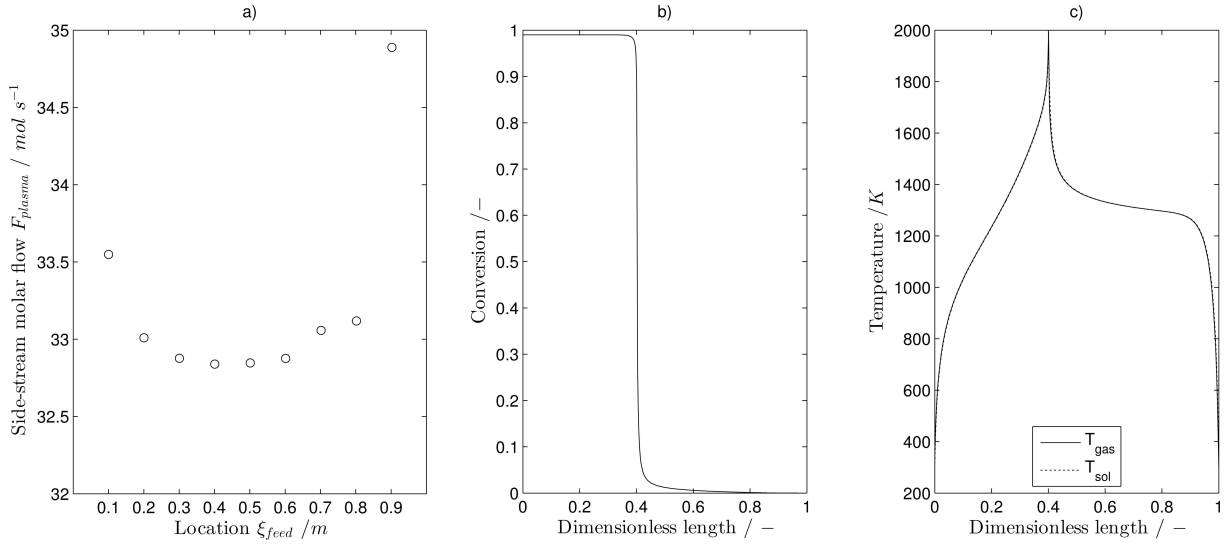


Figure 4.11.: a) Required plasma flow as a function of feed location b) conversion profile for the optimal location c) gas and temperature profiles for the optimal location.

need for solids is lesser in this concept since the gas flow is not as high as in the previous strategy.

Finally, it can be said from this concept that it presents a lesser potential for optimization, especially compared with the previous strategy. The advantages of this concept lie in a lower CAPEX, due to the smaller reactor and not needing any additional equipment. Furthermore, the lower solid flow-rates mean an easier solid handling. The disadvantage is still the electricity required to generate the plasma, which was completely avoided in the previous strategy.

4.4.2.3. Resistive Heating

For this strategy, the driving cost for optimization is the power required to generate the heat to provide the heat for the reaction to take place:

$$\min f(\vartheta) = U \cdot I \quad (4.4.14)$$

Assuming the resistivity is constant, the objective function can be then rewritten as:

$$\min f(\vartheta) = \frac{U^2 \cdot A}{\rho_M \cdot L_{middle}} \quad (4.4.15)$$

The additional decision variables for this strategy are the length of the 3 regions, and the potential difference in the reaction zone.

$$\psi = (L_{top} \ L_{middle} \ L_{bottom} \ U) \quad (4.4.16)$$

From the objective function, it is clear that mostly the distance between electrodes (L_{middle}) and the potential play a direct role. However, when the optimization is performed for those variables, the voltage overweights the length and thus, the solver converges to the lowest allowed value of voltage. To supply the energy for the reaction, a very large current is needed, and the distance between the electrodes decreases.

Table 4.9.: Influence of the location of the side stream removal in conversion

U / V	I / A	R / Ω	L_{middle} for $\rho_M = 0.005$ / m	L_{middle} for $\rho_M = 0.04$ / m
20	8.50E+05	2.35E-05	5.91E-02	7.39E-03
165	1.03E+05	1.60E-03	4.02E+00	5.03E-01
470	3.62E+04	1.30E-02	3.27E+01	4.08E+00

For instance, the energy required for the pyrolysis for the given molar flow is in the order of magnitude of 17 MW. For a potential difference of 20 V, a current of 850 kA would be required for the low-resistivity carbon, and the distance between the electrodes would be of 0.059 meters. An industrial application under these conditions is to the authors' knowledge non-existent. The simulation results for this case were very close to those of the plasma reactor, which makes sense comparing the large amount of heat liberated in a very short region.

Since operating at such low potentials is unfeasible, it is thus necessary to decouple the voltage from the optimization in order to obtain results that can still be comparable to other industrial processes. The chosen conditions are summarized in Table 4.9.

From Table 4.9, it can be seen that the resistivity of the material plays a major role in determining the operating conditions. For the low-resistivity carbon, a voltage of 165 V would require a length of 4.02 m whereas for the high-resistivity case, this distance would be of only 0.503 m. From the current perspective, the low-resistivity case would be close to the maximal known values for applications of this type, i.e. around 120-180 kA in electric-arc furnaces (Siemens AG 2010). For the high-resistivity case, the value is closer to the 40 kA of standard electric-arc furnaces for steelmaking.

It was thus decided to use those cases as worse and best case scenarios. The voltages were chosen so that in both cases the zone of reaction was around 4 meters, which is the maximal value for the diameter since the preliminary optimizations showed that larger diameters yielded better results.

An additional difficulty presented itself when carrying the optimization for high conversions. There, the optimizer did not converge for conversion higher than 0.98. The reason behind it is the back reaction. Contrary to the previous strategies, the temperature increases in the direction of the gas flow that means that near the maximal temperature will be the maximal conversion, which leads to the occurrence of the back reaction when the gas cools down. For the optimization, it was then decided to carry out the optimizations first without the back reaction and then plug-in the results into the full model.

In addition, and analogously to the location in the previous strategies, the lengths of the top and bottom sections were not included in the optimization but were parametrized. This was done by increasing intervals of 0.5 m for total reactor lengths of 8 9 and 10 meters, for instance the first optimizations was made for 0.5 m top length, 4 m for the middle, which was left as a decision variable since it directly in-

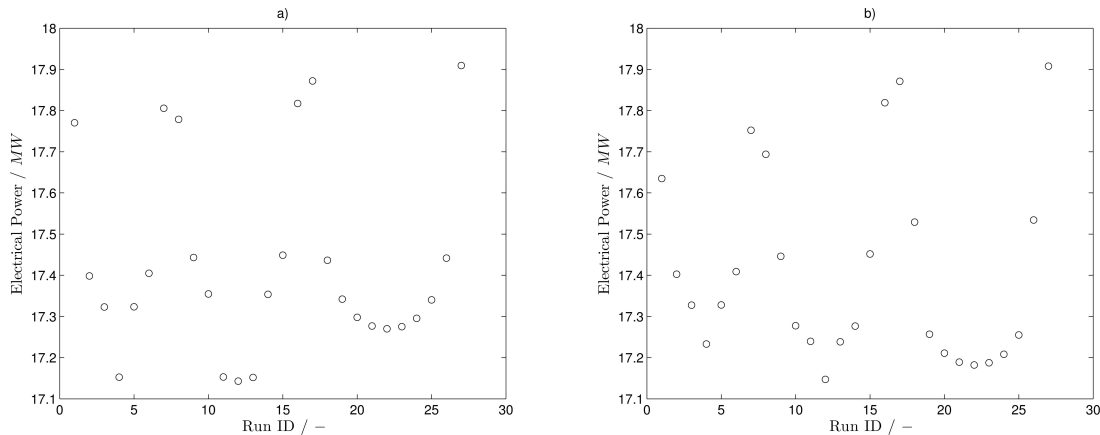


Figure 4.12.: Optimization results for the resistive heating strategy: a) 165 V for low-resistivity carbon b) 470 V for high-resistivity carbon

fluences the objective function, and 3.5 m for the bottom. Then the top length was increased by 0.5 m and the bottom length was decreased by 0.5m. The full results are presented in the appendix (Tables B.5,B.6). Figure 4.12 summarizes the results for the 165 V and 470 V cases.

From the optimization results, it can be observed that for all lengths, the minimum is around the point where the top and bottom length are symmetrical. Nonetheless, the influence of the top and bottom distribution is only of about less than 1% in the total power, the main driving factors remain the length of the middle zone and the solid to gas ratio. The first values converged naturally to a length close to 4 meters as was intended, and the ratio for most cases was around 2.7.

In Figure 4.13, a comparison of the optimized results is presented for the obtained results, which ignored the back reaction and the results that would be obtained when plugging the resulting decision variables in the full model including the back reaction.

From Figure 4.13, it can be seen that the profiles are almost identical when comparing the cases of low and high-resistivity as was the case in Section 4.4.1. The difference is only the infrastructure required to deal with the different currents.

From the resulting profiles, a major difference can be noticed when including the back reaction especially for the temperature profiles. There, a high temperature is achieved, which is due to the fact that when the reaction nears its equilibrium, the reaction rates decrease and thus the heat consumed decreases while the heat being liberated by the solids is the same. For the conversion profiles, it can be observed that the outlet conversion decreased to about 0.985, which could not be increased.

For this concept, if the back reaction occurs, it would be at a disadvantage since it would not be possible to avoid the back reaction and conversions of 0.99 will not be obtained. In the case that the back reaction does not occur, or occurs slower than predicted by the thermodynamics of the equilibrium constant, the concept is promising, and showed potential for optimization and more control over the decision variables compared to the plasma strategy.

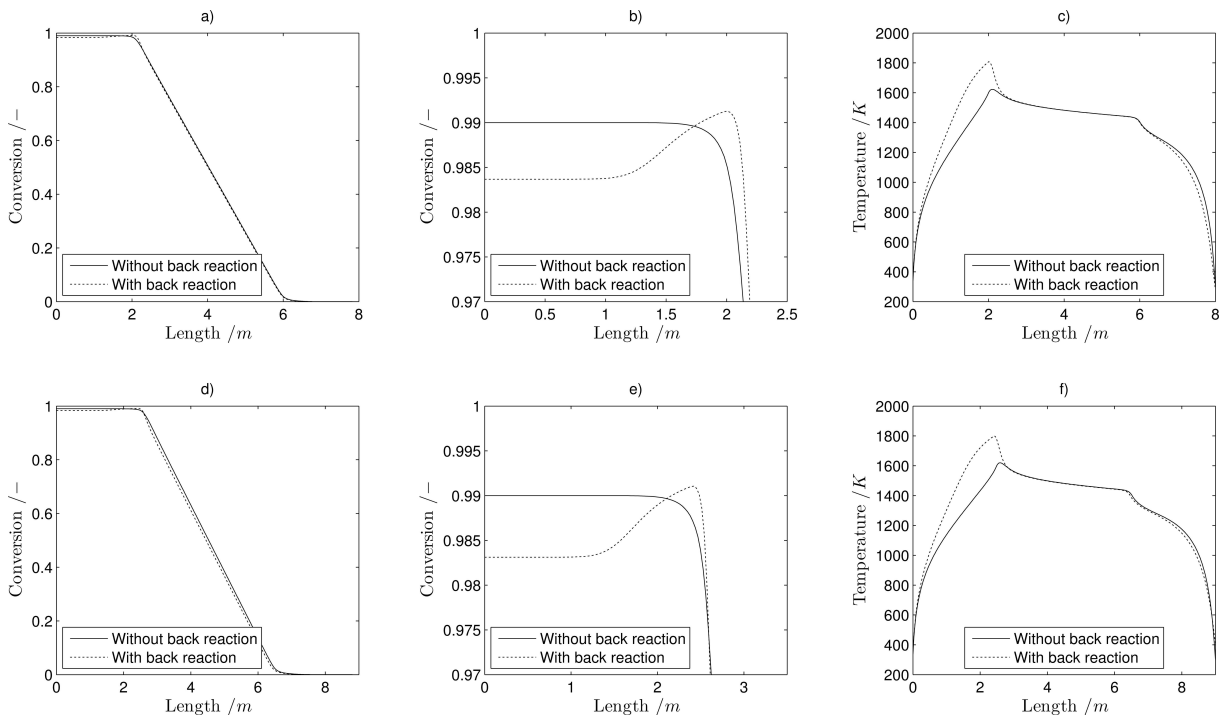


Figure 4.13.: Optimized results for the resistive heating strategy: Top row results for 165 V: a) conversion profiles b) zoom into the conversion profile c) temperature profiles. Bottom row results for 470 V: d) conversion profiles e) zoom into the conversion profile f) temperature profiles

4.4.3. CO₂-Emissions and Technical Feasibility

4.4.3.1. Side-Stream

In this strategy, the optimized result showed that 41.02 mol s^{-1} , equivalent to 12 MW, are needed to provide the reaction heat. However, this value is under the minimum requirement predicted by the thermodynamics of the reaction, which lies around 16-17 MW depending on the reaction temperature.

The reason for this is the way the model is implemented, where the assumed mixing zone had a defined length, provided for a larger conversion than it would in reality and thus underestimated the need for heat input.

A shorter mixing region could be defined; however, it was not possible to carry out simulations for denser grids at the desired reactor length. Nonetheless, the trends from the optimizations obtained were found, for the most part, to be independent from the discretization mesh, and thus, the location of the streams as well as the reactor length and diameter, which in this case where the physical constraints, can be taken as the final result.

The theoretical minimum for the reaction heat would require 51 mol s^{-1} of hydrogen and an equivalent side-stream of 398 mol s^{-1} . Contrary to the length and location, the ratio of solid to gas would affect the optimization, and higher solid flow-rates would be required.

Furthermore, the efficiency of the heat exchanger was not taken into account. For

regenerators, the thermal efficiency is a function of the cycle times. For short cycles, i.e. around 120 s, the efficiency can reach values up to 98%; for long cycles, i.e. 1200 s, the efficiency can be reduced to 50%. Nonetheless, for conservative cycle times of around 600 s, the efficiency is still quite high at around 95% (Kolios 2014).

From the emissions perspectives, for a conversion of 99%, the total flow of methane that would be directly combusted in the system (in the regenerator and in the combustion) would be 1.04 mol s⁻¹ of methane. This leads to a direct emission of 0.0235 kg CO₂ per kg H₂, in addition, the emissions linked to the transport and extraction of methane can be quantified as 1.84 kg CO₂ per kg H₂ (Machhammer et al. 2016) for a total of 1.86 kg CO₂ per kg H₂ which lays well below the state of the art.

This concept is technically promising in regions where electricity is expensive, since it requires no external electrical source. In terms of equipment, the addition of a regenerator which consists of two additional units is the limiting factor, but the technology and materials to withstand the conditions, for both the reactor and regenerator, are already used industrially in different processes, meaning the construction of such a reactor would be of moderate to low risk.

4.4.3.2. Plasma

In this case, the required plasma stream was found to be 32.84 mol s⁻¹, which is equivalent to 14 MW. As was the case in the previous concept, this value lies below the minimum, and the source of disparity is the same. However, in this case, the difference is not as dramatic, and the real minimum value would lay around 36 mol s⁻¹. As in the previous strategy, the location of the plasma stream would remain the same and for the gas to solid ratio, since the difference in the gas flow is negligible, the found ratio can be seen as the optimal value. For the reactor length, slight variations could occur, but as is seen in the optimization, above the 8 meter lower limit, there was nothing to gain.

To generate the required 16-17 MW, needed by the reaction, the plasma has to be generated by means of electrical power. At atmospheric pressures, technologies such as plasma torches have efficiencies of around 50% (Zhukov and Zasytkin 2007), and other methods to generate plasma, such as microwaves, are in the same order of magnitude. Thus, the total electricity needed would be around the 32-34 MW.

The CO₂ emissions for that amount of electricity are directly linked to the source of power. For the case of Germany, in the 2030 electricity mix scenario, the emissions are given as 350 kg CO₂ per MWh. For this case, that would yield 4.85 kg CO₂ per kg H₂ and with the addition of the transport and extraction contribution, the total adds up to 6.69 kg CO₂ per kg H₂ which is above the state of the art, but has potential to improve with changing electrical power.

As for the technical feasibility of this concept, several points would need to be addressed before it could be implemented. Most of plasma arc, torch, or microwave technologies have so far only been proved with capacities up to 5 MW; this is only a third of the capacity for an industrial application that would be comparable to a reformer. Moreover, the additional need for water-cooling that is required for most concepts complicate the construction of the reactor.

4.4.3.3. Resistive Heating

For this strategy, since the heat is distributed, the issues encountered in the two previous concepts were not found present in this case. The optimal value for this concept was found to be around 17 MW, with varying current and voltage depending on the carbon resistivity.

To transfer that power, it is necessary to use a transformer that will take the energy from the high-voltage network to the low voltage required. Depending on the transformer, efficiencies up to 95-98% can be achieved.

The CO₂ emissions for that amount of electricity would those be directly linked to the source of power. For the case of Germany, in the 2030 electricity mix scenario, the emissions are given as 350 kg CO₂ per MWh. For this case, that would yield 2.55 kg CO₂ per kg H₂ and with the addition of the transport and extraction contribution, the total adds up to 4.39 kg CO₂ per kg H₂ which is below the state of the art, and could be still lowered with the inclusion of a larger fraction of renewable energy.

As for the technical feasibility, the electrode design and operation are the major challenges. Similar applications, especially the electrical arc furnaces, present a valuable starting point. A transformer for the power output is industrially available, and the conditions for the reactor are similar to those achieved in other processes such as carbon black production, among others.

4.5. Conclusions

In this work, three strategies to circumvent the difficulty of introducing the reaction heat for the pyrolysis of methane at high temperatures were modeled, simulated and optimized.

From the three strategies, the alternative with the lower associated CO₂ emissions was found to be the side-stream strategy with only 1.86 kg CO₂ per kg H₂ produced, which are almost completely linked to the extraction and transportation of methane. However, this concept necessitates the addition of an additional unit besides the pyrolysis reactor, which is a regenerative heat exchanger, which in terms consists of two pieces of equipment.

The resistive heating strategy contributed with 4.39 kg CO₂ per kg H₂ produced, which is about the half of the SMR. Technically the concept is feasible, and only requires a transformer as an additional unit. Nevertheless, the strategy has a caveat, due to the temperature profile built inside the reactor, the occurrence of the back reaction is unavoidable and the highest conversion achieved was of 98.3%. For higher purities, this concept requires an additional purification unit which makes the concept less appealing.

The plasma strategy had the highest CO₂ emissions with 6.69 kg CO₂ per kg H₂, mainly due to the fact that the electrical efficiency is fairly low. In terms of feasibility, this concept presents the most risks, energy outputs as high as required for the concept have not been industrially proven, with the highest capacity available being around one third of the requirement for the desired hydrogen production.

In terms of optimization potential, the resistive heating presented the wider range, since the temperature profile is axially more distributed. Both the side-stream and the plasma concept presented little potential for optimization, due to the very rapid introduction of heat particularly in the plasma strategy. For the side-stream, it should be noted that due to construction constraints, the optimum was not found with respect to the length. Larger diameters and reactor lengths would lead to improved results.

To sum up, the side-stream strategy can be seen as a concept for producing hydrogen at very low CO₂ emissions, but with very few hurdles for its industrial implementation, which could be a solution at short term in terms of reducing CO₂ emissions. The resistive heating, can be seen as a concept for producing bulk hydrogen for cases where hydrogen purity is not the constraint, technologically, all the elements have been industrially used independently, but not as a whole, and can be seen as a mid-term solution for when electricity can be produced with lower CO₂-associated emissions. Finally, the plasma concept is a long-term alternative for when research in the area further develops, at atmospheric pressures it will probably take longer, but for vacuum conditions, for high hydrogen purity it could be an attractive alternative long-term for places where electricity is cheap and renewable-based.

Part III.

Reverse Water-Gas Shift Reaction

Preamble

The following chapter has been published as:

Munera Parra, A.A, C. Asmanoglo, and D.W. Agar (2017): "Cyclic Steady-State Behavior of a Fixed-Bed Adsorptive Reactor for Reverse Water-Gas Shift Reaction". In: *Chemical Engineering & Technology* 40.5, pp. 915-926

The publication is based on Asmanoglo's calculations from his Master thesis: "Modeling and Optimization of Adsorptive Reactor Concepts for the rWGS Reaction". Conceived and directed by myself and evaluated by Prof. Agar.

Abstract

Processes to use CO₂ on an industrial scale are few and far between. One proposal is to apply the reverse water-gas shift reaction (rWGS) to activate CO₂ and produce syngas, which is one of the most versatile feedstock. The rWGS needs high temperatures to yield a favorable equilibrium, which entails high costs. To circumvent the unfavorable equilibrium at lower temperatures, a fixed-bed adsorptive reactor is proposed as a potential solution. The adsorption functionality leads to a periodic operation, due to the regeneration step. The cyclic steady-state behavior of the system is modeled and then optimized based on a technical objective function. Improvements in the objective function of above 800% can be achieved by manipulating the temperature and concentration profiles inside the reactor.

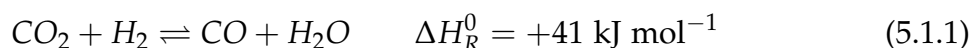
5

Fixed-Bed Adsorptive Reactor

5.1. Introduction

Over the past decades, major concerns have been raised about the increasing concentration of CO₂ in the atmosphere. CO₂ can be viewed as an undesired by-product, and its generation can try to be suppressed or avoided upfront, by for instance using methane pyrolysis instead of methane steam-reforming to produce hydrogen. However, in some cases, such as the production of cement, CO₂ co-production is unavoidable. For such cases, alternatives like Carbon Capture and Storage (CCS) have been proposed as a viable solution. Nonetheless, questions still remain about the feasibility and public acceptance of this technology. Conversely, CO₂ may also be viewed as chemical feedstock. While, this would by no means solve the issue of CO₂ atmospheric concentration, it could serve to recycle 10% of the emissions (Aresta 2010) and reduce the net amount of CO₂ produced. However CO₂ as being the end product of any combustion process is a relatively non-reactive molecule.

CO₂ can be activated with hydrogen using different reaction routes. Firstly, it can be converted to methane via the Sabatier reaction. However, most common uses for methane are linked with CO₂ generation and, thus, this defeats the purpose of CO₂ activation. Furthermore, CO₂ can also be converted directly to methanol, either via CO₂ hydrogenation, or by the photo-catalytic reduction of CO₂. Nonetheless, the catalyst development is still undergoing for production at commercial scale (Ali et al. 2015). Another alternative to activate CO₂ is the reverse water-gas shift reaction:



By using renewable, CO₂-free hydrogen, e.g. from electrolysis with 100% renewable energy, or CO₂-low hydrogen, e.g. electrolysis with current power generation or methane pyrolysis, CO₂ can be activated to more reactive CO, and, by using excess hydrogen, syngas in any given ratio can be produced. Syngas can then be used, among other processes, in the Fischer-Tropsch, methane or methanol synthesis, covering the uses previously discussed. The main challenge in carrying out this reaction is the equilibrium of the rWGS reaction. For a reasonable conversion, temperatures above 800 °C ($K_{eq} = 1.07$) are required, and, since the reaction is endothermic, the need to supply heat at high temperature compromises the feasibility of the concept. Low temperature rWGS, on the other hand, has a very unfavorable equilibrium

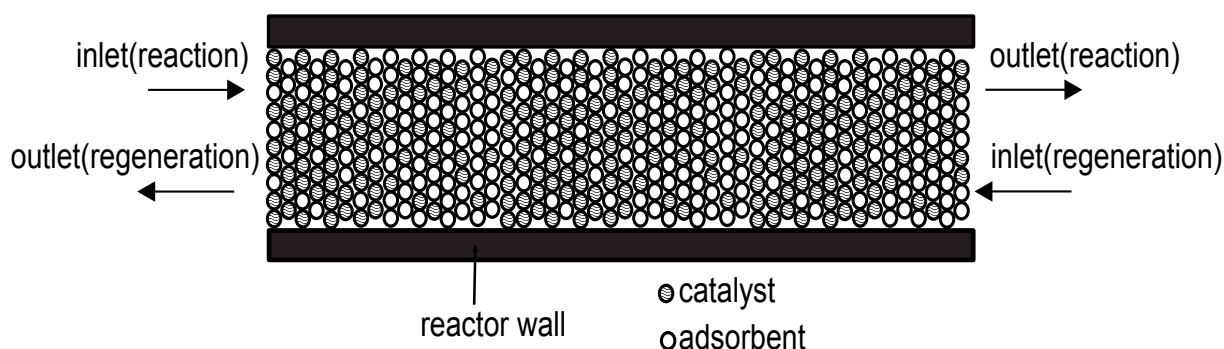


Figure 5.1.: Fixed-bed adsorptive reactor

($K_{eq}(250^{\circ}\text{C}) = 0.012$) but the availability of waste heat from other processes at such temperatures is greater than at high temperature.

To circumvent both issues, i.e. high temperature heat input and poor equilibrium, adsorptive reactors offer a viable solution (Agar 2005). The reactor is multi-functional in that the water separation occurs intrinsically within the reactor, and this separation leads to an enhancement of the equilibrium, by displacing it to the products side. In addition, the heat of reaction is of the same order of magnitude with the heat of adsorption which is reported with values ranging from -43 to -72 kJ mol^{-1} (Simo et al. 2009), allowing for these heat flows to be coupled and hence minimizing the need for external heat input. Preliminary studies on the endothermic rWGS reaction (Jung et al. 2013) as well as in other exothermic processes like the Deacon or Claus processes (Hussainy and Agar 2016) have demonstrated that this concept is an attractive alternative. In this work, the modeling and simulation of the cyclic steady-state (CSS) and the further technical optimization have been carried out.

5.2. Problem Definition

In this work, the case-study considers a lab-scale reactor for low temperature rWGS to produce syngas for the methanol synthesis. An adsorptive reactor, as depicted in Figure 5.1, consists of a fixed-bed that can be either structured or homogeneous containing a certain fraction of catalyst, in this case an industrial Cu/ZnO catalyst, and a complementing fraction of adsorbent, in this case Zeolite 3A. Due to the adsorptive functionality, at a given time the adsorbent will saturate and regeneration will become necessary. To regenerate an adsorbent, several techniques are available. Temperature swing, the most common one, but necessitates temperatures over 270 $^{\circ}\text{C}$ for regeneration, which can damage the zeolites. Pressure swing is another alternative, but, to fully regenerate the adsorbent, in order to maximize the driving force, low pressures are required and, in most cases, an additional gas purging step as well. The change of pressure in a system is usually an important cost factor and therefore, for the initial study, it was decided to carry out the desorption using a purge step: an inert gas with an effective water partial pressure of zero is passed in counter-current flow through the reactor until the desired regeneration is achieved.

Table 5.1.: Parameters for the Langmuir isotherms

b_∞ / $\text{K}^{0.5} \text{Pa}^{-1}$	γ / -	q_{0,H_2O} / mol kg^{-1}	δ / -	T_0 / K
5.3126E-10	23.235	10.7446	0.68792	300

5.3. Mathematical Modeling

For an adsorptive reactor, it is necessary to model the different steps occurring during the process. In this case the system was simplified to just two steps: the reaction and regeneration.

The model for a fixed-bed reactor can be derived from differential balances under the assumptions of plug flow and negligible axial dispersion, and radial mass and heat transport. Initially, the model was developed for a heterogeneous system. However, preliminary runs showed that the mass and heat transfer resistance between bulk and catalyst/adsorbent were negligible, hence simplifying the model to a pseudo-homogeneous one.

5.3.1. Molar Balances

5.3.1.1. Solid Phase

For the solid phase, only a molar balance has to be set-up for the adsorbent, a simple differential balance yields:

$$\frac{\partial q}{\partial t} = k_{LDF} (q_{eq} - q) \quad q(t=0, \forall x) = q_0 \quad (5.3.1)$$

The kinetics for adsorption are given by a Linear Driving Force (LDF) approach neglecting the influence of Knudsen and surface diffusion (Simo et al. 2009), yielding:

$$\frac{1}{k_{LDF}} = \frac{R_p}{3k_G} \frac{q_{eq,H_2O} \cdot \rho_{ads}}{C_{G,H_2O}} + \frac{R_p^2 \cdot \tau_{ads}}{15 \cdot \epsilon_{ads} \cdot D_{macropore}} \frac{q_{eq,H_2O} \cdot \rho_{ads}}{C_{G,H_2O}} \quad (5.3.2)$$

The equilibrium is given by Simo et al. (2009) in the form of a Langmuir isotherm as:

$$q_{eq,H_2O} = q_{s,H_2O}(T) \frac{b(T) p_{H_2O}}{1 + b(T) p_{H_2O}} \quad (5.3.3)$$

$$b(T) = \frac{b_\infty}{\sqrt{T}} \exp\left(\gamma \frac{T_0}{T}\right) \quad (5.3.4)$$

$$q_{s,H_2O} = q_{0,H_2O} \exp\left(\delta \left(1 - \frac{T_0}{T}\right)\right) \quad (5.3.5)$$

with the parameters given in Table 5.1.

5.3.1.2. Gas Phase

For the molar balance in the gas phase, a separate balance is made for water since the adsorption can be assumed to be selective:

$$\frac{\partial C_i}{\partial t} = -\frac{\partial}{\partial x} (u_G \cdot C_i) + \frac{1 - \epsilon_{bed}}{\epsilon_{bed}} \cdot \rho_{cat} \cdot \phi_{cat} \cdot \nu_i \cdot r_{rxn} \quad i = \text{CO}_2, \text{CO}, \text{H}_2, \text{N}_2 \quad (5.3.6)$$

$$\begin{aligned} \frac{\partial C_{\text{H}_2\text{O}}}{\partial t} = & -\frac{\partial}{\partial x} (u_G \cdot C_{\text{H}_2\text{O}}) + \frac{1 - \epsilon_{bed}}{\epsilon_{bed}} \rho_{cat} \cdot \phi_{cat} \cdot \nu_{\text{H}_2\text{O}} \cdot r_{rxn} - \\ & \frac{1 - \epsilon_{bed}}{\epsilon_{bed}} \rho_{ads} \cdot \phi_{ads} \cdot k_{LDF} (q_{eq} - q) \end{aligned} \quad (5.3.7)$$

The kinetics of the rWGS reaction are as proposed by Adams and Barton (2009):

$$\begin{aligned} r_{rxn} = & \left(8.22 \times 10^4 \text{ mol kg}^{-1} \text{ s}^{-1} \exp \left(\frac{-47.4 \text{ kJ mol}^{-1}}{R \cdot T} \right) \right) \\ & \cdot \left(y_{\text{CO}_2} \cdot y_{\text{H}_2} - \frac{y_{\text{CO}} \cdot y_{\text{H}_2\text{O}}}{K_{eq}} \right) \cdot F_p \end{aligned} \quad (5.3.8)$$

where F_p is a pressure correction term defined as:

$$F_p = \left(\frac{P(\text{Pa})}{10^5 \text{ Pa}} \right)^{0.5 - \frac{P(\text{Pa})}{250 \times 10^5 \text{ Pa}}} \quad (5.3.9)$$

and the equilibrium constant is given by:

$$K_{eq}(T) = \exp \left(4.33 - \frac{4577.8 \text{ K}}{T} \right) \quad (5.3.10)$$

The boundary conditions for this case are of the first type, i.e. Dirichlet, taking the inlet concentration values and the location is at $x = 0$ for the reaction step and at $x = L$ for the regeneration step. The initial concentrations value can be set to any given mixture of components.

5.3.2. Energy Balances

Since the system can be considered as pseudo-homogeneous, only one energy balance is needed, the equation being obtained is as follows:

$$\begin{aligned} \frac{\partial T_{GS}}{\partial t} = & -\epsilon_{bed} \frac{C_T \cdot c_{p,G} \cdot u_G}{c_{p,GS}} \frac{\partial T_{GS}}{\partial x} + \frac{1}{c_{p,GS}} \cdot \frac{\partial}{\partial x} \left(\lambda_{S,eff} \cdot \frac{\partial T_{GS}}{\partial x} \right) - \\ & \frac{\epsilon_{bed}}{c_{p,GS}} \cdot \frac{2}{R_R} \cdot h_{GW} \cdot (T_{GS} - T_W) + \frac{1 - \epsilon_{bed}}{c_{p,GS}} \cdot \rho_{cat} \cdot \phi_{cat} \cdot \nu_{\text{H}_2\text{O}} \cdot r_{rxn} \cdot (-\Delta H_R) - \\ & \frac{1 - \epsilon_{bed}}{c_{p,GS}} \cdot \rho_{ads} \cdot \phi_{ads} \cdot k_{LDF} \cdot (q_{eq} - q) \cdot (\Delta H_{ads}) \end{aligned} \quad (5.3.11)$$

The heat transfer coefficient can be obtained from the Gnielinski (2010) correlation for spherical particles:

$$Nu = (1 + 1.5 \cdot (1 - \epsilon_{bed})) \cdot \left(2 + \left((0.664 \cdot Re^{1/2} \cdot Pr^{1/3})^2 + \left(\frac{0.037 \cdot Re^{4/5} \cdot Pr}{1 + 2.443 \cdot Re^{-1/10} \cdot (Pr^{2/3} - 1)} \right)^2 \right)^{0.5} \right) \quad (5.3.12)$$

The boundary conditions for this case are of the first type at $x=0$ with the inlet temperature, due to the low thermal conductivity of the fixed bed, bed and zero slope at $x=L$ for the reaction step. The boundaries are reversed for the regeneration step. Furthermore, the equations are presented for a non-adiabatic case. For adiabatic operation the exchange term with the wall is eliminated.

5.3.3. Velocity Profile

In Section 5.3.1.2, it is to be noted that the velocity cannot be simply taken out of the derivative in Eqs. (5.3.6,5.3.7). For the cases where changes in velocity are only due to thermal expansion, this can usually be done, since the terms cancel out in the derivation. Nonetheless, for the case of adsorption this is not so. By summing the component balances the following equation is obtained:

$$\frac{\partial C_T}{\partial t} = -\frac{\partial}{\partial x} (u_G \cdot C_T) - \frac{1 - \epsilon_{bed}}{\epsilon_{bed}} \rho_{ads} \cdot \phi_{ads} \cdot k_{LDF} \cdot (q_{eq} - q) \quad (5.3.13)$$

By applying the ideal gas law, the total concentration can be expressed in terms of the pressure of the system and its temperature. In addition, the pressure drop encountered for the worst case was of 200 mbar, and thus, neglecting the pressure drop, the following implicit equation for the gas velocity can be obtained:

$$-\frac{P}{T^2 \cdot R} \cdot \frac{\partial T}{\partial t} = u_G \cdot \frac{P}{T^2 \cdot R} \cdot \frac{\partial T}{\partial x} - \frac{P}{T^2 \cdot R} \cdot \frac{\partial u_G}{\partial x} - \frac{1 - \epsilon_{bed}}{\epsilon_{bed}} \cdot \rho_{ads} \cdot \phi_{ads} \cdot k_{LDF} \cdot (q_{eq} - q) \quad (5.3.14)$$

The boundary condition is of the first type and equivalent to the inlet gas velocity at $x = 0$ for the reaction step and at $x = L$ for the regeneration step

5.4. Numerical Methods

5.4.1. Cyclic Steady-State

In the previous section, the models for the reaction step and the regeneration step were presented. However, modeling just one step following the other is not enough.

It is necessary to calculate the CSS defined as the process state where the conditions at the start and the end of the cycle comprising reaction and regeneration are identical.

Several methods to calculate the CSS exist; in this work the direct substitution and the full discretization approach were employed.

5.4.1.1. Direct Substitution

The direct substitution (DS) method consists firstly of the discretization in the spatial domain, which turns the partial differential equations (PDEs) from Section 5.3 into ordinary differential equations (ODEs), which can then be integrated using any time-stepping scheme. To calculate the CSS, the reaction and regeneration step are simulated sequentially, with the results at the end of the previous half cycle used as the initial value for the next iteration. For the variable vector this can be represented as:

$$\Psi_{rxn}(t_{rxn}) = \Psi_{reg}(t_{rxn}) \quad \wedge \quad \Psi_{rxn}(0) = \Psi_{reg}(t_{rxn} + t_{reg}) \quad (5.4.1)$$

The point where the error is calculated was chosen to be the middle of the reaction step. The error is thus defined as:

$$error = \frac{\left[\sum_x \sum_{\Psi} (\Psi_{cycle_n}(t = t_{rxn}/2) - \Psi_{cycle_{n-1}}(t = t_{rxn}/2))^2 \right]^{0.5}}{N_x \cdot N_{\Psi}} \quad (5.4.2)$$

and the simulation is run until the tolerance for the defined error is met.

5.4.1.2. Full Discretization

In the full discretization (FD) approach, as the name indicates, the PDEs are discretized in both the spatial and time domain as shown in Figure 5.2.

The cyclic behavior is enforced by:

$$\Psi(0, X) = \Psi(t_{reg} + t_{rxn}, x) \quad \wedge \quad \Psi_{n_t=1, n_x} = \Psi_{n_t=N_t, n_x} \quad (5.4.3)$$

The resulting set of non-linear equations can be solved by any zero-value problem solver.

5.4.2. Optimization

For the optimization of the CSS, three main approaches may be used: black-box, equation based, or tailored (Jiang et al. 2003), the choice being dependent on the method used to calculate the CSS (Logist et al. 2011).

For DS, the black-box approach is more suitable, due to the fact that the CSS can be calculated independently in each optimization step. This approach is robust and can deal with complex problems. Nonetheless, this comes at the price of high computation costs.

For FD, an equation-oriented method is more suitable, since the calculation of the CSS and the optimization has to be performed simultaneously. This approach is

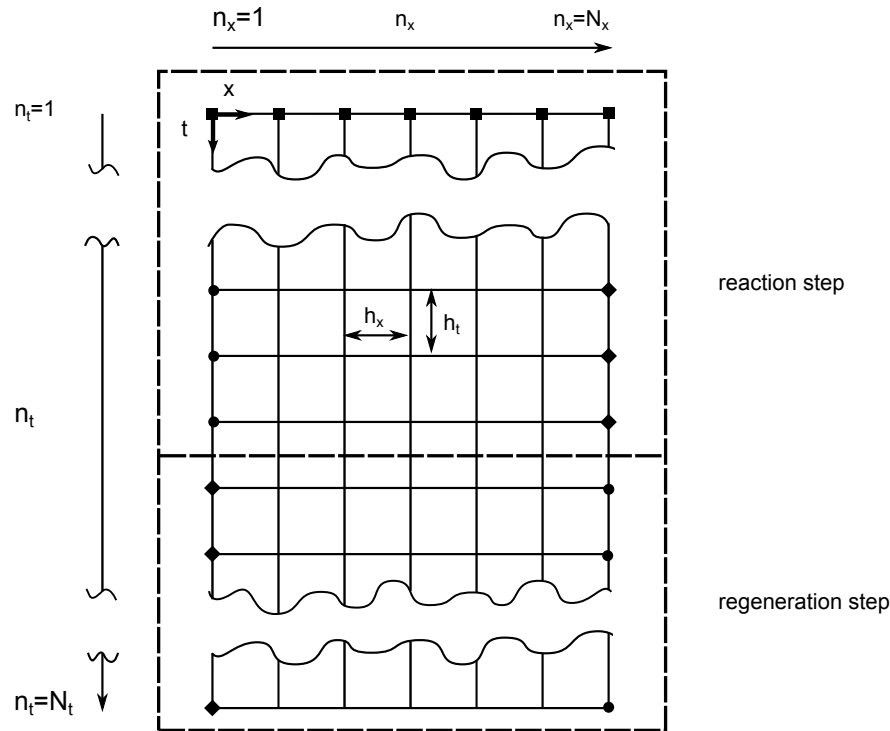


Figure 5.2.: Discretization mesh for the FD approach

efficient for relatively simple problems, but can become unstable for complex systems. To overcome this shortcoming, tailored approaches can be used.

As it will be seen in Sect. 5, the DS method delivered better results, and therefore only the black-box approach will be used. Due to the complex interactions that were revealed during the simulation stages, it was observed that the possible existence of several local optima was very likely. The selected solver was the Nonlinear Optimization by Mesh Adaptive Direct Search NOMAD (Audet et al. 2015; Le Digabel 2011), provided by the OPTI Toolbox in MATLAB® (Currie and Wilson 2012). This solver is based on a Mesh Adaptive Direct Search (MADS) algorithm (Audet and Dennis 2006; Audet et al. 2008b) and is applied to solve global non-linear problems. In addition, the application of a Variable Neighborhood Search (VNS) as a global search strategy can be used as an additional tool. A detailed explanation of this algorithm can be found elsewhere (Audet et al. 2015; Audet and Dennis 2006; Audet et al. 2008b; Le Digabel 2011).

5.5. Results

5.5.1. Calculation of the CSS

To compare the two different approaches of calculating the CSS, the system was simulated using the set of parameters presented in Table 5.2. For the DS and FD, 60 discretization points in the spatial domain were used, with an upwind scheme. The number of discretization points was chosen as a compromise between numerical diffusion and computation time. Since the numerical diffusion occurs only in the initial

Table 5.2.: Parameters for the CSS Simulation

Parameter	Reaction Step	Regeneration Step
Geometric Parameters		
L_R / m		1.0
D_R / m		0.06
ϕ_{cat} / -		0.5
Operational Parameters		
t_{step} / s	200	800
$y_{CO_2,inlet}$ / -	0.5	0
$y_{H_2,inlet}$ / -	0.5	0
$y_{CO,inlet}$ / -	0	0
$y_{H_2O,inlet}$ / -	0	0
$y_{N_2,inlet}$ / -	0	1
$T_{G,inlet}$ / °C	250	250
$T_{GS,initial}$ / °C	250	250
T_W / °C	250	250
P / Pa	3E05	3E05
u_{inlet} / m s ⁻¹	0.2	-0.75

stages, i.e. first residence time, for both the reaction and regeneration steps and those account for not more than 5% of the complete cycle, it was deemed adequate to sacrifice resolution in that 5% for a fast computation time. In the remaining 95% 60 points give the same accuracy as 400 or more points and as it can be seen later, the results depict all the expected physical behaviors. For the DS, MATLAB®'s ode15s solver used 472 points for the complete cycle, while for the FD, 200 points were used in the time domain. The results are presented in Figure 5.3. The difference in discretization points in the time domain for the two schemes was due to computation limitations in the FD approach.

As it can be seen, the resolution obtained with the DS approach was better than that of the FD, for a fraction of the calculation time, 15 s vs 900 s, and that the sharp front present in this kind of system was simulated with adequate resolution with only 60 points. Although the FD approach could be improved by using other discretization techniques, it was deemed that the infrastructure provided by the DS method, in addition to the simplicity of using a solver like MATLAB®'s ode15s was more appropriate for carrying out the optimization.

5.5.2. Analysis of System

In the previous section, only one of the results obtained was presented. In this section, the other profiles obtained at the CSS are presented and analyzed to give a better impression on the physical behavior of the system and the complexities that can be encountered.

In Figure 5.4, the profiles of the molar fractions for both products are presented,

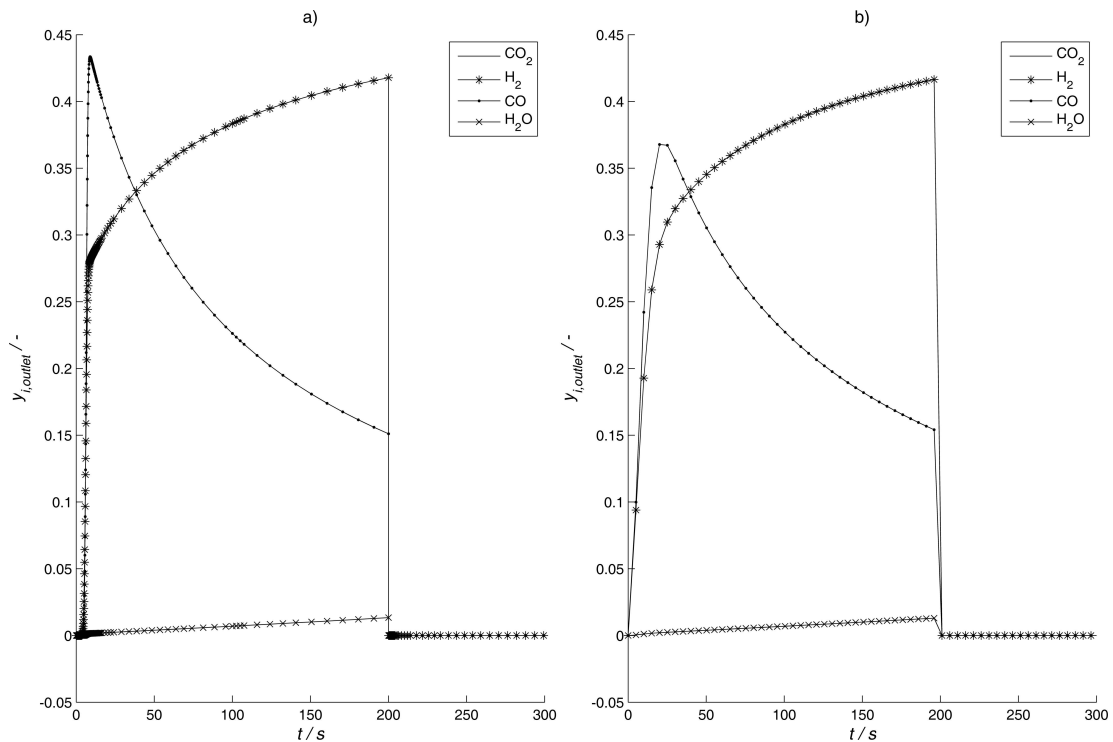


Figure 5.3.: Outlet molar fractions as function of time for: a) Direct Substitution b) Full Discretization

for carbon monoxide, it can be seen that during the whole reaction step (0-200 s), the molar fraction is well above the equilibrium value (0.05) which shows the effect of the adsorptive functionality and the displacement of the equilibrium to more favorable conditions. This can also be observed in the outlet molar fraction profiles presented in Figure 5.3. For water it can be seen that the molar fractions are very low, with values below 0.05. A maximum arises in this case where the adsorption equilibrium becomes less favorable as can also be seen in Figure 5.7. In addition, in Figure 5.4a, it can be seen that the model resolution is good enough to capture the fronts formed, even over the couple of seconds that the purge takes when the counter-current regeneration commences.

In Figure 5.5a, the concentration profile of the reactants, carbon dioxide and hydrogen, is illustrated. Since the feed is equimolar, the profiles are exactly the same. It can be seen that the behavior is opposite to that of the CO profile, with greater reactant consumption at first, which then decreases with time leading to higher reactant concentrations. In Figure 5.5b, the nitrogen profile is depicted. In the reaction step it is, of course, only present at the beginning, since it represents the end of the regeneration step, but it is quickly flushed out of the reactor. This characterizes the moving fronts typical for advective flows, which can also be observed at the beginning of the regeneration step. These results also indicate that the discretization resolution was adequate.

The velocity and temperature profiles are depicted in Figure 5.6. The velocity profile is normalized with respect to the inlet velocity for each step. During the reaction step it decreases along the reactor length, which is to be expected due to the reduction

5. Fixed-Bed Adsorptive Reactor

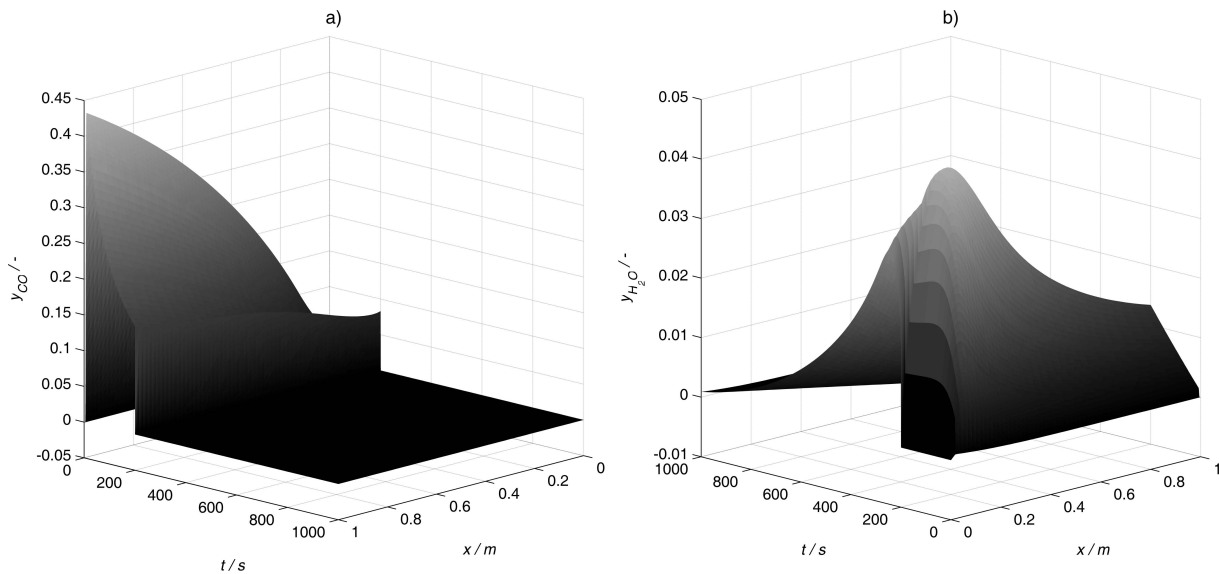


Figure 5.4.: Molar fraction profiles for the reaction products: a) Carbon monoxide b) Water

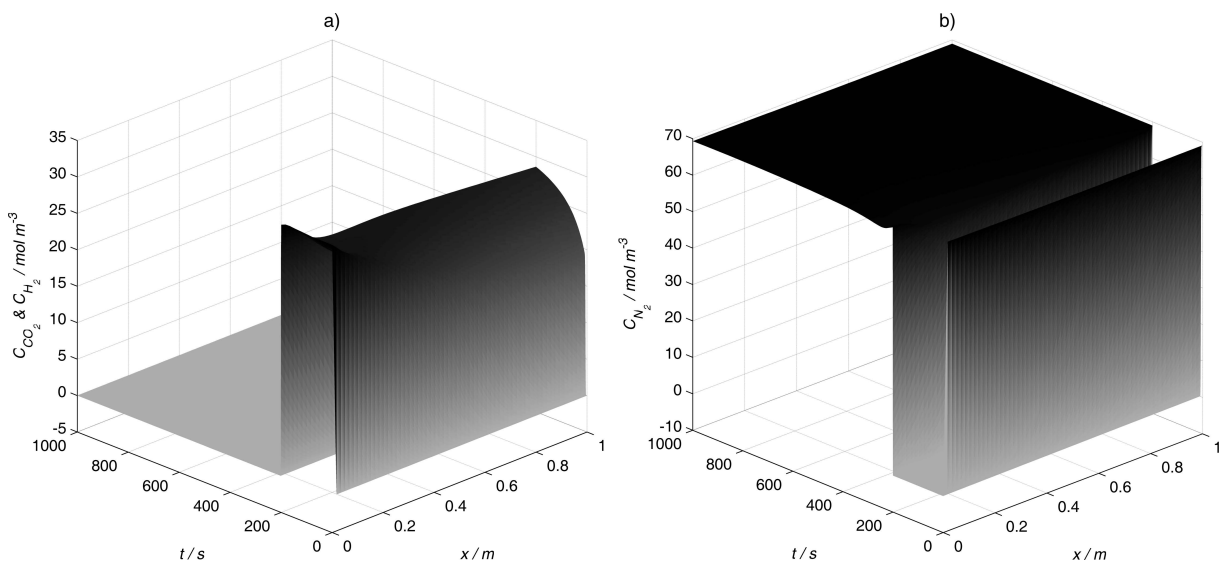


Figure 5.5.: Concentration profiles for a) reactants CO_2 and H_2 b) N_2

in number of moles in the gas phase due to adsorption, an effect that would not be detected if the velocity was not calculated explicitly. In the regeneration step, when the inert passes through the reactor for, it can be seen that the opposite behaviour occurs, i.e. increase of velocity. This is due to desorption taking place and the associated increase in the number of moles. Figure 5.6b shows the temperature profile. For the non-adiabatic case, a minimum and a maximum are observed in the reaction step. This is due to the competing effects of the endothermic reaction and the exothermic adsorption, coupled with the cooling effect of the wall at the end of the reactor. In the regeneration step, the cooling caused by the desorption of water can be observed, which helps bring the reactor temperature down for the next cycle.

Finally, the loading of the adsorbent is presented in Figure 5.7. Here it can be seen that a profile is formed along the reactor. Intuitively, it might be thought that,

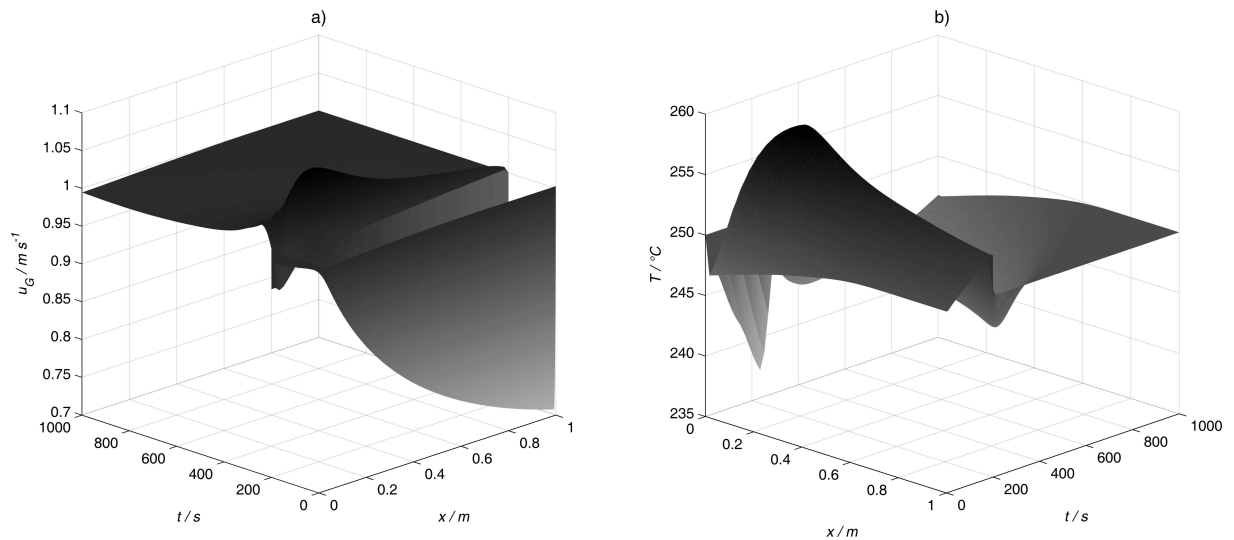


Figure 5.6.: a) Gas phase velocity profile. b) Temperature profile

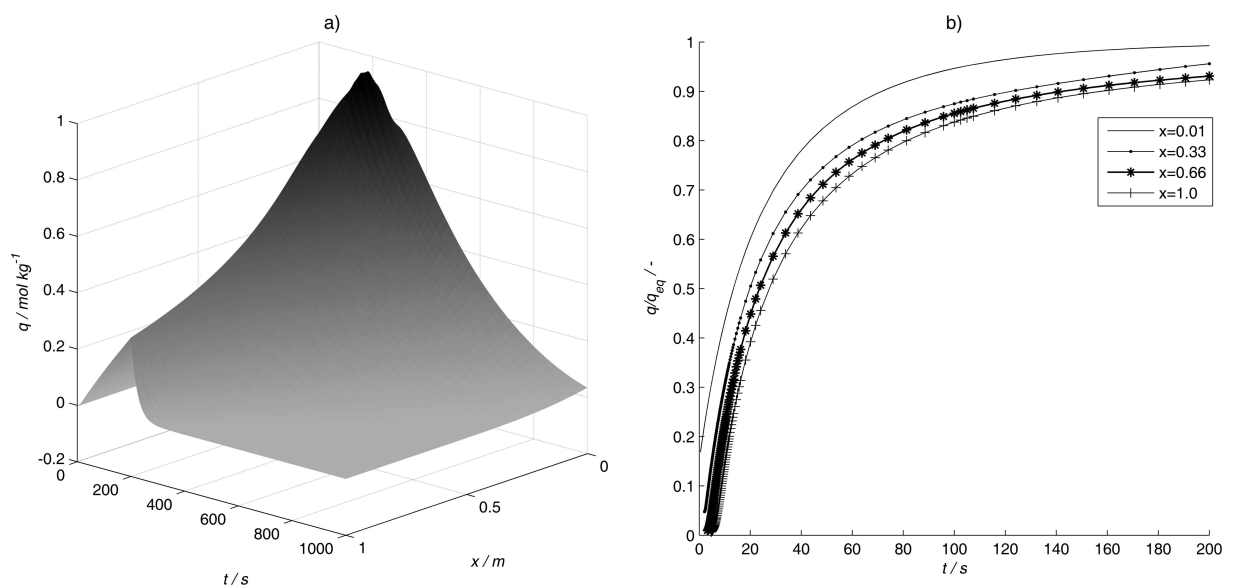


Figure 5.7.: a) Loading of the adsorbent b) Relative loading at different locations

since this profile looks similar to that of the water profile, both are in equilibrium. However, since the equilibrium loading is also a function of the temperature, the actual situation is less simple. In Figure 5.7b, this effect can be easily recognized by defining the relative loading dividing the actual loading by the equilibrium loading at each location. In addition, the loading of the adsorbent is also affected by the coupling of reaction adsorption and advection.

5.5.3. Optimization

5.5.3.1. Definition of the Optimization Problem

The optimization problem was defined as follows:

$$\max f_1(\vartheta) = \frac{\int_{t_{start}}^{t_{rxn}} u_{G,outlet} \cdot \epsilon_{bed} \cdot C_{T,outlet} \cdot dt}{L_R \cdot (t_{rxn} + t_{reg})} \quad (5.5.1)$$

s.t.

$$100 \text{ s} \leq t_{rxn} \leq 600 \text{ s} \quad (5.5.2)$$

$$100 \text{ s} \leq t_{reg} \leq 1000 \text{ s} \quad (5.5.3)$$

$$0.5 \text{ s} \leq t_{start} \leq 75 \text{ s} \quad (5.5.4)$$

$$0.5 \text{ m} \leq L_R \leq 2 \text{ m} \quad (5.5.5)$$

$$0 \leq \phi_{cat,i} \leq 1 \quad i = 1, \dots, N \quad (5.5.6)$$

$$0.05 \text{ m s}^{-1} \leq u_{G,rxn,in} \leq 0.5 \text{ m s}^{-1} \quad (5.5.7)$$

$$0.15 \leq y_{CO_2,rxn,in} \leq 0.5 \quad (5.5.8)$$

$$1 \text{ bar} \leq P \leq 30 \text{ bar} \quad (5.5.9)$$

$$200 \text{ }^\circ\text{C} \leq T_x \leq 260 \text{ }^\circ\text{C} \quad T_{G,rxn,in}, T_{N_2,reg,in}, T_{w,i} \quad (5.5.10)$$

$$\frac{y_{CO,prod} + y_{CO_2,prod}}{y_{H_2,prod} - y_{CO_2,prod}} = \frac{\int_{t_{start}}^{t_{rxn}} u_{G,outlet} (C_{CO,outlet} + C_{CO_2,outlet}) dt}{\int_{t_{start}}^{t_{rxn}} u_{G,outlet} (C_{H_2,outlet} - C_{CO_2,outlet}) dt} \geq 0.5 \quad (5.5.11)$$

$$y_{CO_2,prod} = \frac{\int_{t_{start}}^{t_{rxn}} u_{G,outlet} \cdot C_{CO_2,outlet} dt}{\int_{t_{start}}^{t_{rxn}} u_{G,outlet} \cdot C_{T,outlet} dt} \leq 0.8 \quad (5.5.12)$$

$$y_{N_2,prod} = \frac{\int_{t_{start}}^{t_{rxn}} u_{G,outlet} \cdot C_{N_2,outlet} dt}{\int_{t_{start}}^{t_{rxn}} u_{G,outlet} \cdot C_{T,outlet} dt} \leq 0.02 \quad (5.5.13)$$

$$T_{max} \leq 260 \text{ }^\circ\text{C} \quad (5.5.14)$$

The objective function represents the overall space-time yield (STY), which is commonly used for other transient processes, e.g. batch reactors, and which is basically the number of moles produced per unit time and per unit volume which is to be maximized. It is to be noted, that the objective function is based on the overall concentration and not only the concentration of CO, in this case the idea is to produce a mixture that can be used directly for the methanol synthesis. The vector of decision variables is given by:

$$\vartheta^T = (t_{rxn}, t_{reg}, t_{start}, L_R, \phi_{cat,1} \dots \phi_{cat,N}, u_{G,rxn,in}, y_{CO_2,rxn,in}, P, T_{G,rxn,in}, T_{N_2,reg,in}, T_{W,1} \dots T_{W,N}) \quad (5.5.15)$$

Of these decision variables, some are atypical: t_{start} is a time set so that the flushing of nitrogen, occurring at the beginning of the reaction step, is not included in the final

product. In addition, the reactor can be divided in N zones (5 in this case) so that the catalyst fraction and the wall temperature can be set independently in each section. For all the decision variables, a range was given based either on physical limitations or on the results obtained from previous simulations, and, unless the optimum did not hit either boundary, these remained unchanged. The reasoning for each constraint is given in the appendix (Table C.1).

In addition to these boundaries, some process related constraints were imposed. Eq. (5.5.11) represents the minimal ratio from carbon monoxide to hydrogen needed for the methanol synthesis taking into consideration the carbon dioxide present as well. It should be noted that this is not an end constraint but that it is integrated over the time to account for the high CO concentrations obtained at the start of the cycle. Eq. (5.5.12) represents the maximal amount of CO₂ allowed for the methanol synthesis. Eq. (5.5.13) is to prevent flushing of nitrogen into the final product. These constraints guarantee that the product fulfills the specifications needed for the methanol synthesis without the need for further purification steps. Finally, the maximum temperature in the reactor is set to be always below 260°C to avoid damaging the adsorbent.

For adiabatic operation it should be noted that the number of decision variables is reduced since the wall temperature is no longer a parameter.

5.5.3.2. Preliminary Optimizations

Using the available solvers in the Opti Toolbox, the model was optimized to see which of the solvers for global optimization performed better. In the end NOMAD outperformed PSWARM (particle swarm) and NLopt (non-linear optimization). In addition some other evolutionary strategies were used to look for better solutions than those provided by NOMAD. Nonetheless, none of the regions obtained provided any improvement in the results already achieved by NOMAD. Furthermore, the inclusion of the VNS functionality further improved the results by an average 55% in the objective function value. The main downside was that NOMAD was not able to deterministically find the global optimum and the optimal result varied slightly depending upon initial values. Nonetheless, in comparison with the results presented in Section 5.5.2, the objective function value could be increased by 370%.

5.5.3.3. Optimization Results

Using the insights gained in the preliminary runs, the optimization was finally performed for two different sets of initial values (appendix Table C.2) using the objective function presented in Eq. (5.5.1) and for 3 different runs. The description of the runs and their results are presented in Table 5.3 with the detailed results given in the appendix (Table C.3). In Table 5.3, the initial value given corresponds to the value of the objective function prior to the optimization.

As it can be seen, the optimizer improves the objective function drastically in all cases. However, it can also be recognized that a slight variation between the optimal values is found, although the deviation is consistent with the optimizer's documentation (Audet et al. 2015). Furthermore, for some cases, the results for the runs having a

5. Fixed-Bed Adsorptive Reactor

Table 5.3.: Optimization runs description and results

Run ID	Description	Adiabatic		Non-adiabatic	
		Initial / mol m ⁻³ s ⁻¹	Optimized (STY) / mol m ⁻³ s ⁻¹	Initial / mol m ⁻³ s ⁻¹	Optimized (STY) / mol m ⁻³ s ⁻¹
1	Variation of all decision variables	0.39	1.98	0.39	1.88
		0.43	1.77	0.43	1.94
2	Only one catalyst fraction	0.38	1.99	0.39	1.83
		0.43	1.78	0.43	1.99
3	Only one wall temperature	N.A.		0.39	1.78
				0.43	1.68

Table 5.4.: Optimization runs description and results for fixed reactor length

Run ID	Description	Adiabatic			Non-adiabatic		
		Initial / mol m ⁻² s ⁻¹	Objective function / mol m ⁻² s ⁻¹	STY / mol m ⁻³ s ⁻¹	Initial / mol m ⁻² s ⁻¹	Objective function / mol m ⁻² s ⁻¹	STY / mol m ⁻³ s ⁻¹
4	$L_R = 1\text{ m}$	0.39	1.87	1.87	0.39	2.32	2.32
		0.66	2.05	2.05	0.66	2.02	2.02
5	$L_R = 1.5\text{ m}$	0.41	2.59	1.73	0.41	2.89	1.93
		0.64	3.06	2.04	0.64	2.91	1.94
6	$L_R = 2\text{ m}$	0.42	3.13	1.56	0.42	3.47	1.74
		0.63	3.36	1.68	0.63	3.61	1.80

single catalyst fraction outperformed those of the reactor divided in 5 sections, which does not appear logical, because by having more degrees of freedom, the optimizer should be able to generate a better solution, since it would have more control over the concentration profile inside the reactor. Nonetheless, the values are very close to each other and accounting for the different starting points and the corresponding discrepancy, a clear conclusion cannot be drawn from these results.

The question then arose as to whether the objective function could be biased toward the reactor length or not. For batch processes, the STY is usually an appropriate objective function, because an increase in the reactor volume depends linearly on an increase in the productivity. However, in this case this is not true. In the preliminary studies it was noted that by increasing the reactor length, at some point the benefit one could obtain in terms of conversion started to diminish considerably. Hence, three further runs were carried out by fixing the reactor length, and modifying the objective function to:

$$\max f_2(\vartheta) = \frac{\int_{t_{start}}^{t_{rxn}} u_{G,outlet} \cdot \epsilon_{bed} \cdot C_{T,outlet} \cdot dt}{(t_{rxn} + t_{reg})} \quad (5.5.16)$$

The result obtained was then divided by the length and compared to the 3 previous runs. These results are presented in Table 5.4.

From this results it can be seen, that there was indeed a bias in the previous objective function, as it can be seen that by fixing the length, a better result was obtained for both the adiabatic and non-adiabatic cases. Particularly in the latter case, the improvement obtained was significant. In the STY optimization runs, the reactor length obtained was in between 1.3 and 1.84 m. In the new runs it can be seen that for shorter reactors, higher STY were obtained, which suggests that the new objective

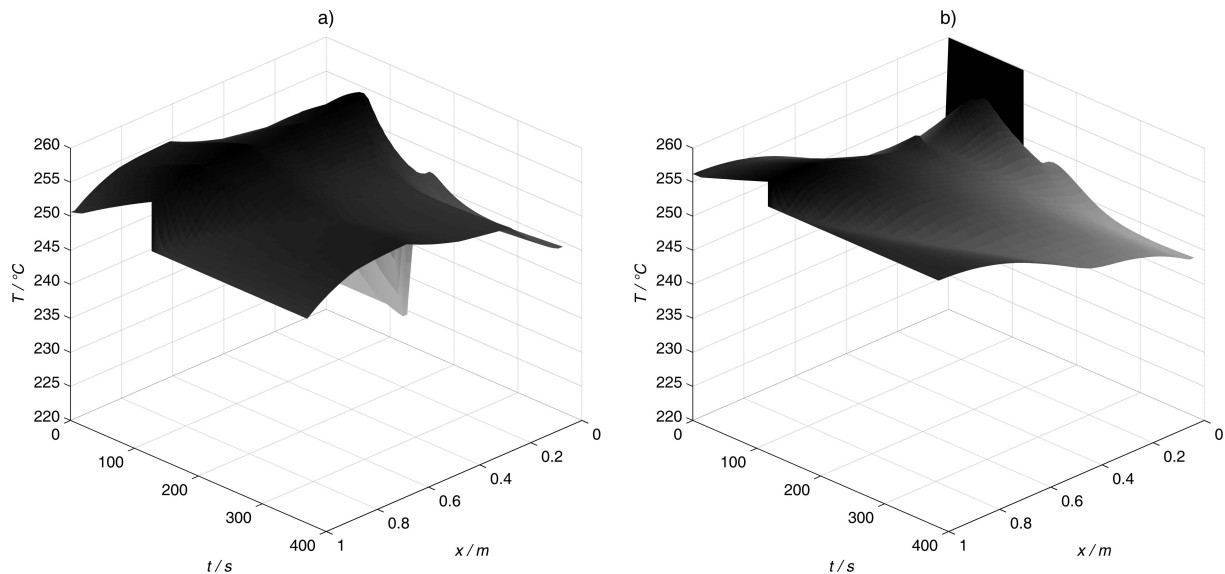


Figure 5.8.: Optimized temperature profiles. a) non-adiabatic b) adiabatic

function is more suitable for this system.

5.5.3.4. Optimized Reactor Analysis

From the optimization results the best case was found to be run 4 for the non-adiabatic case, and for the adiabatic case, although the values are pretty close, run 4 could arguably be chosen as the best result as well. In this section, the profiles obtained from this runs are investigated in more detail.

The main difference with the profiles presented in Section 5.5.2 is seen in the temperature profiles, which are presented in Figure 5.8.

It can be seen that during the reaction step, the temperature tends to remain as close as possible to the 260 °C maximum to take advantage of the faster reaction kinetics, although this is to the detriment of the adsorption capacity. However, the adsorption proved to be slower than the reaction so a full use of the capacity was in any case not possible. In addition, the catalyst distribution presented in detail in the appendix (Table C.3) varies depending on the situation examined but the main conclusion is that these changes are such as to balance the ratio of heat of reaction and heat of adsorption so that the maximal temperature of 260 °C is not violated inside the reactor. The concentration profiles are similar to those already presented in Section 5.5.2, so for the sake of conciseness they are not shown. The main conclusion that can be drawn from the concentration profiles is that for all the cases, the behavior was limited by the kinetics of adsorption for the reaction step and the kinetics for desorption in the regeneration step. In the former, a faster kinetics would allow for a larger uptake of water and therefore higher conversions of carbon monoxide could be obtained. For the latter, more rapid kinetics would allow for a faster or a more complete regeneration of the fixed-bed which would permit shorter cycle times, and thus, a higher product STY.

From the catalyst fraction results presented in the appendix (Table C.3) it can be

seen that this value ranges between 30 and 70%, with a downward tendency. The reason behind this tendency is that an increase of the adsorbent fraction along the reactor allows for a faster adsorption of water in a region where the reduction of the overall reaction rate by the reverse reaction becomes significant. Additionally, taking into account that the equilibrium between the rate of reaction and adsorption is formed closer to the reactor outlet, the increase in the adsorbent fraction allows for a compensation of the decrease in the linear driving force which is due to a lower concentration of water.

For the adiabatic case, the optimal initial temperatures are found for the case where inside the reactor the temperature does not exceed 260 °C.

Regarding the temperature distribution in the non-adiabatic case, it can be seen that an increase in the optimized wall temperature can be noticed from the reactor inlet to its outlet. Taking into account the results achieved in the analysis of the system. As it can be seen in Figure 5.8, this trend can be explained since a low wall temperature, which allows for a cooling of the inside of the reactor, is provided in a region close to the reactor inlet where the heat release by adsorption governs the temperature profile. As the system is limited by its maximal temperature, a low wall temperature near the inlet allows for a higher heat release by the adsorption and, consequently, for a higher productivity. Moving towards the outlet, as both the reaction and adsorption rates converge, the heat from reaction consumes most of the heat of adsorption and therefore it is possible to operate at higher temperatures.

5.6. Conclusions

In this work, the modeling and simulation of an adsorptive reactor for the rWGS reaction was carried out. The numerical methods for calculating the CSS were compared, giving the DS approach an edge in this instance. A more refined discretization method, especially in the time domain, could improve the performance of the FD approach, but as seen with the DS, the resolution of the profiles was adequate and the simplicity of working with an off-the-shelf time-stepping approach was deemed appropriate for this system.

Based on the CSS calculation, an optimization was carried out using the NOMAD solver. Although the solver was not able to establish a global optimum, the improvements generated from the initial solutions obtained manually were considerable reaching up to 837%. Two different objective functions were examined. The STY was found to be biased and while the solutions were good, the use of the throughput as the objective function and the posterior subsequent with respect to length outperformed the STY results.

From these results it can be concluded that this system offer excellent potential for optimization and that the NOMAD solver delivers noticeable improvement for complex objective functions. The next step would be to take advantage of the potential for optimization and to carry out an economic optimization for a larger scale system in order to benchmark it against alternative CO₂ activation processes.

Preamble

The following chapter has been published as:

Munera Parra, A.A, C. Asmanoglo, and D.W. Agar (2018): "Modeling and Optimization of a Moving-Bed Adsorptive Reactor for the Reverse Water-Gas Shift Reaction". In: *Computers & Chemical Engineering* 109, pp.203-215

The publication is partly based on Asmanoglo's calculations in his Master thesis: "Modeling and Optimization of Adsorptive Reactor Concepts for the rWGS Reaction". Conceived and directed by myself and evaluated by Prof. Agar.

The calculations for the bi-objective optimization are my own.

Abstract

In this work, a novel variant of the reverse water-gas shift reaction is proposed as a promising route to valorize CO₂ as syngas. The reactor concept used is that of an adsorptive moving-bed in order to permit low-temperature operation with high conversions and to improve upon the fixed-bed adsorptive concept previously investigated. The reactor has been modeled for several configurations and subsequently optimized. The results show that an increase up to an order of magnitude in the space-time-yield (STY) is possible by using the moving-bed configuration in comparison to fixed-bed operation. Finally, a bi-objective optimization is carried out to identify the trade-off between operating at higher STY and higher adsorbent loadings.

6

Moving-Bed Adsorptive Reactor

6.1. Introduction

Carbon dioxide concentration in the atmosphere has been steadily increasing over the past few decades. Concerns about the resultant climate change, led to the adoption of the Paris Agreement after the COP21 meeting (UNFCCC. Conference of the Parties (COP) 2015). The main proposed goal is to minimize CO₂ emissions in order to keep the mean global temperature increase below 2 °C. To accomplish this objective, it is clear that drastic reductions must be achieved in all CO₂-emitting industries. Since CO₂ has become to be regarded as an unwanted by-product, alternative CO₂-free technologies have started to emerge.

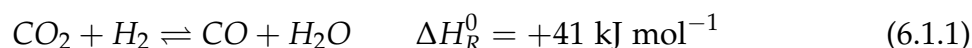
Nonetheless, when CO₂ generation is unavoidable, it is crucial to address what needs to be done with the CO₂ produced. Alternatives such as Carbon Capture and Storage (CCS) have been proposed as solution. However, the feasibility of CCS, as well as its public acceptance, still represent major hurdles for its adoption on a large-scale. The main challenges for CCS are still: (i) reduction of costs, (ii) understanding of long term risk factors and (iii) quantification and understanding of reservoir options (Muradov and Veziroglu 2008; Muradov 2017).

Should CO₂ be used as a chemical feedstock, it has been estimated that a 10% recycle of the total emissions would be accomplished and therefore, the net amount of CO₂ produced would be reduced correspondingly (Aresta 2010). Carbon Capture and Utilization (CCU) is the term used to describe this approach. In addition, some authors have mentioned the possibility of joint sequestration and utilization (CCUS) as another viable alternative (Hasan et al. 2015).

The main issue with utilizing CO₂ is that it is a chemically inert molecule and its activation for use as feedstock is a non-trivial process. A recent review by Klankermayer et al. (2016) elucidates the various transformations for CO₂ and classifies them according to the reduction level and the bond-forming processes. From an application point of view, it divides them into high-volume and high-value products.

For the sake of reducing emissions it is clear that high-volume products are of interest. These include methanol, formaldehyde and formic acid derivatives. These products can not only be used as base chemicals, but they also have potential as energy carriers or storage systems. The common denominator in these products is the

need for hydrogen in the reactions involved. At the core of these reaction networks, the reverse water-gas shift (rWGS) reaction is encountered:



This reaction can be used to activate CO_2 using hydrogen obtained, for instance, from electrolysis using renewable energy, or, in the worst-case scenario, using "CO₂-low" hydrogen, such as that obtained from the pyrolysis of methane, or through electrolysis using a mix of electricity sources. The more reactive product CO can be mixed with excess hydrogen in any given ratio to obtain syngas, which is perhaps one of the most versatile chemical feedstocks. Syngas can namely be converted into methanol, which can itself be further processed to diverse chemicals or olefins; it can be used in the Fischer-Tropsch synthesis for fuels, amongst many other uses (Baliban et al. 2012).

Industrially, the rWGS reaction has not been used for this purpose and is mostly used to control the C/H ratio in gas mixtures. The main challenge this reaction faces is the unfavorable equilibrium. For reasonable conversions, temperatures above 1073K are required ($X_{eq}(1073 \text{ K}) = 0.51$), and, since the reaction is endothermic, this means that a high temperature heat source must be available. The feasibility of this reaction has thus always been subject to question. As an alternative, low-temperature rWGS suffers from a very unfavorable equilibrium, but at temperatures around 523 K, several downstream heat sources can be exploited to provide the necessary heat of reaction. To circumvent the equilibrium challenge, an adsorptive reactor has been proposed as a solution (Agar 2005). By adsorbing the water vapor formed, the equilibrium can be shifted to the product side. In addition, the exothermicity of the adsorption provides heat for the reaction of the same order of magnitude as the reaction enthalpy (Simo et al. 2009), thereby minimizing the need for external heat input.

For adsorptive reactors, the conventional reactor concept is that of a fixed-bed, for the rWGS, preliminary studies (Jung et al. 2013) as well as theoretical optimizations (Munera Parra et al. 2017) have been performed to demonstrate its feasibility for the rWGS. Moreover, adsorptive reactors can be found in other applications such as the Claus and Deacon process (Hussainy and Agar 2016), or for sorption enhanced dry reforming (Iyer et al. 2017).

Although this concept is very promising, the inherently transient operation that is required for the fixed-bed configuration makes the concept somewhat unwieldy. In addition, the regeneration of the adsorbent has to be carried out at the same equipment as the reaction, which limits its design operational flexibility to a certain degree. Contrary to other applications, where the improvement in performance of the fixed-bed reactor is performed by using a simulated moving-bed (SMB), for this application, the proposed alternative is that of a true moving-bed reactor. A SMB is useful for cases where a breakthrough-like profile is formed inside the fixed-bed reactor and thus, circulating that breakthrough through different beds can maximize the efficiency of the system. However as seen in the fixed-bed study performed before (Munera Parra et al. 2017), this breakthrough phenomenon is not present and thus the use of a SMB would present no advantage over the fixed bed.

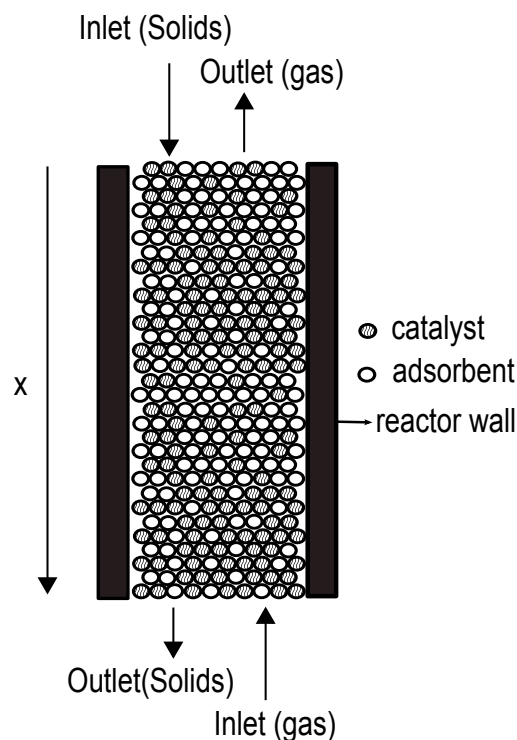


Figure 6.1.: Moving-bed reactor concept

The concept proposed in this work is a moving-bed reactor, sometimes called true moving-bed reactor to differentiate it from the SMB. This reactor is depicted in Figure 6.1. The reactor shown is in counter-current configuration where the gas enters the reaction from the bottom and encounters a downward, continuous flow of solids, which are fed through the top of the reactor. The reactor can be operated co-currently, where the gas and the solids are both fed from the top.

The moving-bed configuration offers several advantages; the first one is that it is a continuous process which can be operated in steady-state, reducing the need for switching and transient operation. Once the reactor is started up, concentration and temperature profiles are formed and become time invariant, this simplifies the numerical calculations compared with fixed-beds or SMB. Moreover, compared to those concepts, the regeneration of the adsorbent is completely decoupled from the unit operation in which the reaction also takes place. Thus, an additional unit could be designed and optimized for the adsorbent regeneration, this could be done either in another moving-bed or in batch reactors. The main disadvantage of moving-bed reactors is the necessary handling of the solids, which is not the case in fixed-beds and SMB. However, as will be shown in this work, the advantages that can be gained from this configuration outweigh this shortcoming.

The modeling of moving bed reactors is non-trivial, and in some cases even multiple steady-states can arise, even for allothermic processes (Munera Parra et al. 2016). In addition, a rigorous optimization of such reactors is needed, since the results obtained cannot always be deduced intuitively, as will be manifest from the following sections.

In this work, a lab-scale reactor for the low-temperature rWGS is considered as the case-study. The aim is to generate a syngas with the specifications required for

Table 6.1.: Dimensionless variables

Variable	Reference value	Dimensionless form
x	L_R	$X = \frac{x}{L_R}$
u	$u_0 = u_{G,inlet}$	$U = \frac{u}{u_0}$
t	$\tau_0 = \frac{L_R}{u_0}$	$\tau = \frac{t}{\tau_0}$
T	$T_0 = T_{G,inlet}$	$\theta = \frac{T}{T_0}$
c	$c_0 = \frac{P}{RT_0}$	$C = \frac{c}{c_0}$
q	$q_0 = q_{eq}(P, T)$	$Q = \frac{q}{q_0}$

the methanol synthesis, which are given in the optimization problem definition in Section 6.4.2.1. The moving-bed reactor can be set up to operate with different catalyst to adsorbent ratios, where the catalyst is taken as an industrial Cu/ZnO catalyst and the adsorbent employed is zeolite 3A.

6.2. Mathematical Modeling

To model the moving-bed, the axial coordinate is first defined. For all simulations, the origin is at the top of the reactor, where the solids are introduced. In order to facilitate the numerical procedures and to facilitate the optimization, the equations were derived and then transformed into their dimensionless forms; the dimensionless variables are defined in Table 6.1. In addition, the dimensionless numbers resulting from this procedure are presented in Table 6.2.

All equations were derived from the differential balances. However, for the sake of conciseness, only the final equation is presented. The assumptions for the derivation of the model include plug flow behavior for both the solid and gas phases. For the gas phase, this is a widely adopted and reasonable assumption. For the solid phase, with proper design of the solid handling, it is certainly possible to achieve such flow characteristics, which is also expedient, since it will allow better reactor performance. The axial dispersion can be neglected, since the Péclet numbers were found to be of the order of magnitude of 1000. Additionally, radial heat and mass transfer are neglected due to the $L/D/D_p$ ratios used in the simulations. Furthermore, the model was first developed heterogeneously for both mass and heat transfer. However, preliminary simulations revealed that the mass resistances between the reaction medium and the catalyst and within the latter were negligible hence simplifying the molar balance to its pseudo-homogeneous form.

The resulting model equations are presented in Table 6.3. It should be noted that the model is contrived in such a way that the change in velocity in the gas phase due to adsorption is considered. Although not commonly considered for reasons of simplicity, changes in the gas velocity are of major importance, since they are coupled with the residence time, and hence have a considerable effect on the simulation re-

Table 6.2.: Dimensionless numbers

$$St_{m,ads,i} = \frac{1-\varepsilon_{bed}}{\varepsilon_{bed}} \cdot \rho_{ads} \cdot \phi_{ads} \cdot \frac{q_{ads,eq,0}}{c_0} \cdot k_{LDF,ads,i} \cdot \tau_0$$

$$Da_i = \frac{1-\varepsilon_{bed}}{\varepsilon_{bed}} \cdot \rho_{cat} \cdot \phi_{cat} \cdot \frac{v_i \cdot r_{rxn}}{c_0} \cdot \tau_0$$

$$St_{h,GW} = \frac{1}{c_0 \cdot c_{p,G} \cdot u_0} \cdot \frac{4 \cdot L_R}{D_R} \cdot h_{h,GW}$$

$$St_{h,GS} = \frac{L_R}{c_0 \cdot c_{p,G} \cdot u_0} \cdot \frac{1-\varepsilon_{bed}}{\varepsilon_{bed}} \cdot \left(\phi_{ads} \cdot \frac{A_{ads}}{V_{ads}} \cdot h_{h,G,ads} + \phi_{cat} \cdot \frac{A_{cat}}{V_{cat}} \cdot h_{h,G,cat} \right)$$

$$Pe_{h,S} = \frac{(1-\varepsilon_{bed}) \cdot c_{p,S} \cdot u_{S,0} \cdot L_R}{\lambda_{S,eff}}$$

$$\kappa_S = \frac{1}{(1-\varepsilon_{bed}) \cdot c_{p,S} \cdot u_{S,0} \cdot L_R} \frac{d\lambda_{S,eff}}{dX}$$

$$St_{h,SW} = \frac{32 \cdot \lambda_{S,eff}}{c_{p,S} \cdot u_{S,0}} \cdot \frac{L_R}{D_R^2}$$

$$St_{h,SG} = \frac{L_R}{c_0 \cdot c_{p,S} \cdot u_{S,0}} \cdot \frac{1-\varepsilon_{bed}}{\varepsilon_{bed}} \cdot \left(\phi_{ads} \cdot \frac{A_{ads}}{V_{ads}} \cdot h_{h,G,ads} + \phi_{cat} \cdot \frac{A_{cat}}{V_{cat}} \cdot h_{h,G,cat} \right)$$

$$\Delta\theta_{ad,rxn} = \frac{\phi_{cat} \cdot \rho_{cat} \cdot r_{rxn} \cdot (-\Delta H_{rxn}) \cdot L_R}{c_{p,S} \cdot u_{S,0}} \cdot \frac{1}{T_0}$$

$$\Delta\theta_{ad,ads} = \frac{\phi_{ads} \cdot \rho_{ads} \cdot k_{LDF,ad,H_2O} \cdot q_0 \cdot (-\Delta H_{ads}) \cdot L_R}{c_{p,S} \cdot u_{S,0}} \cdot \frac{1}{T_0}$$

sults. The equation to solve for the gas velocity can be derived from the overall molar balance. To be able to solve this equation, it is necessary to assume both the ideal gas law and negligible pressure changes. Both assumptions can be justified for the gases studied. The compressibility factor was calculated up to 30 bar, and the result was always above 0.99 and below 1.02. The pressure drop was also calculated, and, in the worst case, it was found to be 200 mbar which, as will be seen later, is also negligible for the higher pressures favored.

To complete the model, the equations necessary to ascertain the reaction rates, adsorption rates and the transport coefficients required are given below.

To calculate the adsorption rate, the Linear Driving Force (LDF) approach was used. For the particular system studied, surface and Knudsen diffusion can be neglected (Simo et al. 2009). The rate coefficient can thus be calculated as:

$$\frac{1}{k_{LDF}} = \frac{D_p}{6 \cdot k_G} \cdot \frac{q_{eq,H_2O} \cdot \rho_{ads}}{c_{G,H_2O}} + \frac{D_p^2 \cdot \tau_{ads}}{60 \cdot \varepsilon_{ads} \cdot D_{macropore}} \cdot \frac{q_{eq,H_2O} \cdot \rho_{ads}}{c_{G,H_2O}} \quad (6.2.1)$$

To calculate the equilibrium, a Langmuir-isotherm is used (Simo et al. 2009):

$$q_{eq,H_2O} = q_{s,H_2O}(T) \frac{b(T) p_{H_2O}}{1 + b(T) p_{H_2O}} \quad (6.2.2)$$

$$b(T) = \frac{b_\infty}{\sqrt{T}} \exp\left(\gamma \frac{T_0}{T}\right) \quad (6.2.3)$$

Table 6.3.: Model equations for the moving-bed reactor

Component molar balance	$0 = \frac{d}{dX} (U_G \cdot C_{G,i}) - St_{m,ads,i} \cdot (Q_{ads,eq,i} - Q_{ads,i}) + Da_i$ $C_{G,i} _{X=1} = C_{G,i,inlet}$
Global molar balance	$0 = U_G \cdot \frac{1}{\theta_G^2} \cdot \frac{d\theta}{dX} - \frac{1}{\theta_G} \cdot \frac{dU_G}{dX} - St_{m,ads,H_2O} \cdot (Q_{ads,eq,H_2O} - Q_{ads,H_2O})$ $U_G _{X=1} = 1$
Adsorbent Loading	$0 = -\frac{dQ_{H_2O}}{dX} + Da_{ads} \cdot (Q_{ads,eq,H_2O} - Q_{ads,H_2O})$ $Q_{H_2O} _{X=0} = Q_{H_2O,inlet}$
Gas phase temperature	$0 = -U_G \cdot \frac{d\theta_G}{dX} - \frac{St_{h,GW}}{C_G} \cdot (\theta_G - \theta_W) - \frac{St_{h,GS}}{C_G} \cdot (\theta_G - \theta_S)$ $\theta_G _{X=1} = \theta_{G,inlet}$
Solid phase temperature	$0 = -\frac{d\theta_S}{dX} + \frac{1}{Pe_{h,S}} \cdot \frac{d^2\theta_S}{dX^2} + \kappa_S \cdot \frac{d\theta_S}{dX} + St_{h,SW} \cdot (\theta_W - \theta_S) + St_{h,SG} \cdot (\theta_G - \theta_S)$ $+ \Delta\theta_{ad,rxn} + \Delta\theta_{ad,ads} \cdot (Q_{ads,eq,H_2O} - Q_{ads,H_2O})$ $\theta_S _{X=0} = \theta_{S,inlet} \quad \left. \frac{d\theta_S}{dX} \right _{X=1} = 0$

Table 6.4.: Parameters for the Langmuir isotherms

τ_{ads} /-	b_∞ / $K^{0.5} Pa^{-1}$	γ /-	q_{0,H_2O} / $mol kg^{-1}$	δ /-	T_0 / K
2	5.3126E-10	23.235	10.7446	0.68792	300

$$q_{s,H_2O} = q_{0,H_2O} \exp \left(\delta \left(1 - \frac{T_0}{T} \right) \right) \quad (6.2.4)$$

The pertinent adsorption parameters are given in Table 6.4. The kinetic model for the rWGS reaction can be described by the elementary steps which take place at the catalyst's surface. However, in general a detailed kinetic model is not required to describe the overall reaction rate with adequate accuracy. As stated by Adams and Barton (2009) a simple power law model is favored in most applications. The reaction rate is calculated as:

$$r_{rxn} = \left(8.22 \cdot 10^4 \text{ mol kg}^{-1} \text{ s}^{-1} \exp \left(\frac{-47.4 \text{ kJ mol}^{-1}}{RT(K)} \right) \right) \left(y_{CO_2} y_{H_2} - \frac{y_{CO} y_{H_2O}}{K_{eq}} \right) F_p \quad (6.2.5)$$

Table 6.5.: Catalyst and adsorbent properties

Property	Units	Catalyst ¹	Adsorbent ²
Diameter (D)	/ mm	1.6	3.57
Density (ρ)	/ kg m ⁻³	2656	1199.3
Porosity (ϵ)	/ -	0.55	0.37
Heat capacity (c_p)	/ J K ⁻¹ kg ⁻¹	687	1045
Thermal Conductivity (λ)	/ J K ⁻¹ m ⁻¹ s ⁻¹	1.163	0.12

This rate is valid for temperatures between 120-300 °C, and with the introduction of a correction term for higher pressures:

$$F_p = \left(\frac{P(\text{Pa})}{10^5 \text{Pa}} \right)^{0.5 - \frac{P(\text{Pa})}{250 \times 10^5 \text{Pa}}} \quad (6.2.6)$$

The validity in terms of pressure is increased up to 30 atm. The equilibrium constant is given by:

$$K_{eq}(T) = \exp \left(4.33 - \frac{4577.8 \text{ K}}{T} \right) \quad (6.2.7)$$

The heat transfer coefficients can be found using the correlation given by Gnielinski, assuming spherical particles (Gnielinski 2010):

$$Nu = (1 + 1.5 (1 - \epsilon_{bed})) \left(2 + \left(\left(0.664 \text{Re}^{1/2} \text{Pr}^{1/3} \right)^2 + \left(\frac{0.037 \text{Re}^{4/5} \text{Pr}}{1 + 2.443 \text{Re}^{-1/10} (\text{Pr}^{2/3} - 1)} \right)^2 \right)^{0.5} \right) \quad (6.2.8)$$

The gas-wall heat transfer is given by (Li and Finlayson 1977):

$$Nu = 0.19 \cdot \text{Re}^{0.79} \text{Pr}^{1/3} \quad (6.2.9)$$

The gas properties required, i.e. viscosity, thermal conductivity and diffusion coefficients, were calculated using standard mixture properties for a multicomponent gas (Poling et al. 2001). The solid properties for the adsorbent and catalyst are given in Table 6.5. The properties of the bed are weighted according to their respective fractions.

6.3. Numerical Methods

To solve the model equations presented above in the counter-current case, the governing equations were discretized using a first-order upwind scheme to reduce the ODE system into a set of non-linear equations, which could be solved using a zero-value

¹(Adams and Barton 2009)

²(Simo et al. 2009)

problem solver. In the co-current case, the ODE's can be solved using an off-the-shelf time stepping scheme. The models were implemented in MATLAB®.

For the discretization, a mesh independence study was carried out to determine the minimum number of discretization points, for this case the minimum number of discretization points was found 60 points. This value was used for the model analysis in Section 6.4.1. For the optimizations in Section 6.4.2, the final number amount of points was chosen conservatively as 200 to account for the possibility of stiffer solutions during the optimization. Furthermore, to speed up the calculations, the sparsity structure of the Jacobian was given to the solver.

For the optimization, although a derivative based optimizer could have been utilized using the direct solution of the zero-value problem, a derivative-free optimizer was utilized instead. This was done in order to compare the results obtained with those of a previous study in a fixed-bed reactor (Munera Parra et al. 2017), and thus to avoid having the optimizer be an uncertainty factor. The solver used was NOMAD (Audet et al. 2015; Le Digabel 2011), which is part of the OPTI Toolbox (Currie and Wilson 2012) available for MATLAB®. This solver is based on a Mesh Adaptive Direct Search (MADS) algorithm (Audet and Dennis 2006; Audet et al. 2008b) and is applied to solve global non-linear problems. A Variable Neighborhood Search (VNS) is also available as a global search strategy. In addition, the algorithm BiMADS is available which can be used for bi-objective optimization (Audet et al. 2008a). A detailed explanation of the algorithms can be found elsewhere (Audet et al. 2015; Audet and Dennis 2006; Audet et al. 2008a,b; Le Digabel 2011)

6.4. Results

The model described in Section 6.2 was implemented in MATLAB® as a first step to gain insight into the underlying system behavior for various configurations as described in the following section. Using the insights obtained, the reactor was optimized using a technical objective function.

6.4.1. Modeling and Simulation

The simulations were carried out for three cases: co-current, and two different counter-current arrangements. The parameters used for the simulations are presented in Table 6.6 and the results are discussed in the following sections.

6.4.1.1. Co-Current

Although it could be deduced a priori that the co-current option would perform worse than the counter-current set-up due to the lower driving force for adsorption, some useful insights into the behavior of the system can be gained from the results of co-current simulations. From the parameters given in Table 6.6, it can be noted that the gas and solid temperatures are different. This was done intentionally in order to observe the convergence of the temperature profiles. The remaining parameters were

Table 6.6.: Parameters for simulations

Parameter	Co-current	Counter-current case 1	Counter-current case 2
Geometric Parameters			
L_R / m	1	1	3.0
D_R / m	0.06	0.06	0.06
$\phi_{cat} / -$	0.5	0.5	0.5
Operational Parameters			
$y_{CO_2,inlet} / -$	0.5	0.5	0.5
$y_{H_2,inlet} / -$	0.5	0.5	0.5
$y_{CO,inlet} / -$	0	0	0
$y_{H_2O,inlet} / -$	0	0	0
$T_{G,inlet} / K$	513	523	523
$T_{GS,initial} / K$	523	523	523
T_W / K	523	523	523
P / Pa	3E05	3E05	3E05
$u_{inlet} / m s^{-1}$	0.2	-0.2	-0.1
$u_S / m s^{-1}$	0.01	0.01	0.001

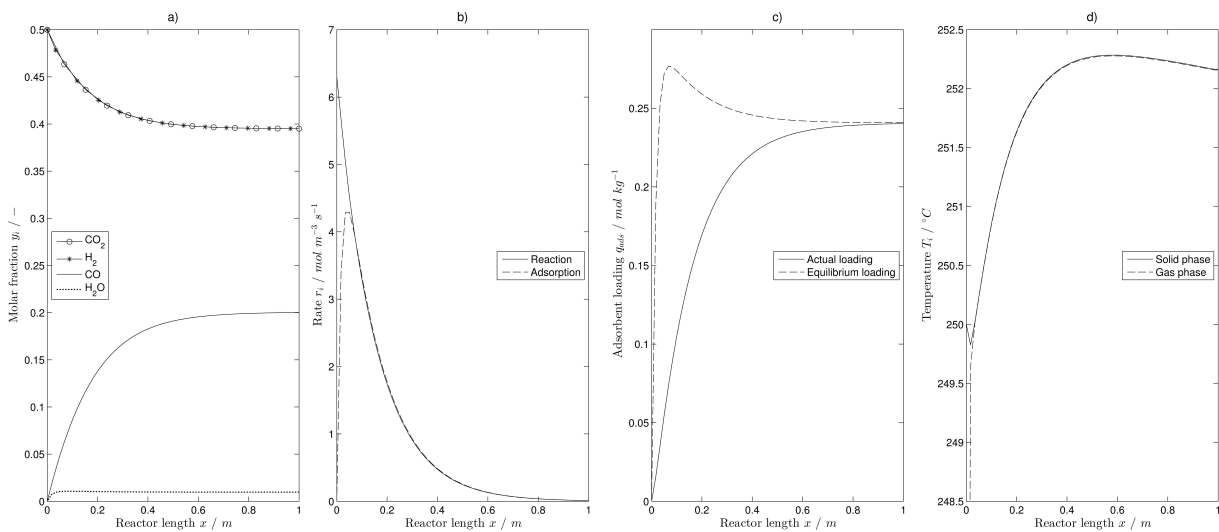


Figure 6.2.: Simulation results for the co-current moving-bed a) molar fractions b) adsorption and reaction rates c) adsorbent loading d) gas and solid temperatures

chosen for the results to be comparable with those in the fixed-bed studied previously (Munera Parra et al. 2017). The simulation results are presented in Figure 6.2.

From the mole fraction results shown in Figure 6.2a, it can be seen that only about 60% of the reactor length contributes significantly to the conversion. The molar fraction of CO reached at the outlet ($y_{CO,outlet} \sim 20\%$) is considerably higher than the equilibrium at 523 K ($y_{CO,outlet} \sim 5\%$), showing the improvement due to the adsorptive functionality. Nonetheless, this value is lower than that obtained in the fixed bed reactor ($\sim 30\%$). Moreover, it can be seen that a maximum is present in the water molar

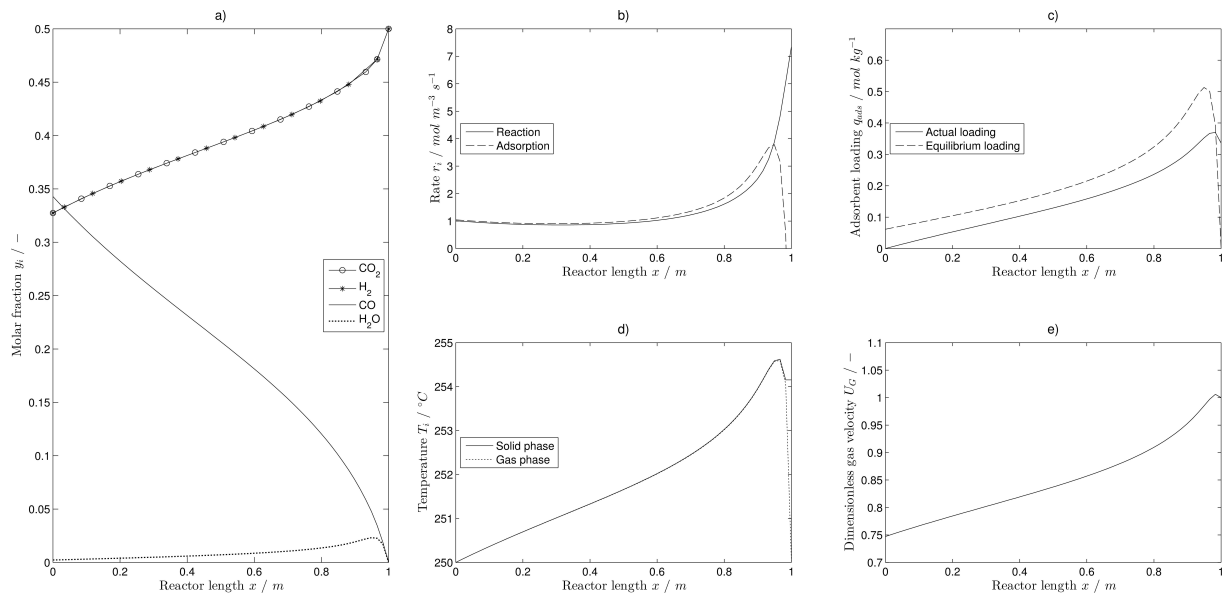


Figure 6.3.: Simulation results for the counter-current moving-bed at high solids velocity: a) molar fractions b) adsorption and reaction rates c) adsorbent loading d) gas and solid temperature e) gas phase velocity

fraction, which is linked to the relative rates of adsorption and reaction. Water is generated at the inlet faster than it can be adsorbed until both rates converge and the adsorption rate becomes the limiting factor, as depicted in Figure 6.2b.

To further analyze how the adsorption is the limiting rate, an inspection of the loading of the solids presented in Figure 6.2c can be helpful. The equilibrium loading at the respective temperature as well as the actual loading are illustrated. At the reactor inlet, the driving force is larger, allowing for a rapid increase in loading. Thereafter, the driving force falls considerably along the reactor length making the equilibrium displacement the limiting factor and, thus the adsorbent capacity as the only possibility for improvement. Comparing this to the fixed-bed operation, it is then clear that the co-current case cannot outperform it, since the fixed-bed is the asymptote that allows for full bed utilization. This is due to the traveling water vapor and loading fronts with higher concentrations in the gas phase, resulting in higher driving forces than the moving bed in the co-current mode.

From the temperature profiles in Figure 6.2d, a convergence of both profiles can be observed near the entrance of the reactor, in addition to the cold spot due to both the introduction of a cooler gas, and the endothermicity of the reaction, which occurs at higher rates in the inlet. Also, in comparison to a fixed-bed, the temperature range is clearly narrower due to the improved heat transfer due to solid convection.

6.4.1.2. Counter-Current Case 1

In counter-current operation, it is to be expected that the driving force will be greater, on average, and thus that the performance will improve. As in the co-current case, the parameters were set for the results to be comparable to each other. The simulation results are presented in Figure 6.3.

In comparison to the co-current case, the outlet molar fraction (Figure 6.3a) reaches a value of 35%, which is higher than both the co-current and the fixed-bed cases, and the water vapor content at the gas outlet is an order of magnitude lower as well. As was the case in the preceding section, a maximum is present in the water profile thereby dividing the reactor into two regions; the first, where the reaction kinetics are faster than the adsorption and thus the water concentration increases, and the second where the adsorption is faster than the reaction and thus the water concentration decreases. This can be seen clearly in Figure 6.3b. In most of the reactor for this configuration, the process is limited by the adsorption rates.

Figure 6.3c also elucidates the advantage of the counter-current operation. It can be seen that the driving force is larger on average than for the co-current case. Nevertheless, in the co-current case, a larger driving force is present at the inlet, sooner or later this value will drop until adsorption can no longer take place anymore, which is behavior that does not arise in counter-current operation. In addition, it can be seen that at the solids' outlet minor desorption occurs, which is commonly encountered in adsorption processes but whose extent in this case accounts only for 4% of the total loading.

As for the temperature profiles depicted in Figure 6.3d, it can be concluded that the solid and gas temperature difference is minimal. As in the previous case, the temperature range can be kept very narrow. A hot spot is present near the entrance of the reactor, which is due to the heat of adsorption. Contrary to both the co-current and fixed-bed configurations, there is no formation of a cold spot due to the fact that the heat transferred convectively by the solids is enough to compensate for the reaction enthalpy near the entrance of the reactor.

Finally, the need to include the change of velocity in the model is justified by the results presented in Figure 6.3e. The decrease in velocity from the gas inlet ($x = 1$ m) to the outlet is around 25%, which has a significant influence on the mean residence time.

6.4.1.3. Counter-Current Case 2

To demonstrate the occasionally non-intuitive behavior of a moving-bed, the reactor was simulated with lower solid velocities. Lacking the previous analysis, in principle, it could be argued that a lower solid velocity would improve the performance of the reactor from the economical perspective, since a lower amount of material would have to be transported, regenerated, and/or preheated/cooled. As this would more likely yield a lower driving force, a proposed solution could be to increase the reactor length and reduce the gas velocity to compensate for the loss in driving force with longer contact time between the phases. The results of such a configuration are presented in Figure 6.4.

As can be seen in Figure 6.4a, such rationale would lead to inferior reactor performance, for which the outlet concentration of CO is almost halved for a larger reactor. A mostly flat region is formed in the middle of the reactor where almost no gains are achieved in terms of conversion. This is confirmed by observing the rates of reaction and adsorption in Figure 6.4b. where it can be seen that only at the inlet and outlet

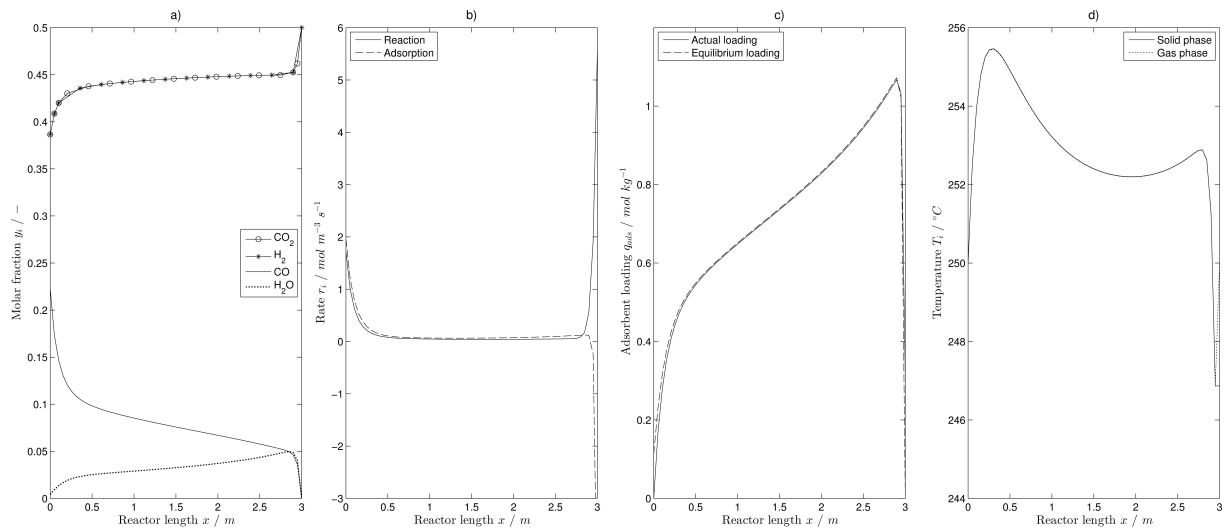


Figure 6.4.: Simulation results for counter-current moving-bed with slower solids velocities a) molar fractions b) adsorption and reaction rates c) adsorbent loading d) gas and solid temperature

of the reactor is anything occurring. In this case, the poor behavior results from a concoction of deficiencies:

First, a rapid saturation of the adsorbent, as indicated in Figure 6.4c, is caused by the unfavorable gas-to-solid ratio. Since the system is limited by the adsorption capacity, this leads to an almost complete cessation of both the reaction and adsorption rates.

Furthermore, at the solids outlet, due to the large driving force present when water-free gases are introduced, a major desorption of water takes place; in this case 37% of the water is released into the incoming gas phase, which in turns reduces the rate of reaction considerably due to the reverse reaction.

Moreover, the temperature profile is nothing like those obtained before. Peculiar behavior can be observed: two hot spots are present and a local minimum is also formed around the center of the reactor, with the minimal temperature being close to the solid phase outlet. The first hot spot can be explained by the heat of adsorption released by the introduction of fresh adsorbent to a gas flow with a moderately high concentration of water (compared to the previous cases). The minimum following the hot spot can be explained because, in absence of reaction and adsorption, the wall cools both phases. After the middle of the reactor, adsorption starts taking place again at a low rate and thus the temperature starts rising, peaking at the second hot spot which is rapidly cooled due to the endothermicity of the reaction and the desorption taking place.

From this analysis, it can be concluded that, if the correct combinations of parameters to improve the performance of the reactor are to be found, a rigorous optimization is of advantage, since the complex coupling of variables would not permit a simpler parametric study.

6.4.2. Optimization

To carry out a technical optimization of the reactor, first an appropriate objective function and the set of parameters to optimize must be chosen. Since the co-current performance was way inferior to the counter-current case, only the latter was optimized.

6.4.2.1. Single Objective

By analogy with the fixed-bed reactor, and to acquire a reasonably objective comparison, the objective function chosen was the product molar flux. The idea is to maximize the outlet of the product which in this case is syngas which fulfills the specifications for the methanol synthesis.

The optimization problem is then formulated as:

$$\max f_1(\vartheta) = \dot{N}_{G,prod} = -u_{G,prod} \cdot \varepsilon_{bed} \cdot c_{G,prod} \quad (6.4.1)$$

s.t.

$$0 \leq \phi_{cat} \leq 1 \quad (6.4.2)$$

$$-0.05 \text{ m s}^{-1} \leq u_{G,inlet} \leq -0.75 \text{ m s}^{-1} \quad (6.4.3)$$

$$0.15 \leq y_{CO_2,inlet} \leq 0.5 \quad (6.4.4)$$

$$1 \text{ bar} \leq P \leq 30 \text{ bar} \quad (6.4.5)$$

$$473 \text{ K} \leq T_x \leq 533 \text{ K} \quad T_{G,inlet}, T_{S,inlet}, T_{W,1...5} \quad (6.4.6)$$

$$\frac{y_{CO,prod} + y_{CO_2,prod}}{y_{H_2,prod} - y_{CO_2,prod}} \geq 0.5 \quad (6.4.7)$$

$$y_{CO_2,prod} \leq 0.8 \quad (6.4.8)$$

$$T_{max} \leq 533 \text{ K} \quad (6.4.9)$$

$$u_{G,max} = \max(u_S - u_G) \leq 0.8 \cdot u_{mf} \quad (6.4.10)$$

The decision variable ϑ consists of the following parameters:

$$\vartheta^T = (\phi_{cat} \quad u_{G,inlet} \quad y_{CO_2,inlet} \quad P \quad T_{G,inlet} \quad T_{S,inlet} \quad T_{W,1} \quad \dots \quad T_{W,5}) \quad (6.4.11)$$

For each variable, the upper and lower boundaries are defined in Eqs. (6.4.2-6.4.6). Furthermore, four additional constraints are included, the first two, Eqs. (6.4.7,6.4.8), are the constraints required to meet the specifications of syngas for the methanol synthesis, the first one is the ratio of carbon monoxide to hydrogen, and the second one the maximum amount of carbon dioxide that can be in the stream. The remaining two constraints, Eqs. (6.4.9,6.4.10), are design considerations. Firstly, the maximal temperature should not exceed 533 K; otherwise the adsorbent may be damaged. Secondly, the maximal gas velocity inside the reactor cannot exceed 80% of the minimum fluidization velocity, in order to avoid any fluidization or entrainment inside the reactor.

From the decision variables, it can be noted that neither the reactor length nor the solid phase velocity are included. The reasoning behind this is that, given the

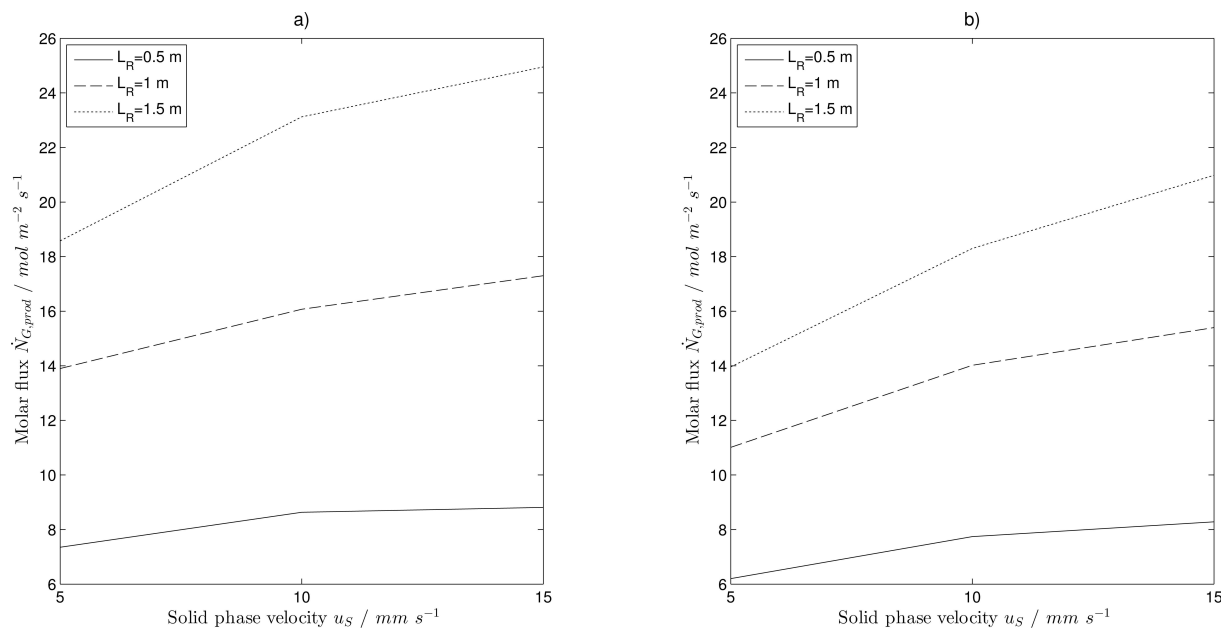


Figure 6.5.: Results for a single objective optimization for a) Non-adiabatic b) adiabatic operation.

cost function used, the optimizer would always favor the highest solid velocity and the longer reactor, which influence the process economics. This is not ideal, since it would be more expensive due to a larger reactor volume and due to the regeneration of more material with lower utilization factors. To gain insights into the optimization process, a finite bounded set of parameters for these variables was chosen to try to reveal general trends, which could then allow a definitive conclusion as to where the reactor should operate. In addition, the model was also simulated for adiabatic operation to acquire an understanding of the influence of the temperature profiles within the reactor.

The optimization was then run for three different sets of initial values and for nine combinations of lengths and solids' velocities. The results of these optimizations are presented in Figure 6.5. The initial values for the runs are presented in the appendix (Table D.1).

In Figure 6.5, a comparison of the maximum achievable molar flux as a function of the solid phase velocity and with the reactor length as a parameterized variable is presented for both adiabatic and non-adiabatic operation. The value presented is the maximum obtained from the three runs. Compared to the initial value of the molar flux using the initial guess as a benchmark, improvements of up to a factor of 17 were found. In general, a difference of less than 5% between runs was observed, which is in accordance with the tolerance of the solver (Audet et al. 2015). The full optimization results are presented in the appendix ((Tables D.2,D.3).

The first result that can be deduced is the fact that the molar fluxes found, and thus the space-time-yields (STY), i.e. molar flux per unit length, are vastly superior to those obtained for a fixed-bed reactor (Munera Parra et al. 2017). These results are compared in Table 6.7, where it can be observed that the results are almost an order of magnitude higher than those obtained from the optimized fixed-bed reactor. This

6. Moving-Bed Adsorptive Reactor

Table 6.7.: Space-time yield results ranges in $\text{mol m}^{-3} \text{s}^{-1}$. Comparison between the fixed-bed (Munera Parra et al. 2017) and the moving-bed reactor concepts

	Fixed-bed	Moving Bed
Non-adiabatic	1.74-2.32	12.38-17.62
Adiabatic	1.56-2.04	9.31-16.57

Table 6.8.: Ratio of molar flux compared to the smallest reactor $\dot{N}_{G,prod}/\dot{N}_{G,prod}$ ($L_R = 0.5 \text{ m}$)

		Non-Adiabatic			Adiabatic		
		Solid phase velocity $u_S / \text{mm s}^{-1}$					
		5	10	15	5	10	15
Reactor length L_R / m	0.5	1	1	1	1	1	1
	1	1.89	1.86	1.96	1.77	1.81	1.86
	1.5	2.53	2.68	2.83	2.25	2.36	2.53

Table 6.9.: Ratio of molar flux compared to the lowest solid phase velocity $\dot{N}_{G,prod}/\dot{N}_{G,prod}$ ($u_s = 5 \text{ mm s}^{-1}$)

		Non-Adiabatic			Adiabatic		
		Solid phase velocity $u_S / \text{mm s}^{-1}$					
		5	10	15	5	10	15
Reactor length L_R / m	0.5	1	1.17	1.19	1	1.24	1.33
	1	1	1.15	1.24	1	1.27	1.4
	1.5	1	1.24	1.34	1	1.31	1.5

comparison is not completely fair, due to the fact that the regeneration is included in the STY for the fixed-bed reactor, whereas for the moving-bed the regeneration occurs externally and completely decoupled from the reaction. This complements the advantages of the moving-bed reactor over the fixed bed reactor.

Furthermore, from the optimization results, three trends can be clearly identified. First, for a given solid phase velocity, an increase in reactor length yields an increase in molar flux, the dependency of which is shown in Table 6.8. It can be seen that the increase in molar flux with respect to reactor length is sub-linear. This is due to the fact that, alongside the reactor length, a decrease in the rate of adsorption and reaction is to be expected. For this reason, favoring an infinitely long reactor does not constitute a feasible solution.

Moreover, the influence of the reactor length also affects the residence times of both phases. This is the second trend. For increasing reactor lengths, the effects of an increasing solid phase velocity become larger. This is summarized in Table 6.9. It can be seen that the influence is not as significant as it was for the reactor length, but it nonetheless plays a role, implying a kinetic limitation in the process.

The effect of the operation mode is the third trend observed. The non-adiabatic op-

Table 6.10.: Improvement in percentage of molar flux production for the non-adiabatic compared to the adiabatic operation $(\dot{N}_{G,prod,non-ad} - \dot{N}_{G,prod,ad}) / \dot{N}_{G,prod,ad} \cdot 100\%$

		Solid phase velocity		
		$u_s / \text{mm s}^{-1}$		
		5	10	15
Reactor length L_R / m	0.5	18.52	11.51	6.39
	1	26.28	14.6	12.31
	1.5	33.04	26.36	18.39

eration is always superior to that of the adiabatic case, which, given the extra degrees of freedom that a temperature control provides, is to be expected. The improvement of the non-adiabatic compared to the adiabatic operation is presented in Table 6.10. For increasing reactor lengths, the performance of the non-adiabatic operation increases, whereas for increasing solid velocities, the performance benefit decreases. This can be explained as follows: for lower velocities and larger reactors, the temperature control obtained from the non-adiabatic operation starts playing a larger role, since the residence times are higher, and thus an increase in velocity or a decrease in reactor size minimizes this effect and the improvement over the adiabatic operation becomes less pronounced.

From these results, the trends of the main parameters of interest were determined. However, no real decision on the appropriate operational window can be made based on these results alone, since they would always suggest operating using the larger reactor and the highest possible solid phase velocity. For the reactor size, it could be shown that an indefinite increase in reactor size will, at certain point, will yield no or only very minor improvements in operation. From a technical perspective, operating at too-high solid velocities leads to minimal utilization of the adsorbent and to a more complicated regeneration for a larger amount of material. This means that a compromise needs to be found, which was implemented using a bi-objective formulation presented in Section 6.4.2.3.

However, before continuing with the optimization, the results and analysis of the optimized reactor in this section is performed to comprehend how the bi-objective optimization might be improved.

6.4.2.2. Analysis of the Optimized Reactor

In addition to the final result obtained from the optimization, considerable insight can be gained by analyzing the corresponding profiles within the reactor. Since the overall evolution of the profiles are similar for all the optimizations performed, the results for the configuration $L_R = 1 \text{ m}$ and $u_s = 10 \text{ mm s}^{-1}$ were selected arbitrarily for purposes of illustration. The results are depicted in Figure 6.6.

In Figure 6.6a-b the molar fractions for all components are shown for the non-adiabatic and adiabatic operation, respectively. In both cases, the conversion of CO_2 is about 70%, which lies well above the maximum equilibrium conversion possible in

6. Moving-Bed Adsorptive Reactor

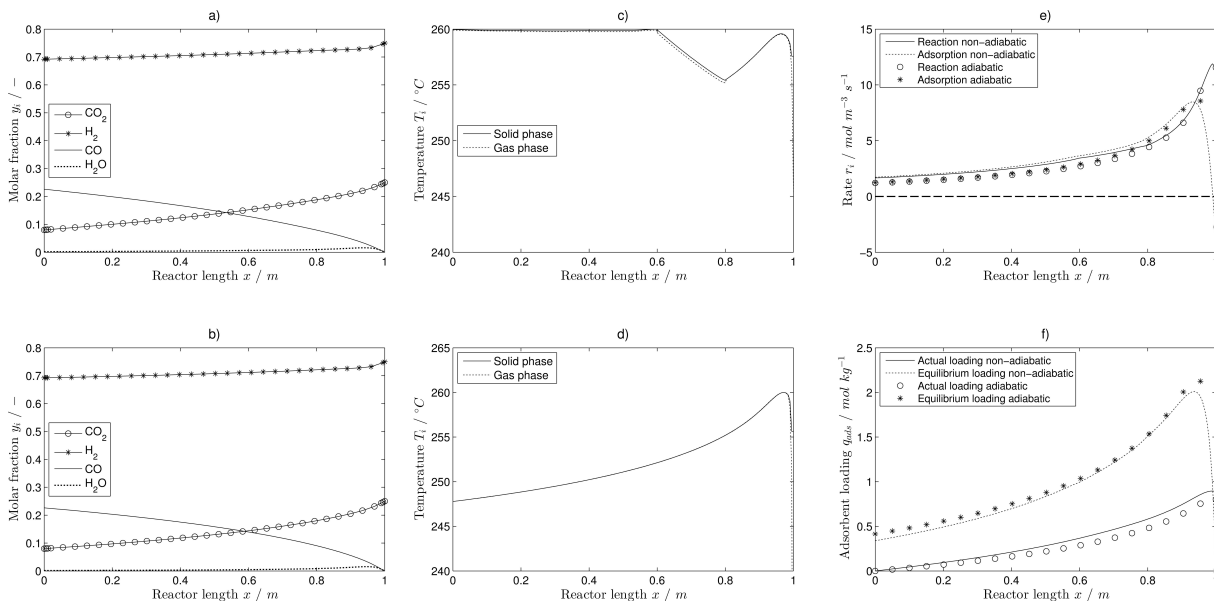


Figure 6.6.: Optimized profiles for a) molar fractions non-adiabatic operation b) mole fractions adiabatic operation c) temperature for non-adiabatic operation d) Temperature for adiabatic operation e) rates of adsorption and reaction for both operating modes f) adsorbent loading for both operating modes

the system of 18% without the adsorptive functionality. As can be seen, the profiles are virtually identical. Nevertheless, as seen earlier, the molar flux in the non-adiabatic case is higher and thus, other profiles are investigated to elucidate the discrepancy.

The main difference evidently lies in the temperature profiles. Figure 6.6c illustrates the temperature profile for the non-adiabatic operation, where it can be seen that for most of the reactor, the temperature is kept at its maximum, since the rates of reaction and adsorption are very similar (Figure 6.6e), and the endothermic reaction heat is largely balanced by the exothermic heat of adsorption, in addition to the heat exchanged with the reactor walls. In the region where the temperature decreases, the adsorption rate is higher than the rate of reaction and thus the optimizer chooses a lower wall temperature to avoid violating that constraint which, in this case, leads to a drop in temperature.

In contrast to the non-adiabatic case, the adiabatic operation depicted in Figure 6.6d, exhibits a completely different profile. The temperature maximum is in the region where the adsorption is faster than the reaction, and thus where most of the heat is released. In this case, the optimizer cannot control the wall temperature; therefore the only way to avoid violating the maximum temperature constraint is by decreasing the solids input temperature.

Figure 6.6e shows the difference between the rates of reaction and adsorption for both operating modes. Whereas in the solid outlets the rates are almost identical, as are their temperature profiles, after a given point the non-adiabatic rates are higher than those of the adiabatic case, which can be explained by the temperature difference between the two operation modes.

Finally, in Figure 6.6f, the loading of the adsorbent compared to the equilibrium

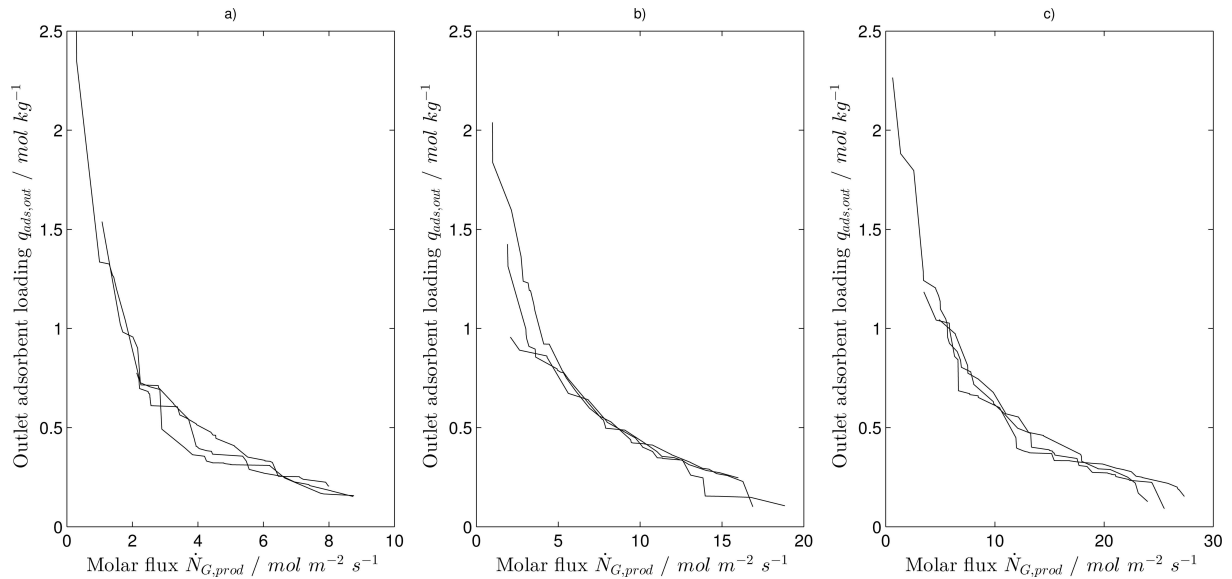


Figure 6.7.: Pareto fronts for different reactor lengths a) 0.5 m b) 1m c) 1.5m

loading is presented. As can be observed for the non-adiabatic mode, the adsorbent is used slightly more effectively than in the adiabatic case. The explanation for this is the same as the reason why the non-adiabatic operation is superior. Taking a look at the inlet gas velocities (Tables D.2,D.3) and averaging the three runs, the non-adiabatic gas velocity is 22% higher than in the adiabatic case. This means that for the same reactor volume, the molar flow is higher in the non-adiabatic case leading to more product being generated, even though the molar fraction profiles are basically the same. This 22% rise is due to the temperature profiles which permits faster rates and also for better adsorbent utilization.

6.4.2.3. Bi-Objective

As disclosed in Section 6.4.2.1, it is necessary to consider the adsorbent utilization in order to obtain more meaningful results. The only change in the optimization formulation, presented for the single objective problem, is the inclusion of a second objective defined as:

$$\max f_2(\vartheta) = q_{ads}(X = 1) \quad (6.4.12)$$

This value represents the loading of the adsorbent at the solids' outlet, and its maximization is of interest since it represents the degree of utilization of the adsorbent.

The resulting Pareto fronts are presented in Figure 6.7. Runs for three different sets of initial values were performed. Since the non-adiabatic operation was superior, only such an operating mode was simulated. The initial values can be found in the appendix (Table D.4).

From the results obtained, it can be seen that slight deviations are encountered amongst the runs. Nonetheless, the overall trend remains clear. It is important to notice that the adsorbent utilization mostly remains in the same region, whereas the molar flux span increases considerably with increasing reactor length. This suggests a limitation in the adsorption capabilities of the system. In order to obtain a fairer

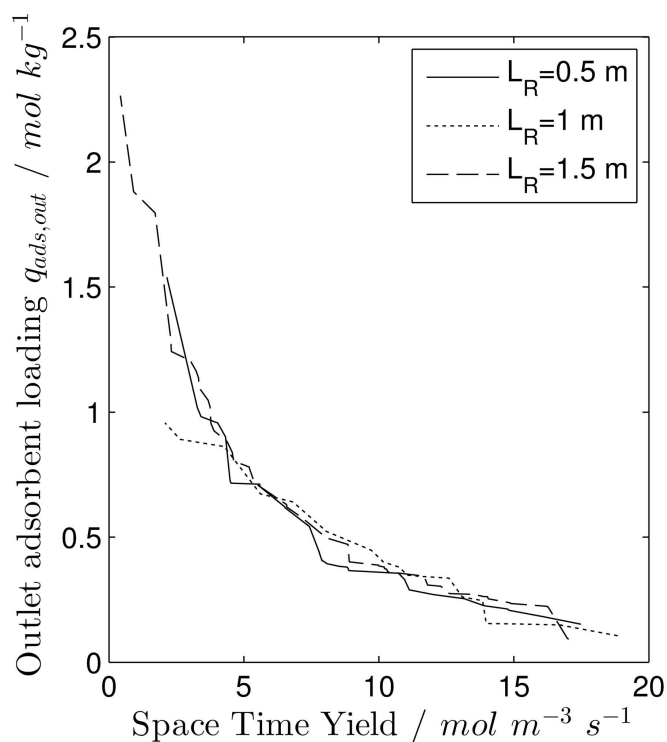


Figure 6.8.: Pareto front for the space time yield

comparison between the three fronts, the space time yield, i.e. the molar flux per unit length, was calculated for an arbitrary run with the same initial values. The results for the third run are presented in Figure 6.8. Ideally an average value would be better, however, the number of points and ranges of the Pareto fronts for different runs are different, and some degree of extrapolation and interpolation would be required for averaging out the fronts, which could lead to falsified tendencies at the boundaries.

From Figure 6.8, the most relevant aspect is the fact that the optimal STY fronts seem very similar for different reactor lengths. Although a priori, and especially looking at the molar flux fronts, it could be supposed that a larger reactor would be superior. Nevertheless, it is observed that for the space time yield this is not the case. This can be explained by the fact that the limiting factor is the adsorbent capacity. For a fixed length, the optimizer will find the solution that maximizes the use of the adsorbent, but, as seen above, this is very similar for all reactor lengths and thus, with the remaining parameters, the STY will attain similar values.

Finally, from the fronts it can be recognized that a region is formed where the STY can be increased with only minor loss in the adsorbent loading at the outlet, which would be advantageous for processes where an infrastructure for regenerating the adsorbent is available at low cost.

Conversely, should the regeneration cost be the decisive factor, the reactor could be operated at lower STY with higher adsorbent utilization. Nonetheless, the STY for a moving-bed reactor operated at higher adsorbent loadings would be larger, or at least of the same order of magnitude as that of the fixed-bed reactor, with the advantage that the regeneration can be decoupled from the reaction, which is not the case for the fixed-bed reactor.

6.5. Summary and Conclusions

The modeling and simulation of a moving-bed adsorptive reactor for the rWGS reaction were performed. Valuable insights were acquired from the profiles formed inside the reactor for several operational modes and the results were used to optimize the most promising arrangement.

The optimization was first carried out with a single objective function, in order to maximize the throughput for a fixed set of reactor lengths and solid phase velocities. The results showed that the STY obtained was an order of magnitude higher than that obtained in an optimized fixed-bed reactor for the same volumes.

The trends in the optimization showed a sub-linear increase of molar flux with increasing length and a greater effect of the influences of the solid phase velocity with increasing length. In addition, the non-adiabatic case showed a significant advantage over the adiabatic case, which was not the case for a fixed-bed.

The optimized reactor was also analyzed to compare its performance parameters with those of the non-optimized case, and the capacity of the adsorbent was found to be the limiting factor. This was also greatly influenced by the temperature profile obtained, which allowed interpretation of the improvement of the non-adiabatic over the adiabatic operation. This means that for the non-adiabatic case, the temperature can be geared towards the temperature that favors the dominant phenomenon, whether it is reaction or adsorption, whereas in the adiabatic case, the temperature is dictated by either the exo- or endothermicity of the dominant phenomenon.

Finally, a bi-objective optimization was carried out to establish a technically feasible operating region where both the STY as well as the adsorbent utilization were maximized. The Pareto fronts obtained were analyzed and the regions of possible operation described. Both regions of operation presented more favorable conditions than the fixed-bed approach.

The next step will be to carry out the economic optimization of the reactor for an industrial-scale system and benchmark it against the fixed-bed reactor and other alternative CO₂ activation processes.

Conclusions

Part I

In the first part of this work, molten-media based reactor concepts were studied.

For the capillary reactor, improvements in the gas separation, operability of the plant were obtained by the introduction of a low-temperature alloy, GaInSn. By utilizing this alloy, greater insights in the behavior of the slug-flow could be gained, and the use of pumps for the liquid media allowed for a more precise control of the liquid phase velocity.

In addition, qualitative studies with the new alloy, showed that the promise of a better contact angle was limited to the presence of metal oxides which cannot be present in the pyrolysis reactor. Thus, the wettability of the quartz glass remains a hurdle to tackle. Although the wetting could be forced hydrodynamically by increasing the liquid velocity, for the current window of operating conditions, this was not possible to achieve and the tendency was more towards the disruption of the slug flow than towards the formation of a film.

The acquisition of a pump that could handle higher throughputs could validate this result. Nonetheless, operating at a high velocity means longer reactors and higher pressure drops which hurt the feasibility of this concept. Though from a reaction engineering perspective, the capillary reactor remains a very interesting system, its feasibility depends upon finding a material which is wetted by the melt, and in which the gas-liquid operating window allows for the formation of a film in the slug-flow.

The second liquid-based concept was that of a falling-film reactor. Contrary to the capillary reactor, the gas and liquid phase velocities can be decoupled from each other giving an additional degree of freedom to its operation. Although the heat transfer and residence time distribution are not as excellent as in the capillary reactor, the falling-film still presents major advantages compared to the bubble column counterpart.

The theoretical results showed an important feature, which was that the behavior of the film had little effect on the performance of the reactor, mainly due to the heat transfer properties of the liquid media. However, the same problems with the wetting of the reactor were found experimentally; the use of a larger liquid throughput could force the wetting of the wall hydrodynamically in this concept as well. The main conclusion that can be drawn is, again, the need for a material that the molten media can wet. Various wall materials with varying heat transfer characteristics were simulated.

As for the liquid media, the wall material influence was negligible. This serves the concept since the conductive properties of the wall material are not a limiting factor.

Furthermore, simulations were carried out with molten salts that, in principle, could have better wetting behavior than the metals, although this has not been corroborated experimentally. The simulation results were comparable with those of the molten metals.

From the simulations, it was proved that the falling-film is a very robust concept in terms of sensitivity to changes in parameters, and thus once the right combination of liquid velocity, wall material, and melt is found, the simulation results can predict the behavior of the system adequately without having major changes in outlet conversion.

Finally, it was necessary to prove that the wetting of the wall could be forced hydrodynamically as a worst case scenario. For that, a rotating reactor was utilized experimentally, and it was shown that, with a determined hold-up, a stable film that wetted the whole surface could be established. This indirectly proves that a higher velocity in the falling film would eventually lead to the wetting of the film. For the capillary reactor, this assertion cannot be made, since there the gas-liquid interaction plays a major role. The rotating reactor could also serve as a worse-scenario concept in which no material is found that allows the melts to wet the wall.

To sum up the first part it can be concluded that the molten media concepts are subject to the availability of an apt wall material. Moreover, these concepts still represent the easiest way to introduce heat into the reactor in a mixture of convective and recuperative heat. Although its integration to the planned energetic structure may be difficult in Germany, in other countries where generation IV nuclear reactors operated with molten salts or metals will be available, the integration of molten media reactors to achieve near-zero CO₂ production of hydrogen is an interesting possibility in the near future.

Part II

In the second part, solid-based moving-bed reactors were studied.

First, using a generalized model for moving-bed reactors, the influence of several parameters and modeling extensions in the multiplicity of steady-states was analyzed using continuation methods. The results showed that the system is influenced the most by the Stanton number. From the model extension, it was shown that the change in the number of moles and in heat capacity due to the reaction affect the system in a greater way than could be anticipated. The conclusion drawn from this section is that conscientious modelling is of high importance when dealing with systems that span large regions in their variables, since omitting such changes would lead to missing complex behaviors such as multiple steady-states.

In addition, the bifurcation study was carried out for the case study of the pyrolysis of methane, specifically, for the case when the heat is introduced via resistive heating. This was done in order to prove that allothermic processes could exhibit multiplicities for non-linear heat inputs. In general, although the case-study was not the most ideal. It was shown that when the reaction and the change of the non-linear heat

input are coupled in the same temperature range, multiple steady-states can occur. Nonetheless, for the carbon materials studied this was not the case, and this behavior was only achieved by shifting the resistivity profiles towards higher temperatures.

In the bifurcation studies, the focus was set only on the resistive heating strategy, since its particular non-linear behavior was of interest and the other alternatives which could supply the reaction heat at high-temperatures were not expected to possess multiple steady-states.

Besides the bifurcation analysis, the strategies available to circumvent the challenge of introducing heat at high-temperatures were modeled in detail. To gain insight into their results, the models were simulated for similar parameters, and with the knowledge obtained from these simulations, the concepts were optimized based on technical objective functions.

From the optimized results, the three heating strategies were identified as solutions in short-, mid- and long-term.

The side-stream strategy is the most feasible short-term solution to avoid most of the CO₂ emissions associated with hydrogen production. This concept accounts mostly only for the emissions associated with the extraction and transportation of methane. Should, for instance, synthetic methane be used to produce hydrogen, the emissions would sink to zero/near-zero. For the case where methane is obtained with the current means, the emissions linked to this concept are 1.86 kg CO₂ per kg H₂, which is well below the state of the art, which on average produces 10 kg CO₂ per kg H₂. The only downfall regarding the technical feasibility is the need for an additional process unit, which is the regenerator in which the heat liberated by the combustion of a fraction of the produced hydrogen is transferred into the side-stream that is introduced in the reactor.

The resistive heat strategy is a solution for the mid-term, when the CO₂ emissions linked to electricity production decrease from the current values. For the German scenario for 2030, this strategy would emit 4.39 CO₂ per kg H₂, and again, if the methane used is not linked with any emissions, the value would be 2.58. This concept necessitates the introduction of a transformer, but the technology required has been applied successfully to electric arc furnaces, among others. The main problem with this strategy is that the purity of hydrogen that can be obtained is limited, if the back reaction takes place as fast as thermodynamically predicted. With the maximum conversion being 98.3%, the maximum hydrogen purity that could be obtained is 99.1%. Higher purities would necessitate the introduction of additional purification units making the concept less attractive.

The plasma strategy is a solution long-term. With the current efficiency and the scenario for Germany in 2030, the emissions linked to this concept are 6.69 kg CO₂ per kg H₂, still under the state of the art. Moreover, the technical feasibility is also a question, since nowadays the highest capacity achieved lies in the region of 5 MW and the requirement for a reactor of a capacity similar to that of a large scale reformer is of 16-17 MW. Alternatives with vacuum conditions and higher efficiencies could be a solution, but at a higher capital needed for the construction.

In terms of optimization, especially compared to the results obtained in the following part, not much could be gained from optimizing the reactors. The minimal energy

input as well with the constraints on reactor size limit the degrees of freedom for optimization. Nonetheless, the choice of incorrect process parameters such as the solid to gas ratio could hurt the concept. Form the three concepts, the resistive heating presents the most potential for optimization, since the heat is introduced in a more distributed way in comparison to the plasma and side-stream concepts.

Finally, it can be seen that the solid-based moving-bed reactor serves as a ready-to-implement technology to reduce the CO₂ emissions pertaining to hydrogen production. The question of costs of production was not dealt within this work since for the pyrolysis of methane, it is mainly based on the carbon price, the possibility of penalizing emissions and the use of carbon credits. Recent financial analysis of the methane pyrolysis can be found elsewhere (Machhammer et al. 2016; Parkinson et al. 2017).

Part III

In the last part, the rWGS was studied theoretically on lab-scale multifunctional adsorptive reactors. Two concepts were investigated, a fixed- and a moving-bed reactor for the production of synthesis gas, specifically for the case of methanol synthesis.

For the fixed-bed concepts, first the numerical methods to calculate the cyclic steady-state were compared. There, the direct substitution method proved better for this particular case, since the resolution obtained in the profiles was adequate and the simplicity of working with off-the-shelf time steppers was found advantageous.

With the efficient calculation of the CSS, the concept was optimized. Although arguably the solver did not find the global optimum, improvements over the converged initial solutions were up to over 800%. This concept, thus, shows great potential for optimization with the several degrees of freedom available and could be easily scaled up by means of a multi-tubular arrangement which would also allow for a non-adiabatic operation.

The moving bed reactor was then proposed as an alternative and also as a potential improvement upon the fixed-bed configuration.

The reactor was modeled and simulated to gain insight into the operational modes of the moving-bed reactor. Based on these results, the counter-current configuration was optimized in the same platform as the fixed-bed in order to guarantee a fair comparison where the solver was not a factor.

The results showed improvements over the initial converged solution of up to 1700% for non-adiabatic operation and up to 1300% for adiabatic operation. Moreover, the STY of the moving-bed reactor was an order of magnitude higher of those from its fixed-bed counterpart.

The trends in the optimization showed a sub-linear increase of molar flux with increasing length and a greater effect of the influences of the solid velocity with increasing length. In addition, the non-adiabatic case showed a considerable advantage over the adiabatic one, which was not the case for a fixed-bed.

Since the two desired outcomes were in conflict, i.e. high STY with low adsorbent utilization, a bi-objective optimization was carried out to establish a technically fea-

sible operating region where both the STY as well as the adsorbent utilization were maximized. The Pareto fronts obtained were analyzed and the regions of possible operation were elucidated. The most important result is that both operating regions outperformed the fixed-bed strategy in terms of STY.

The moving-bed concept can also be scaled up to industrial scales by increasing the diameter and adjusting the residence time and solids distribution accordingly.

Outlook

For the methane pyrolysis, it can be seen that using the solid-based moving-bed reactor, industrially ready solutions can be technically achieved that could reduce the emissions associated with hydrogen production in the short-term. Electricity-based concepts for the mid- to long-term were also elucidated.

Pilot concepts for the strategies are the only logical next step, where the constituents of the reactors can be tested as a whole, since the reactor materials required for high-temperature, atmospheric pressure, and hydrogen environments are already industrially used.

As for the molten media concepts, for its further development, it is necessary to look for adequate materials that allow for the melt to wet the walls and thus utilize their full potential for near-zero CO₂ hydrogen production, especially when linked with nuclear energy. There, the falling-film reactor is a front-runner in terms of robustness, and industrial use in other applications.

For the adsorptive rWGS, contrary to the methane pyrolysis, first some fundamentals need to be proven. The catalyst activity under conditions where no water is present must be studied in terms of activity and selectivity to side reactions. Should the catalyst withstand these conditions, after an economic analysis, both the fixed-bed and moving-bed reactors would be ready for adoption in an industrial level. The moving-bed being a stationary process, and given the decoupling from reaction and regeneration compared to its fixed-bed counterpart, is the industrially more apt concept to carry out this reaction.

Bibliography

References

- Abánades, A., C. Rubbia, and D. Salmieri (2012):** “Technological challenges for industrial development of hydrogen production based on methane cracking”. In: *Energy* 46.1, pp. 359–363. DOI: 10.1016/j.energy.2012.08.015.
- Abánades, A., R. K. Rathnam, T. Geissler, A. Heinzl, K. Mehravaran, G. Müller, M. Plevan, C. Rubbia, D. Salmieri, L. Stoppel, S. Stückrad, A. Weisenburger, H. Wenninger, and T. Wetzel (2016):** “Development of methane decarbonisation based on liquid metal technology for CO₂-free production of hydrogen”. In: *International Journal of Hydrogen Energy* 41.19, pp. 8159–8167. DOI: 10.1016/j.ijhydene.2015.11.164.
- Abanades, S. and G. Flamant (2006):** “Solar hydrogen production from the thermal splitting of methane in a high temperature solar chemical reactor”. In: *Solar Energy* 80.10, pp. 1321–1332. DOI: 10.1016/j.solener.2005.11.004.
- Abanades, S., S. Tescari, S. Rodat, and G. Flamant (2009):** “Natural gas pyrolysis in double-walled reactor tubes using thermal plasma or concentrated solar radiation as external heating source”. In: *Journal of Natural Gas Chemistry* 18.1, pp. 1–8. DOI: 10.1016/S1003-9953(08)60077-8.
- Abbas, H. F. and W. M. A. Wan Daud (2010):** “Hydrogen production by methane decomposition: A review”. In: *International Journal of Hydrogen Energy* 35.3, pp. 1160–1190. DOI: 10.1016/j.ijhydene.2009.11.036.
- Abe, Y., H. Akimoto, and Y. Murao (1991):** “Estimation of Shear Stress in Counter-Current Annular Flow”. In: *Journal of Nuclear Science and Technology* 28.3, pp. 208–217. DOI: 10.1080/18811248.1991.9731346.
- Abram, T. and S. Ion (2008):** “Generation-IV nuclear power: A review of the state of the science”. In: *Energy Policy* 36.12, pp. 4323–4330. DOI: 10.1016/j.enpol.2008.09.059.
- Adams, T. A. and P. I. Barton (2009):** “A dynamic two-dimensional heterogeneous model for water gas shift reactors”. In: *International Journal of Hydrogen Energy* 34.21, pp. 8877–8891. DOI: 10.1016/j.ijhydene.2009.08.045.
- Agar, D. W. (2005):** “The Dos and Don’ts of Adsorptive Reactors”. In: *Integrated Chemical Processes: Synthesis, Operation, Analysis, and Control*, pp. 203–232. DOI: 10.1002/3527605738.ch7.

- Agar, D. W. and I. Schultz (2014):** "Apparatus, used to produce hydrogen by thermal decomposition of e.g. methane, comprises pyrolysis reactor having reaction chamber present in form of capillary, and unit for adjusting flow rate of high-temperature heat transfer medium". In: *German Patent DE 102013112205 A1*.
- Agar, D. (2003):** "Multifunctional Reactors: Integration of Reaction and Heat Transfer". In: *Re-Engineering the Chemical Processing Plant*: ed. by Andrzej Stankiewicz and Jacob A. Moulin. 1st. New York Basel: Marcel Dekker. Chap. 10, pp. 355–384.
- Akanksha, K. K. Pant, and V. K. Srivastava (2007):** "Modeling of sulphonation of tridecylbenzene in a falling film reactor". In: *Mathematical and Computer Modelling* 46.9-10, pp. 1332–1344. DOI: 10.1016/j.mcm.2007.01.007.
- Ali, K. A., A. Z. Abdullah, and A. R. Mohamed (2015):** "Recent development in catalytic technologies for methanol synthesis from renewable sources: A critical review". In: *Renewable and Sustainable Energy Reviews* 44, pp. 508–518. DOI: <https://doi.org/10.1016/j.rser.2015.01.010>.
- Allgower, E. and K Georg (2003):** *Introduction to numerical continuation methods*. 1st ed. Philadelphia, PA: SIAM.
- Anggono, J (2005):** "Mullite ceramics: its properties structure and synthesis". In: *Jurnal Teknik Mesin* 7.1, p. 1. DOI: 10.9744/jtm.7.1.pp.
- Aresta, M. (2010):** *Carbon Dioxide as Chemical Feedstock*. DOI: 10.1002/9783527629916. arXiv: arXiv:1011.1669v3.
- Audet, C, S. Le Digabel, and C Tribes (2015):** *NOMAD User Guide*. Montreal: Les Cahiers du GERAD.
- Audet, C. and J. E. Dennis (2006):** "Mesh Adaptive Direct Search Algorithms for Constrained Optimization". In: *SIAM Journal on Optimization* 17.1, pp. 188–217. DOI: 10.1137/040603371.
- Audet, C., G. Savard, and W. Zghal (2008a):** "Multiobjective Optimization Through a Series of Single-Objective Formulations". In: *SIAM Journal on Optimization* 19.1, pp. 188–210. DOI: 10.1137/060677513.
- Audet, C., V. Béchar, and S. L. Digabel (2008b):** "Nonsmooth optimization through Mesh Adaptive Direct Search and Variable Neighborhood Search". In: *Journal of Global Optimization* 41.2, pp. 299–318. DOI: 10.1007/s10898-007-9234-1.
- Auerkari, P (1996):** *Mechanical and physical properties of engineering alumina ceramics*. Technical Research Centre of Finland.
- Ausubel, J. H. (2000):** "Where is energy going". In: *The Industrial Physicist* 1, pp. 16–19.
- Bai, Z., H. Chen, B. Li, and W. Li (2005):** "Catalytic decomposition of methane over activated carbon". In: *Journal of Analytical and Applied Pyrolysis* 73.2, pp. 335–341. DOI: 10.1016/j.jaap.2005.03.004.
- Baliban, R. C., J. A. Elia, V. Weekman, and C. A. Floudas (2012):** "Process synthesis of hybrid coal, biomass, and natural gas to liquids via Fischer-Tropsch synthesis, ZSM-5 catalytic conversion, methanol synthesis, methanol-to-gasoline, and methanol-to-olefins/distillate technologies". In: *Computers & Chemical Engineering* 47, pp. 29–56. DOI: 10.1016/j.compchemeng.2012.06.032.
- Barreto, L, A Makihira, and K Riahi (2003):** "The hydrogen economy in the 21st century: a sustainable development scenario". In: *International Journal of Hydrogen Energy* 28.3, pp. 267–284. DOI: 10.1016/S0360-3199(02)00074-5.

- Bautista, O, F Mendez, and C Trevino (2008):** "Theoretical analysis of the direct decomposition of methane gas in a laminar stagnation-point flow: CO₂-free production of hydrogen". In: *International Journal of Hydrogen Energy* 33.24, pp. 7419–7426. DOI: 10.1016/j.ijhydene.2008.09.060.
- Bode, A., D. W. Agar, K. Bükler, V. Göke, M. Hensmann, U. Janhsen, D. Klingler, J. Schlichting, and S. A. Schunk (2014):** "Research cooperation develops innovative technology for environmentally sustainable syngas production from carbon dioxide and hydrogen". In: *20th World Hydrogen Energy Conference 2014*.
- Carey, G. and B. Finlayson (1975):** "Orthogonal collocation on finite elements". In: *Chemical Engineering Science* 30.5-6, pp. 587–596. DOI: 10.1016/0009-2509(75)80031-5.
- Currie, J and D. Wilson (2012):** "OPTI: lowering the barrier between open source optimizers and the industrial MATLAB user". In: *Foundations of computer-aided*.
- Czernichowski, A and P Czernichowski (2000):** "Pyrolysis of natural gas in the gliding electric discharges". In: *10th Canadian Hydrogen Conference*. Quebec.
- Dabir, B., M. Riazi, and H. Davoudirad (1996):** "Modelling of falling film reactors". In: *Chemical Engineering Science* 51.11, pp. 2553–2558. DOI: 10.1016/0009-2509(96)00113-3.
- Dahl, J. K., J. Tamburini, A. W. Weimer, A. Lewandowski, R. Pitts, and C. Bingham (2001):** "Solar-Thermal Processing of Methane to Produce Hydrogen and Syngas". In: *Energy & Fuels* 15.5, pp. 1227–1232. DOI: 10.1021/ef0100606.
- Dicks, A. L. (1996):** "Hydrogen generation from natural gas for the fuel cell systems of tomorrow". In: *Journal of Power Sources* 61.1-2, pp. 113–124. DOI: 10.1016/S0378-7753(96)02347-6.
- Domínguez, A, B Fidalgo, Y Fernández, J. J. Pis, and J Menéndez (2007):** "Microwave-assisted catalytic decomposition of methane over activated carbon for CO₂-free hydrogen production". In: *International Journal of Hydrogen Energy* 32.18, pp. 4792–4799. DOI: 10.1016/j.ijhydene.2007.07.041.
- Dunker, A and J Ortmann (2006):** "Kinetic modeling of hydrogen production by thermal decomposition of methane". In: *International Journal of Hydrogen Energy* 31.14, pp. 1989–1998. DOI: 10.1016/j.ijhydene.2006.01.013.
- Dunn, S (2002):** "Hydrogen futures: toward a sustainable energy system". In: *International Journal of Hydrogen Energy* 27.3, pp. 235–264. DOI: 10.1016/S0360-3199(01)00131-8.
- Eidem, P., M Tangstad, and J. Bakken (2008):** "Determination of electrical resistivity of dry coke beds". In: *Metallurgical and materials* 39.1, pp. 7–15. DOI: 10.1007/s11663-007-9105-7.
- El-Genk, M. S. and H. H. Saber (2001):** "Minimum thickness of a flowing down liquid film on a vertical surface". In: *International Journal of Heat and Mass Transfer* 44.15, pp. 2809–2825. DOI: 10.1016/S0017-9310(00)00326-4.
- Fincke, J. R., R. P. Anderson, T. A. Hyde, and B. A. Detering (2002):** "Plasma Pyrolysis of Methane to Hydrogen and Carbon Black". In: *Industrial & Engineering Chemistry Research* 41.6, pp. 1425–1435. DOI: 10.1021/ie010722e.

- Fulcheri, L and Y Schwob (1995):** "From methane to hydrogen, carbon black and water". In: *International Journal of Hydrogen Energy* 20.3, pp. 197–202. DOI: 10.1016/0360-3199(94)E0022-Q.
- Gaudernack, B. and S. Lynum (1998):** "Hydrogen from natural gas without release of CO₂ to the atmosphere". In: *International Journal of Hydrogen Energy* 23.12, pp. 1087–1093. DOI: 10.1016/S0360-3199(98)00004-4.
- Geissler, T., M. Plevan, A. Abánades, A. Heinzl, K. Mehravar, R. Rathnam, C. Rubbia, D. Salmieri, L. Stoppel, S. Stückrad, A. Weisenburger, H. Wenninger, and T. Wetzel (2015):** "Experimental investigation and thermo-chemical modeling of methane pyrolysis in a liquid metal bubble column reactor with a packed bed". In: *International Journal of Hydrogen Energy* 40.41, pp. 14134–14146. DOI: 10.1016/j.ijhydene.2015.08.102.
- Geissler, T., A. Abánades, A. Heinzl, K. Mehravar, G. Müller, R. Rathnam, C. Rubbia, D. Salmieri, L. Stoppel, S. Stückrad, A. Weisenburger, H. Wenninger, and T. Wetzel (2016):** "Hydrogen production via methane pyrolysis in a liquid metal bubble column reactor with a packed bed". In: *Chemical Engineering Journal* 299, pp. 192–200. DOI: 10.1016/j.cej.2016.04.066.
- Giordanengo, B., N. Benazzi, J. Vinckel, J. Gasser, and L. Roubi (1999):** "Thermal conductivity of liquid metals and metallic alloys". In: *Journal of Non-Crystalline Solids* 250, pp. 377–383. DOI: 10.1016/S0022-3093(99)00268-9.
- Gnielinski, V. (2010):** "G9 Fluid-Particle Heat Transfer in Flow Through Packed Beds of Solids". In: *VDI Heat Atlas*. Berlin, Heidelberg: Springer Berlin Heidelberg, pp. 743–744. DOI: 10.1007/978-3-540-77877-6_42.
- Goebel, F. (2015):** "Experimentelle Untersuchungen zur Hochtemperatur - Methanpyrolyse im Schmelzmetall - Kapillarreaktor und analytische Betrachtung von Nebenprodukten". Bachelor's Thesis. TU Dortmund, p. 52.
- Gómez Mendoza, N. A., I. Dobrosz-Gómez, and M. Á. Gómez García (2014):** "Modeling and simulation of an industrial falling film reactor using the method of lines with adaptive mesh. Study case: Industrial sulfonation of tridecylbenzene". In: *Computers & Chemical Engineering* 68, pp. 233–241. DOI: 10.1016/j.compchemeng.2014.05.023.
- Gulevich, A., P. Martynov, V. Gulevsky, and V. Ulyanov (2008):** "Technologies for hydrogen production based on direct contact of gaseous hydrocarbons and evaporated water with molten Pb or Pb-Bi". In: *Energy Conversion and Management* 49.7, pp. 1946–1950. DOI: 10.1016/j.enconman.2007.12.028.
- Günther, P, P Kunz, R Stierle, G Eigenberger, and U Nieken (2014):** "Prozesssimulation einer Adsorptionskältemaschine: True-Moving-Bed-Approximation". In: *Chemie Ingenieur Technik* 86.1-2, pp. 112–118. DOI: 10.1002/cite.201300073.
- Gutierrez-Gonzalez, J, C Mans-Teixido, and J Costa-Lopez (1988):** "Improved mathematical model for a falling film sulfonation reactor". In: *Industrial & Engineering Chemistry research* 27.9, pp. 1701–1707. DOI: 10.1021/ie00081a023.
- Gutsol, A, A Rabinovich, and A Fridman (2011):** "Combustion-assisted plasma in fuel conversion". In: *Journal of Physics D: Applied Physics* 44.27, p. 274001. DOI: 10.1088/0022-3727/44/27/274001.

- Han, Z., B. Yang, Y. Qi, and J. Cumings (2011):** "Synthesis of low-melting-point metallic nanoparticles with an ultrasonic nanoemulsion method". In: *Ultrasonics* 51.4, pp. 485–488. doi: 10.1016/j.ultras.2010.11.015.
- Hartley, D. and W. Murgatroyd (1964):** "Criteria for the break-up of thin liquid layers flowing isothermally over solid surfaces". In: *International Journal of Heat and Mass Transfer* 7.9, pp. 1003–1015. doi: 10.1016/0017-9310(64)90042-0.
- Hasan, M. M. F., E. L. First, F. Boukouvala, and C. A. Floudas (2015):** "A multi-scale framework for CO₂ capture, utilization, and sequestration: CCUS and CCU". In: *Computers and Chemical Engineering* 81, pp. 2–21. doi: 10.1016/j.compchemeng.2015.04.034.
- Hellmann, D. (2013):** "Experimentelle Untersuchungen zur Vermeidung von Kohlenstoffablagerungen im porösen Fluid-Wandfilmreaktor bei der Hochtemperatur-Methanpyrolyse". Bachelor's Thesis. TU Dortmund.
- Hirsch, D (2001):** "The solar thermal decarbonization of natural gas". In: *International Journal of Hydrogen Energy* 26.10, pp. 1023–1033. doi: 10.1016/S0360-3199(01)00040-4.
- Hussainy, M and D. Agar (2016):** "Structural and Operational Optimality of Adsorptive Reactors". In: *Chemical Engineering & Technology* 39.11, pp. 2135–2141. doi: 10.1002/ceat.201600197.
- Iyer, S. S., I. Bajaj, P. Balasubramanian, and M. M. F. Hasan (2017):** "Integrated Carbon Capture and Conversion To Produce Syngas: Novel Process Design, Intensification, and Optimization". In: *Industrial & Engineering Chemistry Research* 56.30, pp. 8622–8648. doi: 10.1021/acs.iecr.7b01688.
- Jacobson, M. Z., M. A. Delucchi, Z. A. Bauer, S. C. Goodman, W. E. Chapman, M. A. Cameron, C. Bozonnat, L. Chobadi, H. A. Clonts, P. Enevoldsen, J. R. Erwin, S. N. Fobi, O. K. Goldstrom, E. M. Hennessy, J. Liu, J. Lo, C. B. Meyer, S. B. Morris, K. R. Moy, P. L. O'Neill, I. Petkov, S. Redfern, R. Schucker, M. A. Sontag, J. Wang, E. Weiner, and A. S. Yachanin (2017):** "100% Clean and Renewable Wind, Water, and Sunlight All-Sector Energy Roadmaps for 139 Countries of the World". In: *Joule* 7.0, pp. 709–715. doi: 10.1016/j.joule.2017.07.005.
- Jahnig, C., P. Silveston, and C. Tyson (1964):** "Hydrocarbon conversion process". In: *US Patent* 3,163,496.
- James Davis, E., M. Van Ouwkerk, and S. Venkatesh (1979):** "An analysis of the falling film gas-liquid reactor". In: *Chemical Engineering Science* 34.4, pp. 539–550. doi: 10.1016/0009-2509(79)85099-X.
- Janz, G. (1988):** *Thermodynamic and transport properties for molten salts: correlation equations for critically evaluated density, surface tension, electrical conductance, and viscosity data (Vol 17)*. American Institute of Physics.
- Jiang, L, L. Biegler, and V. Fox (2003):** "Simulation and optimization of pressure-swing adsorption systems for air separation". In: *AIChE Journal* 49.5, pp. 1140–1157. doi: 10.1002/aic.690490508.
- Johnson, G. R. and B. L. Crynes (1974):** "Modeling of a thin-film sulfur trioxide sulfonation reactor". In: *Ind. Eng. Chem., Process Des. Develop.* 13.1, pp. 6–14.
- Jones, W., S. Macknight, and L Teng (1973):** "Kinetics of atomic hydrogen reactions in the gas phase". In: *Chemical Reviews* 73.5, pp. 407–440.

- Jung, S., S. Reining, S. Schindler, and D. Agar (2013):** "Anwendung von adsorptiven Reaktoren für die reverse Wassergas-Shift-Reaktion". In: *Chemie Ingenieur Technik* 85.4, pp. 484–488. DOI: 10.1002/cite.201200213.
- Kashiwaya, Y. and M. Watanabe (2012):** "Kinetic Analysis of the Decomposition Reaction of CH₄ Injecting into Molten Slag". In: *ISIJ International* 52.8, pp. 1394–1403. DOI: 10.2355/isijinternational.52.1394.
- Keller, H. (1987):** *Lectures on numerical methods in bifurcation problems*. 1st ed. Berlin Heidelberg New York Tokyo: Springer-Verlag.
- Kim, M, E Lee, J Jun, S Kong, G Han, B Lee, T Lee, and K Yoon (2004):** "Hydrogen production by catalytic decomposition of methane over activated carbons: kinetic study". In: *International Journal of Hydrogen Energy* 29.2, pp. 187–193. DOI: 10.1016/S0360-3199(03)00111-3.
- Blankmayer, J., S. Wesselbaum, K. Beydoun, and W. Leitner (2016):** "Selective Catalytic Synthesis Using the Combination of Carbon Dioxide and Hydrogen: Catalytic Chess at the Interface of Energy and Chemistry". In: *Angewandte Chemie International Edition* 55.26, pp. 7296–7343. DOI: 10.1002/anie.201507458.
- Kogan, M and A Kogan (2003):** "Production of hydrogen and carbon by solar thermal methane splitting. I. The unseeded reactor". In: *International Journal of Hydrogen Energy* 28.11, pp. 1187–1198. DOI: 10.1016/S0360-3199(02)00282-3.
- Kolios, G (2014):** "Regenerative fixed-bed processes: approximative analysis and efficient computation of the cyclic steady state". Habilitation. Universität Stuttgart.
- Kreysa, G, D. W. Agar, and I Schultz (2010):** "Decarbonisation of Fossil Energy via Methane Pyrolysis". In: *Preprints of the DGMK Conference "The Future Role of Hydrogen in Petrochemistry and Energy Supply"*. Ed. by S. Ernst. Vol. 2010,3. Tagungsbericht / Deutsche Wissenschaftliche Gesellschaft für Erdöl, Erdgas und Kohle. Hamburg: DGMK.
- Kreysa, G. (2009):** "Climate Protection by an Alternative Use of Methane-The Carbon Moratorium". In: *ChemSusChem* 2.1, pp. 49–55. DOI: 10.1002/cssc.200800232.
- Le Digabel, S. (2011):** "Algorithm 909: NOMAD: Nonlinear Optimization with the MADS Algorithm". In: *ACM Transactions on Mathematical Software* 37.4, pp. 1–15. DOI: 10.1145/1916461.1916468.
- Lee, C. Y. and S. Y. Lee (2008):** "Influence of surface wettability on transition of two-phase flow pattern in round mini-channels". In: *International Journal of Multiphase Flow* 34.7, pp. 706–711. DOI: 10.1016/j.ijmultiphaseflow.2008.01.002.
- Lee, D. (2015):** "Hydrogen production via the Kværner process and plasma reforming". In: *Compendium of Hydrogen Energy: Hydrogen Production and Purification*. Ed. by V. Subramani, A. Basile, and T. Veziroglu. 1st. Cambridge: Woodhead, Elsevier. Chap. 12, pp. 349–391. DOI: <http://dx.doi.org/10.1016/B978-1-78242-361-4.00012-1>.
- Li, C.-H. and B. Finlayson (1977):** "Heat transfer in packed beds: a reevaluation". In: *Chemical Engineering Science* 32.9, pp. 1055–1066. DOI: 10.1016/0009-2509(77)80143-7.
- Linstrom, P. J. P. and W. G. Mallard (2001):** "NIST Chemistry webbook; NIST standard reference database No. 69". In: *NIST Chemistry WebBook*.

- Liu, T., P. Sen, and C.-J. Kim (2012):** "Characterization of Nontoxic Liquid-Metal Alloy Galinstan for Applications in Microdevices". In: *Journal of Microelectromechanical Systems* 21.2, pp. 443–450. DOI: 10.1109/JMEMS.2011.2174421.
- Logist, F., J. Lauwers, B. Trigaux, and J. F. Van Impe (2011):** "Model based optimisation of a cyclic reactor for the production of hydrogen". In: *Proceedings of the 21st European Symposium on Computer Aided Process Engineering - ESCAPE 21*.
- Maag, G, W Lipiński, and A Steinfeld (2009):** "Particle–gas reacting flow under concentrated solar irradiation". In: *International Journal of Heat and Mass Transfer* 52.21–22, pp. 4997–5004. DOI: 10.1016/j.ijheatmasstransfer.2009.02.049.
- Machhammer, O, A Bode, and W Hormuth (2016):** "Financial and Ecological Evaluation of Hydrogen Production Processes on Large Scale". In: *Chemical Engineering & Technology* 39.6, pp. 1185–1193. DOI: 10.1002/ceat.201600023.
- Marb, C. M. and D Vortmeyer (1988):** "Multiple steady states of a crossflow moving bed reactor: Theory and experiment". In: *Chemical Engineering Science* 43.4, pp. 811–819. DOI: 10.1016/0009-2509(88)80076-9.
- Marbán, G. and T. Valdés-Solís (2007):** "Towards the hydrogen economy?" In: *International Journal of Hydrogen Energy* 32.12, pp. 1625–1637. DOI: 10.1016/j.ijhydene.2006.12.017.
- Martynov, P., A. Gulevich, Y. Orlov, and V. Gulevsky (2005):** "Water and hydrogen in heavy liquid metal coolant technology". In: *Progress in Nuclear Energy* 47.1–4, pp. 604–615. DOI: 10.1016/j.pnucene.2005.05.063.
- Mobley, R. K. (2001):** "21 - Coal and Ash". In: *Plant Engineer's Handbook*. Butterworth Heinemann. Chap. 21, pp. 335–352. DOI: 10.1016/B978-075067328-0/50023-9.
- Morel, C. (1970):** *Surface tensions of molten salts and contact angle measurements of molten salts on solids*. Commission of the European Communities. (No. EUR-4482).
- Moriarty, P. and D. Honnery (2007):** "Intermittent renewable energy: The only future source of hydrogen?" In: *International Journal of Hydrogen Energy* 32.12, pp. 1616–1624. DOI: 10.1016/j.ijhydene.2006.12.008.
- Morison, K., Q. Worth, and N. O’dea (2006):** "Minimum Wetting and Distribution Rates in Falling Film Evaporators". In: *Food and Bioproducts Processing* 84.4, pp. 302–310. DOI: 10.1205/fbp06031.
- Morley, N. B., J. Burris, L. C. Cadwallader, and M. D. Nornberg (2008):** "GaInSn usage in the research laboratory". In: *Review of Scientific Instruments* 79.5, p. 056107. DOI: 10.1063/1.2930813.
- Munera Parra, A., F Platte, and D. Agar (2016):** "Multiplicity Regions in a Moving-Bed Reactor: Bifurcation Analysis, Model Extension, and Application for the High-Temperature Pyrolysis of Methane". In: *Chemie Ingenieur Technik* 88.11, pp. 1703–1717. DOI: 10.1002/cite.201600069.
- Munera Parra, A., N. Antweiler, R. Nagpal, and D. Agar (2014):** "Stability Analysis of Reactive Multiphase Slug Flows in Microchannels". In: *Processes* 2.2, pp. 371–391. DOI: 10.3390/pr2020371.
- Munera Parra, A. A. and D. W. Agar (2017):** "Molten metal capillary reactor for the high-temperature pyrolysis of methane". In: *International Journal of Hydrogen Energy* 42.19, pp. 13641–13648. DOI: 10.1016/j.ijhydene.2016.12.044.

- Munera Parra, A. A., C. Asmanoglo, and D. W. Agar (2017):** "Cyclic Steady-State Behavior of a Fixed-Bed Adsorptive Reactor for Reverse Water-Gas Shift Reaction". In: *Chemical Engineering & Technology* 40.5, pp. 915–926. doi: 10.1002/ceat.201600611.
- Muradov, N (2000):** "Thermocatalytic CO₂-Free Production of Hydrogen from Hydrocarbon Fuels". In: *Proceedings of the 2000 Hydrogen Program Review*, pp. 1–29.
- Muradov, N (2001):** "Catalysis of methane decomposition over elemental carbon". In: *Catalysis Communications* 2.3-4, pp. 89–94. doi: 10.1016/S1566-7367(01)00013-9.
- Muradov, N and T Veziroglu (2008):** "'Green' path from fossil-based to hydrogen economy: An overview of carbon-neutral technologies". In: *International Journal of Hydrogen Energy* 33.23, pp. 6804–6839. doi: 10.1016/j.ijhydene.2008.08.054.
- Muradov, N. (2017):** "Low to near-zero CO₂ production of hydrogen from fossil fuels: Status and perspectives". In: *International Journal of Hydrogen Energy* 42.20, pp. 14058–14088. doi: 10.1016/j.ijhydene.2017.04.101.
- Muradov, N., F. Smith, and A. T-Raissi (2005):** "Catalytic activity of carbons for methane decomposition reaction". In: *Catalysis Today* 102-103, pp. 225–233. doi: 10.1016/j.cattod.2005.02.018.
- Nalpanitidis, K, F Platte, D. Agar, and S Turek (2006):** "Elucidation of hybrid N₂O decomposition using axially structured catalyst in reverse flow reactor". In: *Chemical engineering science* 61.10, pp. 3176–3185. doi: 10.1016/j.ces.2005.11.017.
- Nogi, K., K. Oishi, and K. Ogino (1989):** "Wettability of Solid Oxides by Liquid Pure Metals". In: *Materials Transactions, JIM* 30.2, pp. 137–145. doi: 10.2320/matertrans1989.30.137.
- Nozaki, T., Y. Kimura, and K. Okazaki (2002):** "Carbon Nanotubes and Hydrogen Co-production from Methane using Atmospheric Pressure Non-equilibrium plasmas". In: *16th ESCAMPIG and 5th ICRP Joint Conference* Vol. 1.No. -, pp. 37–38.
- Ozalp, N, A Kogan, and M Epstein (2009):** "Solar decomposition of fossil fuels as an option for sustainability". In: *International Journal of Hydrogen Energy* 34.2, pp. 710–720. doi: 10.1016/j.ijhydene.2008.11.019.
- Parkinson, B., J. W. Matthews, T. B. McConnaughy, D. C. Upham, and E. W. McFarland (2017):** "Techno-Economic Analysis of Methane Pyrolysis in Molten Metals: Decarbonizing Natural Gas". In: *Chemical Engineering & Technology* 40.6, pp. 1022–1030. doi: 10.1002/ceat.201600414.
- Patrianakos, G., M. Kostoglou, and A. Konstandopoulos (2011):** "One-dimensional model of solar thermal reactors for the co-production of hydrogen and carbon black from methane decomposition". In: *International Journal of Hydrogen Energy* 36.1, pp. 189–202. doi: 10.1016/j.ijhydene.2010.09.061.
- Paxman, D, S Trottier, M Nikoo, M Secanell, and G Ordorica-Garcia (2014):** "Initial Experimental and Theoretical Investigation of Solar Molten Media Methane Cracking for Hydrogen Production". In: *Energy Procedia* 49, pp. 2027–2036. doi: 10.1016/j.egypro.2014.03.215.
- Pinilla, J, R Moliner, I Suelves, M Lazaro, Y Echevoyen, and J Palacios (2007):** "Production of hydrogen and carbon nanofibers by thermal decomposition of methane

- using metal catalysts in a fluidized bed reactor". In: *International Journal of Hydrogen Energy* 32.18, pp. 4821–4829. DOI: 10.1016/j.ijhydene.2007.08.013.
- Plevachuk, Y., V. Sklyarchuk, W. Hoyer, and I. Kaban (2006):** "Electrical conductivity, thermoelectric power and viscosity of liquid Sn-based alloys". In: *Journal of Materials Science* 41.14, pp. 4632–4635. DOI: 10.1007/s10853-006-0053-4.
- Poling, B. E., J. M. Prausnitz, and J. P. O'Connell (2001):** *The Properties of Gases and Liquids (Vol 5.)* Vol. 1. New York: Mcgraw-hill, p. 803. DOI: 10.1036/0070116822.
- Ponter, A., G. Davies, T. Ross, and P. Thornley (1967):** "The influence of mass transfer on liquid film breakdown". In: *International Journal of Heat and Mass Transfer* 10.3, pp. 349–352. DOI: 10.1016/0017-9310(67)90151-2.
- Potapkin, B., A Babaritski, and M Deminskiy (1999):** "Plasma catalysis of hydrocarbon reactions in pulse microwave discharge". In: *33rd Thermophysics*.
- Pregger, T., D. Graf, W. Krewitt, C. Sattler, M. Roeb, and S. Möller (2009):** "Prospects of solar thermal hydrogen production processes". In: *International Journal of Hydrogen Energy* 34.10, pp. 4256–4267. DOI: 10.1016/j.ijhydene.2009.03.025.
- Rischen, S. (2016):** "Hydrodynamische Untersuchung von gas-fluessig-fluessig Pfropfenstroemungen". Master Thesis. TU Dortmund.
- Rodat, S., S. Abanades, J.-L. Sans, and G. Flamant (2009):** "Hydrogen production from solar thermal dissociation of natural gas: development of a 10kW solar chemical reactor prototype". In: *Solar Energy* 83.9, pp. 1599–1610. DOI: 10.1016/j.solener.2009.05.010.
- Rodat, S., S. Abanades, J.-L. Sans, and G. Flamant (2010):** "A pilot-scale solar reactor for the production of hydrogen and carbon black from methane splitting". In: *International Journal of Hydrogen Energy* 35.15, pp. 7748–7758. DOI: 10.1016/j.ijhydene.2010.05.057.
- Rodat, S., S. Abanades, and G. Flamant (2011):** "Co-production of hydrogen and carbon black from solar thermal methane splitting in a tubular reactor prototype". In: *Solar Energy* 85.4, pp. 645–652. DOI: 10.1016/j.solener.2010.02.016.
- Salinger, A. and G Eigenberger (1996a):** "The direct calculation of periodic states of the reverse flow reactor-I. Methodology and propane combustion results". In: *Chemical Engineering Science* 51.21, pp. 4903–4913. DOI: 10.1016/0009-2509(96)00328-4.
- Salinger, A. and G Eigenberger (1996b):** "The direct calculation of periodic states of the reverse flow reactor-II. Multiplicity and instability". In: *Chemical Engineering Science* 51.21, pp. 4915–4922. DOI: 10.1016/0009-2509(96)00327-2.
- Schaefer, R. J., D Vortmeyer, and C. C. Watson (1974):** "Steady state behavior of moving bed reactors". In: *Chemical Engineering Science* 29.1, pp. 119–127. DOI: 10.1016/0009-2509(74)85037-2.
- Schultz, I. and D. W. Agar (2015):** "Decarbonisation of fossil energy via methane pyrolysis using two reactor concepts: Fluid wall flow reactor and molten metal capillary reactor". In: *International Journal of Hydrogen Energy* 40.35, pp. 11422–11427.
- Serban, M., M. A. Lewis, C. L. Marshall, and R. D. Doctor (2003):** "Hydrogen Production by Direct Contact Pyrolysis of Natural Gas". In: *Energy & Fuels* 17.3, pp. 705–713. DOI: 10.1021/ef020271q.

- Shao, N., A. Gavriilidis, and P. Angeli (2009):** "Flow regimes for adiabatic gas–liquid flow in microchannels". In: *Chemical Engineering Science* 64.11, pp. 2749–2761. DOI: 10.1016/j.ces.2009.01.067.
- Sharafat, S and N Ghoniem (2000):** "Summary of thermo-physical properties of Sn and compounds of Sn-H, Sn-O, Sn-C, Sn-Li, Sn-Si and comparison of properties of Sn, Sn-Li, Li, Pb-Li". In: *University of California UCLA-UCMEP-00-31 Report*.
- Siegel, R and J. Howell (2013):** *Wärmeübertragung durch Strahlung: Teil 1 Grundlagen und Materialeigenschaften*. 2nd ed. Berlin Heidelberg New York Tokyo: Springer-Verlag. DOI: 10.1007/978-3-642-83267-3.
- Siemens AG (2010):** *Tougher than any challenge*. Tech. rep. Erlangen: Siemens AG, pp. 1–8.
- Simo, M., S. Sivashanmugam, C. J. Brown, and V. Hlavacek (2009):** "Adsorption / Desorption of Water and Ethanol on 3A Zeolite in Near-Adiabatic Fixed Bed". In: *Industrial & Engineering Chemistry Research* 48.20, pp. 9247–9260. DOI: 10.1021/ie900446v.
- Sohal, M. S., M. A. Ebner, P. Sabharwall, and P. Sharpe (2010):** "Engineering database of liquid salt thermophysical and thermochemical properties". In: *Idaho National Laboratory, Idaho Falls*.
- Steinberg, M (1989):** "Modern and prospective technologies for hydrogen production from fossil fuels". In: *International Journal of Hydrogen Energy* 14.11, pp. 797–820. DOI: 10.1016/0360-3199(89)90018-9.
- Steinberg, M (1999):** "Fossil fuel decarbonization technology for mitigating global warming". In: *International Journal of Hydrogen Energy* 24.8, pp. 771–777. DOI: 10.1016/S0360-3199(98)00128-1.
- Steinfeld, A, V Kirillov, G Kuvshinov, Y Mogilnykh, and A Reller (1997):** "Production of filamentous carbon and hydrogen by solarthermal catalytic cracking of methane". In: *Chemical Engineering Science* 52.20, pp. 3599–3603. DOI: 10.1016/S0009-2509(97)00166-8.
- Steinfeld, A. (2005):** "Solar thermochemical production of hydrogen—a review". In: *Solar Energy* 78.5, pp. 603–615. DOI: 10.1016/j.solener.2003.12.012.
- Suelves, I, M. J. Lázaro, R Moliner, J. L. Pinilla, and H Cubero (2007):** "Hydrogen production by methane decarbonization: Carbonaceous catalysts". In: *International Journal of Hydrogen Energy* 32.15, pp. 3320–3326. DOI: 10.1016/j.ijhydene.2007.05.028.
- Szymanska, M., A. Malaika, P. Rechnia, A. Miklaszewska, and M. Kozłowski (2015):** "Metal/activated carbon systems as catalysts of methane decomposition reaction". In: *Catalysis Today* 249. Carbon in Catalysis, pp. 94–102. DOI: <http://dx.doi.org/10.1016/j.cattod.2014.11.025>.
- Talens-Alesson, F. I. (1999):** "The modelling of falling film chemical reactors". In: *Chemical Engineering Science* 54.12, pp. 1871–1881. DOI: 10.1016/S0009-2509(98)00497-7.
- Thoma, K (1978):** "Multiple Reaktionszustände eines Wanderbettreaktors: Theorie u. Experiment". PhD thesis.
- Torres-Ortega, J. A., G Morales Medina, O. Y. Surez Palacios, and F. J. Snchez Castellanos (2009):** "Mathematical model of a falling film reactor for methyl ester

- sulfonation". In: *Chemical Product and Process Modeling* 4.5. DOI: 10.2202/1934-2659.1393.
- Trachsel, F., A. Günther, S. Khan, and K. F. Jensen (2005):** "Measurement of residence time distribution in microfluidic systems". In: *Chemical Engineering Science* 60.21, pp. 5729–5737. DOI: 10.1016/j.ces.2005.04.039.
- Trambouze, P and J. Euzen (2004):** *Chemical reactors*. Editions OPHRYS.
- Turner, J. A. (1999):** "A Realizable Renewable Energy Future". In: *Science* 285.5428, pp. 687–689. DOI: 10.1126/science.285.5428.687.
- Tyrer, D (1931):** "Production of hydrogen". In: *US Patent 1,803,221*.
- UNFCCC. Conference of the Parties (COP) (2015):** "Adoption of the Paris Agreement. Proposal by the President." In: *Paris Climate Change Conference - November 2015, COP 21 21932*. December, p. 32. DOI: FCCC/CP/2015/L.9/Rev.1. arXiv: arXiv:1011.1669v3.
- United Nations Environment Programme. Division of Technology, I. (2006):** *Hydrogen economy: a non-technical review*. UNEP DTIE Energy Branch, p. 39.
- U.S. Energy Information Administration:** *International Energy Statistics*. URL: <http://www.eia.gov/cfapps/ipdbproject/iedindex3.cfm?tid=3&pid=3&aid=6&cid=regions&syid=1980&eyid=2015&unit=TCF> (visited on 05/26/2017).
- VDI-e.V., ed. (2013):** *VDI-Wärmeatlas*. Ed. by VDI-e.V. Berlin, Heidelberg: Springer-Verlag, p. 1760. DOI: 10.1007/978-3-642-19981-3T4-Mit320TabellenY3-14.12.2015M4-Citavi.
- Veziroglu, T (1987):** "Hydrogen technology for energy needs of human settlements". In: *International Journal of Hydrogen Energy* 12.2, pp. 99–129. DOI: 10.1016/0360-3199(87)90086-3.
- Villadsen, J. and W. Stewart (1967):** "Solution of boundary-value problems by orthogonal collocation". In: *Chemical Engineering Science* 22.11, pp. 1483–1501. DOI: 10.1016/0009-2509(67)80074-5.
- Wächter, A. and L. Biegler (2006):** "On the Implementation of a Primal-Dual Interior Point Filter Line Search Algorithm for Large-Scale Nonlinear Programming". In: *Mathematical Programming* 106.1, pp. 25–57. DOI: 10.1007/BF01582568.
- Weger, L., A. Abánades, and T. Butler (2017):** "Methane cracking as a bridge technology to the hydrogen economy". In: *International Journal of Hydrogen Energy* 42.1, pp. 720–731. DOI: 10.1016/j.ijhydene.2016.11.029.
- Williams, D. (2006):** "Assessment of candidate molten salt coolants for the NGNP/NHI Heat-Transfer Loop". In: *ORNL/TM-2006/69, Oak Ridge National Laboratory*,
- Xu, Q., N. Oudalov, Q. Guo, H. M. Jaeger, and E. Brown (2012):** "Effect of oxidation on the mechanical properties of liquid gallium and eutectic gallium-indium". In: *Physics of Fluids* 24.6, pp. 1–13. DOI: 10.1063/1.4724313.
- Zhukov, M. F. and I. M. Zasytkin (2007):** *Thermal plasma torches : design, characteristics, application*. Cambridge International Science Pub, p. 596.

Supervised Theses

Anders, M: "Experimentelle Untersuchung eines Seitenstrahlreaktors zur Hochtemperatur Methanpyrolyse". Bachelor's Thesis, November 2016, Technische Universität Dortmund

Asmanoglo, C: "Modelling and Simulation of a Falling Film Reactor for the High Temperature Pyrolysis of Methane". Bachelor's Thesis, March 2015, Technische Universität Dortmund

Asmanoglo, C: "Modeling and Optimization of Adsorptive Reactor Concepts for the rWGS Reaction". Master Thesis, November 2016, Technische Universität Dortmund

Bürger, M. T.: "Modellgestützte Analyse zum Betriebsverhalten eines RWGS Reaktors unter technisch relevanten Bedingungen". Bachelor's Thesis, April 2015, Technische Universität Dortmund

Krieger, W: "Untersuchungen zur Methanpyrolyse in einem Kapillarreaktor". Master Thesis, April 2016, Technische Universität Dortmund

Schwarz, S: "Simulation und experimentelle Untersuchungen zu Hochtemperatur Methanpyrolyse im Schmelzmetall-Kapillarreaktor". Master Thesis, November 2014, Technische Universität Dortmund

Voß, J. M: "Hydrodynamic Studies on Molten Metal Film Reactors for High Temperature Methane Pyrolysis". Bachelor's Thesis, November 2016, Technische Universität Dortmund

Wölfelschneider, S: "Functionality Structuring to Improve the Performance of an Adsorptive Reactor". Bachelor's Thesis, May 2016, Technische Universität Dortmund

A

Supplementary Data to Chapter 2

A.1. Material Properties

For the simulations, the following data was used. It should be noted that for tin, the data in the literature can be found up to higher temperatures than simulated. However, for FLiNaK, most correlations are up to 1200K or lower so, in the simulations, extrapolations to the higher temperatures were performed.

Table A.1.: Properties of the liquid phase

Property	Tin	FLiNaK
Density	$\rho = \frac{1000}{1.663 \cdot 10^{-5} \cdot (T - 573.15) + 0.1444}$ ¹	$\rho = 2729.3 - 0.73 \cdot T$ ²
Viscosity	$\eta = 4.2 \cdot 10^{-4} \cdot \exp\left(\frac{6.56 \cdot 10^3}{RT}\right)$ ³	$\eta = 4.0 \cdot 10^{-5} \cdot \exp\left(\frac{4170}{T}\right)$ ⁴
Surface tension	$\sigma = (551 - 0.09 \cdot (T - 505)) \cdot 10^{-3}$ ⁵	$\sigma = 0.2726 - 1.014 \cdot 10^{-4} \cdot T$ ⁶
Heat capacity	$c_p = -1.43 \cdot 10^{-2} \cdot (T - 505.15) + 250.41$ ¹	$c_p = 976.78 + 1.0634 \cdot T$ ²
Thermal conductivity	$\lambda = 14.185 + 0.0257 \cdot T$ ⁷	$\lambda = 0.36 + 5.6 \cdot 10^{-4} \cdot T$ ²
Vapor pressure	1.33 Pa at 1462 K ¹	4000 Pa at 1473.15 K ⁴

¹(Sharafat and Ghoniem 2000)

²(Sohal et al. 2010)

³(Plevachuk et al. 2006)

⁴(Williams 2006)

⁵(Nogi et al. 1989)

⁶(Janz 1988)

⁷(Giordanengo et al. 1999)

Table A.2.: Properties of the wall materials

Material	Thermal conductivity
Mullite	$\lambda = 9.075 - 1.055 \cdot 10^{-2} \cdot T + 7.344 \cdot 10^{-6} \cdot T^2 - 1.726 \cdot 10^{-9} \cdot T^3$ ⁸
Alumina	$\lambda = 5.5 + 35.5 \cdot \exp(-0.0033(T - 273))$ ⁹

A.2. Heat and Mass Transfer Correlations

To calculate the heat and mass transport coefficient, correlations based on dimensionless numbers were used. Usually, the correlations should be equivalent. For mass transfer correlations based on both, the Reynolds and Schmidt numbers were used, which are also widely used in the literature (Dabir et al. 1996; Gómez Mendoza et al. 2014). However, for heat transfer due to its wider range of validity, the correlation by Trambouze and Euzen (2004) was used instead. This correlation omits the Prandtl number. Nonetheless, for the simulated conditions, this value is close to unity, so deviations, if any, should be minor.

Table A.3.: Heat and mass transfer correlations

Property	Equation
Heat transfer	$Nu_G = \frac{h_{GL} \cdot (d_R - 2 \cdot \delta_L)}{\lambda_G} = 0.175 \cdot Re_G^{0.82}$ ¹⁰
Mass transfer	$Sh_G = \frac{h_{m,i} \cdot (d_R - 2 \cdot \delta_L)}{D_{i,j}} = 0.0014 \cdot Re_G^{1.00} Sc_G^{0.33}$ $Re < 2000$ 11
	$Sh_G = \frac{h_{m,i} \cdot (d_R - 2 \cdot \delta_L)}{D_{i,j}} = 0.023 \cdot Re_G^{0.83} Sc_G^{0.44}$ $2000 \leq Re < 35000$

For the gas properties, i.e. viscosity, thermal conductivity and diffusion coefficients, the standard mixture properties for a multicomponent gas phase were used (Poling et al. 2001).

⁸(Anggono 2005)

⁹(Auerkari 1996)

¹⁰(Trambouze and Euzen 2004)

¹¹(Abe et al. 1991; Dabir et al. 1996)

B

Supplementary Data to Chapter 4

Table B.1.: Results for side-stream location and reactor length

L_R / m	$\zeta_{feed} = 0.3$		$\zeta_{feed} = 0.4$		$\zeta_{feed} = 0.5$		$\zeta_{feed} = 0.6$		$\zeta_{feed} = 0.7$		$\zeta_{feed} = 0.8$	
	$\frac{F_{side}}{F_{G,0}}$	$\frac{F_{C,0}}{F_{G,0}}$	$\frac{F_{side}}{F_{G,0}}$	$\frac{F_{C,0}}{F_{G,0}}$	$\frac{F_{side}}{F_{G,0}}$	$\frac{F_{C,0}}{F_{G,0}}$	$\frac{F_{side}}{F_{G,0}}$	$\frac{F_{C,0}}{F_{G,0}}$	$\frac{F_{side}}{F_{G,0}}$	$\frac{F_{C,0}}{F_{G,0}}$	$\frac{F_{side}}{F_{G,0}}$	$\frac{F_{C,0}}{F_{G,0}}$
8	2.011	4.644	1.964	4.7	1.944	4.718	1.937	4.709	1.942	4.671	1.965	4.593
9	1.981	4.676	1.941	4.72	1.925	4.73	1.92	4.712	1.926	4.665	1.946	4.579
10	1.955	4.698	1.923	4.736	1.91	4.734	1.907	4.71	1.912	4.556	1.931	4.564
20	1.851	4.78	1.84	4.752	1.837	4.7	1.838	4.635	1.844	4.556	1.857	4.452
40	1.793	4.523	1.789	4.665	1.789	4.594	1.792	4.523	1.798	4.446	1.808	4.35

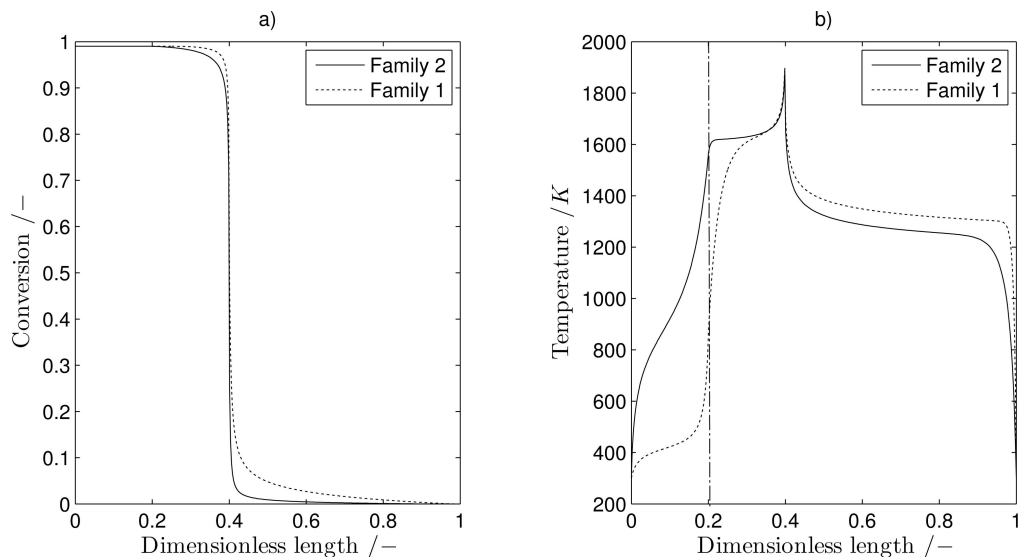


Figure B.1.: Conversion (a) and Temperature (b) profiles for two families of solutions for the side-stream reactor. Family 1: lower outlet gas temperature. Family 2: Higher gas outlet temperature

Table B.2.: Results for side-stream location and reactor length

ξ_{inlet} / -	ξ_{outlet} / -	$T_{G,side-outlet}$ / K	$F_{C,0}/F_{G,0}$ /-	F_{side} / mol s ⁻¹	F_{H_2} / mol s ⁻¹	X_{end} / -
0.401	0.10025	839.2148	4.7738	318.8427	44.1539	0.99
	0.15038	852.5232	4.7702	321.1159	44.1515	0.99
	0.2005	870.3853	4.7618	324.6458	43.947	0.99
	0.25063	908.2552	4.7251	330.8375	43.3874	0.99
	0.30075	374.7625	10.1928	513.859	95.4791	0.99004
0.50125	0.10025	752.6996	4.975	318.3783	47.0866	0.99
	0.15038	846.8709	4.7547	318.5206	43.7645	0.99
	0.2005	849.3834	4.7668	320.1294	43.999	0.99
	0.25063	857.7778	4.769	322.4136	43.9677	0.99
	0.30075	875.8932	4.7577	325.95	43.7584	0.99
0.6015	0.10025	867.3563	4.6767	317.1393	42.9149	0.99
	0.15038	864.3953	4.6998	317.9425	43.008	0.99
	0.2005	860.2233	4.7225	318.9184	43.5041	0.99
	0.25063	857.687	4.7418	320.148	43.6583	0.99
	0.30075	854.7439	4.7651	321.7768	43.8646	0.99
0.70175	0.10025	898.4063	4.5983	317.9436	42.0307	0.99
	0.15038	855.9081	4.8086	329.8383	44.97	0.9934
	0.2005	888.6254	4.647	319.2707	42.5418	0.99
	0.25063	729.6194	5.0675	322.6722	48.3722	0.99
	0.30075	875.796	4.6985	321.113	43.1085	0.99
0.80201	0.10025	693.0005	5.1628	325.6987	49.7976	0.99
	0.15038	937.0526	4.5212	320.5665	41.0236	0.99
	0.2005	932.2383	4.5423	321.1536	41.4632	0.99
	0.25063	924.7831	4.5689	321.8168	41.5105	0.99
	0.30075	851.2824	4.7609	322.8823	44.3877	0.99

Table B.3.: Optimization results for the plasma concept as a function of reactor length for three sets of initial conditions (location = 0.5)

Non-converged solution. Solid to gas ratio =5					
L_R / m	$f(\theta)$ / -	F_{plasma} / mol s ⁻¹	$F_{C,0}/F_{G,0}$ / -	X_{end} / -	End status
4	0.011303	1.9427	3.368	0.99	Infeasible
5	0.198	34.0323	3.3049	0.99	Success
6	0.40387	69.4174	8.0438	0.99	Success
7	0.19636	33.7499	3.369	0.99	Success
8	0.1964	33.7581	3.3986	0.99	Success
9	0.1911	32.8462	3.0816	0.99208	Solved to Acceptable Level
10	0.19154	32.9215	3.1784	0.99003	Success
15	0.19498	33.5129	3.3932	0.99	Success
20	0.22682	38.9866	4.3442	0.99	Success
Non-converged solution. Solid to gas ratio =3					
4	0.20938	35.988	3.5403	0.99	Success
5	0.20476	35.1942	3.5467	0.99	Success
6	0.19658	33.7887	3.3325	0.99002	Success
7	0.19559	33.6188	3.3373	0.99	Success
8	0.21554	37.0466	3.9788	0.99006	Success
9	0.20292	34.8784	3.6326	0.99	Success
10	0.1967	33.809	3.43	0.99	Success
15	0.19893	34.1914	3.5401	0.99	Success
20	0.19067	32.7729	3.1951	0.99	Success
Converged solution. Solid to gas ratio =3					
4	0.20149	34.6326	3.2429	0.99	Success
5	0.20549	35.3206	3.5694	0.99	Success
6	0.19461	33.4497	3.2395	0.99	Success
7	0.17942	30.8386	3.2032	0.99828	Solved to Acceptable Level
8	0.19269	33.1198	3.2245	0.99	Success
9	0.19106	32.8397	2.9868	0.9902	Success
10	0.1997	34.3247	3.537	0.99	Success
15	0.1905	32.7429	3.1331	0.99155	Success
20	0.18942	32.5573	3.1025	0.99755	Success

Table B.4.: Optimization results for the plasma concept as a function of inlet location

ζ_{feed}	$f(\vartheta)$	F_{plasma}	$F_{C,0}/F_{G,0}$	X_{end}	End status
/ -	/ -	/ mol s ⁻¹	/ -	/ -	
0.10025	0.19519	33.5488	3.0043	0.99	Success
0.2005	0.19204	33.0088	3.0418	0.99	Success
0.30075	0.19128	32.8766	3.048	0.99	Success
0.401	0.19105	32.8386	3.0479	0.99	Success
0.50125	0.1911	32.8464	3.0679	0.99	Success
0.6015	0.19127	32.8754	3.0438	0.99	Success
0.70175	0.19232	33.0565	3.1431	0.99	Success
0.80201	0.19268	33.1183	3.0386	0.99	Success
0.90226	0.20298	34.8882	3.4155	0.99	Success

Table B.5.: Optimization results for the resistive heating concept. Low-resistivity carbon. 165 V potential

Run ID	L_{tot} / m	L_{top} /m	L_{middle} /m	L_{bottom} / m	D_R / m	$f(\vartheta)$ / MW	U / V	I / kA	$F_{C,0}/F_{G,0}$ / -	X_{end} / -	ρ_M / Ohm m	End status
1	7.85	0.5	3.85	3.5	4	17.77	165	107.7	2.7	0.99	0.005	Success
2	7.93	1	3.93	3	4	17.4	165	105.44	2.72	0.99	0.005	Success
3	7.95	1.5	3.95	2.5	4	17.32	165	104.99	2.74	0.99	0.005	Success
4	7.99	2	3.99	2	4	17.15	165	103.96	2.75	0.99	0.005	Success
5	7.95	2.5	3.95	1.5	4	17.32	165	104.99	2.76	0.99	0.005	Success
6	7.93	3	3.93	1	4	17.4	165	105.48	2.77	0.99	0.005	Success
7	7.84	3.5	3.84	0.5	4	17.81	165	107.91	2.77	0.99	0.005	Success
8	8.85	0.5	3.85	4.5	4	17.78	165	107.75	2.69	0.99	0.005	Success
9	8.92	1	3.92	4	4	17.44	165	105.72	2.72	0.99	0.005	Success
10	8.94	1.5	3.94	3.5	4	17.35	165	105.18	2.73	0.99	0.005	Success
11	8.99	2	3.99	3	4	17.15	165	103.96	2.74	0.99	0.005	Success
12	8.97	2.5	3.99	2.5	4	17.14	165	103.9	2.75	0.99	0.005	Success
13	8.99	3	3.99	2	4	17.15	165	103.95	2.76	0.99	0.005	Success
14	8.94	3.5	3.94	1.5	4	17.35	165	105.17	2.76	0.99	0.005	Success
15	8.92	4	3.92	1	4	17.45	165	105.75	2.77	0.99	0.005	Success
16	8.84	4.5	3.84	0.5	4	17.82	165	107.98	2.78	0.99	0.005	Success
17	9.83	0.5	3.83	5.5	4	17.87	165	108.31	2.69	0.99	0.005	Success
18	9.92	1	3.92	5	4	17.44	165	105.67	2.71	0.99	0.005	Success
19	9.95	1.5	3.95	4.5	4	17.34	165	105.1	2.73	0.99	0.005	Success
20	9.96	2	3.96	4	4	17.3	165	104.84	2.74	0.99	0.005	Success
21	9.96	2.5	3.96	3.5	4	17.28	165	104.71	2.75	0.99	0.005	Success
22	9.96	3	3.96	3	4	17.27	165	104.67	2.75	0.99	0.005	Success
23	9.96	3.5	3.96	2.5	4	17.28	165	104.7	2.76	0.99	0.005	Success
24	9.96	4	3.96	2	4	17.3	165	104.82	2.76	0.99	0.005	Success
25	9.95	4.5	3.95	1.5	4	17.34	165	105.09	2.77	0.99	0.005	Success
26	9.92	5	3.92	1	4	17.44	165	105.71	2.77	0.99	0.005	Success
27	9.82	5.5	3.82	0.5	4	17.91	165	108.54	2.78	0.99	0.005	Success

Table B.6.: Optimization results for the resistive heating concept. High-resistivity carbon. 470 V potential

Run ID	L_{tot} / m	L_{top} /m	L_{middle} /m	L_{bottom} / m	D_R / m	$f(\vartheta)$ / MW	U / V	I / kA	$F_{C,0}/F_{G,0}$ / -	X_{end} / -	ρ_M / Ohm m	End status
1	7.94	0.5	3.94	3.5	4	17.63	470	37.52	2.7	0.99	0.04	Success
2	7.99	1	3.99	3	4	17.4	470	37.03	2.72	0.99	0.04	Success
3	8.01	1.5	4.01	2.5	4	17.33	470	36.87	2.74	0.99	0.04	Success
4	8.03	2	4.03	2	4	17.23	470	36.67	2.75	0.99	0.04	Success
5	8	2.5	4	1.5	4	17.33	470	36.87	2.76	0.99	0.04	Success
6	7.99	3	3.99	1	4	17.41	470	37.04	2.77	0.99	0.04	Success
7	7.91	3.5	3.91	0.5	4	17.75	470	37.77	2.77	0.99	0.04	Success
8	8.92	0.5	3.92	4.5	4	17.69	470	37.65	2.69	0.99	0.04	Success
9	8.98	1	3.98	4	4	17.45	470	37.12	2.72	0.99	0.04	Success
10	9.02	1.5	4.02	3.5	4	17.28	470	36.76	2.73	0.99	0.04	Success
11	9.03	2	4.03	3	4	17.24	470	36.68	2.74	0.99	0.04	Success
12	9.05	2.4	4.05	2.6	4	17.15	470	36.48	2.75	0.99	0.04	Success
13	9.03	3	4.03	2	4	17.24	470	36.68	2.76	0.99	0.04	Success
14	9.02	3.5	4.02	1.5	4	17.28	470	36.76	2.76	0.99	0.04	Success
15	8.98	4	3.98	1	4	17.45	470	37.13	2.77	0.99	0.04	Success
16	8.89	4.5	3.89	0.5	4	17.82	470	37.91	2.78	0.99	0.04	Success
17	9.88	0.5	3.88	5.5	4	17.87	470	38.02	2.69	0.99	0.04	Success
18	9.96	1	3.96	5	4	17.53	470	37.3	2.71	0.99	0.04	Success
19	10.02	1.5	4.02	4.5	4	17.26	470	36.72	2.73	0.99	0.04	Success
20	10.03	2	4.03	4	4	17.21	470	36.62	2.74	0.99	0.04	Success
21	10.04	2.5	4.04	3.5	4	17.19	470	36.57	2.75	0.99	0.04	Success
22	10.04	3	4.04	3	4	17.18	470	36.56	2.75	0.99	0.04	Success
23	10.04	3.5	4.04	2.5	4	17.19	470	36.57	2.76	0.99	0.04	Success
24	10.03	4	4.03	2	4	17.21	470	36.61	2.76	0.99	0.04	Success
25	10.02	4.5	4.02	1.5	4	17.25	470	36.71	2.77	0.99	0.04	Success
26	9.96	5	3.96	1	4	17.53	470	37.31	2.77	0.99	0.04	Success
27	9.88	5.5	3.88	0.5	4	17.91	470	38.1	2.78	0.99	0.04	Success

C

Supplementary Data to Chapter 5

Table C.1.: Boundaries for the optimization variables

Variable	Lower constraint	Upper constraint	Reason
t_{rxn}	100	600	Lower constraint to avoid infinitesimal cycles, upper constraint to avoid suboptimal long cycles, both based on previous simulations
t_{reg}	100	1000	Same as for reaction but allowing for longer regeneration cycles based on slower rates of desorption
t_{start}	0.5	75	Minimal purging time to be shorter than minimal mean residence time of 1 second. Upper constraint 1.5 longer than maximal residence time.
L_R	0.5	2	Based on analysis of the system and to limit the region for the optimizer. In the case when the optimal solution lies at either end, that value would have been relaxed. However, that was not the case
$\phi_{cat,1...5}$	0	1	Physical limit
u_G	0.05	0.5	Same as for reactor length (L_R)
$y_{CO_2,in}$	0.15	0.5	Upper constraint for equimolar feed, lower constraint to reduce the region of search (could be relaxed if necessary)
P	1	30	Cases in vacuum or high pressures were out of the scope of the paper
T_x	200	260	Upper value to avoid Zeolithe degradation, lower limit to reduce search area (could be relaxed)

Table C.2.: Initial values for the optimization runs

Run ID	t_{rxn} / s	t_{reg} / s	t_{start} / s	L_R / m	$\phi_{cat,1}$ / -	$\phi_{cat,2}$ / -	$\phi_{cat,3}$ / -	$\phi_{cat,4}$ / -	$\phi_{cat,5}$ / -	u_G / $m\ s^{-1}$	$y_{CO_2,in}$ / -	P / bar	$T_{rxn,in}$ / °C	$T_{reg,in}$ / °C	$T_{W,1}$ / °C	$T_{W,2}$ / °C	$T_{W,3}$ / °C	$T_{W,4}$ / °C	$T_{W,5}$ / °C	Objective Function / $mol\ s^{-1}\ m^{-2}$	STY / $mol\ s^{-1}\ m^{-3}$	
Non-adiabatic	1	151	500	14	1.35	0.5	0.5	0.5	0.5	0.12	0.3	3	250	250	229	257	260	244	257	0.53	0.39	
		170	600	30	1.5	0.7	0.6	0.5	0.4	0.3	0.26	5	250	250	230	245	250	250	254	257	0.64	0.43
	2	151	500	14	1.35	0.5	0.5	0.5	0.5	0.12	0.3	3	250	250	229	257	260	244	257	0.53	0.39	
		170	600	30	1.5	0.4	0.4	0.4	0.4	0.4	0.1	0.26	5	250	250	230	245	250	250	254	0.64	0.43
	3	151	500	14	1.35	0.5	0.5	0.5	0.5	0.5	0.12	0.3	3	250	250	250	250	250	250	250	0.52	0.39
		170	600	30	1.5	0.7	0.6	0.5	0.4	0.3	0.1	0.26	5	250	250	250	250	250	250	250	0.64	0.43
Adiabatic	1	151	500	14	1	0.5	0.5	0.5	0.5	0.09	0.3	3	250	250	229	257	260	244	257	0.39	0.39	
		170	600	30	1	0.7	0.6	0.5	0.4	0.3	0.1	0.26	5	250	250	230	245	250	254	257	0.66	0.66
	5	151	500	20	1.5	0.5	0.5	0.5	0.5	0.5	0.1	0.3	3	250	250	229	257	260	244	257	0.41	0.27
		170	600	30	1.5	0.7	0.6	0.5	0.4	0.3	0.1	0.26	5	250	250	230	245	250	250	254	0.64	0.43
	6	151	500	30	2	0.5	0.5	0.5	0.5	0.5	0.11	0.3	3	250	250	229	257	260	244	257	0.41	0.21
		170	600	30	2	0.7	0.6	0.5	0.4	0.3	0.1	0.26	5	250	250	230	245	250	250	254	0.63	0.32
Adiabatic	1	151	500	14	1.35	0.5	0.5	0.5	0.5	0.12	0.3	3	255	255	-	-	-	-	-	-	0.52	0.39
		170	600	30	1.5	0.7	0.6	0.5	0.4	0.3	0.1	0.26	5	250	250	-	-	-	-	-	0.64	0.43
	2	151	500	14	1.35	0.5	0.5	0.5	0.5	0.5	0.12	0.3	3	255	255	-	-	-	-	-	0.52	0.38
		170	600	30	1.5	0.4	0.4	0.4	0.4	0.4	0.1	0.26	5	250	250	-	-	-	-	-	0.64	0.43
	4	151	500	14	1	0.5	0.5	0.5	0.5	0.5	0.09	0.3	3	250	250	-	-	-	-	-	0.39	0.39
		170	600	30	1	0.7	0.6	0.5	0.4	0.3	0.1	0.26	5	250	250	-	-	-	-	-	0.66	0.66
5	151	500	20	1.5	0.5	0.5	0.5	0.5	0.5	0.1	0.3	3	250	250	-	-	-	-	-	0.41	0.27	
	170	600	30	1.5	0.7	0.6	0.5	0.4	0.3	0.1	0.26	5	250	250	-	-	-	-	-	0.64	0.43	
6	151	500	30	2	0.5	0.5	0.5	0.5	0.5	0.11	0.3	3	250	250	-	-	-	-	-	0.42	0.21	
	170	600	30	2	0.7	0.6	0.5	0.4	0.3	0.1	0.26	5	250	250	-	-	-	-	-	0.63	0.32	

Table C.3.: Optimization Results

Run ID	t_{rxn} / s	t_{reg} / s	t_{start} / s	L_R / m	$\phi_{cat,1}$ / -	$\phi_{cat,2}$ / -	$\phi_{cat,3}$ / -	$\phi_{cat,4}$ / -	$\phi_{cat,5}$ / -	μ_G / $m\ s^{-1}$	$y_{CO_2,in}$ / -	P / bar	$T_{rxn,in}$ / °C	$T_{reg,in}$ / °C	$T_{W,1}$ / °C	$T_{W,2}$ / °C	$T_{W,3}$ / °C	$T_{W,4}$ / °C	$T_{W,5}$ / °C	Objective Function / $mol\ s^{-1}\ m^{-2}$	STY / $mol\ s^{-1}\ m^{-3}$	
Non-adiabatic	1	209	394	21	1.83	0.69	0.59	0.51	0.42	0.08	0.25	17.3	225	260	246	251	252	255	254	3.44	1.88	
		241	581	19	1.84	0.52	0.58	0.5	0.4	0.09	0.25	19.8	254	243	245	248	252	253	256	3.58	1.94	
	2	208	429	16	1.51	0.51	0.51	0.51	0.51	0.09	0.25	14.1	251	240	244	250	256	242	260	2.77	1.83	
		304	538	23	1.8	0.41	0.41	0.41	0.41	0.07	0.25	19.5	251	234	245	245	248	255	252	260	3.58	1.99
	3	222	398	17	1.47	0.55	0.54	0.44	0.39	0.33	0.08	0.25	13	248	248	248	248	248	248	248	2.62	1.78
		491	930	26	1.53	0.57	0.52	0.6	0.33	0.52	0.05	0.25	20.7	243	243	243	243	243	243	243	2.57	1.68
Adiabatic	4	127	243	16	1	0.52	0.63	0.52	0.4	0.06	0.25	16.3	225	250	245	253	252	257	259	2.32	2.32	
		165	365	13	1	0.39	0.52	0.25	0.48	0.07	0.25	12.9	236	256	245	244	254	252	255	2.02	2.02	
	5	121	232	15	1.5	0.61	0.59	0.43	0.59	0.53	0.1	12.8	252	258	250	254	254	259	255	2.89	1.93	
		219	470	15	1.5	0.55	0.55	0.39	0.45	0.46	0.09	14.4	259	260	247	247	252	255	254	2.91	1.94	
	6	243	344	28	2	0.72	0.64	0.51	0.44	0.6	0.07	16.6	237	257	253	248	252	255	255	3.47	1.74	
		215	476	19	2	0.54	0.57	0.51	0.41	0.54	0.1	16.5	254	259	247	251	252	255	252	3.61	1.8	
1	149	309	18	1.37	0.68	0.69	0.54	0.38	0.41	0.08	18.3	242	255	-	-	-	-	-	-	2.72	1.98	
	145	412	15	1.68	0.59	0.6	0.44	0.55	0.36	0.11	15.3	242	242	-	-	-	-	-	-	2.96	1.77	
2	158	289	17	1.3	0.54	0.54	0.54	0.54	0.54	0.07	16.9	222	256	-	-	-	-	-	-	2.58	1.99	
	135	327	16	1.59	0.43	0.43	0.43	0.43	0.43	0.1	16.2	229	255	-	-	-	-	-	-	3.06	1.92	
4	120	345	11	1	0.6	0.53	0.51	0.33	0.43	0.09	0.25	11	256	254	-	-	-	-	-	1.87	1.87	
	117	267	11	1	0.64	0.58	0.38	0.44	0.39	0.09	0.25	11.2	260	256	-	-	-	-	-	2.05	2.05	
5	176	404	16	1.5	0.58	0.51	0.5	0.3	0.52	0.09	0.25	16.3	244	254	-	-	-	-	-	2.59	1.73	
	142	243	19	1.5	0.58	0.43	0.6	0.52	0.39	0.08	0.25	19.4	255	256	-	-	-	-	-	3.06	2.04	
6	289	579	19	2	0.64	0.53	0.39	0.4	0.33	0.09	0.25	18.7	242	251	-	-	-	-	-	3.13	1.56	
	179	460	18	2	0.56	0.53	0.5	0.48	0.4	0.11	0.25	17.6	224	254	-	-	-	-	-	3.36	1.68	

D

Supplementary Data to Chapter 6

Table D.1.: Initial values for single objective optimization

	ϕ_{cat} / -	$u_{G,inlet}$ / $m\ s^{-1}$	$T_{S,inlet}$ / °C	$T_{G,inlet}$ / °C	$T_{W,1}$ / °C	$T_{W,2}$ / °C	$T_{W,3}$ / °C	$T_{W,4}$ / °C	$T_{W,5}$ / °C	P / bar	$y_{CO_2,in}$ / -
Non-Adiabatic	0.5	0.06	250	250	229	257	260	244	257	5	0.3
	0.7	0.05	250	250	250	250	250	250	250	10	0.26
	0.4	0.07	255	255	255	255	255	255	255	3	0.25
Adiabatic	0.5	0.06	250	250	-	-	-	-	-	5	0.3
	0.7	0.05	250	250	-	-	-	-	-	10	0.26
	0.4	0.07	255	255	-	-	-	-	-	3	0.25

Table D.2.: Single objective optimization results for the adiabatic operation

L_R / m	$u_{S,inlet}$ / mm s ⁻¹	ϕ_{cat} / -	$u_{G,inlet}$ / m s ⁻¹	$T_{S,inlet}$ / °C	$T_{G,inlet}$ / °C	P / bar	$y_{CO_2,in}$ / -	$f_1(\vartheta_0)$ / mol m ⁻² s ⁻¹	$f_1(\vartheta_{opti})$ / mol m ⁻² s ⁻¹	$f_1(\vartheta_{opti})/f_1(\vartheta_0)$ / -
0.5	5	0.51	0.05	249	223	15.9	0.25	2.04	6.18	3
	10	0.5	0.0515	249	236	15.9	0.25	3.57	6.2	1.7
	15	0.48	0.0502	249	200	14.8	0.25	1.45	6.12	4.2
1	5	0.47	0.0512	254	205	18.3	0.25	2.01	7.61	3.8
	10	0.52	0.053	254	216	18	0.25	3.53	7.56	2.1
	15	0.48	0.0531	254	256	20	0.25	1.43	7.74	5.4
1.5	5	0.48	0.0501	255	207	20.4	0.25	2	8.28	4.1
	10	0.52	0.0522	256	201	19.1	0.25	3.52	8.18	2.3
	15	0.5	0.0526	255	212	19.6	0.25	1.43	8.23	5.8
0.5	5	0.44	0.05	240	237	29	0.25	1.98	11.01	5.6
	10	0.42	0.05	240	217	27.2	0.25	3.45	10.88	3.2
	15	0.53	0.05	240	200	26.1	0.25	1.43	10.77	7.5
1	5	0.46	0.06	248	200	30	0.25	1.94	14.02	7.2
	10	0.5	0.07	248	201	25.1	0.25	3.4	13.75	4
	15	0.44	0.07	248	244	25.7	0.25	1.41	13.75	9.7
1.5	5	0.47	0.07	251	224	27.2	0.25	1.92	15.37	8
	10	0.46	0.1	252	226	18.3	0.25	3.39	14.49	4.3
	15	0.49	0.07	251	202	27.8	0.25	1.41	15.4	10.9
0.5	5	0.54	0.06	234	200	29.9	0.25	1.95	13.72	7
	10	0.46	0.06	233	206	28.5	0.25	3.4	13.87	4.1
	15	0.46	0.06	233	208	30	0.25	1.42	13.96	9.8
1	5	0.45	0.09	243	212	25.7	0.25	1.91	18.25	9.5
	10	0.47	0.09	244	202	25.6	0.25	3.36	18.3	5.4
	15	0.46	0.1	244	214	22	0.25	1.41	17.81	12.6
1.5	5	0.48	0.12	248	235	22	0.25	1.91	20.37	10.7
	10	0.48	0.1	248	204	27	0.25	3.35	20.98	6.3
	15	0.47	0.11	248	242	24.7	0.25	1.41	20.73	14.7

Table D.3.: Single objective optimization results for the non-adiabatic operation

L_R / m	$u_{S,inlet}$ / mm s ⁻¹	ϕ_{cat} / -	$u_{G,inlet}$ / m s ⁻¹	$T_{S,inlet}$ / °C	$T_{G,inlet}$ / °C	P / bar	$y_{CO_2,in}$ / -	$T_{W,1}$ / °C	$T_{W,2}$ / °C	$T_{W,3}$ / °C	$T_{W,4}$ / °C	$T_{W,5}$ / °C	$f_1(\vartheta_0)$ / mol m ⁻² s ⁻¹	$f_1(\vartheta_{opti})$ / mol m ⁻² s ⁻¹	$f_1(\vartheta_{opti})/f_1(\vartheta_0)$ / -
0.5	5	0.45	0.05	260	204	17.3	0.25	218	227	215	201	260	2.04	7.05	3.4
	10	0.49	0.05	260	248	19.8	0.25	224	238	213	221	223	3.57	7.35	2.1
	15	0.45	0.05	260	212	17.7	0.25	234	202	218	207	260	1.45	7.08	4.9
1	5	0.47	0.05	260	235	22.7	0.25	232	246	226	224	200	2.01	8.63	4.3
	10	0.45	0.05	260	200	19.3	0.25	200	219	206	200	260	3.53	7.95	2.3
	15	0.45	0.051	254	250	21.1	0.25	259	253	258	233	257	1.43	7.91	5.5
1.5	5	0.49	0.05	260	203	21.6	0.25	230	230	230	200	252	2	8.81	4.4
	10	0.48	0.05	260	244	23.7	0.25	206	202	259	242	217	3.52	8.81	2.5
	15	0.48	0.05	260	205	21.4	0.25	206	223	248	200	260	1.43	8.7	6.1
0.5	5	0.42	0.055	260	200	30	0.25	246	217	259	200	258	1.98	13.62	6.9
	10	0.4	0.063	259	233	28.7	0.25	251	243	230	231	231	3.45	13.9	4
	15	0.45	0.059	258	203	27.6	0.25	237	251	234	208	256	1.43	13.29	9.3
1	5	0.45	0.082	260	245	26.2	0.25	248	246	243	202	253	1.94	16.07	8.3
	10	0.45	0.069	259	228	29.9	0.25	243	256	201	247	241	3.4	15.93	4.7
	15	0.44	0.087	258	218	22.6	0.25	250	236	252	220	243	1.41	15.4	10.9
1.5	5	0.46	0.094	260	253	24.8	0.25	249	248	244	228	229	1.93	17.16	8.9
	10	0.47	0.072	260	213	30	0.25	240	235	259	213	249	3.39	17.23	5.1
	15	0.45	0.078	259	248	30	0.25	258	249	241	207	255	1.41	17.3	12.3
0.5	5	0.38	0.075	260	200	30	0.25	250	247	245	219	249	1.95	18.58	9.5
	10	0.4	0.075	260	203	30	0.25	246	251	239	215	254	3.4	18.31	5.4
	15	0.38	0.085	259	214	26.7	0.25	251	239	253	231	237	1.42	18.09	12.7
1	5	0.43	0.105	260	247	29.8	0.25	249	250	248	239	227	1.91	23.12	12.1
	10	0.44	0.104	260	240	29.5	0.25	252	244	251	233	237	3.36	22.98	6.8
	15	0.43	0.103	258	252	30	0.25	257	236	258	232	239	1.41	22.66	16.1
1.5	5	0.45	0.109	260	220	28.7	0.25	250	247	249	213	260	1.91	24.48	12.8
	10	0.45	0.121	260	258	28.2	0.25	249	245	252	236	236	3.35	24.74	7.4
	15	0.45	0.114	259	248	29.5	0.25	257	246	247	243	229	1.41	24.95	17.7

Table D.4.: Initial values for bi-objective optimization

ϕ_{cat} / —	$u_{G,inlet}$ / $m s^{-1}$	$T_{S,inlet}$ / $^{\circ}C$	$T_{G,inlet}$ / $^{\circ}C$	$T_{W,1}$ / $^{\circ}C$	$T_{W,2}$ / $^{\circ}C$	$T_{W,3}$ / $^{\circ}C$	$T_{W,4}$ / $^{\circ}C$	$T_{W,5}$ / $^{\circ}C$	P / <i>bar</i>	$u_{S,in}$ / $m s^{-1}$
0.5	0.06	250	250	229	257	260	244	257	5	1.00E-02
0.7	0.05	250	250	250	250	250	250	250	10	1.50E-02
0.4	0.07	255	255	255	255	255	255	255	3	2.00E-02

Curriculum Vitae

Personal Data

Name: Alejandro Augusto Munera Parra
Born: 24.06.1987
Place of Birth: Bogotá, Colombia
Nationality: Colombian

Education and Professional Experience

01/2005-09/2009 Bachelor's Degree in Chemical Engineering, Universidad de los Andes
- Bachelor's Thesis: First Principles Study of Thermoelectric Properties of Half-Heusler Alloys
- Exchange Semester at Texas A& M University

01/2010-07/2010 Engineer, Universidad de los Andes
- Project coordinator

10/2010-04/2013 Master's degree in Chemical Engineering with emphasis in Process System Engineering, TU Dortmund
- Master's thesis: Analysis of the Stability of Reactive Gas-Liquid Flows in Micro-Channels

10/2013-12/2016 Research Associate, TU Dortmund
- Doctoral Project

from 07/2018 Expert in Chemical Reaction Technology, Covestro